

HEAT AND MASS TRANSFER IN PULSED FLUIDIZED BED OF BIOMASS

by

DENING JIA

B.Sc., China University of Petroleum (East China), 2009

M.Sc., China University of Petroleum (East China), 2012

A THESIS SUBMITTED IN PARTIAL FULFILLMENT OF
THE REQUIREMENTS FOR THE DEGREE OF

DOCTOR OF PHILOSOPHY

in

THE FACULTY OF GRADUATE AND POSTDOCTORAL STUDIES
(Chemical and Biological Engineering)

THE UNIVERSITY OF BRITISH COLUMBIA
(Vancouver)

March 2017

© Dening Jia, 2017

ABSTRACT

Biomass is a promising energy source that has been considered in a variety of thermal conversion processes where fluidized beds with their exceptional heat and mass transfer rates, are often considered as potential candidates. However, the fluidization of biomass is held back by its cohesive nature. This work has demonstrated that pulsed gas flow in fluidized bed is highly effective in overcoming channeling, partial and complete defluidization, without the need for inert bed particles. Both heat transfer and mass transfer were investigated in a pulsed fluidized bed with 0.15 m by 0.10 m rectangular cross-section area, and a fluidized bed with a tapered bottom to improve reactor performance. Biomass used in this work included Douglas fir, pine and switchgrass. Batch drying test was selected as an indirect indicator of gas–solid contact, heat and mass transfer.

Mass transfer was evaluated through batch drying tests, where better gas–solid contact and mass transfer was assessed through the water removal efficiency. An optimum operating condition was identified after analyzing the intricate relationship between pulsation frequency, gas flow rate and the hydrodynamics. A two-phase drying model that linked single-particle mass transfer to macroscopic hydrodynamics in fluidized bed was implemented to verify the effect of flow rate, temperature and biomass properties on drying and mass transfer. Good agreement was observed between the modelled effective diffusivity and experimental results.

Bed-to-surface heat transfer coefficients of all three biomass species in two reactor geometries were measured at various operating conditions. The heat transfer coefficient was influenced greatly by the intensity and frequency of gas pulsation, where both particle convection and gas convection existed. A new heat transfer model was proposed to address the influence of gas pulsation. Modelling results showed good agreement with experimental data.

PREFACE

This dissertation is an original, independent work of the author, D. Jia, under the supervision of X. Bi, C.J. Lim and S. Sokhansanj. All of the work presented henceforth was conducted in the Fluidization Research Centre and the Department of Chemical and Biological Engineering, at the University of British Columbia, Point Grey campus.

The hydrodynamics and drying performance in the rectangular fluidized bed discussed in Chapter 3.1–3.2 have been published [Jia D, Cathary O, Peng J, Bi X, Lim CJ, Sokhansanj S, et al. (2015). Fluidization and drying of biomass particles in a vibrating fluidized bed with pulsed gas flow. *Fuel Processing Technology*, 138, 471-482]. I was the lead investigator, responsible for all of the experimental design, most of data collection and analysis, as well as all manuscript preparation. O. Cathary participated in the experiments. X. Bi, C.J. Lim and S. Sokhansanj et al. were the supervisory authors on this project and were involved throughout the project and manuscript review and revision.

Additional drying and mass transfer results of the rectangular fluidized bed covered in Chapter 3.1–3.2 and Chapter 4.1 have been published [Jia, D., Bi, X., Lim, C. J., Sokhansanj, S., & Tsutsumi, A. (2016). Biomass drying in a pulsed fluidized bed without inert bed particles. *Fuel*, 186, 270-284]. The drying and mass transfer study of the tapered fluidized bed covered in Chapter 3.3–3.4 and Chapter 4.2 have been published [Jia, D., Bi, X., Lim, C. J., Sokhansanj, S., & Tsutsumi, A. Gas–solid contact and mass transfer in a tapered fluidized bed of biomass with pulsed gas flow. *Powder Technology*].

Heat transfer studies covered in Chapter 5 have also been published. [Jia, D., Bi, X., Lim, C. J., Sokhansanj, S., & Tsutsumi, A. (2017). Heat Transfer in a Pulsed Fluidized Bed of Biomass Particles. *Industrial & Engineering Chemistry Research*].

TABLE OF CONTENTS

ABSTRACT	ii
PREFACE	iii
TABLE OF CONTENTS	iv
LIST OF TABLES	x
LIST OF FIGURES	xi
LIST OF SYMBOLS.....	xviii
ACKNOWLEDGEMENTS.....	xxiv
DEDICATION	xxv
1. INTRODUCTION.....	1
1.1 Fluidized bed with pulsed gas flow	4
1.2 Vibrated fluidized bed	8
1.3 Tapered fluidized bed.....	12
1.4 Heat transfer in fluidized bed.....	14
1.4.1 Empirical and semi-empirical correlations	14
1.4.2 Mechanistic models.....	17
1.4.3 Heat transfer study in pulsed and vibrated fluidized beds	18
1.5 Drying and mass transfer in fluidized bed.....	19
1.5.1 Drying in fluidized beds	20
1.5.2 Drying models for fluidized bed	21

1.5.3	Mass transfer in fluidized bed	24
1.6	Outstanding issues	25
1.7	Research objectives	26
1.8	Thesis layout.....	27
2.	EXPERIMENTAL METHODS.....	29
2.1	Experimental plan	29
2.2	Fluidized bed with rectangular cross-section	30
2.3	Fluidized bed with tapered bottom section.....	33
2.4	Data acquisition system	35
2.4.1	Pressure measurements.....	36
2.4.2	Temperature and relative humidity measurement.....	37
2.4.3	High-speed imaging.....	38
2.4.4	Solenoid valve control	38
2.5	Particulate material.....	39
2.6	Batch drying test.....	41
2.6.1	Sample preparation	42
2.6.2	Drying test procedure	42
2.7	Bed-to-surface heat transfer measurement.....	45
2.7.1	Heat transfer probe assembly.....	45
2.7.2	Bed-to-surface heat transfer coefficient.....	47
3.	HYDRODYNAMICS AND DRYING IN PULSED FLUIDIZED BED	52

3.1	Hydrodynamics of the rectangular pulsed fluidized bed	52
3.1.1	Pressure fluctuations	52
3.1.2	Gas–solid flow behaviour	53
3.1.3	Effect of moisture on hydrodynamics	57
3.2	Batch drying in rectangular pulsed fluidized bed	59
3.2.1	Effect of gas flow rate	59
3.2.2	Effect of pulsation frequency	61
3.2.3	Effect of vibration intensity	64
3.2.4	Effect of temperature	65
3.2.5	Effect of pulsation duty cycle	67
3.2.6	Effect of particle size and fine particles	69
3.2.7	Drying mechanisms of three biomass species	76
3.2.8	Natural frequency and damping factor	78
3.3	Hydrodynamics of the tapered pulsed fluidized bed.....	83
3.3.1	Low pulsation frequency of 0.25 – 1.5 Hz	84
3.3.2	Intermediate pulsation frequency of 1.5 – 2.5 Hz	87
3.3.3	Pulsation frequency of 3 – 6.67 Hz:	87
3.4	Batch drying and mass transfer in tapered fluidized bed.....	88
3.4.1	Effect of gas flow rate.....	89
3.4.2	Effect of pulsation frequency	92
3.4.3	Initial bed height.....	93

3.4.4	Comparison of two geometries.....	95
3.5	Conclusion	97
4.	A TWO-PHASE DRYING MODEL FOR PULSED FLUIDIZED BEDS	99
4.1	A model for regular pulsed fluidized bed.....	99
4.1.1	Solid particles.....	101
4.1.2	Interstitial gas.....	103
4.1.3	Bubble phase	103
4.1.4	Parameter evaluation.....	105
4.1.5	Method of solution	105
4.1.6	Effect of flow rate.....	107
4.1.7	Effect of pulsation frequency	109
4.1.8	Effect of biomass species	113
4.1.9	Effect of drying temperature	115
4.2	A model for tapered fluidized bed	118
4.2.1	Model basics.....	118
4.2.2	Effect of flow rate.....	120
4.2.3	Effect of pulsation frequency	121
4.2.4	Comparison of two geometries.....	124
4.2.5	Conclusion	126
5.	HEAT TRANSFER IN PULSED FLUIDIZED BED.....	127
5.1	Heat transfer in rectangular fluidized bed	127

5.1.1	Effect of gas flow rate.....	127
5.1.2	Effect of pulsation frequency	129
5.1.3	Heat transfer properties of pine and switchgrass.....	132
5.1.4	Effect of particle size.....	134
5.1.5	Effect of fine particles.....	136
5.1.6	Effect of vibration	138
5.1.7	Heat transfer at various lateral positions	141
5.2	Heat transfer in tapered fluidized bed.....	144
5.2.1	Effect of flow rate.....	144
5.2.2	Heat transfer at various lateral positions	150
5.2.3	Effect of pulsation duty cycle	153
5.2.4	Effect of particle size and fines	156
5.2.5	Pine and switchgrass.....	158
5.3	Comparison of two geometries.....	162
5.4	Heat transfer modelling in pulsed fluidized bed	165
5.4.1	Overview and particle convective heat transfer.....	165
5.4.2	Gas convective heat transfer	167
5.4.3	Application to pulsed fluidized beds.....	168
5.4.4	Model for low pulsation frequency (Model 1).....	169
5.4.5	Model for high pulsation frequency (Model 2).....	170
5.4.6	Results from the heat transfer modelling	171

5.4.7	Conclusion	174
6.	CONCLUSIONS AND RECOMMENDATIONS	177
6.1	Conclusions	177
6.2	Recommendations for future research.....	180
	REFERENCES.....	182
	APPENDICES	191
	Appendix A. Supplementary experimental results.....	191
A1.	Minimum fluidization velocity	191
A2.	Pulsating stream and fluidization stream	193
A3.	Angle of repose of biomass powders.....	195
A4.	The calculation of drying rate and amount of water evaporated	197
A5.	Sample data set from two-phase drying model.....	199
A6.	Equilibrium moisture content of biomass particles	201
	Appendix B. Heat loss estimation	202
	Appendix C. Data acquisition system.....	207
C1.	Pressure and temperature signal acquisition, display and processing	208
C2.	Relative humidity and real time drying rate	209
C3.	Overall block diagram	210
	Appendix D. High-speed camera images.....	211
	Appendix E. Heat transfer probe assembly	214

LIST OF TABLES

Table 2.1 Properties of the biomass samples at 7% moisture content (dry basis).....	41
Table 2.2 Summary of data acquisition device and acquired signals	50
Table 2.3 A brief summary of experimental operating conditions for the batch drying test	51
Table 3.1 Details for the mixture of coarse and fine particle fractions of Douglas fir sawdust.....	71
Table 4.1 Data fitting results and statistical parameters for the Douglas fir drying curves obtained at different flow rates	108
Table 4.2 Summary of key parameters at various pulsation frequencies	112
Table 4.3 Parameters for the drying curves obtained for various biomass materials	113
Table 4.4 Parameters for the drying curves obtained at various drying temperatures.....	118
Table 4.5 Model-fitted effective diffusivity of Douglas fir at different gas flow rates in pulsed fluidized bed with tapered bottom section, $f=1.5$ Hz.....	120
Table 4.6 Model-fitted effective diffusivity at different pulsation frequencies in the pulsed fluidized bed with a tapered bottom section	122
Table 5.1 Details for the mixture of coarse and fine particle fractions of Douglas fir sawdust.....	136
Table A.1 Measured final moisture content and calculated from measured exhaust gas humidity after 30 min of batch drying	197
Table A.2 Model parameters used for drying modelling, for the case of Douglas fir sawdust in rectangular fluidized bed, drying temperature 20°C, flow rate $U/U_{mf}=1.1$	199
Table B.3 Heat loss estimation summary	206

LIST OF FIGURES

Figure 1.1 Various designs for pulsed fluidized beds. (a) Solenoid valve or butterfly valve; (b) Rotating air distributor; (c) Rotating disc with a fractional opening; (d) Rotating slotted horizontal cylinder..7	
Figure 2.1 Dimensions of the rectangular fluidized bed with pulsed gas flow (a) Side view of the rectangular fluidized bed and related dimensions in millimeter; (b) 3D view and features of the rectangular fluidized bed.....	31
Figure 2.2 Schematic of the rectangular pulsed fluidized bed	33
Figure 2.3 Comparison of the two reactor geometries. (a) the rectangular fluidized bed; (b) tapered fluidized bed.....	34
Figure 2.4 Dimensions of the inserted tapered section at the bottom of the fluidized bed (unit: mm). (a) top view; (b) 3D view; (c) front view; (d) side view.	35
Figure 2.5 Particle size distribution of three biomass species	40
Figure 2.6 Assembly of the heat transfer measurement probe	46
Figure 2.7 Heater probe in the rectangular pulsed fluidized bed. (a) section view of the system with important dimensions annotated in inches; (b) top view of the system; (c) 3D view of the system showing the position of the probe and the rigid connection.....	49
Figure 3.1 Pressure fluctuations in PVFB at various pulsation frequencies	54
Figure 3.2 Typical fluid patterns of the bed at various pulsation frequencies. (A1-A4) $f=0.33\text{Hz}$; (B1-B4) $f=1\text{Hz}$; (C1-C4) $f=3\text{Hz}$; (D1-D4) $f=6.67\text{Hz}$	55
Figure 3.3 Power spectra of pressure fluctuations at various pulsation frequencies.....	58
Figure 3.4 Standard deviation of pressure fluctuations at various pulsation frequencies.....	59
Figure 3.5 Effect of gas flow rate on the final moisture content of Douglas fir sawdust after 30 min of drying (experimental data points with least-squares linear regression lines).....	61
Figure 3.6 Effect of pulsation frequency on the final moisture content of Douglas fir sawdust after 30 min of drying; biomass had initial moisture content of 50.1% (dry basis).....	63

Figure 3.7 Effect of vibration intensity on drying of Douglas fir sawdust under 1 Hz pulsation frequency after 30 min of drying; samples had initial moisture content of 46.2%.....	64
Figure 3.8 Effect of temperature on the drying of Douglas fir sawdust at various pulsation frequencies, $U/U_{mf}=1.25$; samples had initial moisture content of 51.8% (dry basis).....	66
Figure 3.9 Standard deviation of pressure fluctuations and peak pressure drop in pulsed fluidized bed of Douglas fir at different pulsation duty cycles (including least-squares linear regression trend lines)	68
Figure 3.10 Effect of pulsation duty cycle on the final moisture ratio of Douglas fir after 30 min drying, samples had initial moisture content of 46.1% (dry basis).....	69
Figure 3.11 Effect of particle size on final moisture ratio of Douglas fir after 30 min drying in pulsed fluidized bed, samples had initial moisture content of 94.5% (dry basis).....	71
Figure 3.12 Drying rates of coarse Douglas fir sawdust mixed with various amount of fine particles in the pulsed fluidized bed dryer	73
Figure 3.13 Predicted and measured final moisture content of coarse Douglas fir sawdust mixed with various amount of fine particles in the pulsed fluidized bed dryer after 30 min of drying; samples had initial moisture content of 57.3% (dry basis).....	75
Figure 3.14 Typical drying curves of three biomass species (a) Drying rate vs. time (b) Bed temperature vs. time	77
Figure 3.15 Schematic drawing of the pulsations at different frequencies and flow rates	80
Figure 3.16 Damping factor of the pulsed fluidized bed during drying of Douglas fir sawdust	82
Figure 3.17 High-speed photographs of the gas–solid flow in a pulsed fluidized bed taken at different pulsation frequencies, $U/U_{mf}=1.3$, initial bed mass=200g, bed material: Douglas fir, particle Sauter diameter=1.449mm	85
Figure 3.18 Instantaneous bed pressure vs. time for different pulsation frequencies, $U/U_{mf}=1.3$, initial bed mass=200g, bed material: Douglas fir, particle Sauter mean diameter=1.45 mm.	86

Figure 3.19 Final moisture ratio of Douglas fir sawdust after 30 min of drying in both original and tapered fluidized bed with pulsed gas flow, operated at different average gas flow rates, $f=1.5$ Hz (experimental data points with least-squares linear regression trend line); samples had initial moisture content of 59.4% (dry basis)..... 90

Figure 3.20 Drying rate curves of Douglas fir sawdust at various average gas velocities in both the original and the tapered fluidized bed with pulsed gas flow, $f=1.5$ Hz 91

Figure 3.21 Final moisture ratio of Douglas fir sawdust after 30 min of drying in both original and tapered fluidized beds with pulsed gas flow, operated at different pulsation frequencies, $U/U_{mf}=1.3$ (experimental data points with spline interpolations), samples had initial moisture content of 59.4% (dry basis)..... 93

Figure 3.22 Effect of initial bed sample weight on the final moisture ratio of the Douglas fir sawdust after 30 min of drying in both original and tapered fluidized beds with pulsed gas flow, operated at $f=1.5$ Hz, $U/U_{mf}=1.3$ (experimental data points and least-squares linear regression trend line) 94

Figure 4.1 Conceptual framework of the two-phase drying model of a fluidized bed 100

Figure 4.2 Experimental and model-fitted drying curves of Douglas fir at various flow rates. (a) $U/U_{mf}=1.1$, $f=1.0$ Hz; (b) $U/U_{mf}=1.4$, $f=1.0$ Hz 108

Figure 4.3 Experimental and model-fitted drying curves at different pulsation frequencies. (a) $U/U_{mf}=1.1$, $f=0.75$ Hz; (b) $U/U_{mf}=1.1$, $f=1.5$ Hz; (c) $U/U_{mf}=1.1$, $f=3.0$ Hz; (d) $U/U_{mf}=1.1$, $f=6.0$ Hz..... 111

Figure 4.4 Comparison of experimentally obtained drying curves and the corresponding model-fitted ones, $U/U_{mf}=1.2$, $f=1.0$ Hz. (a) Experimental drying curves of all three biomass species; (b) Douglas fir; (c) Pine; (d) Switchgrass. 114

Figure 4.5 Experimental and model-fitted drying curves at various drying temperatures. (a) $T=20^{\circ}\text{C}$, $f=1.0$ Hz, $U/U_{mf}=1.1$; (b) $T=30^{\circ}\text{C}$, $f=1.0$ Hz, $U/U_{mf}=1.1$; (c) $T=40^{\circ}\text{C}$, $f=1.0$ Hz, $U/U_{mf}=1.1$; (d) $T=50^{\circ}\text{C}$, $f=1.0$ Hz, $U/U_{mf}=1.1$; R^2 values included in Table 4.4. 116

Figure 4.6 Effective diffusivity for the drying of Douglas fir sawdust in the pulsed fluidized bed dryer as a function of drying temperature 117

Figure 4.7 Schematics of the two-phase drying model in pulsed fluidized bed with tapered bottom section	119
Figure 4.8 Experimental and modelled drying curves for Douglas fir sawdust in pulsed fluidized bed with a tapered bottom section at various gas flow rates. (a) $U/U_{mf}=1.1$, $f=1.5$ Hz; (b) $U/U_{mf}=1.4$, $f=1.5$ Hz	121
Figure 4.9 Experimental and predicted drying curves in pulsed fluidized bed with a tapered bottom section at different pulsation frequencies. (a) $U/U_{mf}=1.1$, $f=0.75$ Hz; (b) $U/U_{mf}=1.1$, $f=1.5$ Hz; (c) $U/U_{mf}=1.1$, $f=3.0$ Hz; (d) $U/U_{mf}=1.1$, $f=6.0$ Hz.	123
Figure 4.10 Effective diffusivity and amount of water removed in two reactor geometries as a function of (a) average superficial gas velocity and (b) pulsation frequency, plot consisted of experimental data points with spline interpolation lines	125
Figure 5.1 Effect of average flow rate on the bed-to-surface heat transfer coefficient at different gas pulsation frequencies in the pulsed fluidized bed of Douglas fir sawdust.....	129
Figure 5.2 Effect of pulsation frequency on heat transfer coefficient at different gas flow rates in the pulsed fluidized bed of Douglas fir sawdust (experimental data points and spline interpolation lines).	131
Figure 5.3 Effect of pulsation frequency on heat transfer coefficient at different gas flow rates in the pulsed fluidized bed (experimental data points and spline interpolation lines). (a) pine; (b) switchgrass.....	133
Figure 5.4 Effect of particle size on heat transfer at different gas flow rates in the pulsed fluidized bed with Douglas fir sawdust at a pulsation frequency of 1.25 Hz	135
Figure 5.5 Effect of fine particles on heat transfer at different superficial gas velocities in the pulsed fluidized bed with Douglas fir sawdust at a pulsation frequency of 1.25 Hz.....	137
Figure 5.6 Effect of mechanical vibration and flow rate on heat transfer at different pulsation frequencies in the pulsed fluidized bed with Douglas fir sawdust.....	139

Figure 5.7 Spectrum analysis of the bed pressure drops during the heat transfer measurement of Douglas fir sawdust. $f=1.25$ Hz, $U=1.05U_{mf}$ with 100% vibration	140
Figure 5.8 Lateral positions of the heater probe in the pulsed fluidized bed of biomass (top view, unit in mm).....	141
Figure 5.9 Heat transfer coefficients at different lateral positions as a function of pulsation frequency. (a) $U/U_{mf}=1.2$; (b) $U/U_{mf}=1.4$	143
Figure 5.10 Flow behaviour at different superficial gas velocities in the pulsed fluidized bed with tapered bottom section. (a) Fixed bed behaviour; (b) Piston-like behaviour; (c) Segregated flow behaviour with a centre fountain; (d) Regular, fully fluidized flow pattern.	145
Figure 5.11 Effect of average gas flow rate on heat transfer in pulsed fluidized bed of Douglas fir sawdust with a tapered bottom section (experimental data points with spline interpolations) Effect of pulsation frequency.....	148
Figure 5.12 Effect of pulsation frequency on heat transfer in pulsed fluidized bed of Douglas fir sawdust with a tapered bottom section (experimental data points with spline interpolations)....	149
Figure 5.13 Heat transfer coefficients at three different lateral positions in the pulsed fluidized bed of Douglas fir sawdust under different average superficial gas velocities. (a) $U/U_{mf}=1.1$; (b) $U/U_{mf}=1.2$; (c) $U/U_{mf}=1.3$; (d) $U/U_{mf}=1.5$	151
Figure 5.14 Average heat transfer coefficients at three different lateral positions in the pulsed fluidized bed of Douglas fir sawdust under different average superficial gas velocities, with error bars indicating the standard deviation of measured h values.....	152
Figure 5.15 Heat transfer coefficient at different gas pulsation duty cycles with Douglas fir sawdust (experimental data points with spline interpolations). (a) $U/U_{mf}=1.1$; (b) $U/U_{mf}=1.3$	154
Figure 5.16 The effect of particle size on heat transfer in the tapered pulsed fluidized bed with Douglas fir sawdust (experimental data points with spline interpolations)	157

Figure 5.17 Effect of fine particles on the bed-to-surface heat transfer of Douglas fir sawdust in the pulsed fluidized bed of tapered bottom section (experimental data points with spline interpolations)	158
Figure 5.18 Heat transfer coefficients of various biomass species in pulsed fluidized bed with tapered bottom section at various pulsation frequencies (experimental data points with spline interpolation lines). (a) Pine; (b) Switchgrass	161
Figure 5.19 Bed-to-surface heat transfer coefficients vs. superficial gas velocity of Douglas fir sawdust at four different pulsation frequencies in two reactor geometries (experimental data points with spline interpolation lines). (a) $f=0.5$ Hz; (b) $f=1.0$ Hz; (c) $f=2.0$ Hz; (d) $f=5.0$ Hz	163
Figure 5.20 Flow behaviour at different superficial gas velocities in the rectangular pulsed fluidized bed. (a) Fixed bed behaviour; (b) Piston-like behaviour; (c) Segregated flow behaviour with severe channeling; (d) Regular, fully fluidized flow pattern	164
Figure 5.21 Experimental and fitted heat transfer coefficients from two models in pulsed fluidized bed, with Douglas fir sawdust at $U = 1.1U_{mf}$	172
Figure 5.22 Experimental and fitted heat transfer coefficients from two models in pulsed fluidized bed, with Douglas fir sawdust at $U = 1.4U_{mf}$	173
Figure A.1 Peak pressure in pulsed fluidized bed of biomass as a function of gas velocity. (a) $f=5.0$ Hz; (b) $f=1.25$ Hz	192
Figure A.2 Final moisture content after 30 min of batch drying in pulsed fluidized bed for Douglas fir at different pulsed flow ratios	193
Figure A.3 Heat transfer coefficient in pulsed fluidized bed for Douglas fir, at different pulsed flow ratios	194
Figure A.4 Angle of repose method of measurement for Douglas fir sawdust. (a) Indicating marks for traditional particles; (b) new approach for biomass particles	196
Figure A.5 Angle of repose for all three biomass species at different moisture contents (experimental data points with spline interpolations)	196

Figure A.6 Drying rate curve of three biomass species in rectangular pulsed fluidized bed, $U/U_{mf}=1.1$	198
Figure A.7 Moisture content distribution within a single biomass particle during the batch drying test at different drying times, Douglas fir sawdust in rectangular fluidized bed, $T=20^{\circ}\text{C}$, flow rate $U/U_{mf}=1.1$	200
Figure A.8 Absolute humidity inside gas bubbles at different bed heights and different drying times, Douglas fir sawdust in rectangular fluidized bed, $T=20^{\circ}\text{C}$, flow rate $U/U_{mf}=1.1$	200
Figure A.9 Equilibrium moisture content of three biomass species at different temperatures (environment relative humidity 0.1%)	201
Figure B.1 Simulation domain for the heat loss estimation. (a) Simplified assembly of the heater probe for heat loss estimation; (b) Simulation domain for the heat loss estimation.....	202
Figure B.2 Graphs from the simulation for heat loss estimation. (a) Temperature profile around and within the heater probe during natural convection; (b) Velocity profile of surrounding air during natural convection simulation.	204
Figure B.3 Temperature gradient inside and outside the heater probe during natural convection	205
Figure C.1 Block diagram of the pressure and temperature measurement virtual instrument in LabVIEW	208
Figure C.2 Block diagram of RH and drying rate processing virtual instrument in LabVIEW	209
Figure C.3 Front panel of the system built in LabVIEW	210
Figure D.1 Images of gas bypassing in pulsed fluidized bed.....	211
Figure D.2 Images of channeling in pulsed fluidized bed.....	212
Figure D.3 Images of core–annulus flow in pulsed fluidized bed	212
Figure D.4 Images of piston-like behaviour in pulsed fluidized bed	213

LIST OF SYMBOLS

A	Cross-section area, m ²
A'	Interfacial area of particle per unit volume of dense phase, m ² /m ³
Ar	Archimedes number
A_s	Heat transfer area of the heat transfer measurement probe, m ²
A_v	Half amplitude of vibration, m
C_A	Concentration of species A in bulk of gas phase, mol/L
C_A^i	Concentration of species A at gas-particle interface, mol/L
C_{pg}	Heat capacity of the gas phase, J/(mol·K)
$C_{p,mf}$	Dense phase heat capacity, J/(mol·K)
C_{pp}	Heat capacity of the solid, J/(kg·K)
d_b	Bubble diameter, m
d_{b0}	Initial bubble diameter at multi-orifice distributor plate, m
d_{bm}	Maximum attainable bubble diameter, m
d_p	Particle diameter, m
D_{eff}	Effective diffusivity, m ² /s
D_{AB}	Molecular diffusivity, m ² /s
D_g	Gas phase diffusion coefficient, m ² /s
D_0	Pre-exponential factor in Arrhenius equation, m ² /s
D_s	Diameter of the heat transfer measurement probe, m
D_t	Hydraulic diameter of the column, m
D_v	Molecular diffusivity of water vapour in air, m ² /s
f	Pulsation frequency, Hz

f_d	Dense phase contact time fraction
f_N	Natural frequency of the fluidized bed, Hz
f'_N	Modified natural frequency of the fluidized bed, Hz
g	Gravitational acceleration, m/s ²
G_b	Gas flow rate in bubble phase per unit volume of bed, m ³ /(m ³ s)
G_d	Gas flow rate in dense phase per unit volume of bed, m ³ /(m ³ s)
\bar{G}_g	Mass flow rate of drying air, kg/s
h	Heat transfer coefficient, W/(m ² ·K)
h_1	Heat transfer coefficient from Model 1, W/(m ² ·K)
h_2	Heat transfer coefficient from Model 2, W/(m ² ·K)
h_c	Conductive-convective heat transfer coefficient, W/(m ² ·K)
h_i	Instantaneous heat transfer coefficient, W/(m ² ·K)
h_g	Heat transfer component from the bubble phase, W/(m ² ·K)
h_{gc}	Gas convective of heat transfer, W/(m ² ·K)
h_{max}	Maximum heat transfer coefficient, W/(m ² ·K)
h_p	Heat transfer coefficient between dense phase and surface, W/(m ² ·K)
h_{pc}	Particle convective heat transfer component, W/(m ² ·K)
h_r	Heat transfer coefficient for radiation, W/(m ² ·K)
h_s	Integral mean gas convective heat transfer coefficient, W/(m ² ·K)
h_w	Wall heat transfer coefficient in fixed beds, W/(m ² ·K)
I	Current, A
j	Integer
k_{bd}	Effective interphase mass transfer coefficient in a freely bubbling fluidized bed, m/s
k_{eff}	Effective thermal conductivity of fixed bed, W/(m·K)
k_{ef}	Turbulent eddy conduction or lateral mixing component of K_{eff} , W/(m·K)

k_{es}	Effective thermal conductivity of fixed bed with motionless fluid, W/(m·K)
k_g	Thermal conductivity of gas, W/(m·K)
$k_{g, bed}$	Average mass transfer coefficient among bed particles, m/s
k_p	Thermal conductivity of solid, W/(m·K)
K_c	Mass transfer coefficient across bubble boundary, m/s
K_i	Particle surface mass transfer coefficient, m/s
l	Lateral position in fluidized bed, m
l_m	Laminar length scale, m
l_t	Turbulent length scale, m
L	Overall length of the fluidized bed, m
L_C	Characteristic length for heat transfer, m
L_p	Length of the particle, m
L_S	Length of the heating surface, m
m_b	Mass of bed, kg
m_{wet}	Water content in wet biomass samples, g
m_{dry}	Water content in dried biomass samples, g
M	Mass flow rate of drying air, g/s
N_A	Mole of species A, mol
N_{or}	Number of orifices in distributor
Nu_p	Particle phase Nusselt number, hL / k_p
p	Water vapour pressure, Pa
p_s	Saturated water vapour pressure, Pa
\bar{P}	Average pressure beneath bed, Pa
$P_{mf, V}$	Gas pressure in vibrated fluidized bed, Pa
$P_{mf, S}$	Gas pressure in conventional fluidized bed, Pa

Pr_g	Gas phase Prandtl number, $C_{pg}\mu_g / k_g$
Q_l	Heat loss, W
r	Radial distance, m
R	Universal gas constant, J/(kg·K)
Re_p	Reynolds number of particles, $\rho_g d_p U / \mu_g$
RH	Relative humidity
R_p	Radius of particle, m
Sc	Schmidt number, $\mu_g / \rho_g D_v$
$S_{ex,p}$	Total surface area of fluidized bed particles, (m ²)
t	Time, s
t_0	Time interval between each frame of footage, s
t_{OFF}	Amount of time in a pulsation cycle when gas is shutoff, s
t_{ON}	Amount of time in a pulsation cycle when gas is turned on, s
T	Temperature, K
T_b	Temperature of the dense phase, K
T_s	Temperature of the probe surface, K
T_w	Temperature of the wall surface, K
U	Superficial gas velocity, m/s
\bar{U}	Average superficial gas velocity, m/s
U_b	Bubble rise velocity, m/s
U_{in}	Initial gas velocity at the beginning of "ON" period, m/s
U_{mf}	Minimum fluidization velocity, m/s
U_{mm}	Minimum mixing velocity, m/s
\bar{U}_{on}	Average superficial gas velocity in the "ON" period, m/s
U_z	Superficial gas velocity at certain bed height z in the tapered section, m/s

V	Voltage, V
V_g	Volume of gas space beneath bed, m ³
w	Weight of the sample, g
W	Drying rate, g/s
X	Moisture content within a biomass particle, dry basis
X_e	Equilibrium moisture content of biomass samples, dry basis
X_{Exp}	Experimentally obtained moisture content of biomass samples, dry basis
X_o	Initial moisture content of biomass samples, dry basis
\bar{X}	Average moisture content of the biomass particles at a given time, dry basis
y	Mole fraction of inert component
Y	Absolute humidity, kg-water/kg-air
Y_b	Absolute humidity in the bubble phase, kg-water/kg-air
Y_d	Absolute humidity in the dense phase interstitial gas, kg-water/kg-air
Y_i	Absolute humidity of the inlet gas, kg-water/kg-air
Y_o	Absolute humidity of the exit gas, kg-water/kg-air
Y_p	Absolute humidity at particle surface, kg-water/kg-air
z	Height above gas distributor, m

Greek Letters

β	Time fraction of the "ON" period
Γ	Dimensionless vibration number, $A_v \omega_v^2 / g$
ε_b	Bubble volume fraction
ε	Voidage fraction
ε_{mf}	Bed voidage at minimum fluidization
λ	distance of a void/bubble travelled, m
η	Percentage of water removed in batch drying tests
η_D	Pulsation duty cycle
μ	Viscosity, kg/(m·s)
ϑ	Mass rate of evaporation of water per unit volume of bed, kg/(m ³ ·s)
μ_g	Gas viscosity, kg/(m·s)
ν	Simplified term, K ⁻¹
ρ_g	Air density, kg/m ³
ρ_p	Particle density, kg/m ³
ρ_{mf}	Density of the dense phase, kg/m ³
τ	<i>Packets</i> residence time, s
φ_v	Particle volume equivalent shape factor
ω	Mass rate of evaporation of water per unit volume of bed, kg/(m ³ ·s)
ω_v	Angular vibration frequency, Hz
Φ	Moisture ratio
Ψ	Moisture removal ratio

ACKNOWLEDGEMENTS

The writer is indebted to the Natural Sciences and Engineering Research Council of Canada for their financial support of this project.

Immense gratitude goes to all who have given their invaluable support and assistance during my study at UBC.

Professors X. Bi, C. J. Lim and S. Sokhansanj have continuously supported me during my PhD research, with their patience, motivation, enthusiasm, and immense knowledge. Special thanks to Prof. X. Bi for his guidance that has helped me tremendously in research, study, as well as formulation of this thesis. I could not have imagined having a better advisor for my PhD research.

Besides my research supervisors, I would like to thank the rest of my thesis committee, Professors N. Ellis and R. Legros for their insightful comments and encouragement.

My sincere thanks also goes to the technical and administrative staff at the Department of Chemical and Biological Engineering. Thanks to Doug, David, Alex, Serge, Charles and Richard for their helpful consultations and assistance in construction of the equipment. Also thanks to Helsa, Lori, Magnolia, Marlene and Amber for the administrative support.

I owe a great deal to my colleagues and friends who shared their experiences, comments and ideas, and who enriched my life and offered their help when I needed it the most.

Last but not least, I would like to thank my family, my parents in particular, for their unconditional love and support during my years abroad and my life in general.

Dedicated to the beloved memories of my grandmother

Xilian Li (1932 – 2010)

who taught me values are the definition of our actions in life

CHAPTER 1

INTRODUCTION

Biomass refers to any organic materials derived from plants or animals. It is an abundantly available energy resource comprised of various types of organic feedstock including forest and agricultural residues as well as municipal solid waste, which have been increasingly utilized for fuel and energy production. Globally, biomass provided 4.1% of the energy consumption in 2013. By the end of 2014, the share of renewable electricity production was 22.8%, among which power generated by biomass increased by approximately 9% to 433 TWh (Secretariat, 2015). Second-generation biofuels produced from ligno-cellulosic biomass by thermochemical or biochemical processes that are aimed at reducing environmental pressure have shown great promise to bring new regional and industrial interests to the biofuel value chain (Mabee et al., 2011). When compared with fossil fuels, it has been demonstrated that bioenergy derived from ligno-cellulosic biomass such as forest residues could reduce CO₂ and other greenhouse gas (GHG) emissions in the long term (Sedjo, 2013; Zanchi et al., 2012). In Canada, the national GHG emissions in 2014 were estimated at 732 million tonnes CO₂-equivalent from all sources (Environment and Climate Change Canada, 2012), nearly one third of which was attributed to the transportation sector. Research by Mabee and Saddler (2010) demonstrated that second-generation feedstock could meet 50% of Canada's transportation fuel needs. As a result, a number of cost-effective thermochemical conversion processes have arrived in the spotlight and shown great promise, including biomass torrefaction, pyrolysis and gasification, which convert biomass into high heating-value solid fuels, liquid fuels or biogas.

To reduce the cost of storage and transport over long distances, biomass resources such as industrial waste, industrial co-products, food waste, agricultural and forest residues are commonly densified into pellets or briquettes. In 2014 the global wood pellet production reached 24 million tonnes, in which United States and Canada were top exporters, with a combined capacity of over 5 million tonnes per year (Secretariat, 2015). In Canada, wood pellet production capacity was approximately 3.4 million tonnes per year as of 2012 (Natural Resources Canada, 2013), and pellet production capacity in British Columbia (BC) alone accounted for 66% of Canada's total pellet capacity (Prov. of BC, 2011). However, there are estimated 32 million tonnes of biomass residues available each year in British Columbia. Should these biomass residues be properly utilized, it would potentially replace half of the fossil fuel consumption within the province.

A reactor needs to be carefully designed so as to accommodate a wide range of raw biomass materials with distinct properties. The fluidized bed is considered as a potential candidate for such thermochemical reactions as it offers excellent heat and mass transfer rates. In addition, higher mass yield was observed in fluidized bed during biomass torrefaction when compared to other reactors such as rotary drum reactor (Dhungana et al., 2012). However, the commercial application of biomass is at times held back by the marked differences between biomass and traditional solid fuels in terms of physical and chemical properties. Compared to traditional fuels, biomass often possesses high moisture and ash content, low bulk density and energy density, irregular shapes and low carbon-to-hydrogen ratio. Sawdust that comes from sawmills contains up to 60% moisture. Depending on the source, municipal solid waste (MSW) from developed countries contains 20–30% water, and in developing countries it is typically 50% and could be as high as 70% (Cheng et al., 2007). Because of the poor flowability and highly cohesive characteristics of biomass, channeling and partial defluidization frequently occur in fluidized beds with pure biomass. To ensure smooth and stable fluidization inert particles such as silica sand and calcite are often mixed with biomass particles. Study has shown the addition of sand particles reduces the occurrence of undesired phenomenon such as channeling (Karmakar et al., 2013). Bed material also serves as heat carrier in

certain cases, for instance during biomass gasification (Fotovvat et al., 2014; Goransson et al., 2015; Han et al., 2008; Zhong et al., 2008). For biomass torrefaction where the main product is solid biofuel instead of biogas, fines of inert bed material generated by attrition often adhere to the product, dramatically increasing the ash content of the solid biofuel. The higher ash content not only undermines the quality of the product, but also poses a threat to biomass operated turbines and boilers, where increased ash content in fuel pellets could lead to sintering and fouling, causing malfunctions of the unit and eventually leading to unscheduled shutdowns (Turnbull, 1993). Therefore, a fluidized bed reactor that is able to handle biomass without inert particles is greatly favoured.

It is highly probable that the poor gas–solid contact and unsatisfactory fluidization quality of biomass stem from its low bulk density, irregular shapes and high moisture content that inevitably lead to strong inter-particle forces. Seville and Clift (1984) revealed that the minimum fluidization velocity and bed voidage increased with liquid loading on particle surfaces, and the resulting stronger inter-particle forces also could explain the fluidization behaviour that transitioned from Geldart Group B toward Group A and Group C. Additional energy from imposed electric field (Elsdon & Shearer, 1977; Kleijn van Willigen et al., 2005; Sun et al., 2015), magnetic field (Al-Qodah & Al-Busoul, 2001; Busciglio et al., 2015; Dahikar & Sonolikar, 2006; Espin et al., 2011; Hristov, 2002), mechanical vibration (Bacelos et al., 2011; Bratu & Jinescu, 1971; Gupta & Mujumdar, 1980; Jin et al., 2007; Kong et al., 2010; Meili et al., 2010; Meili et al., 2012; Shryaeva et al., 1990; Thomas et al., 2000; Zhang et al., 2012) and oscillating gas flow (Devahastin & Mujumdar, 2001; Hadi et al., 2011; Ponomarenko et al., 1989; van der Wielen et al., 1997; Walzel, 2013; Wang & Rhodes, 2005a; Wang & Rhodes, 2005b; Zhang, 2005) could be introduced to the fluidized bed to overcome the cohesive forces so as to achieve good fluidization.

For biomass thermal conversion processes, heat is provided so that desired reaction temperature can be reached and maintained. As a result, external or internal heat exchangers are often installed.

In order to efficiently design and operate the fluidized bed reactor of biomass with integrated heat exchangers, bed-to-surface heat transfer coefficients of pure biomass particles in fluidized beds should be made available. Previous studies have focused heavily on the bed-to-wall heat transfer of biomass-sand mixtures (Liu & Tian, 2008) and inter-particle heat transfer (Okekunle et al., 2011) in fluidized beds, few studies are available on the pressing issue regarding bed-to-surface heat transfer of pure biomass, which is a key piece of information required for the development of a more energy-efficient biomass thermal conversion process.

1.1 Fluidized bed with pulsed gas flow

It is known that chaotic dynamics can be embedded into a periodic orbit of fluctuating parameters that influence the dynamics, so as to make the system more ordered, which is the foundation of chaos control (van den Bleek et al., 2002). Pulsed gas flow is achieved simply by oscillating the gas flow rate of the fluidized bed periodically, which may lead to the transformation of chaotic to stable, remarkably regular bubble patterns, offering new means for intrinsic control and scale-independent hydrodynamics (Coppens & van Ommen, 2003). Pence and Beasley (1998) proved the effectiveness of gas pulsation on chaos control. Pulsation frequency up to 15 Hz was used. The Kolmogorov entropy with pulsed gas flow present was much smaller than that of continuous gas flow, indicating that the degree of chaotic behaviour was greatly reduced in comparison to operating conditions without pulsation.

Compared to conventional fluidized beds with continuous throughput of fluidization medium, pulsed fluidized beds (PFB) are able to accommodate a wider range of particle sizes. The enhanced gas–solid contact in pulsed beds also leads to improved heat and mass transfer rates between gas and solid particles, as well as between the dense phase and heating/cooling surfaces. Kobayashi et al. (1970b) reported a 300% increase in product uniformity and 100% increase in processing

capacity when air was pulsed into a commercial mixer filled with mineral particles. A great number of publications could be found on pulsed fluidized bed drying, including agricultural products such as broccoli (Reyes et al., 2012), coconut pulp (Niamnuy & Devahastin, 2005) and turnip seeds (Reyes et al., 2006); wood residues such as sawdust (Reyes et al., 2008b); pulp and paper sludge (Kudra et al., 2002); chemicals such as sodium acetate (de Souza et al., 2010) and biopolymer (Godoi et al., 2011) as well as brown coal (Liu, 2016) and uranium ore (Levey Jr, 1965). In addition, fluidized beds have also been used for biomass torrefaction (Atienza-Martínez et al., 2013; Li et al., 2012; Prins et al., 2006; Wang et al., 2013) pyrolysis (Mastellone & Arena, 2002) and gasification (Beck Steven et al., 1981; Bi & Liu, 2010; Corella et al., 1991).

There have been many unique designs proposed by researchers to generate gas phase pulsation. Besides solenoid valve and butterfly valve that generate gas pulsations by periodically switching on and off (Akhavan et al., 2008; Hadi et al., 2011; Wong & Baird, 1971), as illustrated in Figure 1.1(a), and rotating air distributor that guides gas into different compartments of the fluidized bed (Kudra et al., 2002; Nitz & Taranto, 2007) in Figure 1.1(b), other designs include rotating disc with a hollow section for the gas to pass through (Reyes et al., 2008a; Reyes et al., 2012; Reyes et al., 2007; Reyes et al., 2008b) shown in Figure 1.1(c), as well as horizontal cylinder with empty slots on opposite sides (Reyes et al., 2006) in Figure 1.1(d). All of these are capable of relocating the gas phase periodically and generating pulsations.

Similar to many mechanical systems, the behaviour of gas pulsation is strongly linked to its frequency. Massimilla et al. (1966) examined three types of pulsed fluidization at different pulsation frequencies, namely intermittent fluidization at low frequencies (1.2–2.7 Hz), piston-like fluidization at medium frequencies (2.7–4.8 Hz) and apparently ‘normal’ fluidization at high frequencies (> 4.8 Hz). However the piston-like behaviour was not observed in experiments carried out by Wong and Baird (1971) in a 4” fluidized bed where pulsation frequency ranged from 1 to 10 Hz. A piston

model proposed in their study gave an approximate prediction of the natural frequency f_N (Hz) of the fluidized bed, around which the pulsation was most effective,

$$f_N = \left(\frac{\gamma \bar{P} A^2}{m_b V_g} \right)^{0.5} \left[1 - \frac{\gamma \bar{P} u_{mf}^2 A^2}{4 m_b g^2 V_g} \right]^{0.5} \quad (1.1)$$

in which \bar{P} (Pa) represents the pressure below the bed, m_b (kg) and A (m²) are mass and cross-sectional area of the fluidized bed, respectively. Vertical oscillation of the bed was observed at 5 Hz, and the gas phase seemed better distributed at 10 Hz. Bed pressure drop data revealed that within each pulsation cycle there were two peaks, corresponding to the gas pulse injection and the pressure recovery because of the falling particles compressing the gas below the support. Better mixing was achieved by pulsation, which was verified by the tracer study where the gas retention time was increased by as much as 50%.

Reyes et al. (2008a) calculated the heat transfer coefficients between the hot gas and bed particles in a PFB dryer with inert particles under different conditions via energy balance. Experiments planned through factorial design showed that by increasing gas velocity and temperature, or simply reducing the processing capacity, Nusselt number (Nu) increased. Meanwhile, the “shock” provided by gas pulsation was of great importance in terms of breaking up the cohesiveness of biomass particles. Godoi et al. (2011) confirmed the role of pulsation during the drying of biopolymers, where pulsation enabled the transition of flowability from cohesive to free-flowing. A PFB dryer for grains of $d_p \approx 6mm$ was tested by Nitz and Taranto (2007). A PFB dryer achieved similar drying performance with only one fourth of the air consumption of the conventional fluidized bed dryer, in addition to improved gas–solid contact efficiency and energy savings.

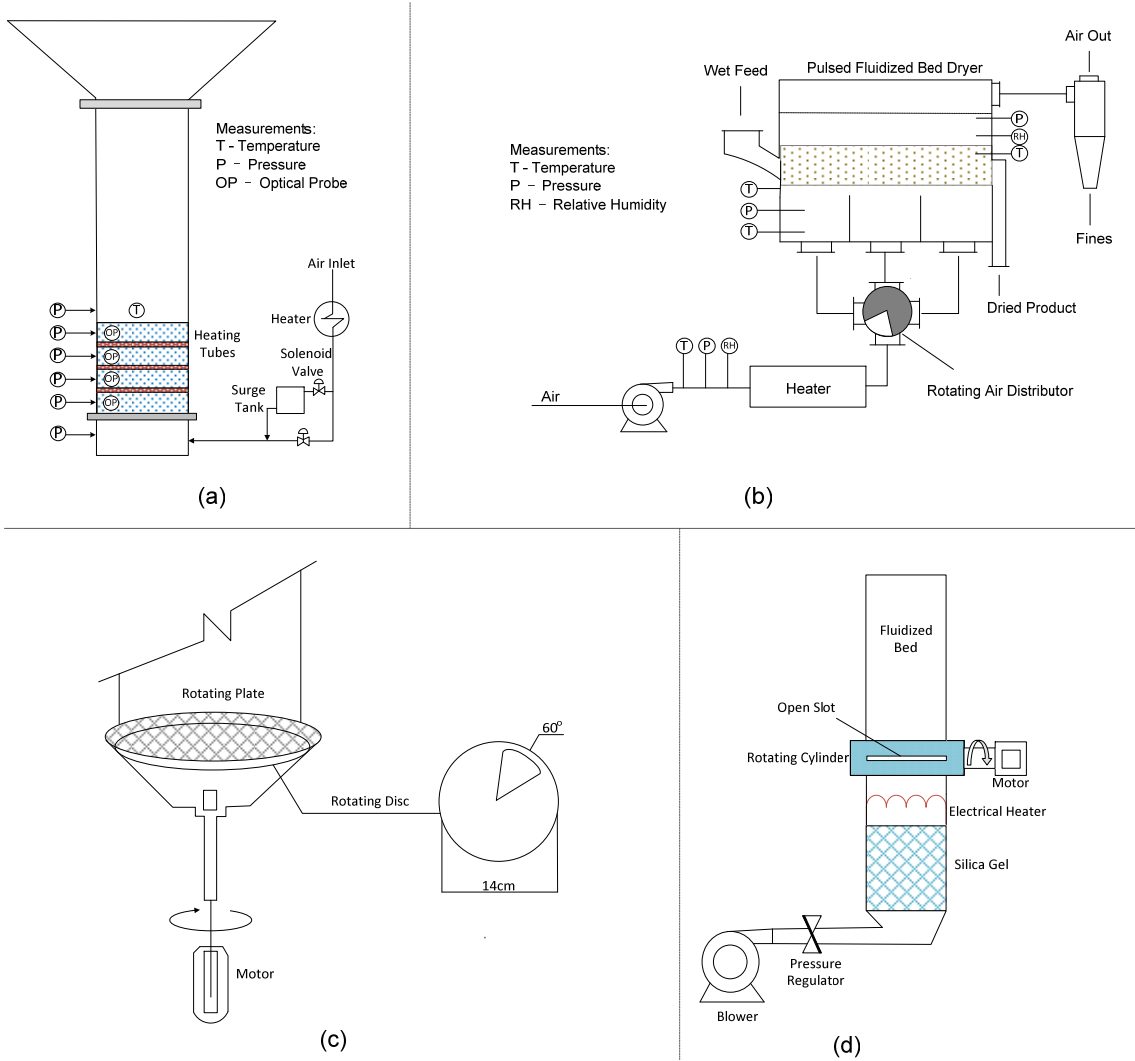


Figure 1.1 Various designs for pulsed fluidized beds. (a) Solenoid valve or butterfly valve; (b) Rotating air distributor; (c) Rotating disc with a fractional opening; (d) Rotating slotted horizontal cylinder.

Akhavan et al. (2008) looked into the relationships between pulsation frequency and drying kinetics. A frequency of 3 Hz was deployed and the pulsation was disabled for the first 10 min of each run with different average air velocities. As soon as pulsation was enabled, power spectrum analysis showed a significant drop in dominant frequency, indicating a shift in fluidization regime. A critical moisture content was discovered, around which drying switched from being heat-transfer limited to mass-transfer limited.

Wang and Rhodes (2005a) applied discrete element model (DEM) to the simulation of pulsed fluidized bed by computational fluid dynamics (CFD). Pressure drop analysis yielded similar conclusions as Wong and Baird (1971). 3–10 Hz and 2.7–7 Hz frequency ranges were visually confirmed to be most effective in ameliorating gas–solid interaction for sinusoidal and square wave pulsations, respectively. Interesting bubble behaviours that were difficult to obtain experimentally were processed and analyzed. Synchronized with gas injection, periodically formed horizontal gas channels were spotted, which quickly evolved into regular bubbles which moved up to the surface of the bubbling bed in a normal fashion. Additionally, bubbles grew faster under square wave pulsation, which was as effective as sinusoidal pulsation. Recently, Martín et al. (2016) successfully replicated the experimentally observed surface patterns in a pulsed fluidized bed by DEM, in which the characteristic length scale of the surface patterns was found to decrease with increasing the pulsation frequency.

1.2 Vibrated fluidized bed

By combining mechanical vibration with upward gas flow, minimum fluidization velocity could be greatly reduced compared to conventional fluidized beds. In addition, vibration also reduces the airflow requirements and improves controllability of particle residence time. Considerable improvement of particle flowability was observed by Yoshida and Kousaka (1969) in a vibrated fluidized bed (VFB). The improved handling and flowability in vibrated fluidized beds was likely associated with the ability of breaking down inter-particle forces of attraction and thus improving fluidization quality. For the handling of wet particles or extremely fine particles ($d_p \leq 5 \mu m$) the presence of vibration is especially beneficial as fines are more prone to agglomeration. Enhanced gas–solid flow was discovered by Zaitsev et al. (1976) in a vibrated fluidized bed, such flow

behaviour could not be replicated in continuous fluidized beds. There are many commercial operations of vibrated fluidized beds, including energizing spray-dried milk powder, increasing surface activity of detergents and drying of polymer chips, chemicals, pharmaceuticals as well as agricultural and food products. Based on one-dimensional particle oscillation in incompressible fluid, Molerus interpreted the effect of vibration on the stabilization of particulate fluidization, and concluded that 50 Hz was a very effective frequency in reducing gas bypassing (Molerus, 1967).

Hydrodynamics of the VFBs at minimum fluidization has been thoroughly investigated by many researchers. The bed behaviour is heavily influenced by the dimensionless vibration number $\Gamma = A_v \omega_v^2 / g$ that characterizes the intensity of vibration, in which A_v and ω_v represents the amplitude and frequency of the vibration, respectively. Studies carried out by Bratu and Jinescu (1971) indicated that vibration could bring uniformity and stability to the gas–solid system. For cases where $\Gamma > 1$, an empirical correlation of the bed pressure drop at minimum fluidization velocity between vibrated and conventional fluidized bed was proposed,

$$\frac{(\Delta P_{mf})_V}{(\Delta P_{mf})_S} = \left(\frac{A_v \omega_v^2}{g} \right)^{-(0.15+24.17d_p \rho_p)} \quad (1.2)$$

in which subscripts V and S refer to vibrated and stationary fluidized bed, respectively. For operating conditions where $\Gamma > 4$, vibration introduced certain negative impact on the system. The minimum fluidization velocity was also found to decrease with increasing dimensionless vibration number Γ . Gupta and Mujumdar (1980) discussed the hydrodynamics and heat transfer properties in VFB and arrived at the following,

$$\frac{(\Delta P_{mf})_V}{(\Delta P_{mf})_S} = 1 - 0.0935 \left(\frac{d_p}{H} \right)^{0.946} \left(\frac{A_v \omega_v^2}{g} \right)^{0.606} \phi_v^{1.637} \quad (1.3)$$

In each setup, both beds had the same static bed height and bed material. Subsequent work by Mushtaev et al. (1991) led to,

$$\frac{(\Delta P_{mf})_V}{(\Delta P_{mf})_S} = \left(\frac{A\omega_v^2}{g} \right)^{-(0.41+19.6d_p\rho_p)} \quad (1.4)$$

$$\frac{(U_{mf})_V}{(U_{mf})_S} = 1 - 0.095 \left(\frac{A\omega_v^2}{g} \right) \quad (1.5)$$

It should be noted that the correlation above was intended for $\Gamma > 1$. Gupta and Mujumdar (1980) pointed out that in the design and operation of VFBS minimum gas velocity at which the system could be successfully operated, namely the minimum mixing velocity U_{mm} (m/s) was more important than the traditionally defined minimum fluidization velocity U_{mf} (m/s). The relationship between the two was given as,

$$\frac{U_{mm}}{U_{mf}} = 1.952 - 0.275 \left(\frac{A\omega_v^2}{g} \right) - 0.686 \left(\frac{A\omega_v^2}{g} \right)^2 \quad (1.6)$$

Malhotra and Mujumdar (1987) investigated drying performance in a VFB, in addition to heat transfer between wet particles and single or multiple immersed horizontal heating tubes. A heat transfer model was proposed based on the observation of flow patterns around the single/multiple heating tubes by means of high-speed photography. Lyczkowski (1982) plotted the diagram for the design of VFBS that provided the optimum operating conditions and clarified that the implementation of vibration must be in good agreement with the gas flow rate to achieve better fluidization. Erdész and Mujumdar (1986) presented a power-law type correlation for the minimum fluidization velocity in VFBS based on Anderson's correlation for minimum fluidization velocity in conventional fluidized beds, with a significantly lower U_{mf} being observed in VFBS.

Nilson and Wimmerstedt (1987) proposed a model for the longitudinal flow in a 2.1 m long VFB dryer based on the sorption equilibrium, drying kinetics and solid transport data gathered from four different bed materials. Results indicated that axial gas dispersion model was better suited than the plug flow model. Savage (1988) conducted mixing and drying of polystyrene beads in a vibrated

fluidized bed, which had a rectangular bed at the top and a horizontal bottom capable of outputting various frequencies and amplitudes. Slow recirculating flows were seen in which the particles were travelling upwards in the centre and downward near the wall. These velocities were in proportion to the vibration frequency and amplitude. A simple analysis of these motions was also derived by modifying the previously proposed constitutive theory.

Eccles and Mujumdar (1992) measured the bed-to-surface heat transfer coefficient in a vertically vibrated fluidized bed of various particles ranging from 27 to 1400 μm such as alumina and zeolite. It was discovered that under the frequency range of 0–25 Hz as the vibration frequency approached the natural frequency of the fluidized bed, heat transfer coefficient increased dramatically and reached a maximum at resonance frequency that was 19 times more than in a fixed bed because of the increased particle mobility. Chen et al. (1991) proved that under suitable operating conditions the vibrated fluidized bed dryer with 38 mm vibration displacement could be highly effective. Experimental study of a pilot scale continuous VFB dryer for wheat and pharmaceutical particles (1.5 m in length and 0.24 m in width) outlined the influences of operating conditions on the heat and mass transfer (Han et al., 1991). It was shown that the continuously operated VFB dryer could be regarded as a plug flow reactor and among many parameters vibration intensity was the most important factor for particle residence time, particle diffusivity and constant drying rate.

New designs of VFBs could also be found in the literature. For instance, instead of installing the fluidized bed on a vibration source, Beeckmans and Macwilliam (1986) placed a network of rods in the fluidized bed that were connected to a vibrator such that the vibration energy was able to be transmitted directly to the bed material without the movement of the bed as a whole. This unique VFB reduced the porosity as well as the minimum fluidization velocity. The bubbling behaviour was reduced and in some cases eliminated as a result.

1.3 Tapered fluidized bed

The concept of using a tapered bed for drying was first proposed by Gishler and Mathur (1957) in the form of spouted beds where a cylindrical spouted bed was introduced for the drying of wheat. Later on, the concept was adopted to fluidized beds. By adding a tapered bottom section to conventional fluidized beds, flow behaviour is altered. In addition to the axial movement of bubbles and particles, a radial velocity component is also introduced, which is similar to the core–annulus flow in spouted beds. A slow circulation of particles is created that may be beneficial to mixing and gas–solid contact. One key difference between tapered fluidized bed and spouted bed is that the former normally operates with Geldart Group A and Group B particles (Gernon et al., 2007; Khanna et al., 2008; Schaafsma et al., 2006; Wiens & Pugsley, 2006), while the latter is often used for Group D particles (Jing et al., 2000; Markowski & Kaminski, 1983; Olazar et al., 1992). Moreover, the tapered fluidized bed normally has a shallow static bed height compared to the spouted bed.

The unique core–annulus flow behaviour in tapered fluidized beds was first discussed by Toyohara and Kawamura (1992) where a partially or completely fluidized core region was observed alongside a partially fluidized annulus region. The particles were carried upwards in the centre and slowly recirculated back to the bottom of the bed. Such a flow behaviour was verified by Schaafsma et al. (2006) through particle tracking in a shallow fluidized bed containing Geldart Group B particles. Similar flow patterns were observed by radioactive particle tracking in a conical fluidized bed of pharmaceutical powders (Khanna et al., 2008). Extensive work was also done by Pugsley et al. (2007) where transient electrical capacitance tomography (ECT) images of a conical fluidized bed that clearly showed the core–annulus flow behaviour. The same ECT technology was also used in the study of the hydrodynamics of a conical fluidized bed of pharmaceutical particles (Wiens & Pugsley, 2006). It was discovered that the bubbling frequency decreased from approximately 10 to 5 Hz over the velocity range of 0.5–2.0 m/s, indicating that bubble coalescence was prevalent in their system over the velocity range studied, and that the cross-sectional area of the core region of the bed

increased with gas velocity. Experiments were carried out by Sau et al. (2007) with different tapered angles of the bed, with regular as well as irregular particles of different sizes and densities. The tapered angles of the beds have been found to affect the characteristics of the bed. Models based on dimensionless analysis have been proposed to predict the minimum fluidization velocity and maximum pressure drop for gas–solid tapered fluidized beds.

Wormsbecker et al. (2009) analyzed pressure signals in a conical fluidized bed of pharmaceutical powders and revealed the link between hydrodynamics and drying through pressure fluctuations and average cycle frequency. The pressure signals clearly indicated a transition in fluidization behaviour that marked the onset of falling-rate periods of drying porous materials. These liquid bridges on particle surface was theorized to be able to stabilize the bed structure that limited bubble formation. Conical fluidized beds have also been used for biomass particles, such as the combustion of sugar cane bagasse with rice husk (Kuprianov et al., 2006), and the drying of tobacco leaves (Legros et al., 1994). Kuprianov and Permchart (2003) also studied mixed sawdust of Thai woods in a conical fluidized bed combustor and measured the concentration profiles for major gaseous emissions (CO, NO_x and CO₂) as well as the temperature and O₂ profiles along the combustor height.

The tapered geometry is not only beneficial to the fluidization of Groups A and B particles, but also effective in fluidizing of cohesive particles in Group C. Using a conical fluidized bed, Venkatesh et al. (1996) improved the fluidization quality of NiO/Al₂O₃ cryogels that did not fluidize well in cylindrical beds. Marked improvements were observed when visually comparing the hydrodynamics of the conical bed to that of a cylindrical bed.

1.4 Heat transfer in fluidized bed

Favourable heat transfer performance is among many reasons that gas–solid fluidized beds are chosen for a wide variety of applications. The bed-to-surface heat transfer coefficients are approximately an order of magnitude better than for fixed beds at comparable gas velocities (Botterill, 1975). The heat transfer coefficient between particles and gas in a bubbling fluidized bed is normally not significant. However due to the large interfacial surface area, interfacial heat transfer rate is extremely high (Chen, 2003a). In addition, fluidized beds also exhibit much improved temperature uniformity compared to other reactors such as fixed bed. Energy balance is of great importance in biomass thermal conversion processes. Moreover, the design and operation of fluidized beds at times depend heavily on heat exchangers and heating/cooling pipes, and a better understanding of the heat transfer mechanism between the bubbling fluidized bed and the immersed surfaces is desired. The bed-to-surface heat transfer coefficient should be obtained. A brief overview of bed-to-surface heat transfer in fluidized bed is included below.

1.4.1 Empirical and semi-empirical correlations

Different approaches among a great number of literatures addressed modelling and prediction of heat transfer coefficient in fluidized beds. Ozkaynak and Chen (1980) observed that during their experiments heat transfer coefficient (h) increased greatly immediately after the system transitioned from a fixed bed to fluidized bed. In addition, an optimum gas velocity (U_{opt}) at which h reached a maximum was discovered. As gas velocity further increased, h slightly decreased. Heat transfer coefficient was also found to decrease with increasing particle diameter.

Many efforts were made to link heat transfer coefficient with gas flow rate and other properties of the fluid and particles. In most cases, empirical correlations were established between Nusselt number (Nu), the fluid Prandtl number (Pr) and Reynolds number (Re). Borodulya et al. (1991)

investigated heat transfer between an immersed vertical tube and a fluidized bed, which led to the following,

$$\begin{aligned} \text{Nu}_p \equiv \frac{h_c d_p}{k_g} = & 0.74(\text{Ar})^{0.1} \left(\frac{\rho_p}{\rho_g}\right)^{0.14} \left(\frac{c_{pp}}{c_{pg}}\right)^{0.24} (1-\varepsilon)^{0.67} \\ & + 0.46(\text{Re}_p \text{Pr}_g) \frac{(1-\varepsilon)^{0.67}}{\varepsilon} \end{aligned} \quad (1.7)$$

Chen (2003b) compared these empirical correlations with experiments conducted in a fluidized bed of 240 μm glass beads. Results revealed that very little agreement among various correlations, nor any between the experimental results and correlations. In addition, these correlations were obtained by analyzing the related dimensional and non-dimensional groups in experimental data sets without any argumentative support. In some cases, deviations as much as 100% were observed. As was emphasized by Chen et al. (2005), the application of these correlations, especially extrapolation should be exercised with caution.

Molerus and Wirth (1997b) derived the maximum heat transfer coefficient h_{max} ($\text{W}/(\text{m}^2\cdot\text{K})$) in fluidized bed under different flow regimes based on the semi-empirical analysis of five closely related non-dimensional groups $\pi_1 - \pi_5$, shown as follows,

$$\begin{aligned} \pi_1 &= d_p^3 g (\rho_p - \rho_g) / \mu^2 \\ \pi_2 &= \rho_p / \rho_g \\ \pi_3 &= c_{pg} \mu / k_g \equiv \text{Pr}_g \\ \pi_4 &= c_{pp} \mu / k_g \\ \pi_5 &= k_p / k_g \end{aligned} \quad (1.8)$$

It was concluded that for laminar flow regime where $\text{Ar} \leq 100$, particle-to-gas convection played a significant role in the heat transfer process, which relied heavily on the gas thermal conductivity k_g ($\text{W}/(\text{m}\cdot\text{K})$). Therefore, only π_1 and π_4 remained relevant. Combined with experimental data h_{max} was,

$$\frac{l_L}{h_{\max}} = \frac{l_L / 0.09}{k_g} + \frac{l_L / 0.09}{2c_{pp}\mu} \quad (1.9)$$

where l_L (m) is the laminar length-scale,

$$l_L = \left(\frac{\mu}{\sqrt{g(\rho_p - \rho_g)}} \right)^{2/3} \quad (1.10)$$

For $10^5 \leq Ar \leq 10^8$, similar analysis revealed that only π_1 , π_2 and π_3 were relevant,

$$\frac{h_{\max} l_t}{k_g} \text{Pr}_g^{-1/3} = 0.165 \quad (1.11)$$

Molerus et al. (1995) also analyzed experimental data from Wunder (1980). As the particle size increased a shift in dominant heat transfer mechanism occurred, from particle convection to gas convection. Both of them were used jointly in a fairly broad and practicable range of intermediate particle sizes ($10^{-1} \text{ mm} < d_p < 1 \text{ mm}$), with a corresponding Archimedes number range $10^2 \leq Ar \leq 10^5$. One of the best predictive equations for this particular important regime is,

$$\begin{aligned} \frac{hl_t}{k_g} = & \frac{0.125(1 - \varepsilon_{mf}) \left[1 + 33.3 \left(\sqrt[3]{\frac{U - U_{mf}}{U_{mf}}} \cdot \sqrt[3]{\frac{\rho_p c_{pp}}{k_g g}} \cdot (U - U_{mf}) \right)^{-1} \right]^{-1}}{1 + \frac{k_g}{2c_{pp}\mu} \left[1 + 0.28(1 - \varepsilon_{mf})^2 \left(\frac{\rho_g}{\rho_p - \rho_g} \right)^{0.5} \left(\sqrt[3]{\frac{\rho_p c_{pp}}{k_g g}} \right) (U - U_{mf})^2 \frac{U_{mf}}{U - U_{mf}} \right]} \\ & + 0.165 \text{Pr}_g^{-1/3} \left(\frac{\rho_g}{\rho_p - \rho_g} \right)^{1/3} \left[1 + 0.05 \left(\frac{U - U_{mf}}{U_{mf}} \right)^{-1} \right]^{-1} \end{aligned} \quad (1.12)$$

where l_t (m) is the turbulent flow regime length scale, given as,

$$l_i = \left(\frac{\mu}{\sqrt{g(\rho_p - \rho_g)\rho_g}} \right)^{2/3} \quad (1.13)$$

1.4.2 Mechanistic models

Empirical correlations are very useful for estimating the heat transfer coefficients in fluidized beds. Nevertheless, such correlations at times fail to predict the heat transfer when the operating conditions are out of the applicable range. Therefore, the mechanistic models are needed. The packet theory proposed by Mickley and Fairbanks (1955) is one of the most appropriate model for fluidized bed heat transfer. An analogy was made with the surface renewal theory for mass transfer (Danckwerts, 1951) where the heat transfer surface is contacted alternately by gas bubbles and the dense phase (or packets). In addition, heat transfer is achieved by transient conduction between packets and heating surface through the gas film, from the brief period of time when the packets reside on the surface. The instantaneous heat transfer coefficient between an isothermal heating surface and the packets is shown to be,

$$h_i = \sqrt{\frac{\rho_{mf} c_{p,mf} k_{eff}}{\pi t}} \quad (1.14)$$

in which k_{eff} , $c_{p,mf}$, ρ_{mf} are the effective thermal conductivity (W/(m·K)), thermal capacity (W/(kg·K)) and density (kg/m³) of the dense phase, respectively. The packet theory is most accurate for heat transfer in a fluidized bed of small particles ($d_p < 0.5 \text{ mm}$). As the particle diameter increases, the penetration depth (the distance between particle surface with temperature T_w (K) and the location with temperature of $0.9(T_w - T_b)$, where T_b (K) is bed temperature) is only one particle diameter or less, compared to 4–5 particle diameters for smaller particles. The local packet properties (e.g. void fraction and effective conductivity) may be drastically different from the bulk properties, causing the packet theory to give higher heat transfer coefficient values than experimental results because

of the overestimated effective conductivity of packets (Ozkaynak & Chen, 1980). Chen (2003b) summarized three basic types of heat transfer in fluidized bed,

- 1) Heat transfer between the gas phase and the surface, h_g
- 2) Heat transfer between dense phase and the surface, h_p
- 3) Radiation between the gas phase and the surface as well as the dense phase and the surface, h_r

$$h = (1 - f_d)h_g + f_d h_p + h_r \quad (1.15)$$

where f_d is the dense phase surface contact time fraction. Although both conduction and convection exist for the heat transfer between dense phase and heating surface, it is worth noting that convective heat transfer coefficient is much larger than that of conduction. The vigorous motion of the gas phase has a much more profound impact on particle-surface convection over conduction. Therefore, the amount of heat transferred by conduction during collision is negligible. As to radiation, its contribution is only relevant above 500 °C. By combining two heat transfer components, the overall convection heat transfer coefficient is obtained,

$$h = (1 - f_d)h_g + f_d h_p \quad (1.16)$$

1.4.3 Heat transfer study in pulsed and vibrated fluidized beds

Malhotra and Mujumdar (1987) studied heat transfer rates in a vertically vibrated fluidized bed with horizontal cylindrical surfaces. Both inter-particle forces and air gaps between the particles and heating surface were found to have adverse effect on heat transfer. Eccles (1990) investigated heat transfer of various particles in a VFB, with particle size ranging from 6 to 3600 μm . Results indicated that bed-to-surface heat transfer between a cylinder and bed particles depended heavily on solid circulation, which varied with vibration parameters. Siebert et al. (1999) studied mechanical vibration and its effect on heat transfer with particles $50 \mu\text{m} < d_p < 170 \mu\text{m}$, vibration frequency

from 20 to 200 Hz, with an amplitude of up to 5 mm. The measured heat transfer coefficient exceeded $1100 \text{ W}/(\text{m}^2\cdot\text{K})$, which was greater than what conventional fluidized bed could achieve. Zhu et al. (2008) proposed a dimensionless mathematical model in order to predict the local heat transfer coefficients between bed particles of VFB and immersed horizontal tubes. The effect of the of gas film thickness and residence time of packets were taken into consideration.

Hydrodynamics and heat transfer in a pulsed fluidized bed of silica sand were studied by Zhang (2005), in which the pulsed bed operated in bubbling regime. It was concluded that pulsation could significantly improve heat transfer by increasing the fluidization quality. Drying tests of sawdust performed by Reyes et al. (2008b) in a pulsed fluidized bed revealed the influence of operating parameters on drying rate. A simple correlation between Nusselt number and particle Reynolds number was also proposed. Sun et al. (2013) looked into heat transfer properties of crushed pellets when being co-fired with coal in a circulating fluidized bed. CFD simulation performed by Papadikis et al. (2010) demonstrated the influence of particle size on bed-to-surface heat, during which the maximum heat transfer coefficients for both $350 \mu\text{m}$ and $550 \mu\text{m}$ particles were measured.

1.5 Drying and mass transfer in fluidized bed

Despite the popularity of pulsed fluidized beds in the drying industry, there is still lacking a mathematical model that incorporates the influence of pulsation on drying. Similarly, a mass transfer model for pulsed fluidized bed is hardly available in the literature. As a result, a brief summary on drying and mass transfer in conventional fluidized beds is included below.

1.5.1 Drying in fluidized beds

Certain advantages of the fluidized bed such as high heat and mass transfer rate, easy material transport inside the reactor, low complexity for control and low maintenance cost have made them a popular choice for drying a variety of products. Utilization of fluidized bed dryer for biomass is mostly held back by the operating cost. In addition, the operation of fluidized bed dryers, normally requires specialist or trained engineers, instead of general technicians for the case of simpler dryers. Other drawbacks of utilizing fluidized bed as a dryer include higher pressure drop and more selective on particle properties compared to rotary drum dryers, as well as entrainment of fines. During the drying process in fluidized beds, moisture inside and outside the particles is being removed, which slowly reduces the cohesive forces and the minimum fluidization velocity. The flow behaviour also varies greatly with the types of particles with reference to the Geldart classification of powders (Geldart et al., 2009). For Group A and B particles smooth fluidization could be established, whereas for Group C particles severe channeling usually takes place until the gas velocity is high enough for turbulent fluidization. Poor fluidization quality is often associated with Group D particles as well, because of the higher density and larger particle size that may generate large bubbles in the bed.

Many experiments in the literature focused on pulsed fluidized bed drying, including a wide variety of chemicals, agricultural and forest products. Prachayawarakorn et al. (2005) performed drying of rice husk in both conventional and pulsed fluidized bed dryer and discovered a 25% reduction in airflow requirement, 30% lower power consumption in pulsed fluidized bed dryers, together with increased drying efficiency. Many drying studies in pulsed fluidized bed also included drying models to better interpret the experimental results, the majority of which are thin-layer drying models where the impact of pulsation frequency, temperature and flow rate are lumped into one parameter.

1.5.2 Drying models for fluidized bed

Drying in fluidized beds is heavily influenced by heat transfer and mass transfer. Attempts have been made to link experimental results to correlations and mathematical models for the prediction and analysis of fluidized bed drying. Based on the premises and assumptions made in such models, they could be roughly categorized as empirical model, single-phase model and two-phase model.

For most empirical models, drying is separated into different drying periods where different drying mechanisms may apply. The falling-rate drying period is of great interest to many researchers. By combining Fick's second law and the microscopic balance of mass transfer, the relationship between bed moisture content and drying time is established. Fick's second law has the following general form,

$$\frac{\partial X}{\partial t} = -\nabla \cdot (D_{eff} \nabla X) \quad (1.17)$$

in which X is the moisture content of a particle as a function of location and time. D_{eff} is the effective diffusivity. The above equation could be integrated for different particle shapes such as cube, cylinder, and sphere, in addition to different boundary and initial conditions. Analytical solutions for a variety of specific cases with unique boundary conditions are provided in Crank (1979). Simpler analytical solutions are also available if particle shrinkage is considered negligible and internal diffusion treated as the rate-controlling step (Sablani et al., 2000). Reyes et al. (2007) adopted Eqn. (1.17) to Cartesian coordinates for drying of potato cubes. Moisture content in the x -axis, $X(x, t)$ with no external resistance is,

$$\frac{X(t) - X_e}{X_0 - X_e} = \left(\frac{8}{\pi^2} \right) \sum_{n=0}^{\infty} \frac{1}{(2n-1)^2} \left\{ \exp \left[- (2n-1) \frac{\pi}{2} \right]^2 \frac{D_{eff}}{L_p^2} t \right\} \quad (1.18)$$

in which L_p is the length of the particle. Similarly, in spherical particles, moisture content is shown to be,

$$\frac{X(t) - X_e}{X_0 - X_e} = \frac{6}{\pi^2} \sum_{n=1}^{\infty} \frac{1}{n^2} \exp\left(-n^2 \frac{\pi^2 D_{eff} t}{R_p^2}\right) \quad (1.19)$$

where R_p is particle radius (Reyes et al., 2008b). It is clear that general solutions of the diffusion equation often consist of exponential functions. Many empirical exponential correlations have been proposed, parameters of which usually come from fitting experimental results. It is noteworthy that many process parameters including gas velocity, temperature and relative humidity are lumped into one or more coefficients in this type of models, and the contribution of a single parameter cannot be distinguished. Lewis (1921) pointed out that the rate of drying could be expressed as,

$$\frac{dX(t)}{dt} = k(X - X_e) \quad (1.20)$$

Consequently, by simply integrating the above equation the well-known Lewis equation is obtained,

$$\frac{X(t) - X_e}{X_0 - X_e} = e^{-kt} \quad (1.21)$$

Page (1949) studied the drying of shelled corn in thin layers and presented the following,

$$\frac{X(t) - X_e}{X_0 - X_e} = e^{-kt^n} \quad (1.22)$$

Although useful in the industrial settings, empirical correlations normally do not contain parameters of the fluidized bed, the effect of operating conditions and particle properties cannot be addressed. The single-phase model proposed by Martinez-Vera et al. (1995) attempted to link the macroscopic mass balance of moisture in a fluidized bed with single-particle drying dynamics. In this model, the fluidized bed is considered as a continuum where heat and mass balances are applied. Both the particle phase and the gas phase are assumed to be perfectly mixed (CSTR). The mass balance for moisture is given as,

$$-m_b \frac{d\bar{X}}{dt} = G_g (Y_o - Y_i) \quad (1.23)$$

here Y_o and Y_i (kg-water/kg-air) are the absolute humidity at the outlet and inlet, respectively. The fluidized bed is divided into a dense phase and a bubble phase. Any gas in excess of minimum fluidization velocity flows through the bubble phase, whereas the dense phase stays stagnant at minimum fluidization conditions. Both phases are assumed to be perfectly mixed. For a single particle in fluidized bed, moisture migration inside a spherical particle is,

$$\frac{\partial X}{\partial t} = -D_{eff} \left(\frac{\partial^2 X}{\partial r^2} + \frac{2}{r} \frac{\partial X}{\partial r} \right) \quad (1.24)$$

For the dense phase particles, mass balance of moisture leads to,

$$-\rho_p (1 - \varepsilon_{mf})(1 - \varepsilon_b) \frac{dm_b}{dt} = \vartheta \quad (1.25)$$

here m_b is the weight of the bed (kg), ϑ is the mass rate of evaporation of water (kg/m³.s). For steady-state operations, mass balance for interstitial gas is,

$$G_d \rho_g (Y_d - Y_i) = \vartheta + \frac{6K_c \rho_g \varepsilon_b}{d_b} (Y_b - Y_d) \quad (1.26)$$

in which G_d stands for the gas flow rate in bubble phase (m³/m³.s), K_c is the mass transfer coefficient across particle boundary (m/s). Similarly, mass balance of moisture in the bubble phase arrives at the following,

$$\rho_b \varepsilon_b \frac{dY_b}{dt} + \rho_g G_b (Y_b - Y_i) = \frac{6K_c \varepsilon_b}{d_b} (Y_d - Y_b) \quad (1.27)$$

In order to solve above equations, the particle surface was assumed to be in instant equilibrium with surrounding air. Good agreement with experimental work was reported for the drying of cereal grains in a fluidized bed.

1.5.3 Mass transfer in fluidized bed

Gas–solid fluidized beds are widely used for many chemical reactions such as catalytic combustion, fluid catalytic cracking, steam methane reforming and tar cleaning. In order to better design such reactors, a clear understanding of the interphase mass transfer is of great importance. There are two major mechanisms for mass transfer in fluidized beds (Levenspiel, 1998),

- (1) Convective mass transfer between particles and gas phase
- (2) Diffusion across the boundary

For Group B and D particles, the former is often dominant, whereas for Group A particles the latter is more important. Two different approaches for modelling the mass transfer in fluidized beds exist in the literature, the homogenous approach and the bubbling bed approach. In the homogenous approach, particles are treated as if they are in a fixed-bed reactor on a plug-flow model, and the rate of interphase mass transfer can be expressed by following,

$$\frac{dN_A}{dt} = k_{g,bed} S_{ex,p} (C_A^i - C_A) \quad (1.28)$$

where dN_A/dt stands for the mass transfer rate of A from particle surface to the gas phase, $k_{g,bed}$ (m/s) is the mass transfer coefficient of bed particles and $S_{ex,p}$ (m²) is the total surface area of fluidized bed particles. Extensive studies have been done on the mass transfer between a moving fluid and objects of certain shapes, including flat plates, spheres and cylinders. Such data have been correlated in terms of dimensionless parameters and the equations obtained are used to estimate the mass transfer coefficients in other moving fluids and geometrically similar surfaces. For a single spherical particle at low Reynolds number, the relation is given by (Froessling, 1938),

$$Sh = 2 + 0.552 Re^{1/2} Sc^{1/3} \quad (1.29)$$

The above correlation is intended for Reynolds numbers ranging from 2 to 800 and Schmidt number ranging from 0.6 to 2.7.

The heterogeneity of gas–solid fluidized bed is addressed in the bubbling bed approach. Specifically, both the bubble phase and the dense phase are taken into consideration. A widely-used expression that accounts for both the convective mass transfer and diffusion across boundary is,

$$k_{bd} = \frac{U_{mf}}{3} + \left(\frac{4D_{AB}\varepsilon_{mf}\bar{U}_b}{\pi\bar{d}_b} \right)^{0.25} \quad (1.30)$$

where \bar{U}_b and \bar{d}_b are the average bubble rise velocity and bubble diameter, respectively (Sit & Grace, 1981).

1.6 Outstanding issues

- Despite the abundance of studies and publications regarding biomass fluidization, few have been successfully carried out without the need of inert bed particles. In the meanwhile, aided by the presence of gas pulsations and mechanical vibration some agricultural and forest products have been reported to be successfully fluidized. As the physical and chemical properties of such powders vary significantly, the effectiveness of gas pulsation, as well as vibration on the fluidization of individual biomass species such as Douglas fir and pine is still largely unknown. Parameters such as superficial gas velocity, vibration intensity, pulsation frequency, temperature, pulsation duty cycle and fines that could potentially influence gas–solid contact and hydrodynamics during biomass fluidization have not yet been identified and investigated.
- Besides simple visual observations and measurements (e.g. bed pressure drop and voidage), there is an apparent lack of benchmarks that could reflect the quality of gas–solid contact as well as mass transfer.

- Although pulsed fluidized beds show promise in terms of overcoming difficulties brought up by the properties of unconventional biomass materials such as high moisture content, irregular shape, wide particle size distribution and low bulk density, the design, operation and scaling-up of fluidized bed reactors of biomass are still limited by the lack of understanding in heat transfer. Data on bed-to-surface heat transfer coefficients of biomass particles in fluidized bed are largely unavailable.
- Drying is one of the thoroughly studied topics related to biomass fluidization, as drying of agriculture, municipal waste and chemical products is often carried out in fluidized beds. Many publications focused on the experimental aspect of drying, some of which were accompanied by simple mathematical models. Such models normally only apply to a single particle or a single layer of particles while assuming the particle surface is in equilibrium with surrounding air, and failed to address the gas–solid flow and its possible effect on drying and mass transfer in fluidized beds. There is also lacking a drying model for pulsed fluidized bed, in which the effect of gas pulsation is addressed.
- Enhanced heat transfer in pulsed fluidized beds has already been reported by a number of researchers. However, the mechanism behind the possible influence of pulsation on heat transfer is rarely discussed. No model can be found on heat transfer in pulsed fluidized bed that incorporates pulsation frequency and related parameters.

1.7 Research objectives

The overall objective of this project is to develop a pulsed fluidized bed for the fluidization of biomass without the presence of inert bed particles so that it can be applied for biomass drying, torrefaction and pyrolysis, with desired solids product. The specific tasks include:

- To investigate the effect of pulsation and vibration on the fluidization of various biomass particles, namely Douglas fir, pine and switchgrass. Batch drying test is chosen as the indirect benchmark indicator for mass transfer rate and gas–solid contact efficiency. By performing such tests with different biomass materials, under different operating conditions, the optimum conditions around which pulsation and vibration are most effective could be determined. Parameters include average superficial gas velocity, pulsation frequency and duty cycle, vibration intensity, drying temperature and particle size distribution.
- To improve the performance in terms of heat and mass transfer in pulsed fluidized beds, tapered bottom section will be introduced to eliminate solids flow dead zones observed in preliminary studies in the original rectangular column.
- To assemble a simple mathematical model for biomass drying in pulsed fluidized bed, so that the effect of flow rate, pulsation and temperature on mass transfer among different biomass species could be further quantified.
- To obtain the bed-to-surface heat transfer coefficients of biomass in pulsed fluidized bed without the presence of inert bed particles under various operating conditions.

To adopt existing heat transfer models for fluidized bed to the pulsed fluidized bed of biomass. Find the missing link between continuous fluidized bed and pulsed fluidized bed in terms of heat transfer and shed light on the higher heat transfer rates in pulsed fluidized beds.

1.8 Thesis layout

The thesis consists of six chapters. Chapter 2 covers the experimental setup, experimental procedures as well as data acquisition and analysis methods in order to meet the objectives listed

in Chapter 1. Chapter 3 presents the experimental results of batch drying of various biomass species in two reactor geometries, namely the rectangular fluidized bed and the tapered fluidized bed. The hydrodynamics and gas–solid flow behaviour observed during drying process are also discussed. A comparison in terms of drying performance between the two reactor geometries is also provided. Chapter 4 presents a two-phase model for the pulsed fluidized bed drying process. Both geometries are considered, with results being laid out separately. The focus shifts from mass transfer and drying to heat transfer in Chapter 5. The experimentally obtained bed-to-surface heat transfer coefficients are reported in this chapter. Besides a brief comparison in terms of heat transfer rates between the rectangular and tapered fluidized bed, a simple model for pulsed fluidized bed is heat transfer also presented, contributing to a better understanding of the effect of pulsation on heat transfer.

The appendices include additional information that is relevant to this work. The procedure to measure the minimum fluidization velocity in pulsed fluidized beds where the superficial gas velocity is constantly oscillating is documented in Appendix A1. The intricate relationship between pulsating gas stream and the fluidization stream is discussed in Appendix A2. The angle of repose data for biomass particles containing different amount of moisture that were used for the design of the tapered bottom section is documented in Appendix A3. Appendix A4 confirms the accuracy of the drying rate estimation through relative humidity probes. Appendix A5 contains a complete set of data for the two-phase drying model. Appendix A6 shows the measured equilibrium moisture content data. Appendix B elaborates the heat loss calculation estimated from a simple CFD simulation. The design of the complex data acquisition system specifically programmed for this work so that signals from multiple sources at different sampling rates could be collected is illustrated in the Appendix D, with the dimensions and assembly of the heat transfer probe designed to measure the bed-to-surface heat transfer coefficient given in Appendix E.

CHAPTER 2

EXPERIMENTAL METHODS

2.1 Experimental plan

In order to achieve the objectives stated in the previous chapter, both experiments and modelling were planned and conducted. The experiments were performed at the Fluidization Research Centre facility in the University of British Columbia. Two fluidized bed geometries were utilized and investigated, namely rectangular fluidized bed and a tapered fluidized bed. The gas–solid contact efficiency and mass transfer capabilities were benchmarked by batch drying tests in the pulsed fluidized beds, with the following parameters investigated: biomass species (Douglas fir, pine and switchgrass), average superficial gas velocity, pulsation frequency, vibration intensity, air temperature, pulsation duty cycle, particle size distribution and fraction of fine particles. The experimental data were then fitted into the proposed two-phase drying model to obtain parameters such as effective diffusivity to provide additional insights.

For the bed-to-surface heat transfer study, heat transfer coefficients were measured in both reactor geometries against a variety of parameters, including different biomass species, superficial gas velocity, pulsation frequency, vibration intensity, pulsation duty cycle, probe lateral position, particle size distribution and presence of fine particles. A simple heat transfer model for the pulsed fluidized bed of biomass was also developed so that the influence of pulsation on heat transfer could be simulated.

2.2 Fluidized bed with rectangular cross-section

The pulsed fluidized bed unit had previously been used by Zhang et al. (2012) for the study of fluidization characteristics and charging behaviour of fly ash. Dimensions of the rectangular fluidized bed unit are illustrated in Figure 2.1, while a schematic is shown in Figure 2.2. The fluidized bed column was made of Plexiglas with a rectangular cross-sectional area. The height of the fluidized bed column was 1.0 m, and the cross-section was 0.15 m \times 0.10 m. Along the height of the column there were measurement ports on the side, the first of which was located 25 mm (1 in) above the distributor plate, with the others being 102 mm (4 in) apart. A perforated aluminum plate with triangular-patterned 3.18 mm (0.125 in) diameter orifices and a 40% opening ratio was selected as the distributor. The higher than normal opening ratio was chosen such that pressure drop across the grid could be reduced. In addition, low pressure drop across the grid also allowed stronger gas pulsations to pass through with minimal damping. To prevent particles from falling into the plenum chamber, a fine mesh was sandwiched between the distributor plate and a base plate, which had slightly larger orifices with the same layout as the top plate. To prevent particles from escaping, a bag filter was installed at the gas outlet.

In order to verify the effect of vibration on biomass fluidization and its ability to eliminate undesired flow behaviour such as channeling that may occur during the experiments, the fluidized bed column was securely mounted to a vibratory base (Eriez 48A, Eriez Manufacturing Co., USA). The vibratory based operated on a fixed vibration frequency of 60 Hz, with the amplitude fully adjustable from 0% to 100% and a maximum vertical displacement of 0.381 mm.

Dehumidified high-pressure building air (40 PSIG, 276 kPa) was used for all the experiments in this work. After being regulated by a pressure regulator (AR-40-N04H-Z, SMC Pneumatics, Canada), building air was split into two streams, labelled FL1 and FL2 in Figure 2.2. FL2 was the pulsating stream where gas pulsation had been generated. On this stream, a solenoid valve (8212G034-120/60, ASCO Valve, USA) was installed. To ensure stable supply of drying air during the experiments,

a surge tank was placed before the solenoid valve. The surge tank also kept the rotameters from oscillating due to pressure fluctuations caused by the gas pulsations.

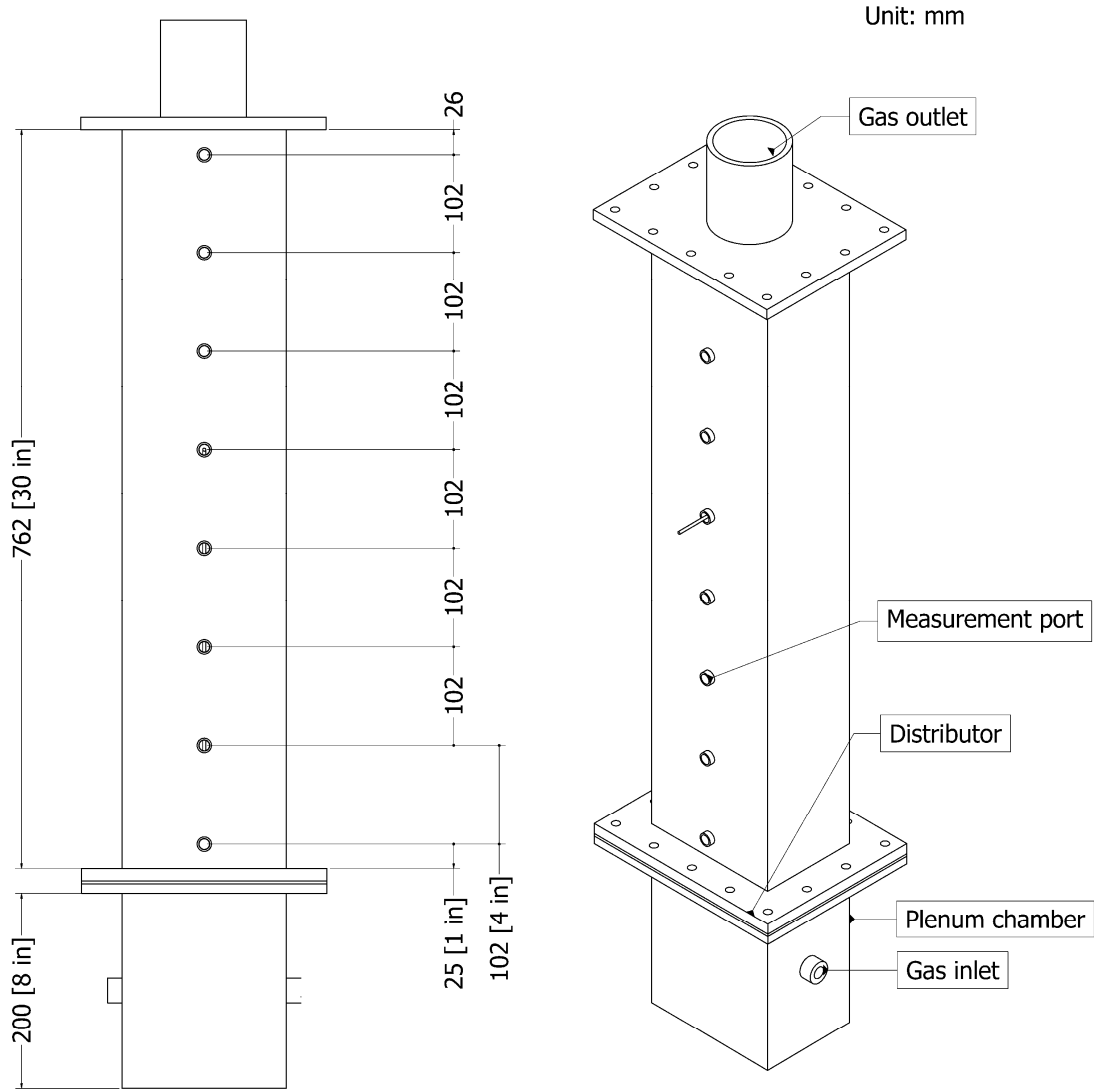


Figure 2.1 Dimensions of the rectangular fluidized bed with pulsed gas flow (a) Side view of the rectangular fluidized bed and related dimensions in millimeter; (b) 3D view and features of the rectangular fluidized bed.

The other stream labelled as Stream FL1 in Figure 2.2 was the fluidization stream with a constant flow rate. A constant but small airflow was also supplied to the fluidized bed so that particles could maintain mobilized when the flow rate of the pulsating stream was low. Preliminary studies as well as results from Reyes et al. (2008a) revealed that under the same combined flow rate, splitting the gas flow into two streams and only using a portion of it for pulsation generation while leaving the rest as a constant fluidization stream could potentially weaken the “shock” generated by the pulsation, undermining the effect of pulsation on cohesive particle fluidization. This was also confirmed in a preliminary test, as shown in Appendix A2. Therefore, only the pulsating stream was used. Rotameters with needle valves (FL6212-V and FL-6213-V, respectively, Omega, Canada) were installed to control the flow rate on each stream. The two streams then merged into one before entering an inline gas heater (AHP-7561, Omega, Canada). The temperature was managed by a controller (CN4316, Omega, Canada). A three-way valve that served as a bypass was placed before air could enter the plenum chamber, so that at the end of a drying session samples could be taken out of the fluidized bed from the top without being carried away by the fluidizing air. Packings were placed in the plenum chamber to better distribute the fluidization medium. In addition, packings allowed further reduction in the overall volume of the plenum chamber, which reduced the dampening effect on gas pulsation.

The air exited the fluidized bed through the top, where a bag filter was placed in order to capture the biomass particles from escaping. Pressure transducers were installed to measure absolute and differential pressure in the pulsed fluidized bed, as well as the plenum chamber. Multiple T-type thermocouples were also implemented, along with relative humidity probes and a high-speed camera. Details are provided in Section 2.4.

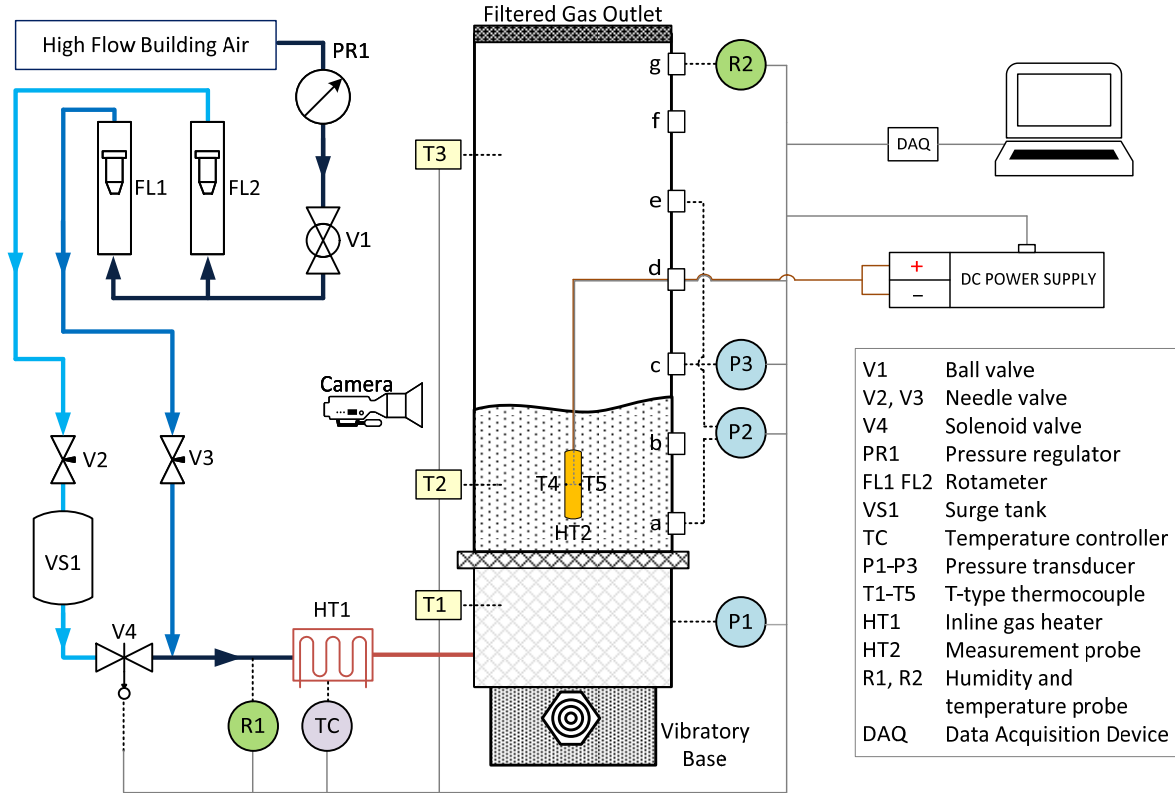


Figure 2.2 Schematic of the rectangular pulsed fluidized bed

2.3 Fluidized bed with tapered bottom section

Preliminary experiments revealed that during the fluidization of biomass dead zones were formed at the bottom corners of the rectangular fluidized bed. The poor flowability of biomass particles was likely a contributor, especially when wet. By testing the angle of repose of the biomass particles used in this study, a new tapered bottom section was fabricated. As can be seen in Figure 2.3, the tapered channel was inserted between the original rectangular column and the plenum chamber. Distributor with the same orifice diameter (3.18 mm, 0.125 in) and opening-area ratio (40%) as the rectangular bed was used on the tapered bed. However, the dimension of the distributor was reduced to 76.2 mm by 100 mm, compared to the original 150 mm by 100 mm. The angle of the diverging channel was determined from the angle of repose (AOR) experiments. Details of the AOR

values for all three biomass species at different moisture content are included in Appendix A3. The goal was that the tapered bottom section would have a side wall steeper than the angle of repose of wet biomass particles, so that even at their most cohesive state biomass particles could still fall down to the bottom of the bed. Dimensions of the tapered channel are displayed in Figure 2.4.

No further changes were made to the system besides the addition of a tapered bottom section. Experiments with the same operating conditions were carried out in both geometries so that the heat and mass transfer performances could be evaluated and compared.

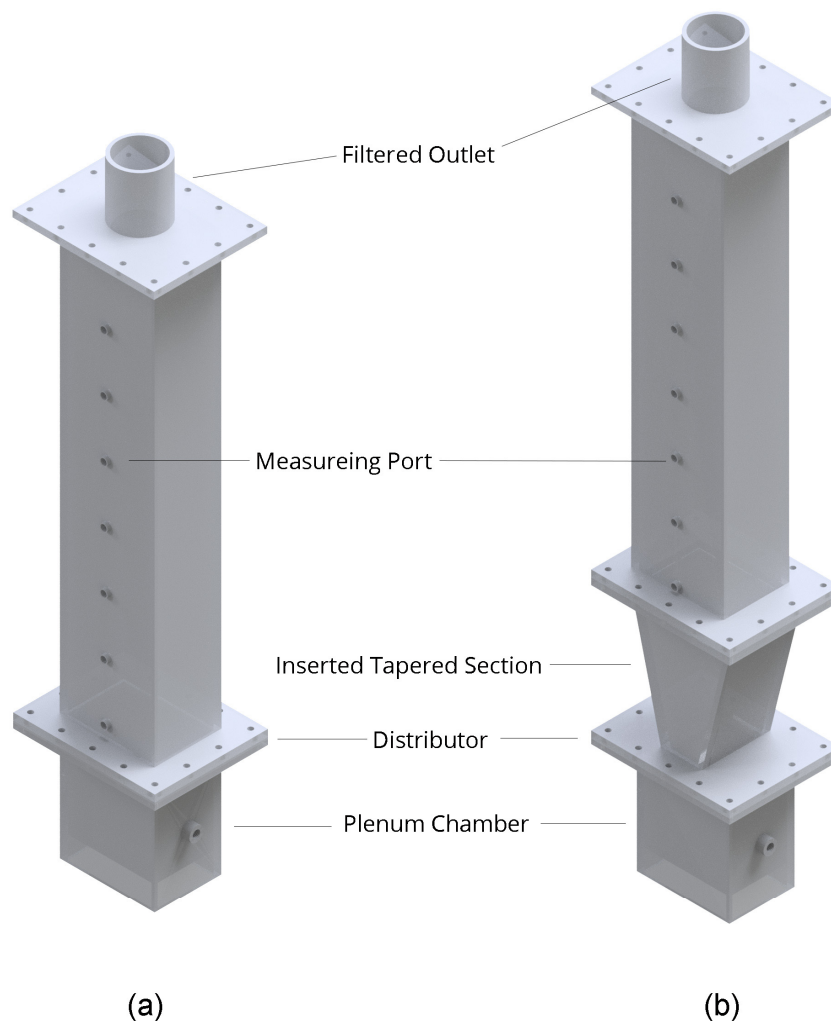


Figure 2.3 Comparison of the two reactor geometries. (a) the rectangular fluidized bed; (b) tapered fluidized bed.

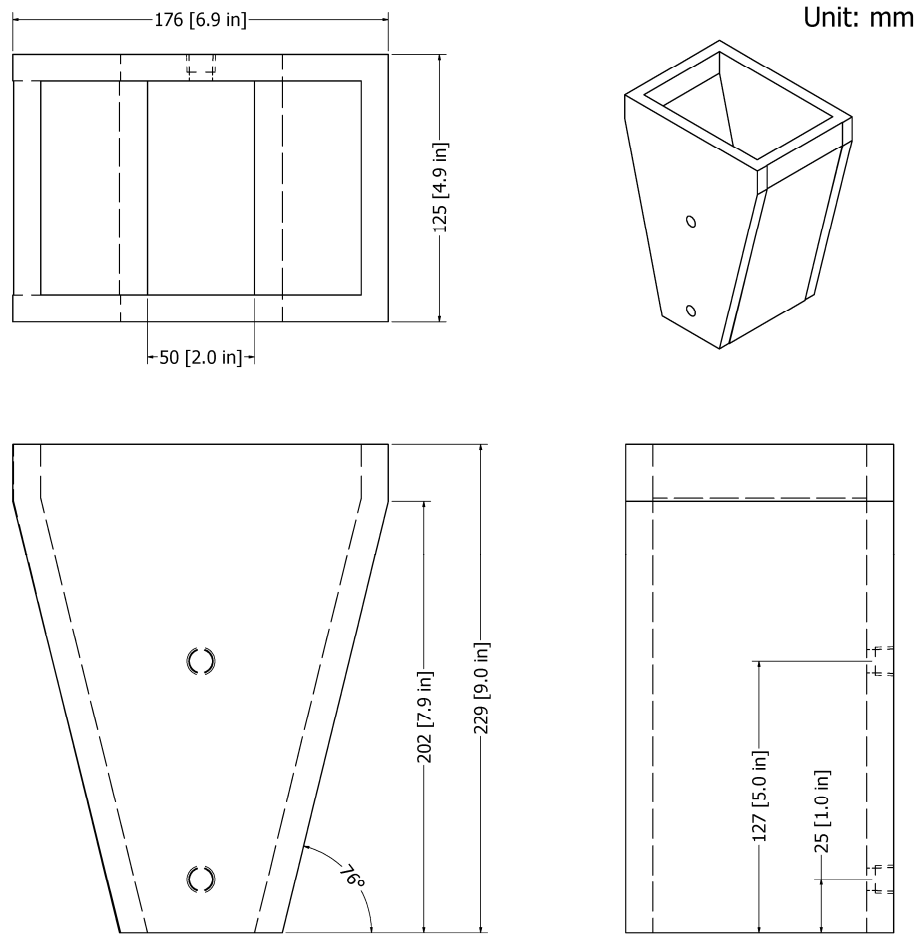


Figure 2.4 Dimensions of the inserted tapered section at the bottom of the fluidized bed (unit: mm). (a) top view; (b) 3D view; (c) front view; (d) side view.

2.4 Data acquisition system

In order to monitor and later analyze the hydrodynamics as well as heat and mass transfer performances of the pulsed fluidized bed, multiple pressure transducers, thermocouples and relative humidity probes were installed at various locations of the pulsed fluidized bed. A lab computer with AMD Phenom™ II X4 processor (Model number B93, 4 physical cores, clock speed 2.8 GHz) and 8 GB RAM was used for the data acquisition and data processing. The operating system was Microsoft Windows 7 (Service Pack 1, 64bit). A computer program compiled in LabVIEW

(National Instruments, Version 2015 SP1) was used to capture data, analyze related parameters in real-time, plot, display essential information, and record all data to files. The block diagram and front panel of the LabVIEW program are included in Appendix C.

2.4.1 Pressure measurements

As mentioned in Section 2.2, there were seven measurement ports on the side of the Plexiglas column in the rectangular fluidized bed, which were labelled (a) through (g). Ports (a) and (g) were used to measure the pressure drop across the bed with a pressure transducer (PX164-0105DV, Omega, Canada), while port (c) measured the absolute pressure of the column (PX163-005BD5V). The pressure of the plenum chamber was also monitored (PX142-005D5V). All pressure transducers were calibrated prior to being installed on to the unit, and calibration data were included in the LabVIEW program. A fine stainless steel mesh was placed at pressure measurement ports to avoid fine particles from entering. For the tapered bed, three additional ports were added to the system. Location of the probes was kept the same as for the rectangular bed.

A PCI-DAS08 data acquisition board (Measurement Computing, Norton, MA, USA) was used to collect and convert analog voltage signals from the pressure transducers to digital forms on the computer. Normally the bed behaviour of interest has a frequency of less than 10 Hz. Consequently, the sampling frequency should be at least 50 Hz in order to capture said behaviours, in addition to the minute changes in bed pressure drops. The sampling frequency for pressure signals in this study was set to 400 Hz, which should be sufficient to capture the dynamics of the pulsed gas–solid flow behaviour in the fluidized bed.

2.4.2 Temperature and relative humidity measurement

T-type thermocouples were placed at various locations to measure the temperatures of the dense phase, freeboard, plenum chamber and the gas inlet. In order to reduce the response time, ready-made thermocouple wires with perfluoroalkoxy alkanes (PFA) insulation and 30 AWG diameter were selected (5TC-TT-T-30-72, Omega, Canada). The thermocouple readings were collected and converted into digital signals by NI-9214 isothermal thermocouple measurement system (National Instruments, USA), which offered up to 0.02 °C measurement sensitivity and 0.45 °C accuracy. According to the specifications from the manufacturer, chosen thermocouple had a thermal response time of 0.38 s. To capture all the possible changes and dynamics in the pulsed fluidized bed, the sampling rate for temperature measurements was set to 20 Hz, which was greater than the rate of change of thermocouple readings.

For the air inlet, relative humidity was measured and recorded by a humidity indicator (HM141, Vaisala, Finland). Since the relative humidity and temperature of the building air were very stable, only a few percentages of variation were observed within a day. Consequently, the relative humidity readings were only updated every 60 seconds for the inlet. In order to obtain desired drying temperatures, an inline gas heater was installed (AHP-7561, Omega, Canada). The heater was controlled by a programmable controller (CN4316, Omega, Canada) so that the air temperature could be precisely managed. Another humidity probe (HMT335, Vaisala, Finland) was installed at the top on port (g), right next to the gas exit so that both temperature and relative humidity of the exiting air were measured. The voltage output from HMT335 was collected by NI USB-6008 data acquisition device (National Instruments, USA) at a sampling rate of 10 Hz.

2.4.3 High-speed imaging

To understand the transient flow behaviour of the pulsed fluidized bed, a high-speed camera was placed in front of the column (240 frames per second at 1280×720 pixels, $f/2.0$ aperture). The videos captured during the experiments were slowed down and played back at 30 frames per second so that both gas–solid contact and bubble patterns were better identified. Alternatively, individual frames were also extracted from the video so that bed behaviour at any given time within a pulsation cycle could be thoroughly examined. Video editing was completed in VideoLAN Movie Creator (VideoLan, Paris, France). Frame extraction was performed with PotPlayer (Daum Communications Corp.). The extracted images were processed by Paint.NET (dotPDN LLC) to enhance contrast and sharpness. Abovementioned programs are all freeware and permitted for education use.

2.4.4 Solenoid valve control

Gas pulsation is a key aspect of this study, which is generated by a solenoid valve. The actuation of the solenoid valve was controlled by the lab computer, on which a simple LabVIEW program was written so that the state of the solenoid valve (on and off) could correspond to the high and low state generated by the digital output. Duration of the “ON” period and “OFF” period was separately controlled to allow variations in both pulsation frequency and duty cycle. The digital output was transmitted through NI USB-6009 (National Instruments, USA) and relayed to the solenoid valve where gas pulsations was achieved. The refresh rate of the digital output channel was 100 Hz, so that the accuracy of the “ON” and “OFF” period for each pulsation cycle was 10 milliseconds.

2.5 Particulate material

Three biomass species were investigated in this work, which were Douglas fir, pine and switchgrass. Pine and Douglas fir were chosen as the biomass species to be studied in this work because most of the available woody biomass in BC are SPF (spruce-pine-fir), with the majority being pine (80%). By choosing pine and Douglas fir sawdust as the particles under investigation, the biomass available for future thermochemical conversions could be well represented. Switchgrass from Manitoba, Canada, was also tested in this work. Switchgrass is one of the major energy crops in North America, which was identified as a model energy crop by the United States Department of Energy (Keshwani & Cheng, 2010). The majority of the experiments were performed with pine and Douglas fir. A small number of experiments were performed with switchgrass to contrast results of Douglas fir and pine. Both pine and Douglas fir sawdust was generously donated by Tolko Industries Ltd. (Vernon, British Columbia, Canada), along with pine sawdust. Biomass material received from the sawmill contained a significant amount of water that could have led to molding if not properly treated. As a result, biomass particles were first dried in the oven, followed by preliminary sieving with 3.5 mm screen so that particles too big for fluidization were removed.

Minimum fluidization velocities in the rectangular pulsed fluidized bed were also measured. Unlike conventional fluidized beds where the gas supply is continuous and mostly stable, the superficial gas velocity and bed pressure drops in pulsed fluidized beds are often oscillating around an average value. Therefore, minimum fluidization velocity could not be derived from the plot of differential bed pressure drop vs. superficial gas velocity. The peak pressure drop and average superficial gas velocity were used instead. The details are shown in Appendix A1.

Both true density and bulk density were measured and recorded. The former was measured by a nitrogen gas pycnometer (Model MVP-D160-E, Quantachrome Instruments, Boynton Beach, FL, USA), and the latter by a graduated glass cylinder (25 ml capacity, 0.875" diameter, 0.5 ml scale intervals). The switchgrass sample contained more fines and needle-shaped particles, which

Table 2.1 Properties of the biomass samples at 7% moisture content (dry basis)

Biomass species	Bulk density, kg/m³	True density, kg/m³	Sauter mean diameter, mm	Sphericity	Minimum fluidization velocity, m/s	BET surface area, m²/g
Douglas fir	164	1.38×10 ³	1.45	0.42	0.238	3.09
Pine	139	1.24×10 ³	1.47	0.43	0.212	3.86
Switchgrass	184	1.45×10 ³	0.76	0.34	0.185	5.87

2.6 Batch drying test

Operating conditions have been found influential on drying in pulsed fluidized beds (Bhattacharya & Harrison, 1976; Reyes et al., 2008b). To investigate such influence of operating conditions on gas–solid contact and more importantly heat and mass transfer, batch drying test was selected as an indirect indicator. The idea is that good gas–solid contact and fluidization behaviour should lead to higher heat/mass transfer rates and subsequently faster drying process. By comparing drying rate and the amount of water removed from certain amount of biomass particles, mixing and heat/mass transfer performance could be compared between different operating conditions. Parameters such as temperature, flow rate, pulsation frequency, pulsation duty cycle, particle size distribution and bed height were evaluated. By drying the same amount of biomass particles under different operating conditions, the fluidization quality is also indirectly reflected by the drying efficiency, or simply how much moisture is removed from the biomass samples. Certain experiments were performed in both reactor geometries with identical operating conditions so that the performance improvement of the tapered design could be quantified. Error bars are used for some of graphs in the following chapters to indicate standard error (Everitt, 2006).

2.6.1 Sample preparation

Prior to being transported to the laboratory biomass had been kept outdoors in the sawmill, therefore high moisture content was found in the samples. As a result, biomass was first dried in ovens at a low temperature (50–60 °C) to remove excess water. Particles too big for fluidization were then removed by sieving through a 3.5 mm screen. The remaining particles were bagged and stored in a cold room (maintained at 5 °C) to prevent degradation from any microbial activities.

To prepare samples for the batch drying test, particles were well mixed with water and placed into a dedicated refrigerator at 4 °C for 24 h to ensure uniformity of the moisture content within. Sufficient time was also allowed for the sample to reach room temperature before being dried.

2.6.2 Drying test procedure

Before each run, 200 g of sample were placed into the fluidized bed column. The only exception was the study of bed height effect, where a range of biomass sample weights from 200 to 350 g was used. Biomass particles were then fluidized at different operating conditions such as average superficial gas velocity, pulsation frequency and vibration intensity. Certain experiments were repeated five times to ensure the integrity of the data and to calculate standard errors.

In addition to the original wet sample, at the end of each run a few grams of dried particles were also collected. The moisture contents of both samples were obtained so that the amount of water that had been removed as a result of drying could be determined. Final moisture contents of the samples were determined according to ASTM D4442-07 standard. Specifically, samples were placed in 3" aluminum foil pans and dried in an oven with precise temperature control. The oven was kept at 103 °C for 24 h to remove all residual moisture in the samples. The weight before and after oven drying was measured by an electronic balance (0.0001g accuracy).

Moisture content is often used to express the amount of water in a sample. There are different moisture content definitions, such as dry basis and wet basis moisture content. In this work, dry basis moisture content is exclusively used. The moisture content (dry basis, wt., d.b.) is defined as,

$$X_{Exp} = \frac{m_{wet} - m_{dry}}{m_{dry}} \quad (2.1)$$

Here m_{wet} (g) and m_{dry} (g) are the weight of the samples before and after drying. Since the initial moisture contents from different set of experiments might not be exactly the same, the results should be normalized for better comparison. Ψ denotes the moisture removal ratio during drying,

$$\Psi = \frac{X_{Exp} - X_e}{X_0 - X_e} \quad (2.2)$$

in which X_e (dry basis) and X_0 (dry basis) represents the equilibrium moisture content and the initial moisture content, respectively. The equilibrium moisture content of biomass materials often changes with temperature and relative humidity. Since drying air used in this work had a relative humidity of less than 2%, the equilibrium of three biomass species under this humidity and at 20–50 °C were less than 3% (more data are listed in Appendix A6). A moisture ratio (Φ) as defined below is used in this study to present experimental data (Celma et al., 2012; Doymaz et al., 2004; Forest Products Laboratory, 2010; Karunanithy et al., 2013; Sacilik & Elicin, 2006),

$$\Phi = \frac{X_{Exp}}{X_0} \quad (2.3)$$

Similarly, the percentage of water removed from the sample could be calculated by,

$$\eta = \frac{X_0 - X_{Exp}}{X_0} \quad (2.4)$$

Because relative humidity of the air at both inlet and outlet was constantly monitored as a known gas flow rate, the amount of water entering and exiting the fluidized bed column could be calculated. Drying rate could also be derived from the difference between two readings. Therefore, the instantaneous drying rate W (g-water/s) at any given time during the drying process is calculated based on,

$$W = \frac{dw}{dt} = M \cdot (Y_o - Y_i) \quad (2.5)$$

M (kg/s) is defined as the mass flow rate of the drying air, whereas Y_o and Y_i stand for the absolute humidity of air (kg-water/kg-air) at the outlet and inlet, respectively. The mass ratio of water vapour and dry air, or absolute humidity Y is calculated by,

$$Y = 0.622 \left(\frac{p_s}{p - p_s} \right) \quad (2.6)$$

here p_s (Pa) stands for the water vapour saturation pressure. The probes measured temperature and relative humidity at this temperature, so conversion was needed between relative humidity and absolute humidity. Relative humidity is defined as the ratio of the water vapour pressure to the saturation water vapour pressure (over water) at this gas temperature,

$$RH = \frac{p}{p_s} \times 100\% \quad (2.7)$$

Equations (2.1) to (2.7) were incorporated into the LabVIEW program. With the relative humidity readings and temperature readings, plus a known gas flow rate, drying rate was obtained during the experiment in real time, which was displayed on the computer monitor with other vital pieces information during drying. Such data were also saved to a series of files along with the rest of the parameters for further analysis after the conclusion of drying tests.

2.7 Bed-to-surface heat transfer measurement

For the heat transfer measurements moisture contents of all biomass powders were kept at approximately 7% (dry basis), which was close to the equilibrium moisture content at room temperature and room humidity, so that moisture content would not become a contributing factor leading to the possible differences in heat transfer coefficients. The same bed height of 0.15 m was chosen for all heat transfer experiments to ensure that the heat transfer probe was fully immersed. This also ensured that results could be better compared.

2.7.1 Heat transfer probe assembly

In order to measure the heat transfer coefficients from an immersed surface to the bed, or the bed-to-surface heat transfer coefficient, a probe was assembled and installed in the fluidized bed column, shown as HT2 in Figure 2.2. Detailed design of the heater probe is illustrated in Figure 2.6.

26 AWG (0.4 mm OD) Ni–Cr heating wire was embedded to the heater probe to generate heat necessary for the measurements. To ensure uniform temperature distribution the wire was wrapped tightly around a hollow 9.53 mm OD (6.35 mm ID) polytetrafluoroethylene (PTFE) tube in a spiral fashion. The spacing between each revolution of the wire was carefully maintained the same. The PTFE tube with heating wire was then inserted into a copper shell with slightly larger diameter (15.88 mm OD, 14.25 mm ID). The external surface of the copper shell was the actual heat transfer surface. Length of the shell was 2" (50 mm). The small gap between the PTFE core and copper shell was filled with chemically conductive yet electrically insulating cement (OB 600, Omega, Canada). To prevent air bubbles being trapped between the gap and interfere with heat conduction, the filling process was completed in vacuum on a vibrating table.

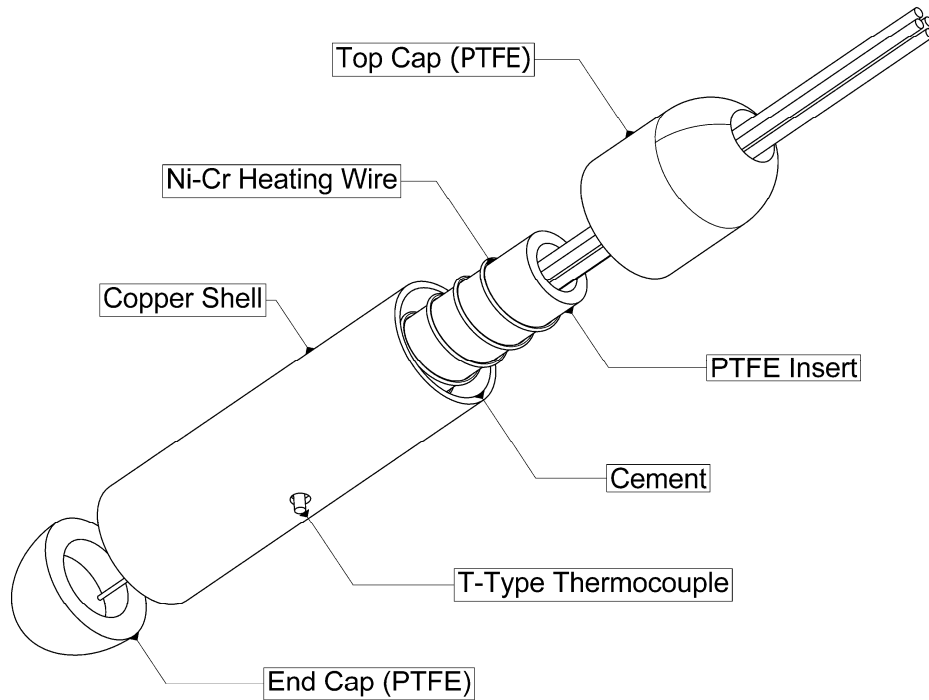


Figure 2.6 Assembly of the heat transfer measurement probe

On both sides of the copper shell, a cap was installed. Since the probe was lowered vertically into the fluidized bed, the caps were named as “top cap” and “end cap”. Both caps were made of PTFE so that heat loss through axial heat conduction was reduced. 40 AWG T-type thermocouples (5TC-TT-T-40-72, Omega, Canada) with PFA insulation (T4 and T5 in Figure 2.2) were used to measure the probe surface temperature, T_s . Two holes were drilled in the middle of the copper shell on opposite sides to allow the tip of thermocouple wire to reach out. Both tips were precisely cemented on the surface. The heating wire was powered by a B&K Precision DC power supply (Model No.1785B, USA) with adjustable voltage (0–18 V). Bed temperature was measured by two 40 AWG T-type thermocouples wires (5TC-TT-T-40-72, Omega, Canada) mounted on the opposite side of the pressure taps. The locations of the thermocouples are illustrated in Figure 2.7. Tips of the

thermocouples were 20 mm away from the wall so that heat loss could be eliminated. The average of the two thermocouples were taken as the bed temperature.

The power supply was equipped with a TTL-serial interface and native software for easy monitoring and control of the current and voltage outputs. The instantaneous voltage and current values could be exported to LabVIEW in real time with a sampling frequency of 10 Hz. These data were saved along with other process parameters.

The probe was vertically mounted in the fluidized bed column; dimensions and position of the heater probe are illustrated in Figure 2.7. To prevent heater probe from swinging around in the fluidized bed during fluidization because of uprising gas flow and particles, a rigid connection was used. The probe was supported by an acrylic tube. Not only did it offer good insulation to further reduce heat loss through axial heat conduction, but also allowed the heating wires and thermocouple wires to pass through.

The bottom of the probe was 2" (50 mm) above the distributor. In most experiments, the probe was located in the centre of the bed, which had a 2" (50 mm) side clearance with the walls. In order to measure heat transfer coefficients at different lateral positions, the probe was moved horizontally by ± 20 mm.

2.7.2 Bed-to-surface heat transfer coefficient

The bed-to-surface heat transfer coefficient was calculated according to an energy balance, which is defined as,

$$h = \frac{VI - Q_l}{A_s(T_s - T_b)} \quad (2.8)$$

in which V and I are the voltage and current read from the DC power supply. Q_l (W) is the estimated heat loss. T_s and T_b represent surface temperature of the probe and temperature of the dense phase,

respectively. A_s (m^2) is the vertical surface area of the copper shell where heat transfer takes place. In order to determine the heat loss Q_l (W), experiments and computational fluid dynamics (CFD) simulations were conducted during which the probe was used to measure heat transfer between the heating surface and surrounding air, with measured temperatures of the top cap and end cap as boundary conditions. Details of the heat loss estimation are available in Appendix B. Results indicated a heat loss of less than 1%. As a result, heat loss was considered negligible and Eqn. (2.8) is further simplified to,

$$h = \frac{VI}{A_s(T_s - T_b)} \quad (2.9)$$

Only steady-state heat transfer studies were performed in this work. Sufficient power was provided by the DC power supply to the heater probe such that there existed a temperature difference between the probe surface and dense phase. This temperature difference ($T_s - T_b$) is approximately 20 °C, which not only was significant enough to reduce error in Eqn. (2.9) for calculating h , but also ensures that the probe surface temperature was not so high that it greatly alters properties of surrounding air. For each operating condition, at least 5 min was allowed for the system to stabilize so that temperature fluctuation on the probe surface was kept within 1 °C. After reaching such a steady state, one minute of the data was recorded at 20 Hz that would yield approximately 1200 data points. Heat transfer measurement for each operating condition was repeated at least five times. Parameters investigated included average gas flow rate, pulsation frequency, pulsation duty cycle, particle size, effect of fines, lateral position as well as biomass species.

A summary of data acquisition system is listed in Table 2.2. Parameters investigated in batch drying tests and heat transfer studies are summarized in Table 2.3.

Unit: mm

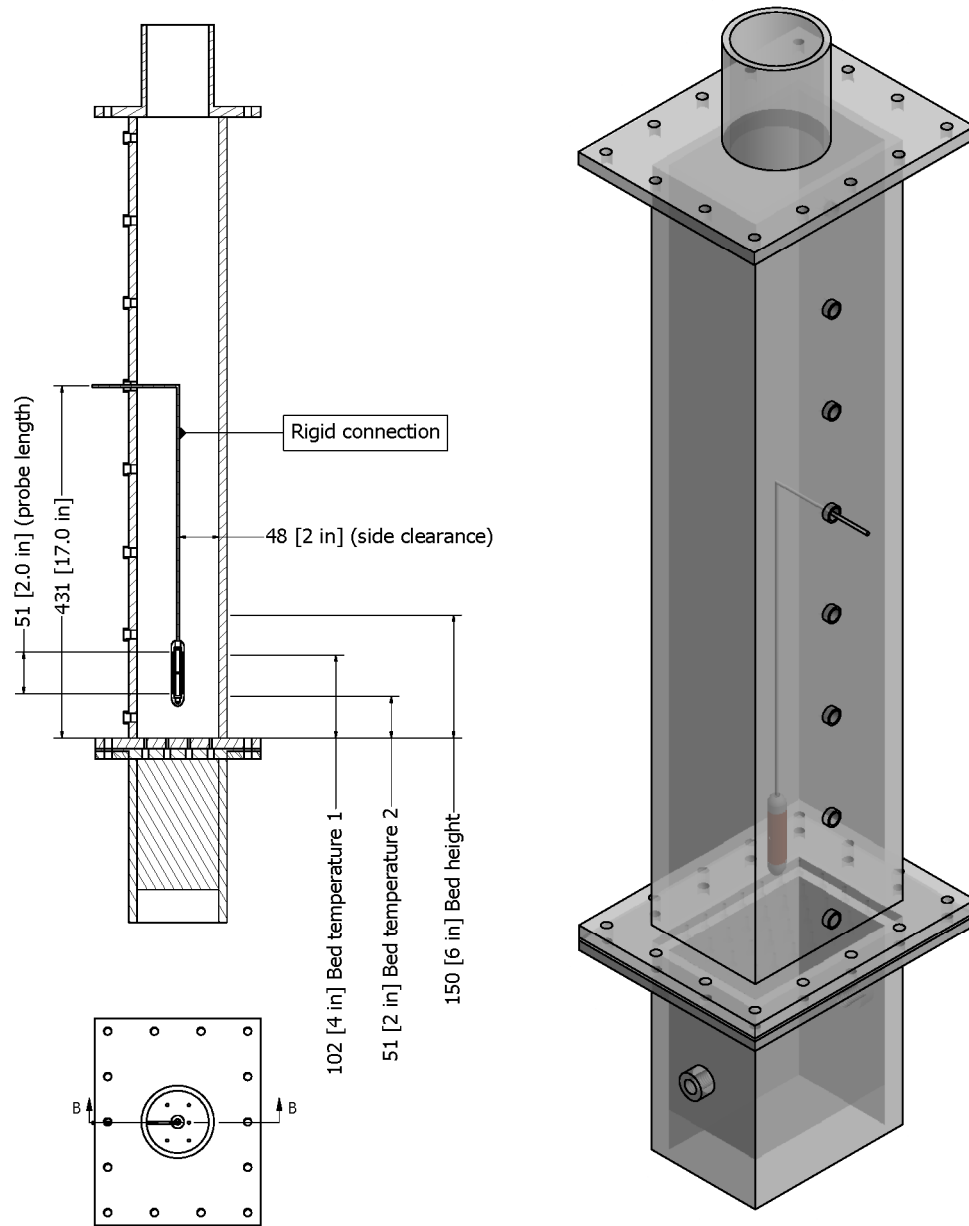


Figure 2.7 Heater probe in the rectangular pulsed fluidized bed. (a) section view of the system with important dimensions annotated in inches; (b) top view of the system; (c) 3D view of the system showing the position of the probe and the rigid connection.

Table 2.2 Summary of data acquisition device and acquired signals

Signal Name	Sensor/Actuator	DAQ Model	Sampling Rate
Pressure	Pressure transducer	MC DAS-08 PCI	400 Hz
Temperature	T-type thermocouple	NI 9214	20 Hz
Relative humidity with temperature	Vaisala humidity probes	NI USB-6008	10 Hz
Digital control	Solenoid valve	NI USB-6009	100 Hz
Voltage and current	TTL serial interface	BK Precision IT-E132B	10 Hz

Table 2.3 A brief summary of experimental operating conditions for the batch drying test

Batch Drying Test		
Reactor geometry	Rectangular bed	
Parameter	Operating condition	Chapter/Section
Flow rate	$f=0.5$ Hz, 3.0 Hz, $\bar{U}=0.95$ - $2.15U_{mf}$, Douglas fir	3.2.1
Pulsation frequency	$\bar{U}=0.8$, $1.3U_{mf}$, $f=0.33$ - 6.67 Hz, Douglas fir	3.2.2
Vibration intensity	$\bar{U}=0.8$, $1.3U_{mf}$, vibration=0%, 25%, 50%, 75% and 100%	3.2.3
Temperature	$T=20$ °C, 30 °C, 40 °C, 50 °C, $f=0.33$, 1.0 and 3 Hz	3.2.4
Duty cycle	$f=0.75$ Hz, $\bar{U}=1.1U_{mf}$, On/Off=1/3, 1 and 3	3.2.5
Particle size	$d_p=0$ -1.0, 1.0-3.15 and 3.15-4.0 mm, $\bar{U}=0.29$ m/s	3.2.6
Fine particles	Mixture of particles of 0-1 mm and 3.15-4 mm	3.2.6
Biomass species	Douglas fir, pine and switchgrass, $\bar{U} = 0.31$ m/s	3.2.7
Reactor geometry	Tapered bed	
Parameter	Operating condition	Chapter/Section
Flow rate	$f=0.5$ Hz, $\bar{U}=1.05$ - $1.4U_{mf}$, Douglas fir	3.4.1
Pulsation frequency	$f=0.25$ -6 Hz, $\bar{U}/U_{mf}=1.3$, Douglas fir	3.4.2
Initial bed height	200-350 g of Douglas fir, $f=1.5$ Hz, $\bar{U}/U_{mf}=1.3$	3.4.3
Heat transfer measurement		
Reactor geometry	Rectangular bed	
Parameter	Operating condition	Chapter/Section
Flow rate	$f=0.5$ -5.0 Hz, $\bar{U}=0.68$ - $1.56U_{mf}$, Douglas fir	5.1.1
Pulsation frequency	$f=0.5$ -5.0 Hz, $\bar{U}=1.1$, 1.3, $1.5U_{mf}$, Douglas fir	5.1.2
Biomass species	$f=0.5$ -5.0 Hz, $\bar{U}=0.26$ - 0.36 m/s, pine and switchgrass	5.1.3
Particle size	$d_p=0$ -1, 1-3.15, 3.15-4, 4-7 mm, $\bar{U}=0.22$ - 0.38 m/s	5.1.4
Fine particles	$d_p=0$ -1 mm and 3.15-4 mm mixtures, $\bar{U}=0.22$ - 0.38 m/s	5.1.5
Vibration	$\bar{U}=1.05$, $1.3U_{mf}$, vibration=0% and 100%	5.1.6
Lateral position	$l/L=0.3$, 0.5, 0.7, $\bar{U}/U_{mf}=1.2$ and 1.4, Douglas fir	5.1.7
Reactor geometry	Tapered bed	
Parameter	Operating condition	Chapter/Section
Flow rate	$f=0.5$ -5.0 Hz, $\bar{U}=1.0$ - $1.5U_{mf}$, Douglas fir	5.2.1
Pulsation frequency	$f=0.5$ -5.0 Hz, $\bar{U}=1.0$, 1.3, $1.5U_{mf}$, Douglas fir	0
Lateral position	$l/L=0.3$, 0.5, 0.7, $\bar{U}/U_{mf}=1.2$ and 1.4, Douglas fir	5.2.2
Duty cycle	$\eta_D=0.1$ -0.9, $\bar{U}=1.1$, $1.3U_{mf}$, $f=0.5$, 1, 2.5 Hz, Douglas fir	5.2.3
Particle size	$d_p=0$ -1, 1-3.15, 3.15-4 mm, $\bar{U}=0.24$ - 0.36 m/s	5.2.4
Fines	$d_p=0$ -1 mm and 3.15-4 mm mixtures, $\bar{U}=0.21$ - 0.36 m/s	5.2.4
Biomass species	$f=0.5$ -5.0 Hz, $\bar{U}=0.26$ - 0.36 m/s, pine and switchgrass	5.2.5

CHAPTER 3

HYDRODYNAMICS AND DRYING IN PULSED FLUIDIZED BED

3.1 Hydrodynamics of the rectangular pulsed fluidized bed

3.1.1 Pressure fluctuations

The cohesive nature of the biomass particles makes fluidization rather challenging. Such behaviour of the bed could be improved by restructuring the fluidized bed through external forces generated by pulsed gas flow (Coppens & van Ommen, 2003), in which the fluidizing medium is introduced to the bed periodically with distinct “Flow-On” and “Flow-Off” periods. Typical bed pressure fluctuations as a function of time in the pulsed fluidized bed are displayed in Figure 3.1. For pulsation frequency of 0.33 Hz, each “ON” period started with a dominant peak of bed pressure drop (marked with letter A in Figure 3.1(a)), corresponding to the onset of gas flow immediately after the solenoid valve was switched open. The dominant peak was followed by a damped oscillation (B–C). The contact of uprising gas bubbles with falling particles might have contributed to the oscillatory pressure profile from points B to C. At the end of each “ON” period there was also a brief pressure recovery (C–D) caused by falling particles compressing the gas phase in the plenum chamber. The bed remained stationary during “OFF” period due to the lack of airflow, and the pressure profile flattened (D–E). Similar pattern could be seen at 1 Hz in Figure 3.1(b), with F representing the dominant peak and G–H the pressure oscillation. It is noteworthy that at lower pulsation frequencies, the intensity of the gas pulsation was greater, which led to longer period of damped oscillations. Five or more peaks could be identified during the damped oscillation at 0.33 Hz, while only one was

observed with the relatively low pulsation intensity at 3 Hz. As the pulsation frequency further increased, particles were seen to be carried up by gas phase from the next cycle before reaching the bottom of the fluidized bed. Consequently, pressure went up before it could start oscillating, which explains the disappearance of damped oscillation altogether at 6.67 Hz, as illustrated in Figure 3.1(d).

3.1.2 Gas–solid flow behaviour

Typical flow behaviour in the rectangular pulsed fluidized bed at various pulsation frequencies is shown in Figure 3.2. Average superficial gas velocities (\bar{U}) in all experiments were kept the same and high enough to avoid severe channeling and partial defluidization. At the lower end of all pulsation frequencies investigated in this work, such as 0.33 Hz, the bed was fluidized intermittently because of prolonged “ON” and “OFF” period in each pulsation cycle. The bed remained stationary during the “OFF” period while sufficiently high pressure had built up in the surge tank. As soon as the solenoid valve was opened, pressurized gas stored in the surge tank was quickly discharged into the fluidized bed. A horizontal layer of voids (bubbles or slugs) formed above the distributor, denoted by the rectangle in Figure 3.2(A1). The frequency of void formation remained identical to the pulsation frequency. The voids quickly coalesced forming slugs of relatively large sizes, which quickly reached the top of the bed (A2). Pressure drop reduced significantly at this point, together with the oscillating gas flow rate. The remaining gas in this pulsation cycle was still able to properly mix with biomass particles (A3). The intensity of gas pulsation at 0.33 Hz was so powerful that the entire bed was lifted, therefore the amplitude of bed expansion reached a maximum with significant entrainment. Lots of fines were collected in the bag filter installed at the gas exit. As the air supply diminished and solenoid valve closed, particles eventually fell back to the bed (A4), which remained stationary until the next pulsation cycle.

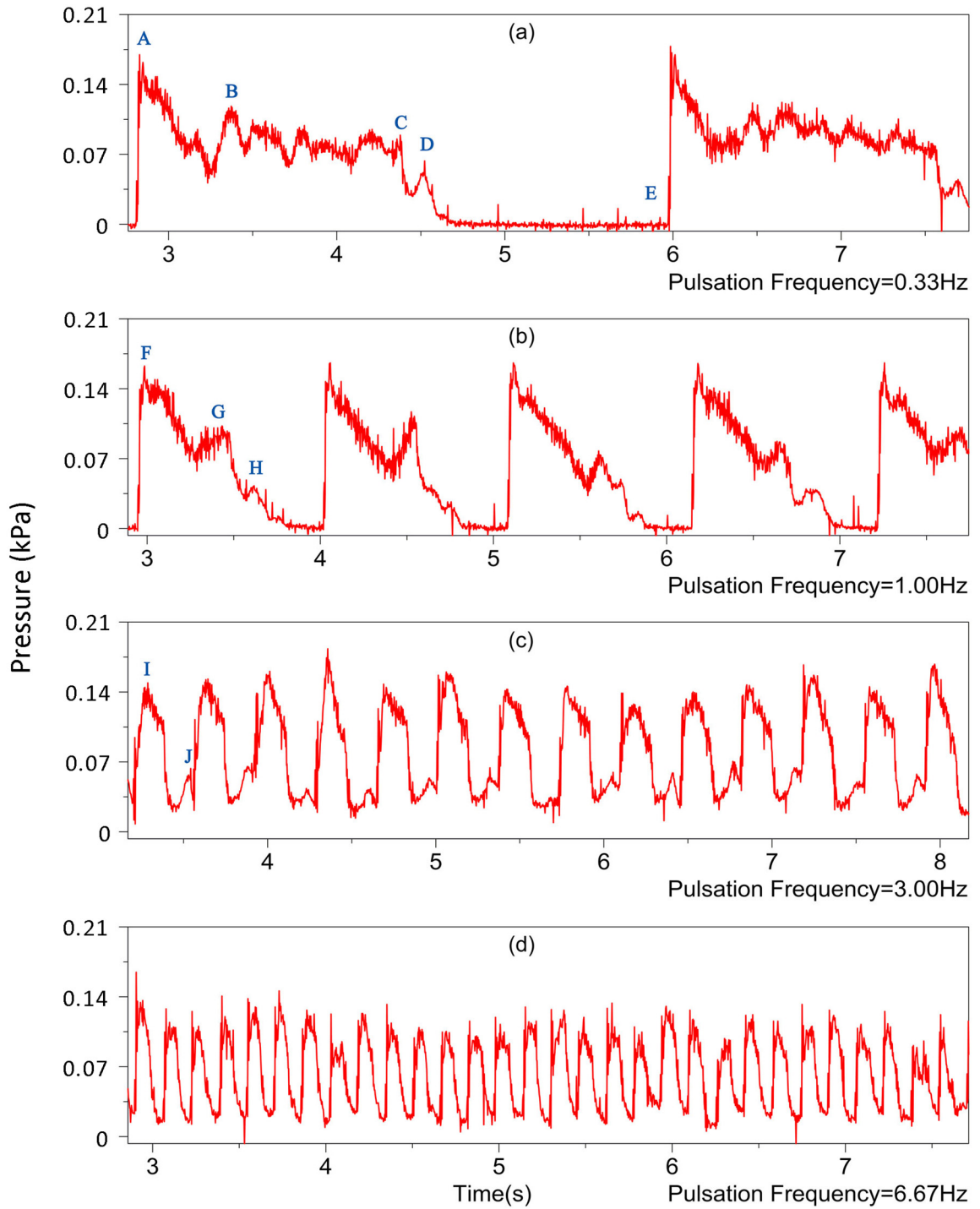


Figure 3.1 Pressure fluctuations in PVFB at various pulsation frequencies

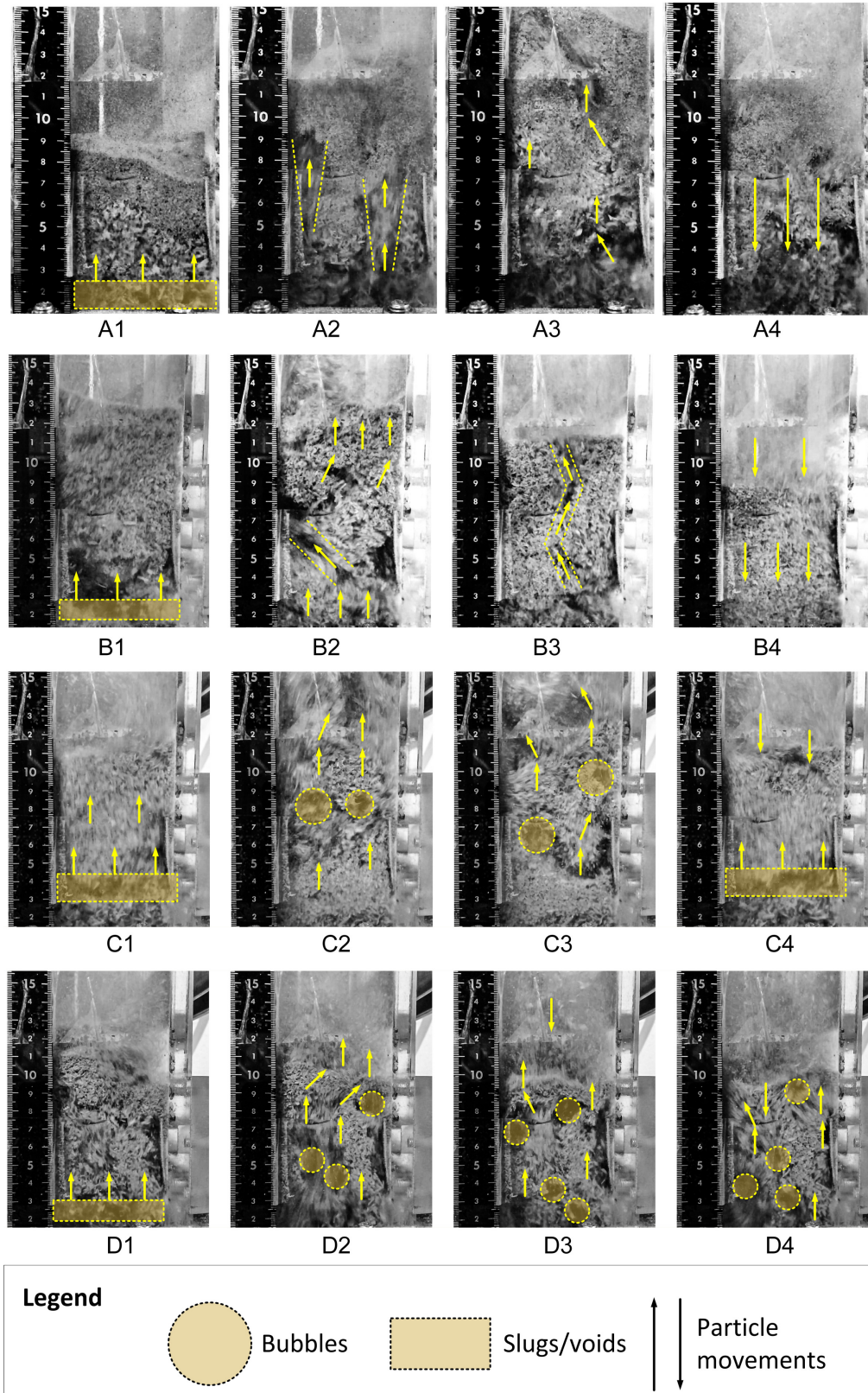


Figure 3.2 Typical fluid patterns of the bed at various pulsation frequencies. (A1-A4) $f=0.33\text{Hz}$; (B1-B4) $f=1\text{Hz}$; (C1-C4) $f=3\text{Hz}$; (D1-D4) $f=6.67\text{Hz}$.

The interval between two adjacent “ON” periods became shorter at 1 Hz. The horizontal layer of voids (Figure 3.2(B1)) quickly evolved into gas channels and zigzagged up the bed, as shown in Figure 3.2(B2) and Figure 3.2(B3). The bed expanded slightly less compared to $f=0.33$ Hz because of reduced pressure build-up and gas velocity. No regular bubble flow pattern could be seen at this frequency because of the cohesiveness of particles and high intensity of pulsation. However, at 3 Hz the horizontal voids (C1) quickly gave rise to large bubbles (circled in Figure 3.2(C2) and Figure 3.2(C3)). The “OFF” period disappeared as the pulsation frequency well exceeded the natural frequency of the fluidized bed. Particles were lifted up during their descent towards the bottom of the bed as they met gas bubbles from the next pulsation cycle. This is consistent with the disappearance of damped pressure oscillations shown in Figure 3.1(c). Due to the limitations of the solenoid valve, the highest pulsation frequency achieved was 6.67 Hz. Initial study also revealed that at such a frequency pulsation was already less intense, which may not be sufficient to overcome the inter-particle forces. The reduction in pulsation intensity was manifested through the oscillating gas flow rate where the maximum in each pulsation cycle at 6.67 Hz was much less than that of 0.33 Hz. There was stronger resistance from particles that may have prevented the formation of bubbles. The combined effect of faster gas renewal and less excessive gas available to bubble formation likely led to the reduction in bubble size and bed expansion. Demonstrated in Figure 3.2(D1), voids formed at 6.67 Hz quickly disappeared and split into regular bubbles (circled in Figure 3.2(D2) and Figure 3.2(D3)). The pulsed fluidized bed at this frequency behaved like a conventional fluidized bed if the biomass particles were able to be fluidized under similar conditions.

Fast Fourier Transform (FFT) analysis was also performed on the differential bed pressure drop data. Similar to conventional fluidized beds where the power spectrum of pressure fluctuations usually reflects the frequency of bubble behaviours, including bubble formation, splitting, coalescence and eruption, the dominant frequency in pulsed fluidized bed is linked directly to pulsation frequency, as shown in Figure 3.3. Peaks were more distinct for the pulsed fluidized bed, and several orders of magnitude higher than that of a conventional fluidized bed. The appearance of overtones of the

dominant frequency could be attributed to the under-dampened pressure oscillations, and the fact the pressure fluctuations in pulsed fluidized bed were not perfect sinusoids.

3.1.3 Effect of moisture on hydrodynamics

The hydrodynamics of the pulsed fluidized bed relates closely to the moisture content of biomass particles. Particles with high moisture content normally exhibit stronger cohesive forces. As the particles are being dried, moisture is continuously being removed. The cohesive force reduces as a result, which affects the hydrodynamics of the fluidized bed significantly. A high moisture content and weak gas pulsation could result in channelling, which easily could be seen during experiments and verified by the high-speed imaging. Mover, pressure drop across the bed may also be affected. Often when channelling occurred, the peak pressure drop reduced as a result. The relationship between moisture content and pressure fluctuations is especially important. Figure 3.4 presents the time-averaged standard deviation of pressure fluctuations at various pulsation frequencies during the batch drying process. Similar to conventional fluidized beds, the standard deviation of pressure fluctuations is mainly associated with bubble size. The highest amplitude of pressure fluctuations was seen at 0.33 Hz, which decreased with increasing pulsation frequency. This is consistent with visual observations obtained during the drying tests. At lower pulsation frequencies, larger voids (slugs or bubbles) and bed expansion were observed. The standard deviation decreased as drying progressed, indicating that the bubble size reduced as drying continued. This may have been caused by the breaking down of cohesive forces between particles, as the bubbles were less inhibited by such cohesive forces from splitting up.

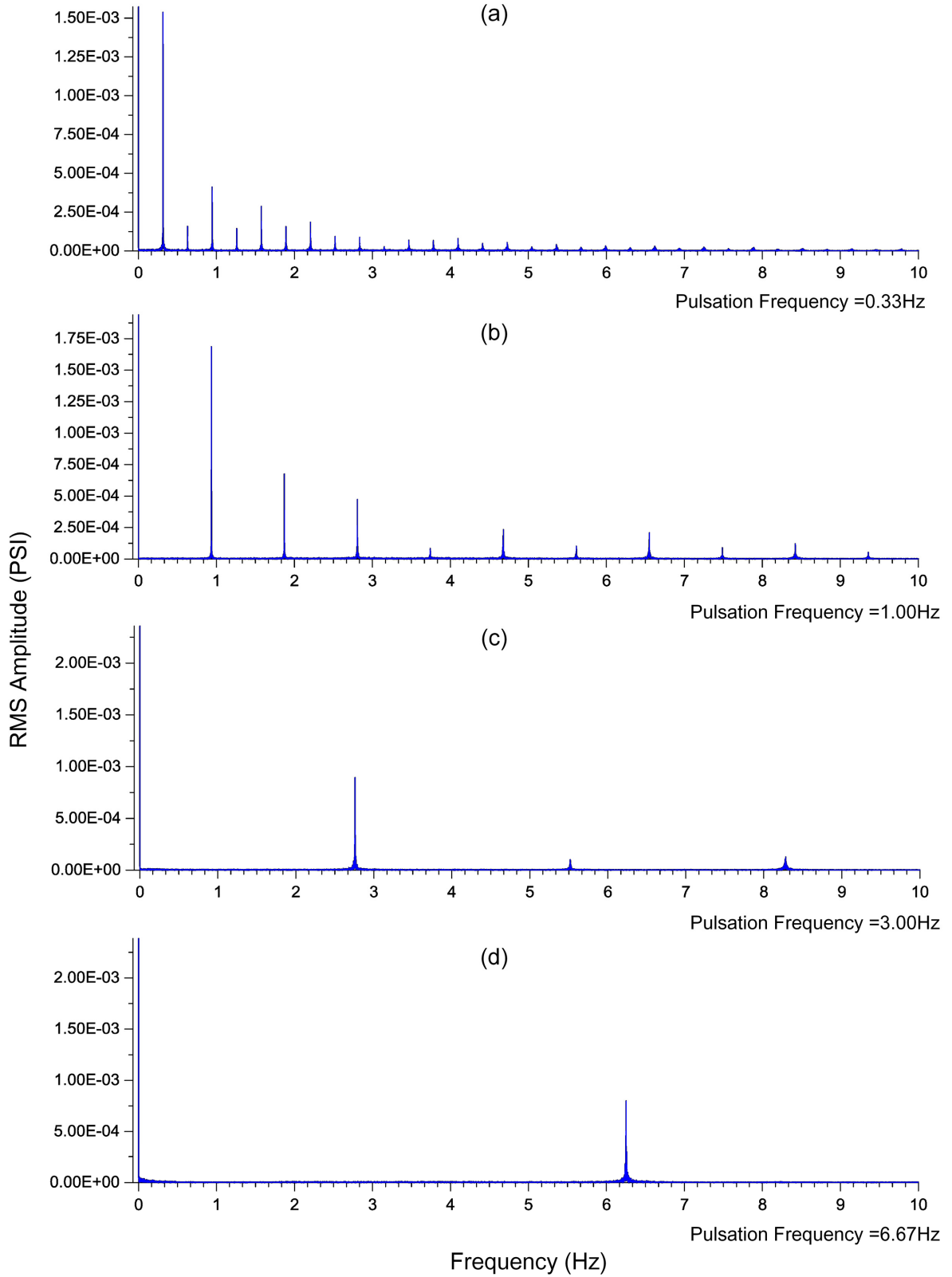


Figure 3.3 Power spectra of pressure fluctuations at various pulsation frequencies

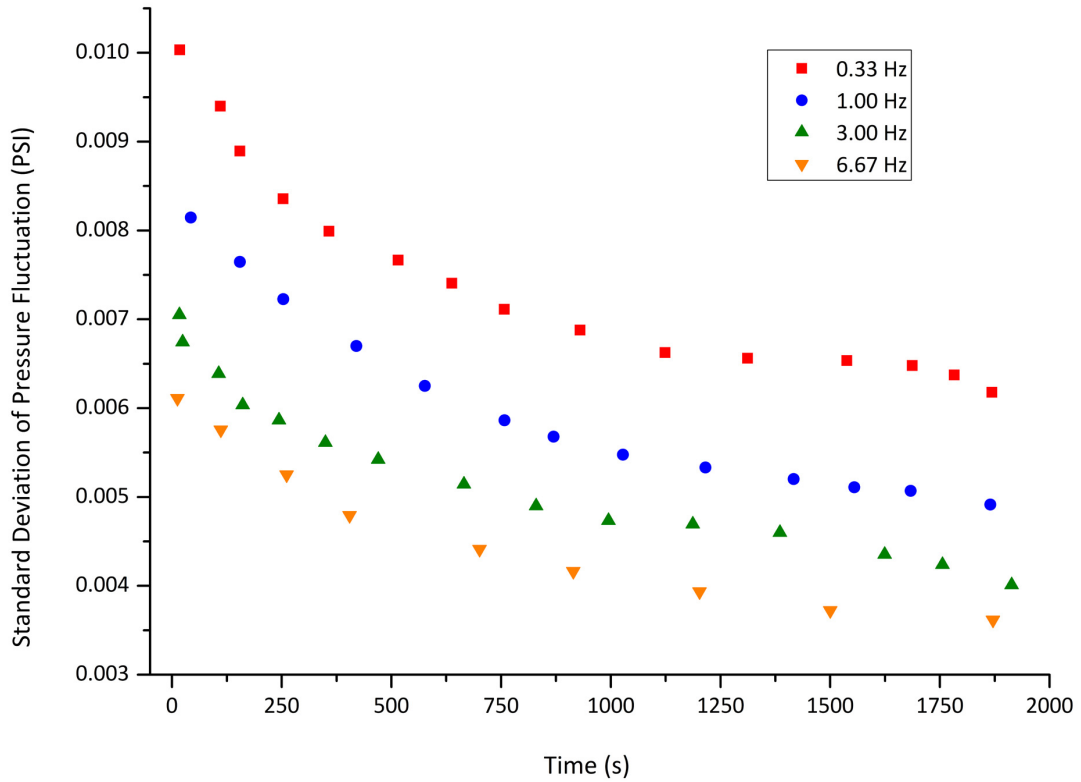


Figure 3.4 Standard deviation of pressure fluctuations at various pulsation frequencies

3.2 Batch drying in rectangular pulsed fluidized bed

3.2.1 Effect of gas flow rate

Gas flow rate has a direct impact on drying. Unlike conventional fluidized beds, pulsed fluidized beds could be operated with a mean gas velocity lower than minimum fluidization velocity. In this work U_{mf} was measured based on the peak pressure drop, which is elaborated in Appendix A1. For Douglas fir samples used in this study, $U_{mf}=0.238$ m/s (measured at 7% moisture content (dry basis)). Initial moisture content of the biomass samples was 34.4%. Good gas–solid flow was achieved with an average gas velocity as low as $0.8U_{mf}$, combined with strong gas pulsations at

0.33 or 0.5 Hz. It seems highly likely that higher moisture content will introduce additional cohesive forces that could cause channeling and partial defluidization, leading to a higher minimum fluidization velocity. $\bar{U} = 1.5U_{mf}$ was found to be the minimum flow rate required at pulsations frequency of 6.67 Hz as the intensity of the pulsed gas flow at this frequency was weak. Figure 3.5 depicts the moisture ratio $\Phi (X/X_0)$ of the Douglas fir sawdust after 30 min of drying at various gas flow rates. Two pulsation frequencies were studied, one below natural frequency ($f = 0.5 \text{ Hz} < f_N = 1.28 \text{ Hz}$) and one above (3.0 Hz). Since 200 g of Douglas fir samples with the same initial moisture content were placed into the fluidized bed before each run, a lower moisture content at the end of drying, as reflected by the $\Phi (X/X_0)$ value, would suggest a faster drying and subsequently a better gas–solid contact. Selected experiments were repeated three times, and good repeatability was obtained. A higher average gas velocity appeared to have led to a higher drying efficiency, which was manifested by a low final moisture ratio, Φ .

For pulsations at 0.5 and 3 Hz, as the average superficial gas velocity increased from $1.5U_{mf}$ to $2.0U_{mf}$, the moisture ratio (Φ) decreased by 8.4% and 13.8%, respectively. In addition, it appears that for drying at a moderate gas flow rate ($1.2U_{mf} < \bar{U} < 1.9U_{mf}$), higher pulsation frequency was favoured. In the case of very low ($\bar{U} < 1.2U_{mf}$) or very high ($\bar{U} > 1.9U_{mf}$) gas flow rates, a lower pulsation frequency was preferred. Specifically, when the flow rate was lower than $1.2U_{mf}$, channeling occurred constantly at higher pulsation frequencies, which significantly hindered mass transfer and gas–solid contact. On the other hand, at a very high flow rate such as $1.9U_{mf}$ and above, “OFF” periods became significant at a low pulsation frequency, as half of the time in a pulsation cycle the bed remained stationary while during the other half gas flow penetrated the bed violently, causing severe entrainment. Therefore, the pulsed fluidized bed should be kept around a moderate gas flow to ensure sufficiently strong gas pulsation for better gas–solid contact and faster heat and mass transfer without undesired complications such as channeling and partial or full defluidization.

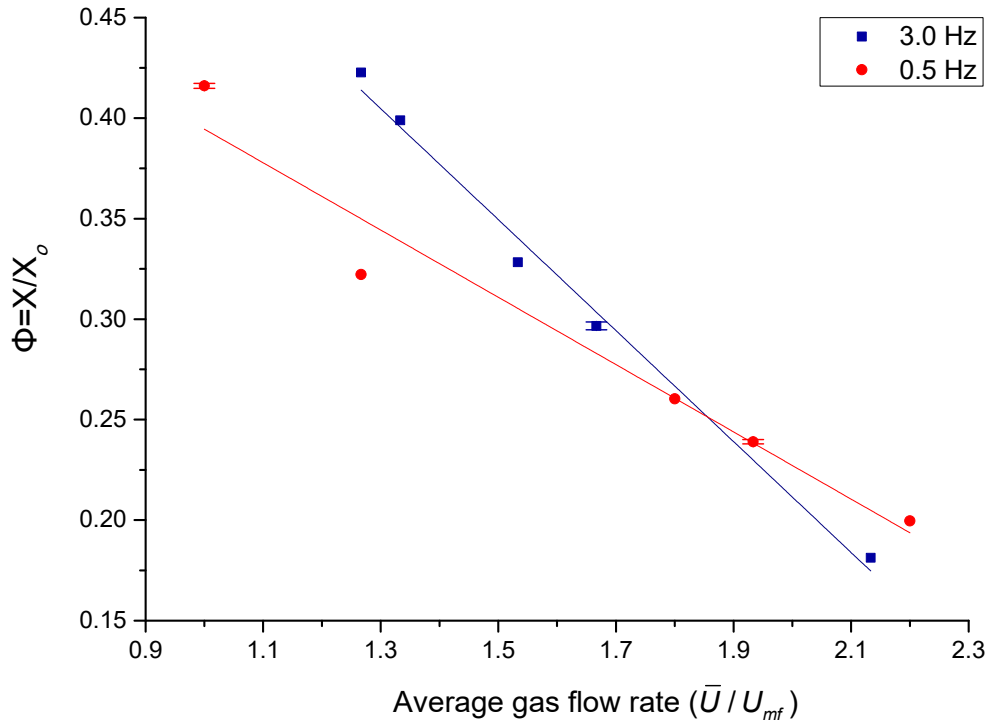


Figure 3.5 Effect of gas flow rate on the final moisture content of Douglas fir sawdust after 30 min of drying (experimental data points with least-squares linear regression lines)

3.2.2 Effect of pulsation frequency

Being a crucial parameter in pulsed fluidized beds, the impact of pulsation frequency on drying was investigated with the results given in Figure 3.6. Biomass had an initial moisture content of 50.1% (dry basis). The maximum pulsation frequency investigated in this study was 6.67 Hz, while the lowest was 0.33 Hz. It has been established that the gas velocity profiles at various pulsation frequencies are vastly different. It is thus imperative that the average superficial gas velocity (\bar{U}) be kept the same to ensure comparability of the results. In this case, two average superficial gas velocities were studied, namely $\bar{U} = 0.8U_{mf}$ and $1.3U_{mf}$.

At a relatively high velocity of $1.3U_{mf}$, the bed could be successfully fluidized for a wide range of pulsation frequencies. No apparent channeling that could hinder drying was observed from 0.33 Hz

to 6.67 Hz. Good gas–solid contact was observed. The system transitioned from being intermittently fluidized at 0.33–0.5 Hz, piston-like flow behaviour at 1–3 Hz, to the seemingly continuous fluidization at 4 Hz and above. The shortened “OFF” period and reduced entrainment may have contributed to the improvement in drying efficiency, as can be seen in Figure 3.6. The moisture ratio ($\Phi = X/X_0$) dropped from 19.3% at 0.33 Hz to 14.5% at 6.67 Hz, indicating that an increase in pulsation frequency was favoured during drying.

A completely different scenario was observed as the average gas velocity was lowered to $\bar{U} = 0.8U_{mf} < U_{mf}$. Channeling was seen at approximately 3.5 Hz and above. Gas bypassed the particles by traveling through the channels without efficiently contacting the solids. The gas phase was not able to remove much moisture from the particles compared to runs with higher flow rates or lower pulsation frequencies where stronger pulsation was present. It seems that poor flow behaviour from weaker pulsations may have played a role in the decline of drying efficiency at 3.3–5 Hz.

No channeling was observed below 3.3 Hz, as pulsation was strong enough to overcome the cohesiveness of biomass particles. However, as stated in the previous section the prolonged “OFF” period at 0.33 Hz hindered drying, causing the final moisture content in biomass samples to have increased slightly from 22.4% at 0.75 Hz to 25.3% at 0.33 Hz. Based on visual observations made during the experiments and results presented in Sections 3.2.1 and 3.2.2, an optimum operating condition could be determined, which guarantees sufficient gas flow through the bed to effectively remove water moisture, and to overcome the cohesiveness of biomass particles resulted from the high moisture content and irregular shape. Pulsation frequencies between 0.75 and 1.5 Hz are among the most effective frequencies for gas–solid contact and drying, especially at the beginning of a batch drying process when the particles are very wet and hard to fluidize. As drying progresses, either a lower flow rate could be used to reduce the consumption of drying medium, or a slightly

higher pulsation frequency to enhance gas–solid contact and improve drying efficiency. As to the gas flow rate, the average superficial gas velocity should be maintained between $1.1 - 1.3U_{mf}$.

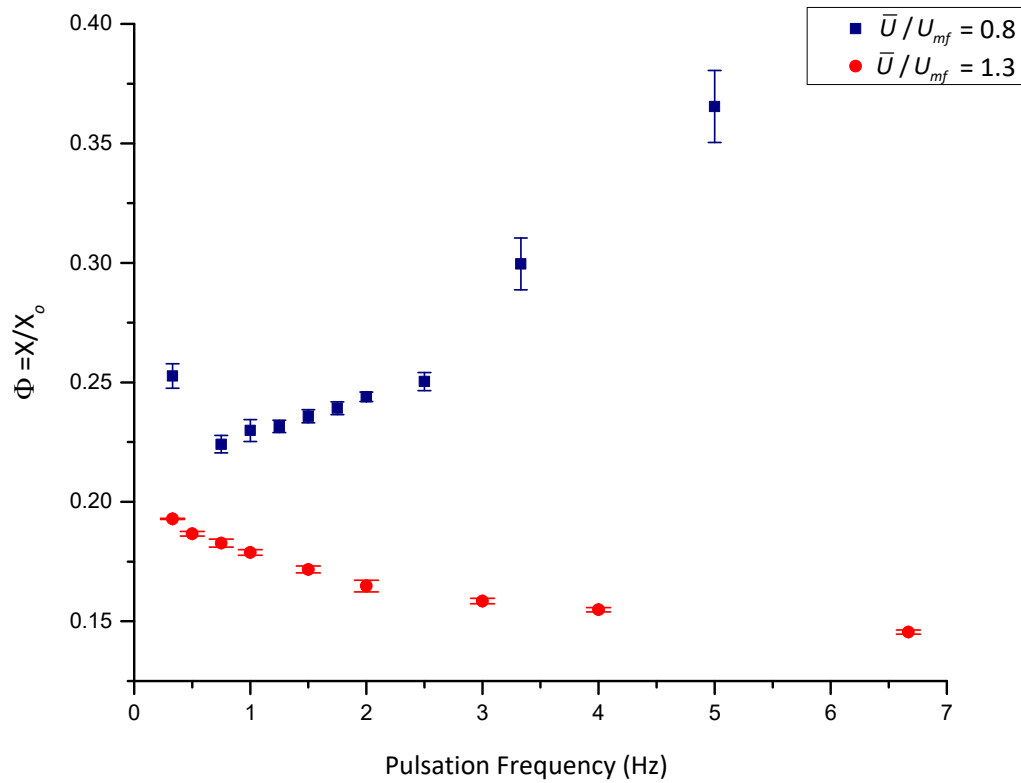


Figure 3.6 Effect of pulsation frequency on the final moisture content of Douglas fir sawdust after 30 min of drying; biomass had initial moisture content of 50.1% (dry basis).

3.2.3 Effect of vibration intensity

Similar drying tests were carried out to verify the contribution of vibration to the fluidization of biomass particles. Visual observation revealed that during the fluidization of wet particles when gas pulsation was insufficient to eliminate channeling, good gas–solid flow sometimes could be restored by turning on vibration. Since the frequency of the vibratory base was fixed, only the intensity (displacement of the vibratory motor) could be varied. Two gas velocities were tested, which were $\bar{U} = 0.8U_{mf}$ and $\bar{U} = 1.3U_{mf}$. The amplitude of vibration was set to 0%, 25%, 50%, 75% and 100%, corresponding to different Γ values. Similar to the tests in the previous chapter, final moisture ratio (X/X_0) of biomass samples after 30 min of drying was also chosen as an indicator of fluidization quality and mass transfer rate. Samples had an initial moisture content of 46.2%. Results are shown in Figure 3.7.

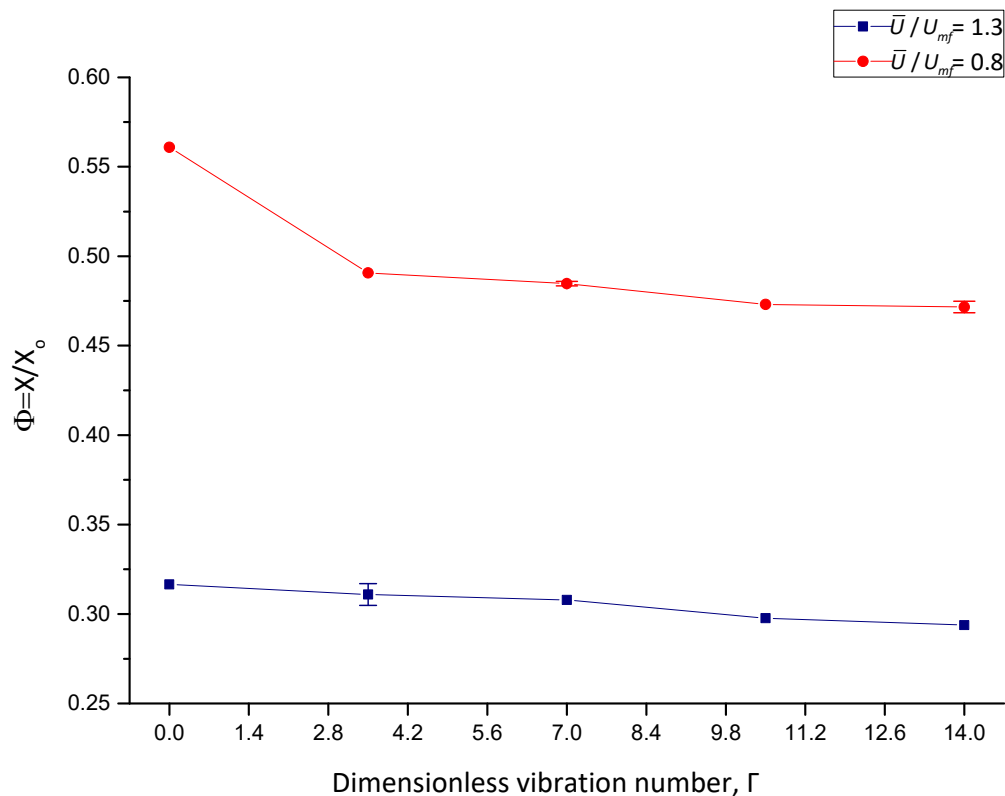


Figure 3.7 Effect of vibration intensity on drying of Douglas fir sawdust under 1 Hz pulsation frequency after 30 min of drying; samples had initial moisture content of 46.2%.

It is evident that biomass dried faster at higher gas velocity of $\bar{U} = 1.3U_{mf}$ compared to $0.8U_{mf}$. A minimum of 17.8% difference in moisture ratio was seen between the two gas flow rates. At $0.8U_{mf}$, less severe channeling was observed in the fluidized bed immediately after vibration was turned on. It appears that even a low vibration intensity of 25% was sufficient to overcome the cohesive forces between biomass particles. Consequently, the final moisture content decreased by 7% compared to the case where no vibration was applied. Higher vibration amplitudes yielded only marginal improvement. In the case of $1.3U_{mf}$ where pulsation was capable of overcoming the inter-particles forces, the contribution of vibration was negligible. Less than 2% difference in moisture ratio suggests that pulsation alone should be sufficient to handle biomass particles, provided that suitable operating conditions with strong pulsations are implemented.

3.2.4 Effect of temperature

Series of drying tests were conducted at different air temperatures to investigate its effect on drying. Due to the limitations imposed by the acrylic fluidized bed column, only temperatures up to 50 °C were tested. The fluidized bed system was pre-heated to the designated temperature for 30 min prior to any drying tests. Despite the pulsating nature of the gas flow, temperature of the inlet air could be controlled within 0.5 °C. The studied temperatures were 20, 30, 40 and 50 °C. Sample initial moisture content was 51.8% (dry basic).

Figure 3.8 depicts the effect of temperature on drying of Douglas fir sawdust at various pulsation frequencies. All three temperatures led to similar trends, as a higher temperature did promote the drying rate. One third of the experiments were repeated three times to ensure credibility of the results with the standard errors less than 1%. For the pulsation frequency of 0.33 Hz, the final moisture ratio (X/X_0) of Douglas fir samples after 30 min of drying dropped from 44.2% to 10.4% as the temperature rose from 20 to 50 °C. Consequently the total amount of water removed from

particles increased by 33.8%. At 1 and 3 Hz, the moisture ratio decreased by 24% and 21%, respectively. For the drying of porous particles, temperature usually affects both external and internal heat and mass transfer. Higher temperature will likely speed up the evaporation of free water on the surfaces of biomass particles, which leads to faster drying in the constant-rate drying period. In the falling-rate drying period where heat transfer from the surface to the core of a particle is important, a higher gas temperature will increase the temperature gradient between particle surface and core, leading to faster migration of bound water from core to the surface and evaporation at the surface. Little difference in moisture ratio was found for pulsation at 1 and 3 Hz at 50 °C, indicating that gas velocity/external mass transfer may be the rate-controlling step.

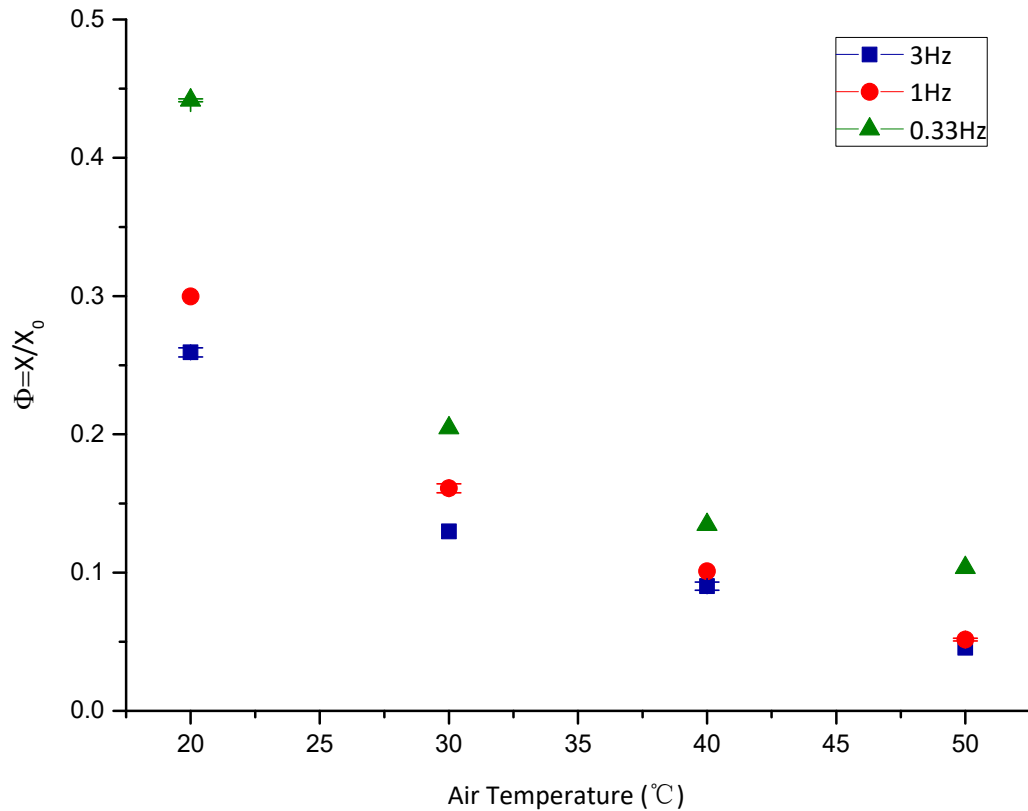


Figure 3.8 Effect of temperature on the drying of Douglas fir sawdust at various pulsation frequencies, $\bar{U}/U_{mf}=1.25$; samples had initial moisture content of 51.8% (dry basis).

3.2.5 Effect of pulsation duty cycle

Duty cycle of gas pulsation is an important variable. A 50% duty cycle was used for all previous experiments. As stated in previous chapters, the superficial gas velocity changed with time, which may have strong influences on bubbles in terms of bubble size and bubble rise velocity. By varying the duty cycle, η_D , which is the time fraction of the “ON” period (t_{ON}) within an entire pulsation cycle ($t_{ON} + t_{OFF}$), the amount of air allowed into the fluidized bed column at the beginning of an “ON” period, as well as the bed pressure drop could be altered. η_D is defined as,

$$\eta_D = \frac{t_{ON}}{t_{ON} + t_{OFF}} \quad (3.1)$$

While maintaining the pulsation frequency ($f = 0.75 \text{ Hz}$) and average gas flow rate ($\bar{U} = 1.1U_{mf}$) at constants, the “ON” period within each pulsation cycle was set to 333 milliseconds ($\eta_D = 25\%$), 667 milliseconds ($\eta_D = 50\%$) and 1000 milliseconds ($\eta_D = 75\%$) during the batch drying tests of Douglas fir. Peak pressure drops during the drying process with different duty cycle configurations were identified with the peak finding function in NI DIAdem (Version 2015, National Instrument, USA). In the meanwhile, moving averages (every 12 s) of the standard deviations of pressure fluctuations were calculated. As plotted in Figure 3.9, because of the longer pressure buildup in the “OFF” period, higher peak pressure was observed for $\eta_D = 25\%$, which is 33% higher than that of $\eta_D = 50\%$ and $\eta_D = 75\%$ cases. Stronger pulsation of $\eta_D = 25\%$ also generated faster bubbles. The relatively shorter duration of “ON” period reduced the size of the bubbles, which was consistent with the lower values of standard deviation of pressure fluctuations. For $\eta_D = 50\%$ and $\eta_D = 75\%$ configurations, similar peak pressures were seen, while the former exhibited higher standard deviation values, indicating larger bubbles likely caused by longer opening time of the solenoid valve. In all three cases the standard deviation of pressure fluctuations was declining as drying

progressed, indicating a reduction in bubble size. It is probably a result of the reduction in cohesive forces, which weakened the inhibition of the coalescence of bubbles.

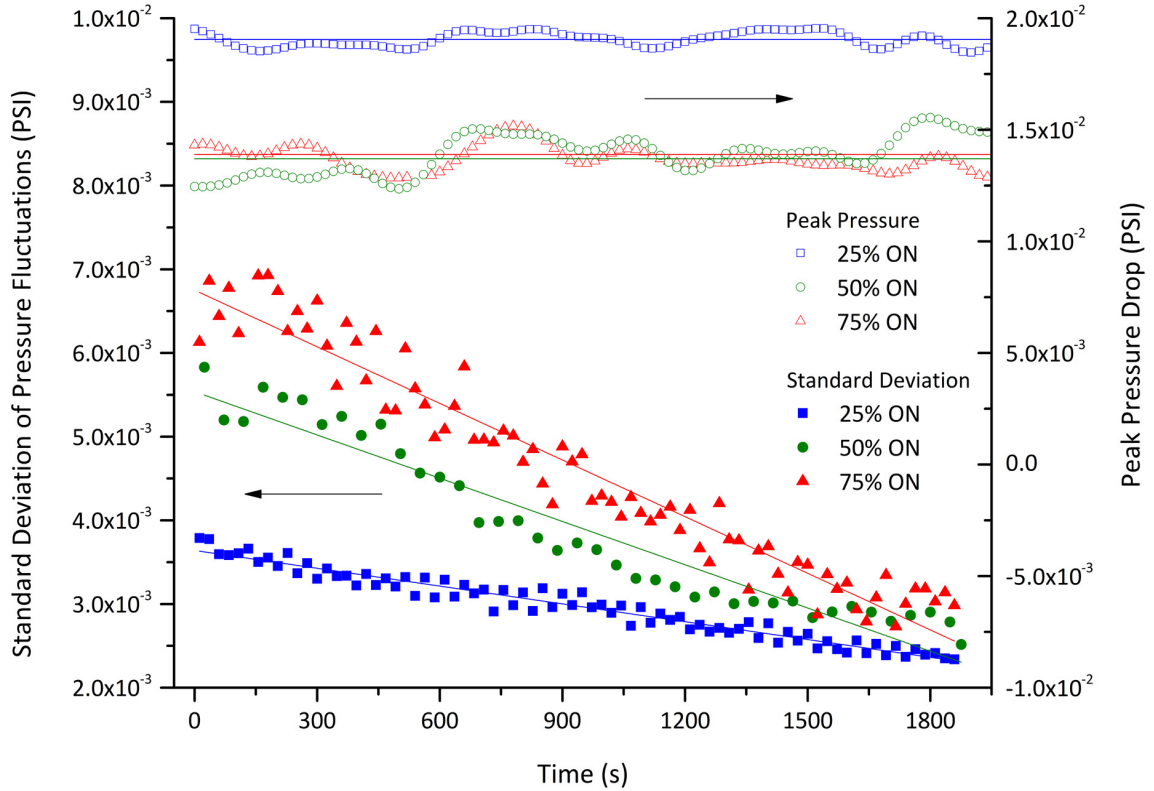


Figure 3.9 Standard deviation of pressure fluctuations and peak pressure drop in pulsed fluidized bed of Douglas fir at different pulsation duty cycles (including least-squares linear regression trend lines)

Moisture ratio (X/X_0) after 30 min of drying is plotted in Figure 3.10. The initial moisture content was 46.1% (dry basis). Both $\eta_D = 50\%$ and $\eta_D = 75\%$ cases had similar drying performances, with the final moisture ratio being 23.8% and 21.8%, respectively, which was expected from their similarities in the standard deviation of pressure fluctuations. The $\eta_D = 25\%$ case manifested in stronger gas pulsation and smaller gas bubbles, which could be helpful to the fluidization of cohesive particles. However, the longer dormant period (1000 ms) in each cycle and larger bubbles

caused more channeling, and limited the contact between gas and solid phase. Eventually mass transfer was hindered, leading to a final moisture content of 34.2% for the $\eta_D = 25\%$ case.

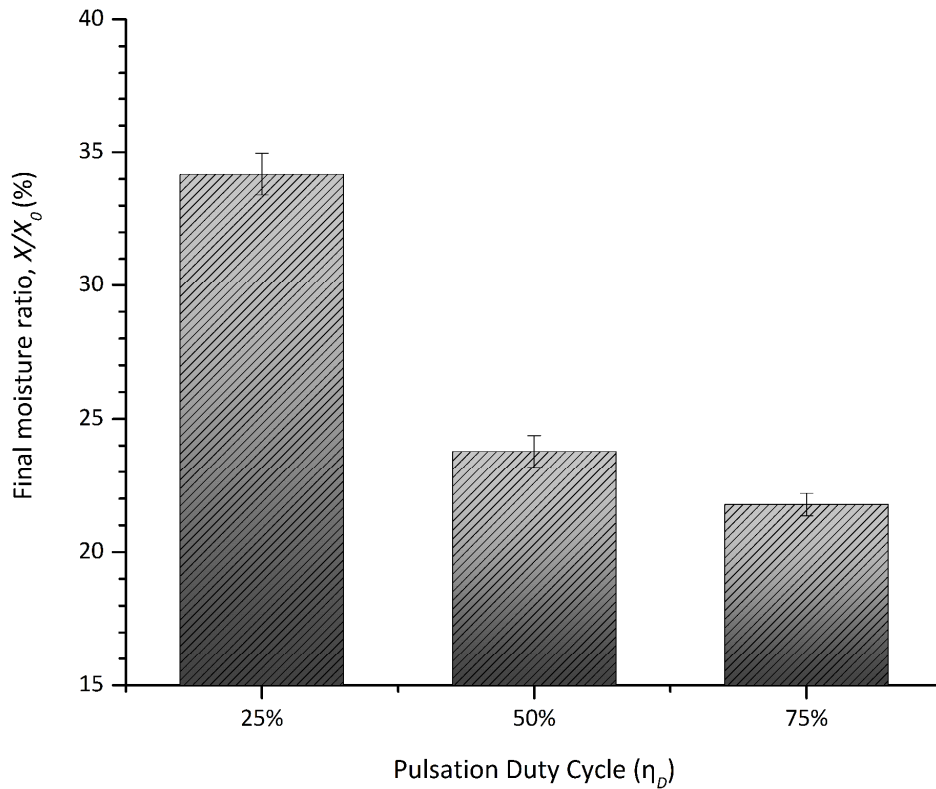


Figure 3.10 Effect of pulsation duty cycle on the final moisture ratio of Douglas fir after 30 min drying, samples had initial moisture content of 46.1% (dry basis).

3.2.6 Effect of particle size and fine particles

To investigate the effect of particle size on drying and mass transfer, Douglas fir sawdust was further screened through a series of sieves to obtain the following particle size fractions: 0–1 mm, 1–3.15 mm and 3.15–4 mm. Water was added to the samples to reach 94.5% (wt.% d.b.) in moisture and dried for 30 min in the pulsed fluidized bed at $\bar{U}=0.29$ m/s with the presence of vibration to eliminate any potential channeling. $\bar{U}=0.29$ m/s was equivalent to $1.2U_{mf}$ for the Douglas fir

particles before additional screening. The final moisture ratio of all three particle fractions can be seen from Figure 3.11, where the 0–1 mm fraction possessed least moisture, only one-fifth the amount of the 3.15–4 mm fraction. One contributing factor may be that for smaller particles water molecules travel less distance to migrate from the centre to the surface, whereas in larger particles the resistance to molecular diffusion of water is greater. Smaller particles also offer larger specific surface area, which could speed up the evaporation of water on the surface. As a result, drying for the fraction of smaller particles tends to be faster.

In addition, it was noticed that less channeling occurred during the drying of 0–1 mm particle fraction compared to the other two fractions that contained coarser particles. Therefore, it is highly likely that the fluidization of biomass materials benefited from the presence of fine particles, or fines. Further investigation was conducted, in which the fraction with fine Douglas fir sawdust (0–1 mm) were added to the coarse fraction (3.15–4 mm) at certain ratios. Five mixtures were prepared with the weight percentage of fine particles ranging from 7.4% to 38.5%. Details of the mixtures, which are named Group 1 to Group 5, are summarized in Table 3.1. It should be noted that even for the 0–1 mm fraction, many particles still belonged to the category of conventionally Geldart Group B particles. The weight percentages of actual fines (e.g. $d_p < 40 \mu\text{m}$) in the mixtures were far less than the abovementioned ratio of 7.4–38.5%. All samples had initial moisture content of 57.3% (dry basis).

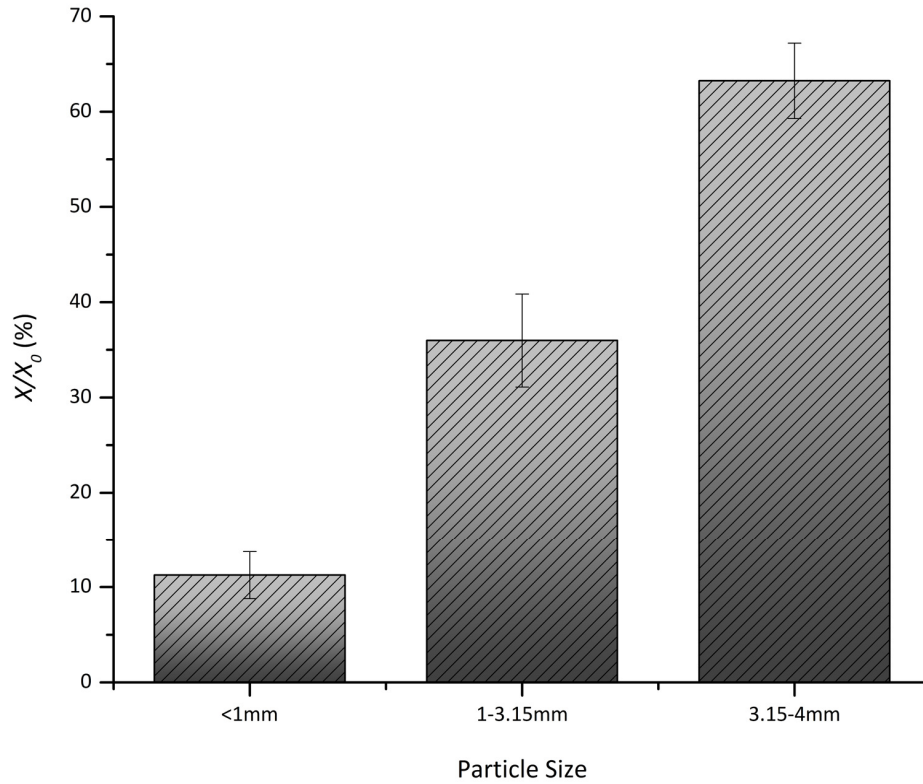


Figure 3.11 Effect of particle size on final moisture ratio of Douglas fir after 30 min drying in pulsed fluidized bed, samples had initial moisture content of 94.5% (dry basis).

Table 3.1 Details for the mixture of coarse and fine particle fractions of Douglas fir sawdust

Group Number	Weight of Particle Fractions (g)		Percentage of Fine Particles (w.t. %)
	0 – 1.0 mm	3.15 – 4.0 mm	
1	125	200	38.5
2	100	225	30.8
3	75	250	23.1
4	50	275	15.4
5	25	300	7.7

Drying went smoothly for Group 1 that contained 38.5% fine particles. As depicted in Figure 3.12, the drying rate curve consisted of mainly three parts, namely the initial system response, constant-rate drying period and falling-rate drying period. The initial system response corresponded to the beginning of each curve where there existed a sharp decline in drying rate. It was likely caused by the freeboard region of the fluidized bed column that had been saturated with moisture prior to the drying tests. The moisture was probably introduced while biomass samples were being loaded from the top of the column. As drying initiated, fresh air entered the fluidized bed column diluting the moist air in the freeboard causing the readings to increase. Eventually the initial moisture in the freeboard region was purged out of the column. Naturally, the humidity probe installed at the exit of the fluidized bed would detect a higher concentration of moisture at the very beginning, and gradually returned to normal. The initial response was followed by the constant-rate drying period with a typical average drying rate of 0.04 g/s. After reaching the critical moisture content at around 900 s, the drying rate started to decline, until the test was terminated after 30 min. Groups 2 and 3 shared the same trend as Group 1, but with slightly lower drying rates. Final moisture ratios for Groups 1, 2 and 3 were 10.1%, 11.1% and 12.8%, respectively.

For Group 4 that contained 15.4% of fine particles mild channeling occurred around $t = 500$ s, which deteriorated into partial defluidization by $t = 600$ s as a gas fountain formed at the centre of the bed. Drying rate in return suffered from the lateral segregation and reduction of gas–solid interaction, which is shown in Figure 3.12 as the saddle on the drying rate curve. Proper fluidization and drying was resumed after another 5 min, presumably because of the removal of moisture and the reduction in cohesive forces.

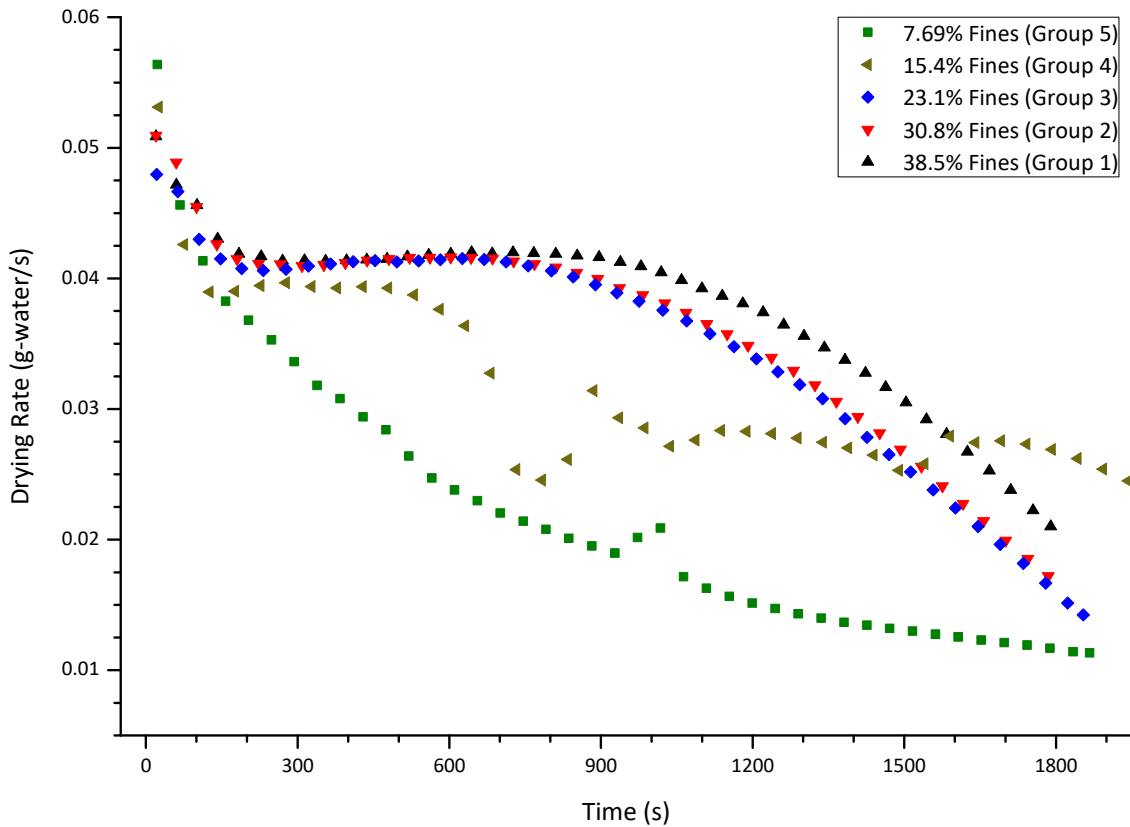


Figure 3.12 Drying rates of coarse Douglas fir sawdust mixed with various amount of fine particles in the pulsed fluidized bed dryer

During the drying of Group 5 particles (containing 7.69% fine particles) channeling occurred at the very beginning. The fluidized bed was completely defluidized within the first 300 s. The centre of the bed was emptied, a huge void appeared where a small portion of biomass particles was repeatedly brought up and fallen back down, while the rest of the bed remained stationary. Samples recovered after 30 min of drying remained wet, indicating very poor drying performance. The drying curve of this group differed greatly in shape from all the other groups likely due to its resemblance to a fixed bed reactor. No constant-rate region could be identified.

The measured Φ values of all five particle groups are plotted in Figure 3.13. Groups 1, 2 and 3 exhibited excellent mass transfer performance, with the final moisture content being 10.1%, 11.1% and 12.8%, respectively. Due to the channeling which occurred around 600 s, the final moisture ratio

for Group 4 was 39.8%. As to Group 5, half of the initial moisture remained within the sample, with the final moisture content being 50.7%. All drying tests were repeated five times, and good repeatability was observed for Groups 1, 2 and 3. Because of the unstable flow behaviour of Groups 4 and 5, repeated experiments showed similar behaviour as described above, but the undesired flow time and duration varied slightly. As a result, the final moisture content varied by as much as 11% for Group 5, and 10% for Group 4. Figure 3.13 shows the predicted final moisture contents, which were calculated by superposition in which the final moisture content of each group was considered as the linear combination of that of the two particle fractions when they were dried separately. The experimental values were much smaller than the model-predicted ones, proving that fine particles had a synergetic effect on the fluidization of coarse particles. It appears that the poor fluidization quality for Groups 4 and 5 may have stemmed from coarse particles in these groups acting more independently than behaving like a continuous medium.

The improvement in fluidization quality and drying efficiency observed during the experiment is likely resulted from the fact that fine particles tend to adhere to coarser particles because of cohesive forces (e.g. van der Waals force) between the particles, as verified by Ma and Kato (1998) via SEM imaging. Consequently, coarse particles with irregular shapes and rough edges are more readily to adhere to each other, which enhances the interaction between particles. Therefore, fluidized bed behaves more uniformly like a continuum and particles become easier to be fluidized. Above hypothesis has been verified by testing the angle of repose (AOR) of all five groups. AOR measurements were performed on the Powder Research Ltd AOR tester (Mark 4) developed by Geldart et al. (2009). Details of these tests are included in the Appendix A3. Summarized results are shown in Figure 3.13. Groups 1–3 had similar AOR values that were close to 50° , while Groups 4 and 5 had elevated AOR values, which were 53.0° and 56.3° , respectively. There is a strong possibility that by adding a small amount of fine particles into the coarse fractions, the coarse particles are lubricated. The internal friction between larger particles is alleviated and the angle of repose lowered.

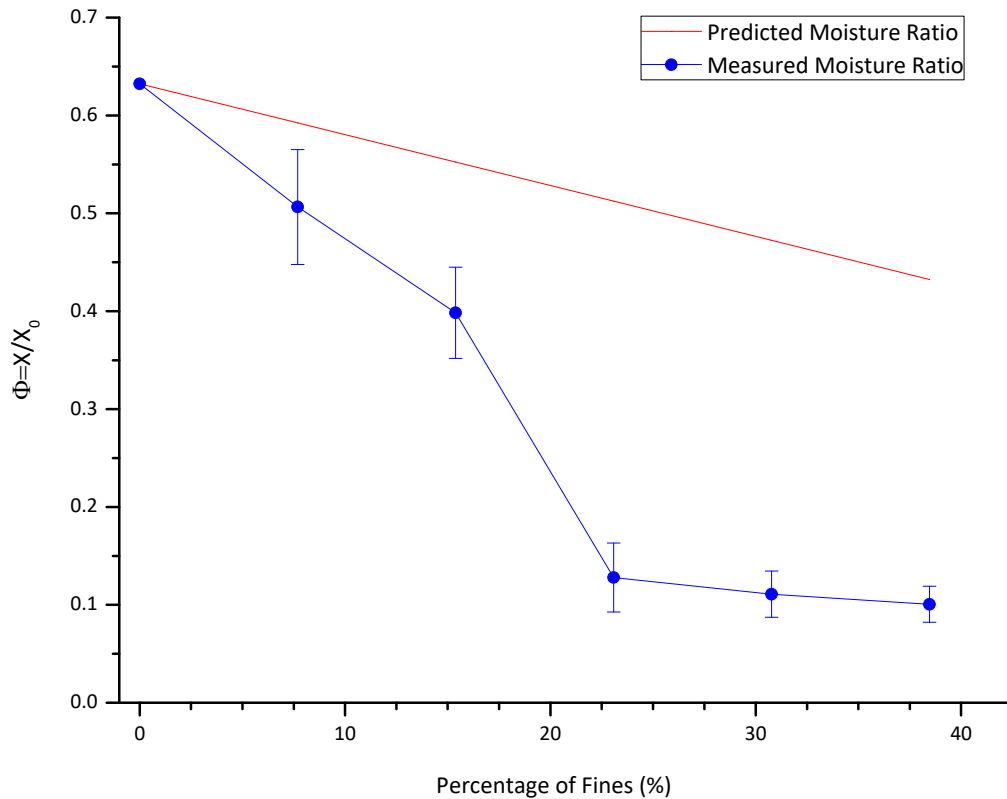


Figure 3.13 Predicted and measured final moisture content of coarse Douglas fir sawdust mixed with various amount of fine particles in the pulsed fluidized bed dryer after 30 min of drying; samples had initial moisture content of 57.3% (dry basis).

Another contributing factor for the improvement in drying, heat and mass transfer could be related to particle size distribution (PSD). Studies have shown that in a low gas-velocity bubbling fluidized bed, a mixture of both coarse and fine particles offers higher chemical conversion against the standalone fine or coarse particles (Sun, 1991). A mixture of fine and coarse particles also contains higher concentration of fine particles in the voids (bubbles and slugs), which enhances the inter-particle heat and mass transfer.

3.2.7 Drying mechanisms of three biomass species

So far in this chapter, attention has been paid to Douglas fir sawdust and its mass transfer performance at different operating conditions, but other biomass species including pine and switchgrass were also studied in the pulsed fluidized bed through batch drying tests. The same average superficial gas velocity $\bar{U} = 0.31\text{m/s}$ (equivalent to $1.3U_{mf}$ for Douglas fir sawdust) was used. The initial moisture contents (dry basis) of Douglas fir, pine and switchgrass were 71%, 60% and 67%, respectively. Drying curves for all three species of biomass including Douglas fir, pine and switchgrass are shown in Figure 3.14(a). Since wet particles were loaded into the fluidized bed dryer prior to each run, some surface moisture on the wet particles evaporated and are cumulated in the freeboard region. It is highly probable that the decline in drying rate during the first 5 min was caused by the removal of accumulated moisture from the freeboard by introduced dry air. In addition, the samples had a slightly higher temperature than the drying air in this set of experiments ($\sim 5^\circ\text{C}$), which also contributed to the higher drying rates as higher temperature promotes drying. The constant rate drying was reached after the initial system response, as indicated by the flat profile of relative humidity in Figure 3.14(a). At this stage, a thin film of water covered the surface of particles, on which the evaporation mainly took place. The rate of drying was limited by the evaporation of water, which could be characterized as a heat-transfer limited process, only to be influenced by external conditions such as temperature, humidity and flow rate of the drying air.

The same set of data is also normalized and plotted against particle moisture content, as shown in Appendix A4, in which the start of falling rate period is better identified.

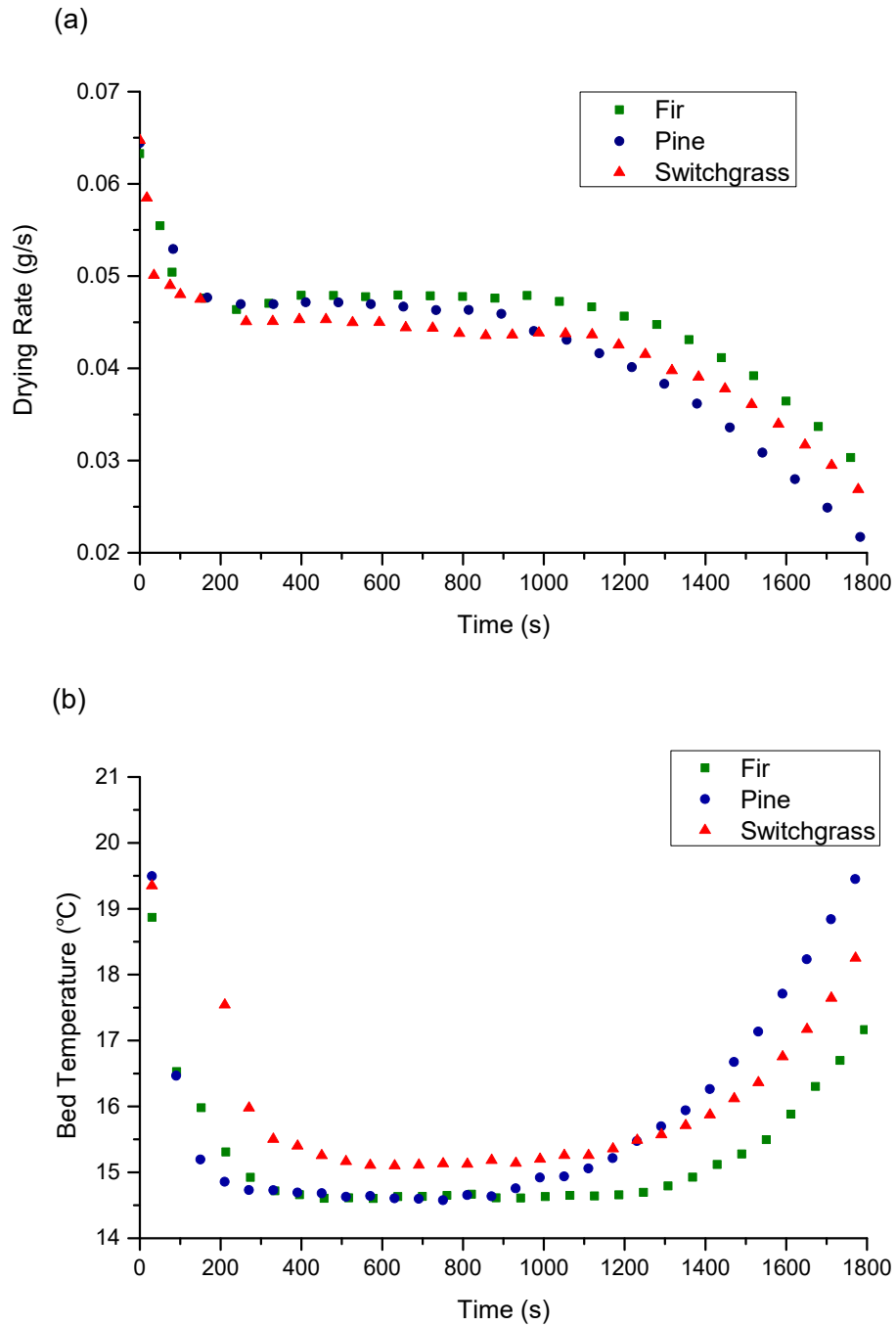


Figure 3.14 Typical drying curves of three biomass species (a) Drying rate vs. time (b) Bed temperature vs. time

Bed temperature remained constant during constant rate drying. However, as drying proceeded, dry spots appeared on the surface of particles once critical moisture content was reached. Although

drying rate per unit wet area remained the same, a reduction in wet areas caused the drying rate to decline. As the surface of the particles completely dried out, surface temperature increased significantly. Drying then became a mass-transfer limited process that was mainly driven by the concentration gradient between the core and surface of the particles. Temperature profiles during drying are illustrated in Figure 3.14(b), in which three distinct regions could be identified, corresponding to the two drying mechanisms that were constant-rate drying and falling-rate drying. The initial temperature drop was most likely caused by the evaporation of water by heat from the bed of particles.

3.2.8 Natural frequency and damping factor

The previous section demonstrated that pulsed fluidized beds could be operated below minimum fluidization velocity with reasonable heat and mass transfer rates, leading to potential energy savings for the operation of compressors or blowers. Figure 3.6 shows that operating the fluidized bed at $\bar{U} = 0.8U_{mf}$ with 0.75 Hz pulsation, the remaining moisture in the biomass sample after 30 min of drying was only 5% higher than that operated at $1.3U_{mf}$ with the same frequency. As pulsation frequency moved away from 0.75 Hz, drying efficiency was reduced for $\bar{U} = 0.8U_{mf}$, whereas for $\bar{U} = 1.3U_{mf}$ drying efficiency monotonically increased with pulsation frequency. One of the possible explanations is provided in Figure 3.15, which shows two gas velocity profiles in the pulsed fluidized bed, $\bar{U} < U_{mf}$ and $\bar{U} > U_{mf}$. Although theoretically the velocity profile should be square waves, in reality because of the actuation time of the solenoid valve (less than 1 second) and the damping of the flow through pipes and plenum chamber, they were much closer to sinusoidal waves. In general, the gas phase is only capable of lifting the biomass particles when it possesses enough kinetic energy, i.e. when the oscillating superficial gas velocity within a pulsation cycle exceeds minimum fluidization velocity ($\bar{U} > U_{mf}$). In each pulsation cycle, there is a fraction of time

that satisfies this condition. These periods are marked as ‘fluidized zones’ in Figure 3.15, with their duration depending on the pulsation frequency and the average flow rate. Figure 3.15(a) represents a typical scenario for $\bar{U} > U_{mf}$. Of the two frequencies portrayed in this figure, $f=1.5$ Hz possessed a longer period where $\bar{U} < U_{mf}$ within each cycle compared to 4.5 Hz. This suggests that increasing the pulsation frequency from 1.5 to 4.5 Hz likely will lead to a larger percentage of time in each cycle where the gas phase is powerful enough to fluidize the particles. It also explains the decreasing moisture ratio with increasing pulsation frequency at $\bar{U} = 1.3U_{mf}$. Situation reverses for $\bar{U} < U_{mf}$ when most of the gas flow in a pulsation cycle is too weak to overcome the bridging forces in the fluidized bed, leaving most effective drying being carried out in a very short period of time. Therefore, it is safe to assume that higher pulsation frequency weakens the pulsation amplitude, with less portions of gas velocity exceeding U_{mf} in each cycle. This is consistent with the observation that only at lower pulsation frequencies could the bed be effectively fluidized for $\bar{U} = 1.3U_{mf}$. On the other side of the spectrum however, an extremely low pulsation frequency brings no benefits either. For instance, at 0.33 Hz the bed remains stationary for 1.5 seconds, providing enough time for the formation of particle bridges, which further indicates that too high or too low frequencies are equally detrimental to the drying of biomass for $\bar{U} < U_{mf}$.

Besides the intensity of pulsation at different frequencies, the inherent nature of the fluidized bed may have affected the drying rate as well. It has been demonstrated that gas–solid fluidized beds could be characterized as a second-order mechanical vibration system, in which the pressure waves represent the output response of such a dynamic system to an external excitation (Hao & Bi, 2005), and the under-damped natural frequency f_N (Hz) could be expressed as,

$$f_N = \frac{1}{2\pi} \sqrt{\frac{g}{H_{mf}}} \quad (3.2)$$

where H_{mf} (m) is the bed height of the fluidized bed. Pressure fluctuations in fluidized beds can originate from the passage of bubbles near a pressure transducer, oscillations of the bed surface, the plenum chamber, or even the gas blower (Bi, 2007; Roy et al., 1990; Zhao & Yang, 2003). In the pulsed fluidized bed, pressure fluctuations are mainly initiated by the gas pulsation. As illustrated in Figure 3.3 from the power spectrum analysis, the dominant frequency of pressure fluctuations in a pulsed bed equaled the frequency of the gas pulsation.

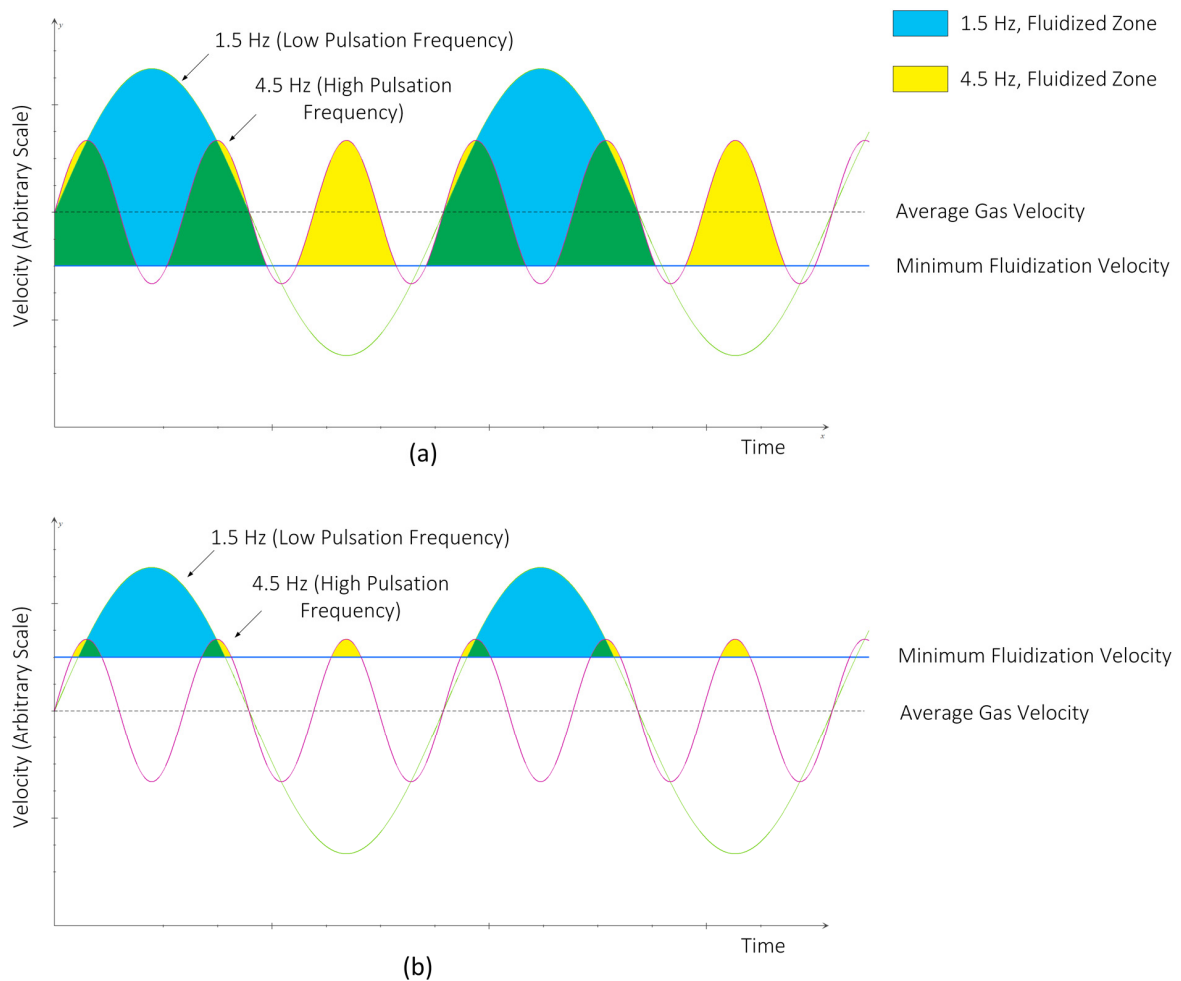


Figure 3.15 Schematic drawing of the pulsations at different frequencies and flow rates

The pressure waves are normally dampened as they travel through the fluidized bed due to inter-particle collision, relative motion between the interstitial gas and the particles, as well as the particle-wall friction. By incorporating the damping factor (ζ), natural frequency is then rewritten as,

$$f'_N = \frac{\sqrt{1-\zeta^2}}{2\pi} \sqrt{\frac{g}{H_{mf}}} \quad (3.3)$$

Since the fluidized bed is mostly an under-dampened system, ζ is less than 1, with typical values reported in the literature being around 0.3 (Hao & Bi, 2005). Many previous studies on the damping of pressure waves were conducted in fluidized beds where particles with controlled size and shape were used. Neither the damping of pressure waves in pulsed fluidized beds, nor the change of damping factor with the moisture content of particles has been investigated. By measuring the amplitude of the first and second peak of the pressure waves in each pulsation cycle (e.g. amplitudes of peaks A and B in Figure 3.1), damping factor ζ could be calculated. It should be noted that the pressure signals of wet biomass particles are different from dry particles as shown in Figure 3.1, the results presented in Figure 3.16 provide the change in damping factor during a typical batch drying process while wet biomass were being dried. Evidently, 0.33 Hz possessed higher damping factors than 1.0 Hz, which is consistent with the findings of Roy et al. (1990) that the damping effect is proportional to the intensity of the excitation signals. At both pulsation frequencies, the damping factor decreased as drying continued, indicating the damping of pressure waves was associated with the change in particle moisture content, or more precisely inter-particle forces. In the beginning of each drying test, biomass contained very high moisture content that made the particles particularly cohesive. Channeling occurred, causing most of the energy being dissipated when a large portion of the gas phase passing through the fluidized bed without effectively contacting the solids. Consequently, the damping factors were very high at the beginning, $\zeta=0.70$ for 0.33 Hz, and $\zeta=0.50$ for 1.00 Hz pulsation, indicating high energy dissipation. As drying

continued, moisture was being removed, the cohesive forces reduced significantly. The bed became free flowing rather than channeling, and the relative motion between gas and particles was enhanced. As more kinetic energy was being absorbed by the particles rather than being dissipated, the damping factor decreased. Moreover, the higher-than-normal damping factor observed in the pulsed fluidized bed reveals the unconventional nature of biomass particles that often cause difficulties in fluidization. By introducing pulsation, the gas–solid and inter-particle interactions can be promoted as a result of the periodic acceleration and deceleration of particle movement.

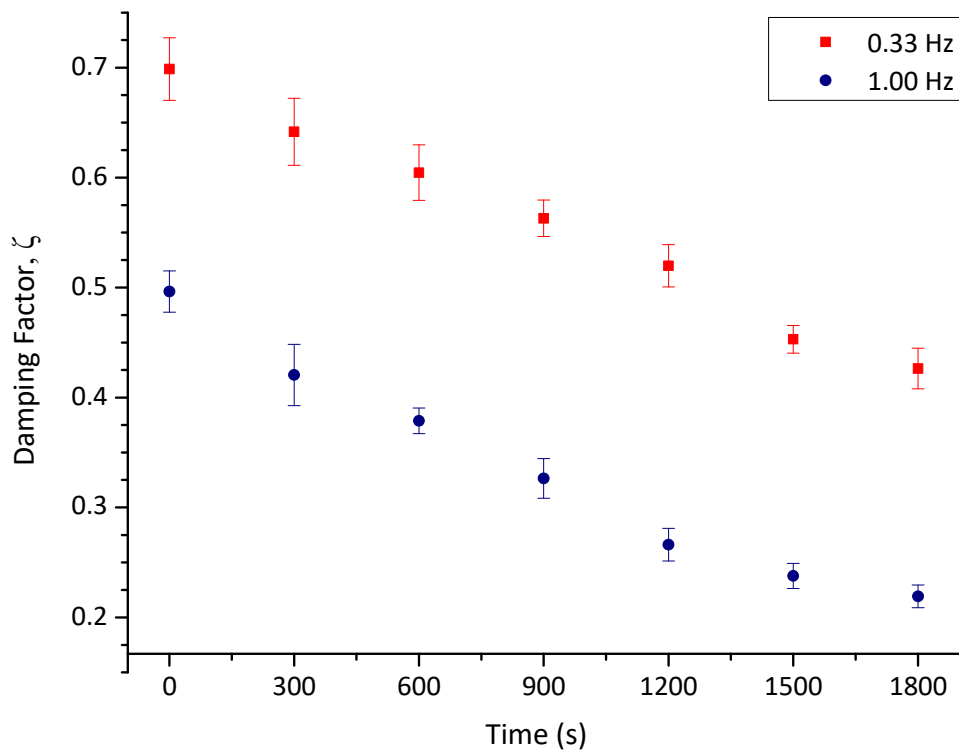


Figure 3.16 Damping factor of the pulsed fluidized bed during drying of Douglas fir sawdust

Based on the experimentally obtained damping factor of $\zeta = 0.2\text{--}0.7$, the natural frequency of the pulsed fluidized bed in this study was calculated to be 0.92–1.54 Hz according to Eqn. (3.3). As the dominant frequency of the system approaches its natural frequency, resonance will occur in the fluidized bed just like in a mechanical system, resulting higher amplitude of pressure fluctuations as well as improved gas–solid contact. This may help explain the experimental result where the

highest drying efficiency for $\bar{U} < U_{mf}$ was seen between 0.75–1.5 Hz, which was close to the natural frequency of the pulsed fluidized bed. As the pulsation frequency departed from the natural frequency, the drying efficiency decreased. As indicated in Eqn. (3.3), natural frequency is a function of bed height and damping factor. Since damping factor changes with moisture content and may be different with different biomass species, natural frequency of the fluidized bed may also vary with different bed material.

3.3 Hydrodynamics of the tapered pulsed fluidized bed

In order to eliminate dead zones observed in the rectangular pulsed fluidized bed, a tapered bottom section was fabricated and inserted so that the cohesive biomass particles could be better fluidized. Dimensions of the inserted section are shown in Figure 2.4. Douglas fir sawdust was chosen as the bed particles, with comparable operating condition to the rectangular geometry. The fluidization behaviour of the Douglas fir sawdust particles was first investigated at various pulsation frequencies. A 50% duty cycle was used in this study, where the “ON” time and “OFF” time in each pulsation cycle were kept the same. A minimum pulsation frequency of 0.5 Hz was selected to avoid the “OFF” period being too long. Considering limitations of the solenoid valve, the maximum frequency was set to 6.67 Hz. Despite the pulsation frequency being relatively narrow, it did envelope the natural frequency of the system calculated according to Hao and Bi (2005), around which the fluidized bed may behave differently. Snapshots of gas–solid flow patterns at four distinct pulsation frequencies are shown in Figure 3.17, while the differential pressure profiles at various frequencies are given in Figure 3.18.

3.3.1 Low pulsation frequency of 0.25 – 1.5 Hz

At this frequency range “ON” and “OFF” periods were visible and distinctive. As can be seen in Figure 3.17(a), at $f=0.5$ Hz the bed remained stationary during the “OFF” period. The rapid bed expansion marked the beginning of the “ON” period, corresponding to the dominant peak of the pressure profile in Figure 3.18(a). Compared to the original rectangular design, no dead-zones were observed at this frequency in the tapered fluidized bed. High amplitudes of bed expansion were observed (Figure 3.17(b)). The relatively high intensity of flow pulsation at this frequency most likely stemmed from the long pressure build-up during the “OFF” period, which induced a high gas velocity at the beginning of the “ON” period. The “ON” period was long enough to allow ample gas flow that enabled falling particles to meet uprising gas. As can be seen in Figure 3.17(c) and Figure 3.17(d), the counter-current flow and vigorous gas–solid contact made this period in a pulsation cycle very favourable for heat and mass transfer, which is represented by the damped oscillations of the pressure in Figure 3.18(a). As “OFF” period commenced, the bed quickly being stationary again, leading to very poor gas–solid contact and heat/mass transfer. Consequently, the overall performance of pulsed gas flow at this low frequency range was dissatisfying.

As the pulsation frequency increased, intermittence of the gas–solid flow caused by the “OFF” period became shorter. As illustrated in Figure 3.18(b), at $f=1.25$ Hz the damped pressure oscillations similar to that of $f=0.5$ Hz were still present, but had started to overlap with the dominant peak of the next pulsation cycle. This indicates that the external pulsation frequency $f=1.25$ Hz was in close vicinity of the natural frequency $f_N=1.25$ Hz, where the resonance effect enhanced gas–solid contact as well as heat and mass transfer.

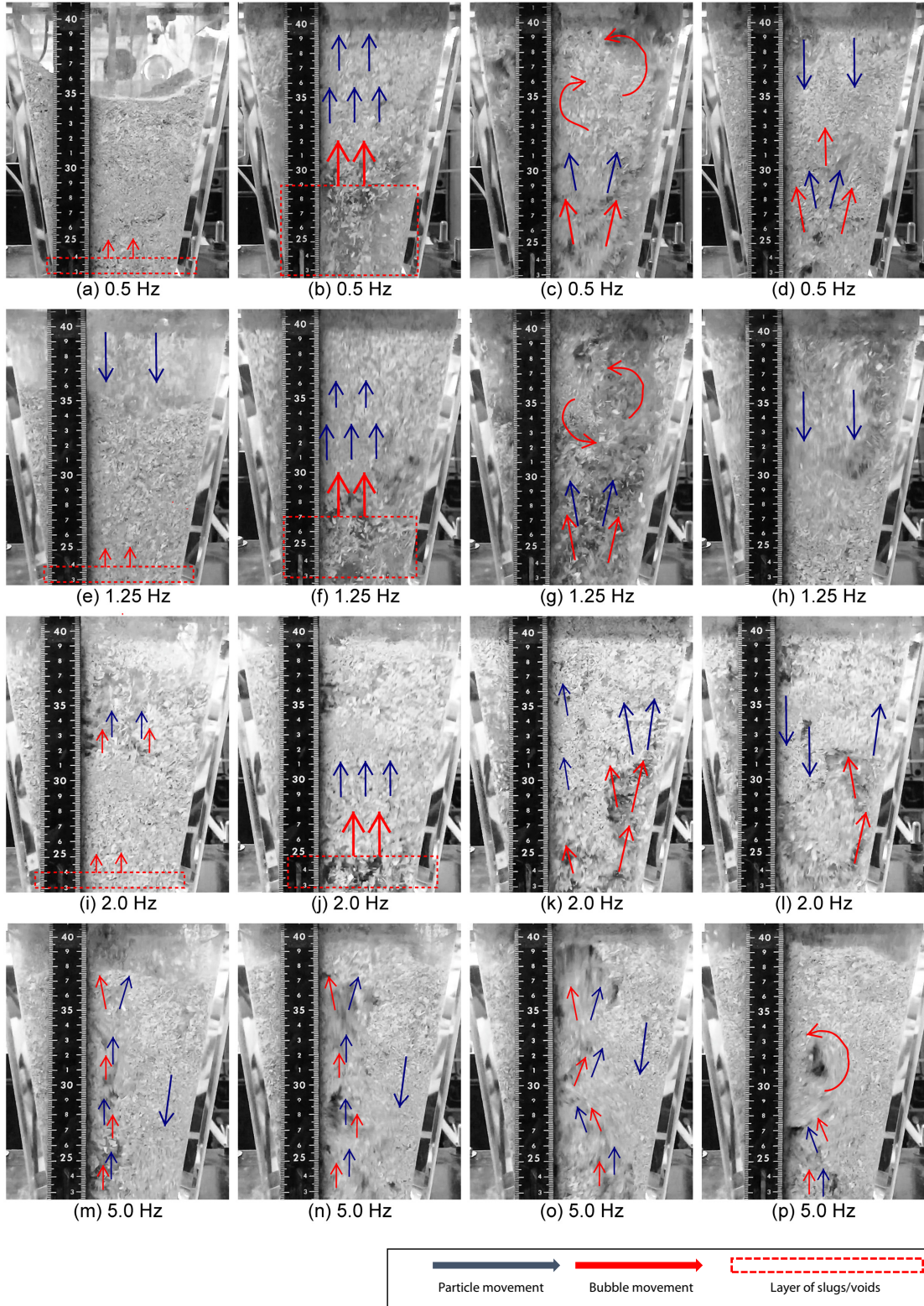


Figure 3.17 High-speed photographs of the gas–solid flow in a pulsed fluidized bed taken at different pulsation frequencies, $\bar{U}/U_{mf}=1.3$, initial bed mass=200g, bed material: Douglas fir, particle Sauter diameter=1.449mm

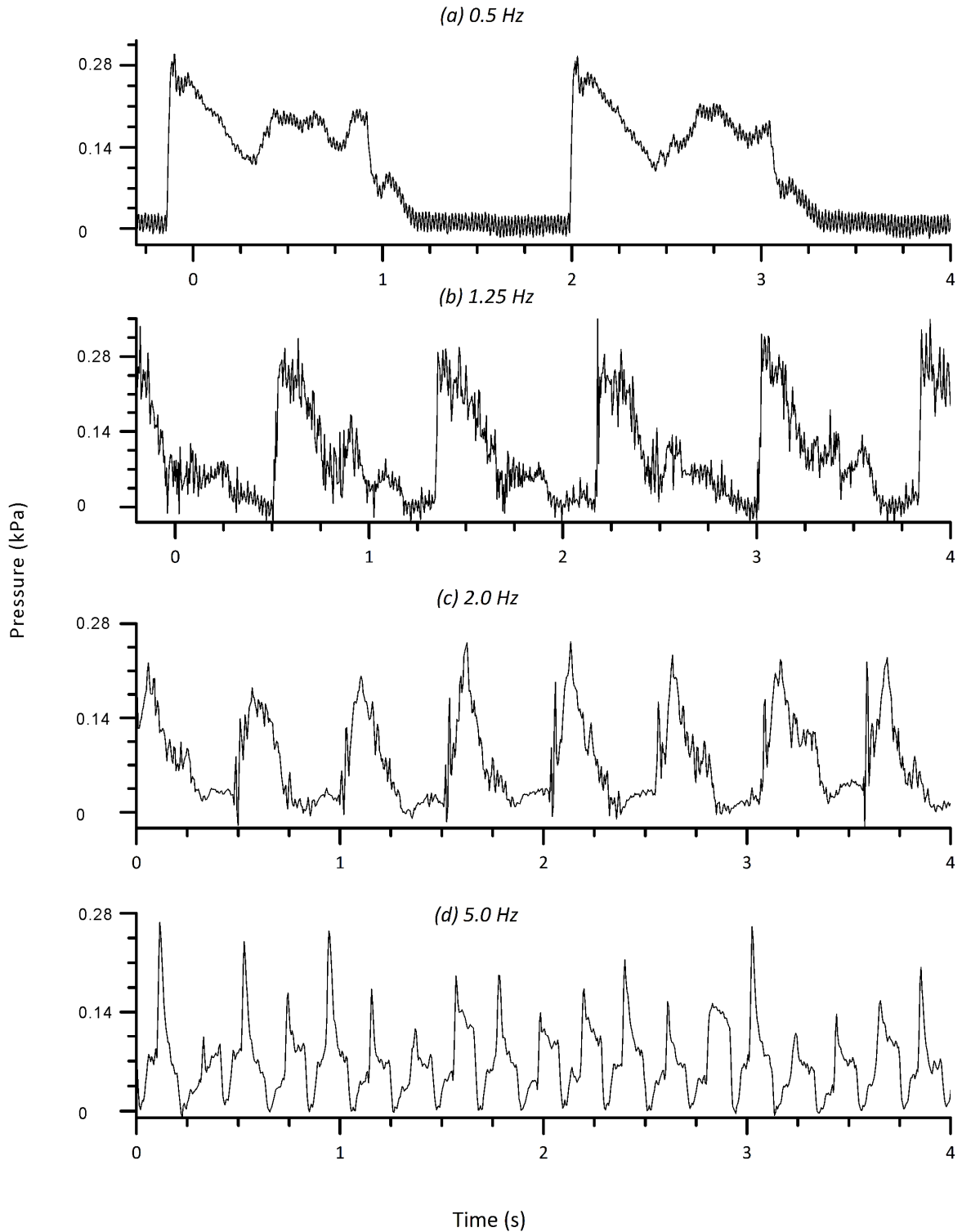


Figure 3.18 Instantaneous bed pressure vs. time for different pulsation frequencies, $\bar{U}/U_{mf}=1.3$, initial bed mass=200g, bed material: Douglas fir, particle Sauter mean diameter=1.45 mm.

3.3.2 Intermediate pulsation frequency of 1.5 – 2.5 Hz

The shorter "OFF" period reduced pressure build-ups, therefore weaker flow pulsations were observed at $f=1.5-2.5$ Hz, which also was reflected in the reduced amplitude of bed expansion (Figure 3.17(j)). The shorter duration of each cycle also reduced intermittence. Depicted in Figure 3.17(i) the commencement of a new cycle (air flow coming through the distributor) already caught up with the residual gas flow from the previous cycle. With the less intense flow pulsation, the fluidizing gas was not capable of lifting the entire bed. Alternatively, gas phase quickly penetrated the upper portion of the bed, in most cases with gas bypassing, which was clearly captured and displayed Figure 3.17(k) and (h). Therefore, it can be concluded that at this frequency range the "ON" period is simply not long enough to sustain counter-current gas–solid contact as lower frequencies could. The gas–solid contact efficiency in the "ON" period is thus expected to be lower compared to 1 Hz. As to the overall efficiency, it could only be evaluated once the negative contribution of "OFF" periods is taken into consideration.

3.3.3 Pulsation frequency of 3 – 6.67 Hz:

A continuous fluidized bed was visually observed at $f=3$ Hz and above, where the frequency of the external excitation was distinctively higher than the natural frequency. Under such circumstances, the system was led by the external excitation. The "OFF" period disappeared, which agreed with the continuously oscillating pressure profile as shown in Figure 3.18(d), in which no intermittence could be observed, with pulsating gas from a new cycle closely following the previous one. Large but regular bubbles formed in the upper section of the bed. The pulsed fluidized bed started to mimic that of a conventional system.

As pulsation frequency further increased, the exterior region of the bed became less fluidized when compared with the centre, where more gas bubbles and particle entrainment took place in the

centre. Particles fell back to the side and slowly recirculated to the bottom. Such a fountain-like flow behaviour is illustrated in Figure 3.17(m), Figure 3.17(n) and Figure 3.17(o). Due to the relatively low particle density, the centre region was not always stable. As captured by Figure 3.17(p), bubbles often ascended in a zigzag motion, causing occasional lateral mixing of particles. However, in most cases the system became laterally segregated, and quickly deteriorated with increasing pulsation frequency and gas flow rate.

It should be noted that the above observations were made with dry biomass particles. When dealing with wet biomass particles during batch drying, especially at the beginning of each session, the stronger cohesive forces could only be alleviated by sufficiently intense gas pulsations. In cases when the pulsations were weak, normally resulting from low gas flow rates or high pulsation frequencies, channeling and even defluidization occurred. Therefore, the drying performance, which reflects gas–solid contact efficiency and mass transfer rates, is limited by the bed behaviour. The effect of pulsation frequency and flow rate on mass transfer should be quantitatively studied by means of biomass drying tests where the rate of drying can be seen as a benchmark for gas–solid contact efficiency and mass transfer rate. Section 3.4 below is dedicated to solving this problem.

3.4 Batch drying and mass transfer in tapered fluidized bed

Batch drying of biomass was conducted in both the original and the tapered fluidized bed with the same operating conditions as in the original fluidized bed, so that the gas–solid contact and heat/mass transfer could be compared. Water was added to Douglas fir sawdust to reach 60% (w.t. dry basis) moisture content for used in the following experiments. Pulsation was first studied with the frequency set to 1.5 Hz. Despite the oscillating nature of the pulsed flow, the volumetric gas flow rate could be kept the same for both geometries. For the study of gas flow rate, five superficial gas velocities were used, which were $1.05U_{mf}$, $1.1U_{mf}$, $1.2U_{mf}$, $1.3U_{mf}$ and $1.4U_{mf}$. It is noteworthy

that minimum fluidization velocity varies with moisture content, aforementioned U_{mf} value (0.238 m/s) belongs to the samples with 7% moisture content (dry basis). As in previous sections, the minimum fluidization velocity was calculated from the volumetric flow rate and a cross-section area of 0.015 m² for the rectangular bed and the non-tapered section of the tapered bed.

3.4.1 Effect of gas flow rate

Final moisture ratio ($\Phi = X/X_0$) data after 30 min of drying at various average gas velocities are plotted in Figure 3.19. The initial moisture content of the Douglas fir sawdust was 59.4% (dry basis). Increasing air throughput enhanced the convective mass transfer of moisture from solids to interstitial gas, resulting in faster drying. The tapered design showed higher drying rate, especially when the superficial gas velocity was low. At $1.05U_{mf}$ the remaining moisture in the tapered design was 12.6% less than from the original non-tapered counterpart, while at $1.1U_{mf}$ it was 16.6%. It is highly probable that given the same volumetric gas flow, the reduced inlet surface-area increased the superficial gas velocity, which promoted gas–solid contact and removal of moisture. The tapered design also inhibited dead-zones found in the bottom corner of the original rectangular design, which may have also contributed to the increase in drying rate. The advantage of the tapered design over the original began to diminish once flow rate was further increased, such as at $1.3U_{mf}$. In essence, the tapered bed offered higher drying efficiency and stability than the original design at $\bar{U}=1.1-1.3U_{mf}$.

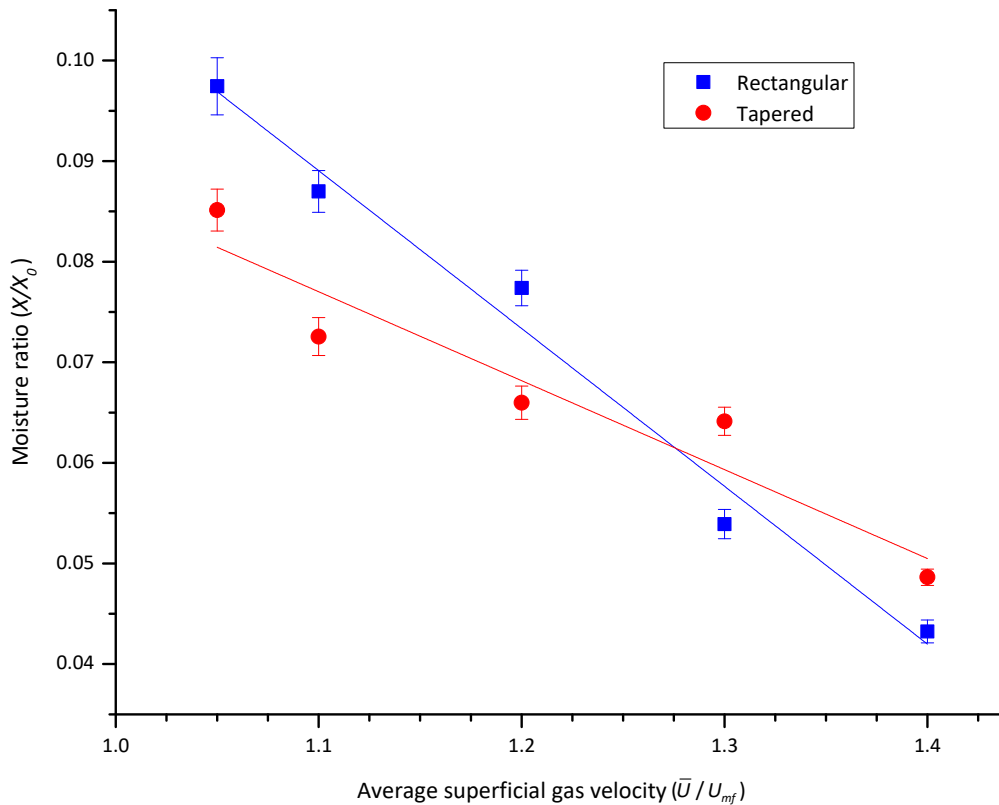


Figure 3.19 Final moisture ratio of Douglas fir sawdust after 30 min of drying in both original and tapered fluidized bed with pulsed gas flow, operated at different average gas flow rates, $f=1.5$ Hz (experimental data points with least-squares linear regression trend line); samples had initial moisture content of 59.4% (dry basis).

Drying rates during the 30-min batch drying tests at $1.1U_{mf}$ and $1.2U_{mf}$ in both geometries are shown in Figure 3.20. All curves could be divided into two major sections representing the constant rate drying period and the falling rate drying period, respectively. In the constant-rate drying period, particles are completely covered with a continuous liquid film. The rate of drying depends entirely on external parameters such as velocity, gas–solid flow pattern, temperature and humidity of the drying air. The resistance to internal mass transfer where moisture migrates from the interior to the surface of a particle is relatively small compared to the external resistance where the moisture is

removed from the particle surface. As long as the external conditions are kept the same, drying rate remains constant.

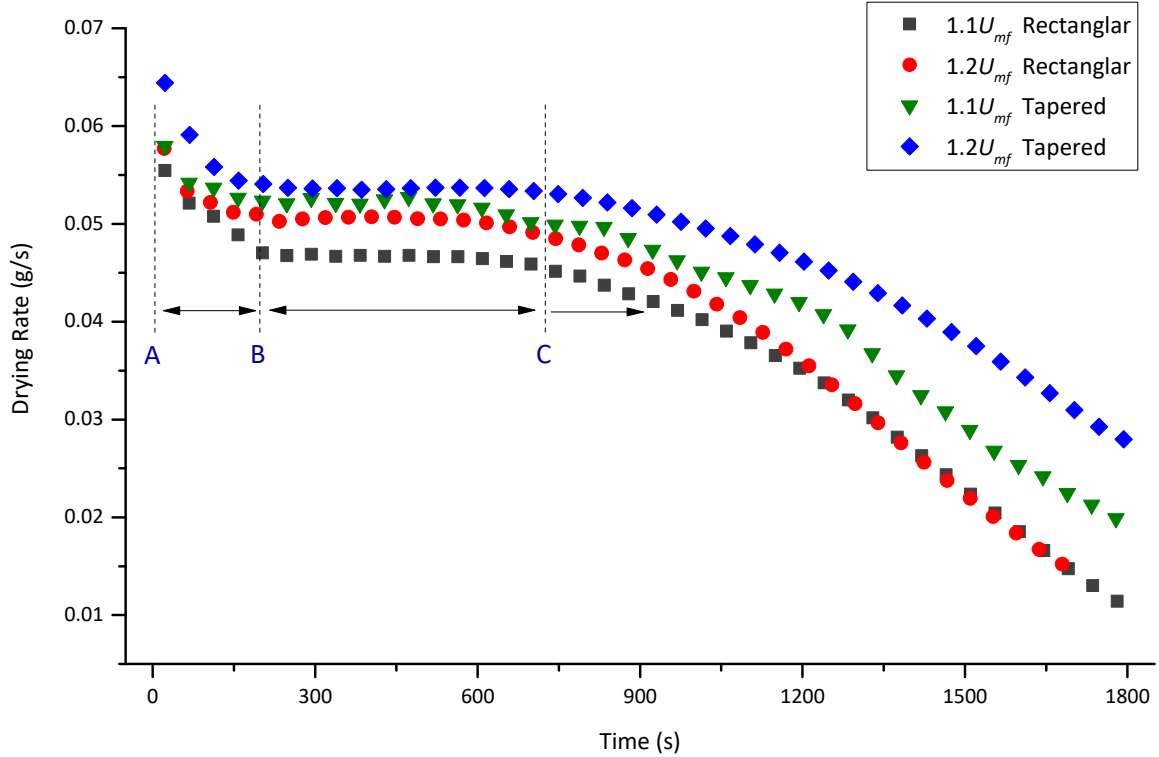


Figure 3.20 Drying rate curves of Douglas fir sawdust at various average gas velocities in both the original and the tapered fluidized bed with pulsed gas flow, $f=1.5$ Hz

The constant-rate drying period can be identified as section B–C in Figure 3.20, followed by the falling-rate period at C and beyond. Over this period, dry spots started to appear on particle surfaces, and resistance to internal diffusion of moisture within a biomass particle can no longer be neglected. Section A–B denotes the first three minutes of the batch drying process where drying rate suffered a sharp decline. It is highly probable that this decline was caused by drying air diluting the moisture-saturated freeboard region. The moisture was brought in when the wet biomass particles were loaded into the column prior to the drying test.

For the same reactor geometry, higher gas flow rate led to faster drying, in both the constant-rate and falling-rate drying periods. Tapered design at $1.2 U_{mf}$ exhibited the highest drying rate.

Furthermore, tapered bed at $1.1U_{mf}$ had the same drying rate as rectangular bed at $1.2U_{mf}$, indicating the tapered bed had higher heat and mass transfer rates. A reduction in the need of drying medium could also lead to energy savings and higher process efficiency.

3.4.2 Effect of pulsation frequency

Results from Sections 3.1.1 and 3.2.2 has demonstrated that hydrodynamics can be heavily influenced by pulsation frequency, which in return dictates heat/mass transfer in the pulsed fluidized bed. To determine the most suitable frequency for heat and mass transfer, batch drying tests were performed at a range of frequencies for the same gas flow rate. Final moisture contents of the biomass particles are plotted in Figure 3.21. The fluidized bed with a tapered bottom section exhibited at least 5% higher drying rate over the original rectangular design. In both original and tapered design, more water was removed at $f=1-3$ Hz, and drying rate declined as the pulsation frequency moved away from this range. It is simple to justify the low drying rates at 1 Hz and below, which was likely caused by longer "OFF" periods. Despite the vigorous motion of the biomass particles during the "ON" period, the overall drying rate was reduced tremendously by the inactivity during the "OFF" period. At higher pulsation frequencies (3.0 Hz and above) the faster renewal of gas phase and the continuous particle movement in theory is ideal for heat and mass transfer. In reality, however, because of shorter pressure build-up during the "OFF" period, pressure fluctuations were too weak to break up the inter-particle forces, especially at the beginning of each drying session where wet biomass particles had been particularly cohesive. Drying rate suffered from poor gas-solid contact and undesirable bed behaviour such as channeling, which eventually led to partial or complete defluidization. This instability might also explain the relatively large variations in the repeated tests, as the final moisture ratio from repeated experiments varied as much as 8%. The substantially intense gas pulsation and short "OFF" periods at $f=1-3$ Hz offered an overall high drying efficiency, as indicated in Figure 3.21. Since the ideal natural frequency of the

system was calculated to be 1.28 Hz according to Eqn. (3.2), the higher heat and mass transfer rates between 1 and 3 Hz may also be attributed to the resonance effect, similar to that of a mechanical system, where greater amplitude of pressure fluctuations and better gas–solid contact occur.

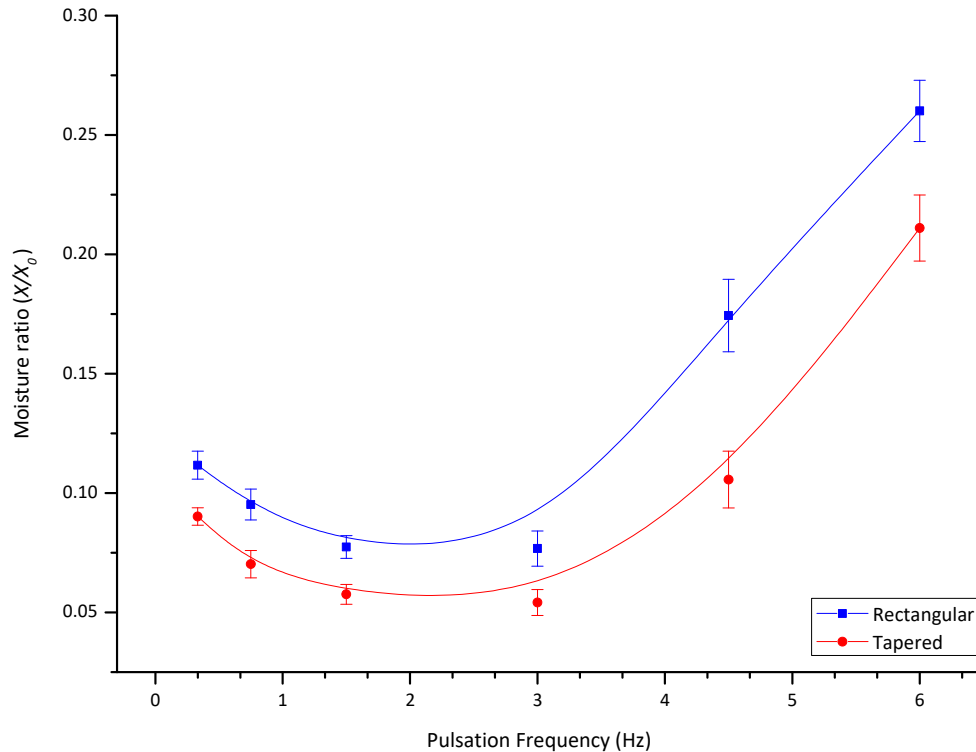


Figure 3.21 Final moisture ratio of Douglas fir sawdust after 30 min of drying in both original and tapered fluidized beds with pulsed gas flow, operated at different pulsation frequencies, $\bar{U}/U_{mf}=1.3$ (experimental data points with spline interpolations), samples had initial moisture content of 59.4% (dry basis).

3.4.3 Initial bed height

In a fluidized bed, the initial bed height affects bubble size and bubble behaviour. To study the influence of bed heights on drying performance, various amounts of biomass were loaded into the fluidized bed column prior to the batch drying tests, ranging from 200 g to 350 g, corresponding to initial bed heights of 120 to 180 mm. Flow rate and pulsation frequency were kept the same ($f=1.5$

Hz, $\bar{U}/U_{mf}=1.3$). Results indicated that by loading additional particles into fluidized bed the overall water removal rate decreased, as shown in Figure 3.22.

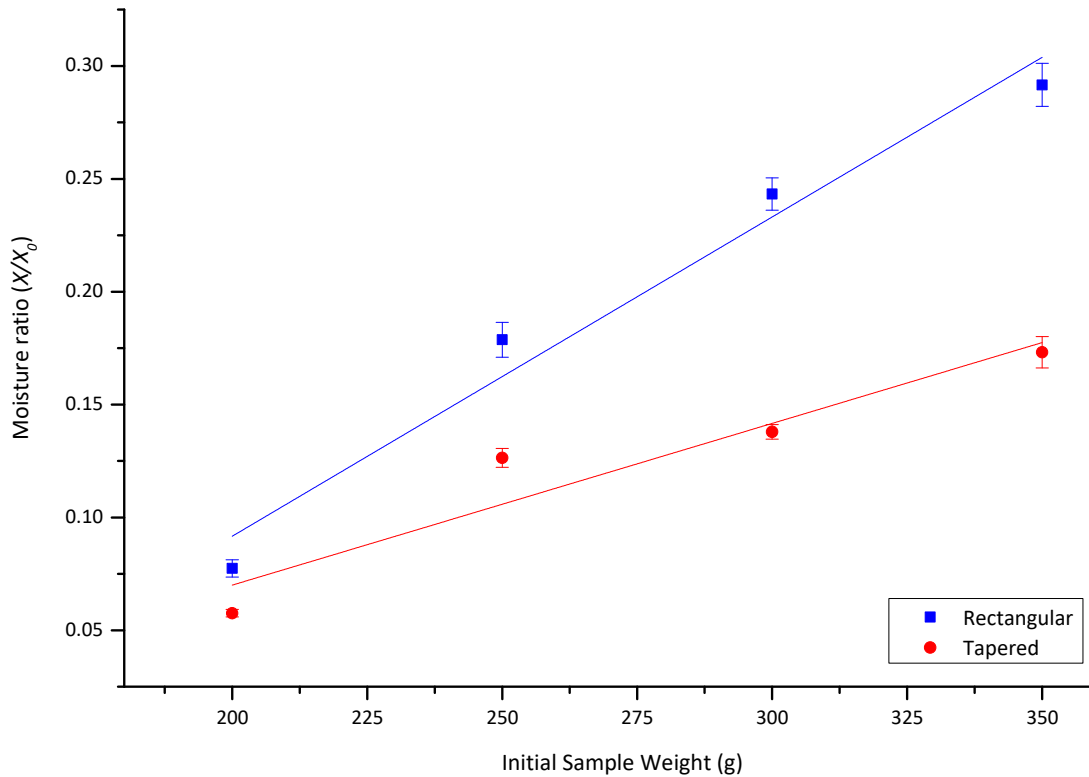


Figure 3.22 Effect of initial bed sample weight on the final moisture ratio of the Douglas fir sawdust after 30 min of drying in both original and tapered fluidized beds with pulsed gas flow, operated at $f=1.5$ Hz, $\bar{U}/U_{mf}=1.3$ (experimental data points and least-squares linear regression trend line)

For the same average gas velocity, the tapered design demonstrated a higher drying efficiency than the original design, especially for the case of 300 and 350 g initial bed weight that corresponded to respective bed heights of 160 mm and 180 mm. As bed height increased, it was more difficult for gas bubbles to penetrate the bed. In the original column, pulsation had become so weak that the upper half of the bed particles was lifted as a whole, exhibiting piston-like behaviour. Such flow behaviour was captured by the high-speed images and snapshots are shown in Appendix D. In the meanwhile, the bottom portion was completely defluidized. The tapered design had a higher superficial gas velocity compared to the rectangular bed, and the angle of the side wall was steeper

than the angle of repose of wet biomass particles, abundant gas–solid contact was observed even when the particles were wet and extremely cohesive, which may have contributed to the improvement in heat and mass transfer. Drying tests performed at different pulsation frequencies showed that the tapered bed was advantageous in terms of mass transfer for all frequencies investigated. Drying rate at $1.1U_{mf}$ in the tapered bed was very close to that of $1.2U_{mf}$ in the rectangular design, indicating that the tapered bed offered comparable performance with less airflow requirement and potentially lower operating cost.

It is noteworthy that when increasing bed height, the effect of pulsation gradually decreased, as more moisture was removed from the bed after 30 min of batch drying, consistent with the fact that gas pulsation is more effective in shallow beds. Further increasing bed height to 200 mm resulted in poor fluidization behaviour including partial defluidization. Even the strongest pulsation at a low frequency of 0.33 Hz was not able to sustain good gas–solid contact. As a result, only bed heights less than 180 mm were studied.

To maximize the effect of gas pulsation, when scaling up such a fluidized bed reactor, the bed height should be limited. One potential approach to scale up the system is to increase the length and width of the system, while the height will be maintained at a constant to retain the effectiveness of gas pulsation. Alternatively, multiple stages could be set up vertically where particles gradually come down. Such a design will be able to maintain a shallow bed, maximizing the effect of gas pulsation, while reducing footprint of the reactor.

3.4.4 Comparison of two geometries

By adding a tapered section to the rectangular fluidized bed, different flow behaviour was observed when compared to the original rectangular design. Dead zones at the bottom of the bed were eliminated to a great degree. Furthermore, biomass particles were less likely to channel and become

defluidized with the tapered channel present. Since the tapered wall of the column was built with an angle steeper than the angle of repose (AOR) of wet biomass particles used in this study, it guaranteed that particles could fall down to the bottom when they come into contact with the wall, rather than piling up by the wall and eventually causing partial defluidization. At relatively low pulsation frequencies it was discovered during the drying tests that once enough particles accumulated along the tapered column wall, they would crumble and fall back to the bulk of the dense phase and gradually make their way back to the bottom of the bed, until carried up again by the fluidizing air. This significantly reduced the chance of severe channeling, even if it did happen, it could quickly recover. At higher frequencies with weaker gas pulsations, particles were carried upwards to the top by the fluidizing air, and fell back to the region closer to the wall. These particles were able to slowly recirculate to the bottom and be carried up again. Such a flow behaviour bears a remote resemblance to a spouted bed with core–annulus flow. Under the same operating conditions in the rectangular fluidized bed, channeling and partial defluidization took place.

The improvement of gas–solid contact and mass transfer in the tapered bed is also manifest through the batch drying results. When operated at the same gas flow rate, the superficial gas velocity above the grid was higher in the tapered bed due to its smaller distributor (roughly one third of that of the rectangular bed), which increased the intensity of the gas pulsation. This may be one contributing factor for the 12.6% lower final moisture ratio at $1.05U_{mf}$ in the tapered bed. Above $1.3U_{mf}$ the positive effect of a smaller distributor started to wear off as it also restricted air flow. In this case, the larger distributor of the rectangular bed became advantageous, and a 5% lower moisture ratio could be seen at $1.4U_{mf}$.

3.5 Conclusion

By performing batch drying tests in both the rectangular and tapered pulsed fluidized beds, the mass transfer performance was benchmarked. In addition, hydrodynamics of the system as well as gas–solid contact characteristics were observed and studied in addition to drying. The bed behaviour changes during drying as a result of moisture content reduction and inter-particle forces abatement were also addressed.

In terms of gas–solid flow behaviour, the system was only fluidized intermittently below 3 Hz with slugs forming above the distributor that quickly gave rise to gas channels. Large bubbles were formed at 3 Hz instead of channels, above which regular bubble patterns could be seen. At even higher pulsation frequencies, the pulsed fluidized bed behaved similar to a conventional one.

Drying test results indicated that temperature and gas velocity played a significant role in biomass drying, as they both were able to boost the mass transfer from surface of the particles to the drying medium. Higher temperature and flow rates resulted in faster drying. Pulsation frequency, on the other hand, influenced the hydrodynamics and tied closely with the natural frequency, as well as the flow regime. The frequency between 0.75 and 1.5Hz with the average gas-velocity around or slightly above minimum fluidization velocity seemed to be a good spot, offering comparable drying performance at much higher gas flow rates. Vibration was found to be useful for fluidizing cohesive particles, especially when the extra acceleration brought by gas pulsation was insufficient to break up the inter-particle forces. However, it can be concluded that as long as pulsation is sufficient in overcoming the cohesiveness of biomass particles, vibration is only optional.

The influence of other key operating parameters such as pulsation duty cycle and particle size was also evaluated in the pulsed fluidized bed. By reducing the duty cycle of the solenoid valve in each pulsation cycle, 33% higher peak pressure drop was observed, which was beneficial to the fluidization of highly cohesive particles, especially when the normal 50% duty cycle was not enough

to break up the stronger cohesive forces. The longer dormant period in each cycle did cause a slight penalty in drying, but it can be applied to the initial drying period when biomass particles are wet and difficult to fluidize. Drying tests of three particle size fractions revealed the importance of fine particles during the fluidization of biomass. With the presence of only coarse particles, fluidized bed behaved like a fixed-bed reactor in terms of drying performance, with multiple gas channels percolating through the bed, causing partial or complete defluidization. Drying rate increased as fine particles were added. The improved flowability and mass transfer performance is likely a result from the lubrication effect brought on by the fine particles where coarse particles are made easier to adhere to each other. The increased solid concentration in bubbles and slugs also played an important role.

Drying characteristics over 30 minutes drying period were also studied. Two major mechanisms were identified during the drying of all three species of biomass, namely the constant rate drying and falling rate drying. Because of the placement of the humidity indicator, a system delay contributed to the decline in the drying curve prior to the constant rate drying section.

Different biomass species may contain different amounts of cellulose, hemicellulose and lignin, contributing to different pore size and pore distribution, subsequently changing the rate of moisture diffusion and rate of overall drying. Experiments or a brief literature review could be performed in future studies on the cellulose, hemicellulose and lignin compositions of studied biomass species, in addition to pore size distributions.

By performing drying tests under the same operating conditions for both reactor geometries, the advantage of the tapered design in terms of mass transfer and drying were revealed. However, to further improve pulsation strategy to enhance fluidization quality, a mathematical model that is able to offer a more precise depiction of the pulsed gas flow is greatly needed. Such a model is introduced in the following chapter.

CHAPTER 4

A TWO-PHASE DRYING MODEL FOR PULSED FLUIDIZED BEDS

4.1 A model for regular pulsed fluidized bed

A drying model based on two-phase theory (Geldart, 1986; Zahed et al., 1995) which links fluidized bed hydrodynamics with drying kinetics has been proposed in this study. Figure 4.1 shows that the fluidized bed consists of a bubble phase and a dense phase. Any gas in excess of the requirement for minimum fluidization passes through the bed as bubbles. The included mass transfer steps are moisture transport within biomass particles, moisture transfer from particle surface to interstitial gas and mass transfer between interstitial gas and bubbles. The overall drying performance relies on the properties of the biomass, in addition to operating conditions of the fluidized bed, for instance superficial gas velocity, bed height, number of orifices on the distributor, particle diameter and particle density.

The following assumptions are made for the bubbling fluidized bed dryer,

- (1) Particles are completely fluidized and the fluidization is operated in the bubbling regime.
- (2) Particles are spherical, isotropic, uniform in size and homogenous. Particle shrinkage is negligible. Perfect mixing is achieved; i.e. solid phase is considered as a CSTR.
- (3) Interstitial gas is stagnant, where uniform moisture concentration in the bulk of interstitial gas is assumed.
- (4) Bubble phase is in plug-flow, with the concentration of moisture changing along axial direction, and the effect of bubble coalescence on bubble distribution and bubble volume is negligible.

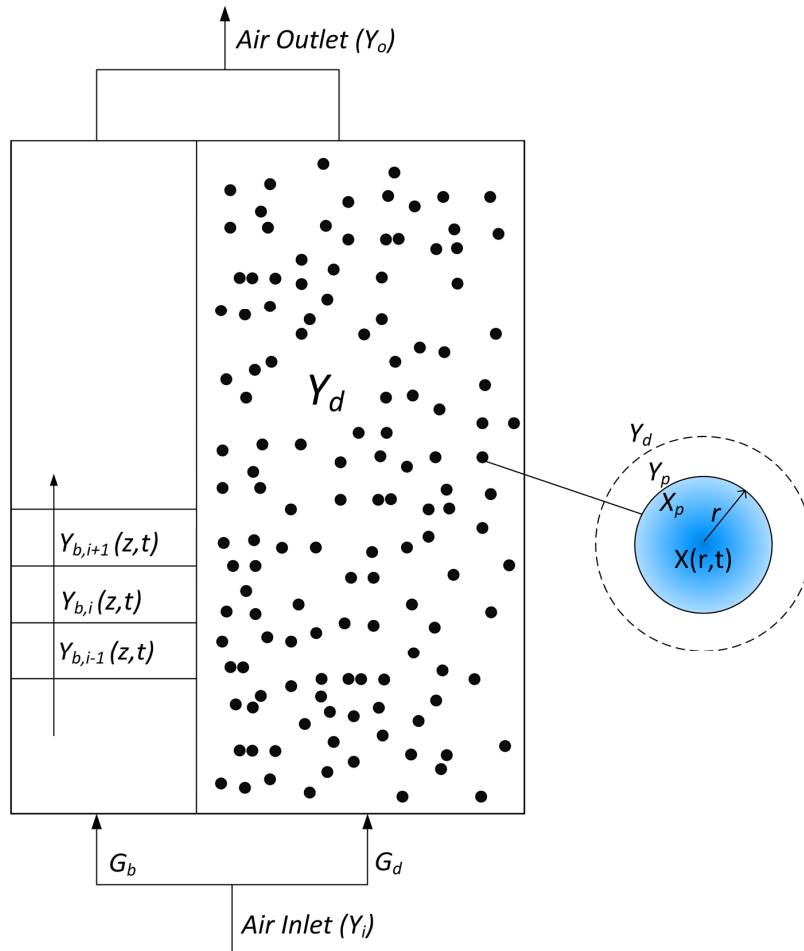


Figure 4.1 Conceptual framework of the two-phase drying model of a fluidized bed

- (5) No solids are associated with bubble phase; the effect of bubble wakes is negligible.
- (6) Radial variation in concentration within both phases is negligible.
- (7) Physical properties of the air and particles are uniform spatially and do not vary much during the course of drying. Specifically, there is no temperature gradient inside the fluidized bed, including no temperature variations within the biomass particles and no temperature difference between the gas phase and solid particles.
- (8) Drying occurs in the falling-rate period. Liquid moisture diffuses radially from the interior of the particle to the surface, evaporation takes place at the surface, and vapour enters interstitial gas by convection.

Driven by the radial concentration gradient, liquid moisture moves through the solid particle body. The particle surface is in equilibrium with surrounding air. Liquid water often needs heat to evaporate from the surface of a particle. Water vapour then enters bulk of the interstitial gas by means of convection. Bubbles generated at the distributor move up and encountered the interstitial gas, where convective mass transfer takes place. Since the bubble phase is considered being in plug-flow, water vapour concentration changes along the height of bed as bubbles ascend.

4.1.1 Solid particles

The falling-rate period is of interest in this study. As drying progresses, dry spots appear on particle surfaces, which will reduce the overall rate of drying. Many studies can be found in the literature that addressed the moisture distribution and moisture movement inside porous media, such as diffusion theory, capillary theory and moving boundary theory. However, diffusion theory is commonly used and investigated. Proposed by Sherwood (1929) and Newman (1931), it is assumed that liquid moisture moves through the solid body as a result of concentration gradient. By applying Fick's second law of diffusion to a single particle, the rate of moisture movement inside a drying solid particle is obtained. In spherical coordinates Fick's law is written as,

$$\frac{\partial X(r,t)}{\partial t} = D_{eff} \left(\frac{\partial^2 X}{\partial r^2} + \frac{2}{r} \frac{\partial X}{\partial r} \right) \quad (4.1)$$

The internal moisture distribution of a biomass particle is a function of radial position r (m) and time t (s), which is denoted by $X(r, t)$. Many different mechanisms may take place during drying of porous media. Besides pure diffusion, there are also surface diffusion, capillary flow and Knudsen diffusion. Diffusivity in this model incorporates the influence of aforementioned processes. In the drying of food and agricultural products, it is often expressed by a single parameter that is effective diffusivity,

D_{eff} (m²/s). The average moisture content of a biomass particle as a function of time $\bar{X}(t)$ is obtained by integration,

$$\bar{X}(t) = \frac{4\pi}{V_p} \int_0^{R_p} r^2 X(r,t) \cdot dr \quad (4.2)$$

In a perfectly mixed reactor with uniform particles, the average moisture content of a single particle $\bar{X}(t)$ is also the average moisture content of the solid phase. Define ω (kg/(m³·s)) as the evaporation rate of water from the particles per unit volume of the bed, moisture lost from biomass particles is as follows,

$$-\rho_p(1 - \varepsilon_{mf})(1 - \varepsilon_b) \frac{d\bar{X}}{dt} = \omega \quad (4.3)$$

To solve the partial differential equation shown in Eqn. (4.1), initial and boundary conditions are also needed. At time zero, it is assumed that biomass particles have a uniform moisture content of X_0 ,

$$\text{I.C.} \quad t = 0, \quad 0 \leq r \leq R_p, \quad X = \bar{X} = X_0 \quad (4.4)$$

At the core of a particle there is no flux, which translates to,

$$\text{B.C.1} \quad t > 0, \quad r = 0, \quad \frac{\partial X}{\partial r} = 0 \quad (4.5)$$

Particle surface is assumed to be in equilibrium with air surrounding it. In addition, a convective mass transfer of water vapour from particle surface to the bulk of interstitial gas also takes place, which gives,

$$\text{B.C.2} \quad t > 0, \quad r = R_p, \quad -D_{eff} \frac{\partial X}{\partial r} = K_i (Y_p - Y_d) \quad (4.6)$$

In which Y_d is the absolute humidity of interstitial gas in the dense phase, Y_p represents the absolute humidity of the air at particle surface, and K_i (m/s) is the mass transfer coefficient between the interstitial gas and particle surface.

4.1.2 Interstitial gas

Since interstitial gas is considered stagnant, the axial variation of the moisture content becomes negligible. The mass balance of water vapour for interstitial gas is,

$$\frac{6K_c \rho_g \varepsilon_b}{d_b} (Y_b - Y_d) - \rho_g G_d (Y_d - Y_i) + \omega = \rho_g \varepsilon_{mf} (1 - \varepsilon_b) \frac{dY_d}{dt} \quad (4.7)$$

here Y_i stands for the absolute humidity of the inlet air. For steady state operations Eqn. (4.7) is simplified to,

$$\frac{6K_c \rho_g \varepsilon_b}{d_b} (Y_b - Y_d) + \omega = \rho_g G_d (Y_d - Y_i) \quad (4.8)$$

The following formula by Sit and Grace (1981) provides interphase mass transfer coefficient K_c (m/s),

$$K_c = \frac{U_{mf}}{3} + \left(\frac{4D_v \varepsilon_{mf} U_b}{\pi d_b} \right)^{0.25} \quad (4.9)$$

4.1.3 Bubble phase

Plug-flow is assumed for the bubble phase, where mass transfer takes place between rising bubbles and interstitial gas. Consequently, not only Y_b is a function of time t , but also height above the gas distributor z (m). The mass balance of water vapour in bubble phase has the form of,

$$\rho_g \varepsilon_b \frac{\partial Y_b}{\partial t} + \rho_g \varepsilon_b \frac{\partial}{\partial z} (Y_b U_b) + \rho_g G_b (Y_b - Y_i) = \frac{6K_c \varepsilon_b}{d_p} (Y_d - Y_b) \quad (4.10)$$

where bubble rise velocity is denoted as U_b (m/s), a parameter related to bubble diameter d_b (m). To calculate bubble size at a given bed height z in a fluidized bed with multi-orifice distributor, the following semi-empirical correlation proposed by Mori and Wen (1975) can be used,

$$d_b = d_{bm} - (d_{bm} - d_{b0}) \exp(-0.3z / D_t) \quad (4.11)$$

$$d_{bm} = 1.64 \left[A(U - U_{mf}) \right]^{0.4} \quad (4.12)$$

$$d_{b0} = \frac{1.38}{g^{0.2}} \left[\frac{A(U - U_{mf})}{N_{or}} \right]^{0.4} \quad (4.13)$$

in which A (m²) stands for the cross-sectional area of the fluidized bed column. The bubble rise velocity is calculated according to Grace (1982),

$$U_b = 0.71 \sqrt{g d_b} + (U - U_{mf}) \quad (4.14)$$

It is noteworthy that above equations were derived for Geldart B particles with regular shape. Switchgrass particles used in this study belong to Group B particles; pine and Douglas fir, on the other hand, are on the border of B/D classification. Attention should be paid when applying such equations to biomass as size, density and sphericity may change significantly among species. Moreover, because of the oscillatory nature of the gas flow, superficial gas velocity U in above equations are replaced by the average gas velocity \bar{U} for the model calculation. The dynamic behaviour of the bed over each cycle of gas pulsation is not considered, but could be done in a refined model by allowing gas velocity variations with time in each pulsation cycle in the future.

4.1.4 Parameter evaluation

The evaporation rate of water ω is directly associated with conditions on particle surfaces. Define $A' = 6(1 - \varepsilon_{mf})/d_p$ as the interfacial area of particles per unit volume of the dense phase (m^2/m^3), the following could be written,

$$\frac{\omega}{1 - \varepsilon_b} = \rho_p A' K_i (Y_p - Y_d) \quad (4.15)$$

Eqn. (4.15) is then incorporated into Eqns. (4.7) and (4.8) to replace the evaporation rate ω . The particle surface is assumed to be in equilibrium with the surrounding air. The particle surface mass transfer coefficient K_i is given by Ranz (1952),

$$K_i = \frac{D_v}{d_p y} (2 + 1.8 \text{Re}_{mf}^{0.5} \text{Sc}^{0.33}) \quad (4.16)$$

Since interstitial gas is considered stagnant, the second term in the above equation is neglected. Absolute humidity of the drying air could be calculated in the same manner as specified in Eqn. (2.6). For woody biomass, the empirical correlation between equilibrium moisture content of Douglas fir X_e and relative humidity of the air RH is given by (Forest Products Laboratory, 2010),

$$RH = -4.428X_e + 0.0465 \quad (4.17)$$

4.1.5 Method of solution

Analytical solutions of many diffusion problems could be found in Crank (1979). Fick's law specified in this study is in the form of a parabolic partial differential equation (PDE) with a second-type boundary condition, by which the moisture content distribution inside biomass particles is a function of radial position (r) and time (t). This may have also resulted in a great deal of variation on

the moisture content within the particle and will affect the drying rate. Coupled with the mass balance of water vapour in the interstitial gas and bubble phase, it may be difficult to obtain an analytical solution. As a result, finite element method was chosen to solve the PDEs numerically. The PDEs were first discretized. Both the interstitial gas and bubble phase were divided into a finite number of control volumes such that the axial change in gas properties (e.g. moisture concentration) could be considered. The solid phase was also divided into a number of control volumes to take the variation of moisture inside the particles into consideration. Initial guess values were assumed for all the dependent variables in the equations as the first step towards solution. It was followed by the GMRES (generalized minimum residual) iterative method (Saad & Schultz, 1986) to solve the PDEs simultaneously. Calculations were first conducted on the first control volume, iterations continued until a solution was converged at a given error tolerance. After the convergence, moisture distributions of the solid as well as other parameters for the gas phase (e.g. moisture contents of the bubble phase and interstitial gas, bubble size and bubble rise velocity) inside the first control volume could be determined. Consequently, calculations were performed on the following control volume until all necessary properties were calculated for the condition of this control volume. The same procedure was carried out until conditions of the last control volume were met.

In this model, drying relies solely on properties of biomass and operating condition of the fluidized bed, given an effective diffusivity value drying rate can be predicted. However, data on effective diffusivity of studied biomass species are scarce in the literature. D_{eff} values of similar biomass species on the other hand, have been reported. It should be noted that besides age and species of the biomass, effective diffusivity might also vary with particle size and shape, geographical location. Chen et al. (2013) tested the effective diffusivity of fir particles of 0.125–0.3 mm in size via a thermogravimetric analyzer under isothermal conditions at five temperatures (50, 60, 70, 80 and 90 °C), and reported an Arrhenius-type correlation between D_{eff} and temperature. At 50 °C, the effective diffusivity was calculated to be $6.22 \times 10^{-9} \text{ m}^2/\text{s}$. Similar drying tests were also performed on

poplar sawdust of 0.125–0.30 mm at 60–90 °C, and the effective diffusivity ranged from 9.38×10^{-10} m²/s at 60 °C to 1.38×10^{-9} m²/s at 90 °C (Chen et al., 2012). Drying rate investigation of 2 inch thick Douglas fir lumber at 71.1 °C by Resch et al. (1989) revealed that the effective diffusivity varied with moisture content, from 6.94×10^{-10} m²/s to 4.44×10^{-9} m²/s.

Experimental results from the batch drying tests were fitted to the above model so that effective diffusivity could be obtained. The best fit was chosen by minimizing the sum of squared residuals (the difference between an experimental value and the fitted value provided by the model) via bound optimization by quadratic approximation (BOBYQA) method (Powell, 2009), where an iteratively constructed quadratic approximation of the objective function that was valid in a region around the current iterate was implemented. A complete set of data is presented in Appendix A5.

4.1.6 Effect of flow rate

Batch drying tests were performed at various average superficial gas velocities (\bar{U}), ranging from $1.1U_{mf}$ to $1.4U_{mf}$, and the experimental data were fitted to the two-phase drying model to obtain the effective diffusivity. Since the model only applies to the falling rate period, the model was fitted to the data within the falling-rate period, with the initial moisture content of biomass samples kept below 35% (dry basis). Both the experimental and model-fitted drying curves for $\bar{U}=1.1U_{mf}$ and $1.4U_{mf}$ are plotted in Figure 4.2, with key parameters listed in Table 4.1. The model fitted drying curve appears to be in good agreement with its respectful experimental result, with the coefficient of determination (R^2) greater than 0.99. The flow rate exerted a direct impact on drying. As the superficial gas velocity increased from $1.1U_{mf}$ to $1.4U_{mf}$, the total amount of water removed from the solids increased by 13.4%. More vigorous gas–solid contact was observed at higher gas flow rates, alongside with greater amplitude of pressure fluctuations across the bed, which enhanced

the interphase mass transfer. Excess gas in the bubble phase increased the throughput, which enabled more moisture to be removed.

Table 4.1 Data fitting results and statistical parameters for the Douglas fir drying curves obtained at different flow rates

Average Superficial Gas Velocity (\bar{U}/U_{mf})	Effective Diffusivity (m^2/s)	Coefficient of Determination (R^2)	Amount of Water Removed
1.1	5.18×10^{-9}	0.996	71.8%
1.2	5.00×10^{-9}	0.996	75.2%
1.4	5.17×10^{-9}	0.994	85.2%

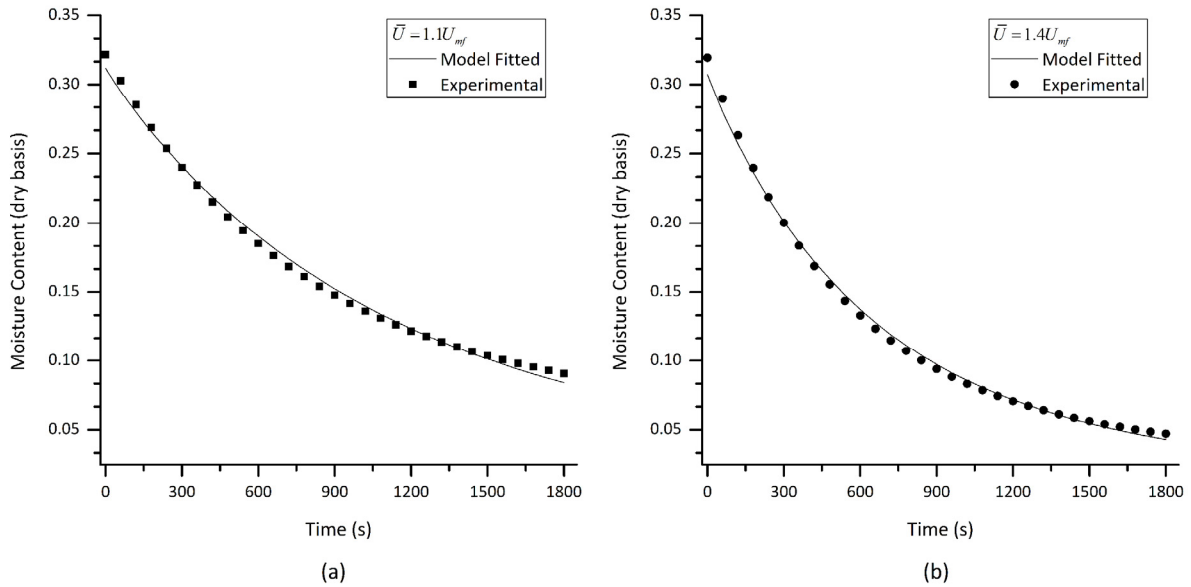


Figure 4.2 Experimental and model-fitted drying curves of Douglas fir at various flow rates. (a) $\bar{U}/U_{mf}=1.1$, $f=1.0$ Hz; (b) $\bar{U}/U_{mf}=1.4$, $f=1.0$ Hz.

The effective diffusivity remained relatively the same for all flow rates, in the vicinity of $5 \times 10^{-9} m^2/s$, which is expected because diffusivity of water in solid particles is often only a function of temperature (Ramesh, 2003; Thorpe et al., 1991). Furthermore, the calculated D_{eff} values are of the same order of magnitude as those reported in the literature (Chen et al., 2012; Chen et al., 2013; Resch et al., 1989), indicating the current two-phase model is adequate for predicting the drying

performance and mass transfer in pulsed fluidized beds. Moreover, the effective diffusivities obtained from the model are in the order of $10^{-9} \text{ m}^2/\text{s}$, which are much closer to the mass diffusivity of liquid water than vapor (e.g. the mass diffusivity between liquid water and acetone is $1.16 \times 10^{-9} \text{ m}^2/\text{s}$, whereas the mass diffusivity between water vapor and air is $0.282 \times 10^{-5} \text{ m}^2/\text{s}$), which supports the assumption of the two-phase drying model that water travels in the biomass particles in liquid form.

4.1.7 Effect of pulsation frequency

The presence of gas pulsation is essential to the fluidization of biomass, especially in the absence of inert bed particles. Pulsation also influences flow pattern, heat and mass transfer, as the oscillatory nature of the pressure and velocity stems from the duration of "ON" and "OFF" period in each pulsation cycle. Four pulsation frequencies were selected for this study, from 0.75 to 6.0 Hz. By increasing pulsation frequency, the system transitioned from periodically and intermittently fluidized at 0.75 and 1.5 Hz to seemingly continuous fluidization at 3.0 and 6.0 Hz. The experimental drying curves are plotted against the model-predicted ones in Figure 4.3, with obtained D_{eff} and R^2 values summarized in Table 4.2. It appears that 1.5 Hz exhibited the fastest drying among all pulsation frequencies, with 0.75 Hz being a close second.

It is noteworthy that in the proposed two-phase drying model, with the same average superficial gas velocity \bar{U} , the hydrodynamics of the pulsed fluidized bed remains the same under different pulsation frequencies, which resulted from the fact that the oscillatory velocity profile in each pulsation cycle is not considered. Therefore, the difference in gas–solid contact and heat/mass transfer at various pulsation frequencies are directly reflected by effective diffusivity.

Above results confirmed that drying performance is deeply associated with the hydrodynamics. Even when the average flow rate was kept the same at $1.1U_{mf}$, the behaviour of the fluidized bed

was found to be significantly different at different pulsation frequencies. This is mainly attributed to the oscillating velocity and pressure of the pulsed fluidized bed. Within each pulsation cycle gas velocity fluctuates in a seemingly sinusoidal fashion, such that the superficial gas velocity periodically fluctuates around the average value \bar{U} . Under the same average flow rate, a lower pulsation frequency will give rise to a stronger pulsation, which is evident in the greater amplitude of velocity and pressure oscillations compared to that at a higher pulsation frequency. Increasing gas velocity will also result in faster interphase mass transfer. Despite that a higher pulsation frequency normally leads to reduced intermittence between each pulsation cycle as well as longer residence time for gas bubbles, the maximum gas velocity in each cycle decreases, which weakens the pulse and its ability to penetrate the bed of cohesive particles. Eventually channeling and other forms of gas bypassing will occur and the drying rate dwindles.

Interestingly effective diffusivity obtained at a constant pulsation frequency but different gas flow rates remained close to each other, but the D_{eff} values obtained at a constant gas flow rate but different pulsation frequencies were quite different from each other. The former might be attributed to the fact the two-phase hydrodynamic model has properly captured the effect of gas velocity on the flow behaviour of the biomass fluidized bed, but the effect of pulsation frequency on bed hydrodynamics, such as bubble size and bubble rise velocity, has not been captured. Because the non-linear nature between flow rate U and K_c , K_c calculated from an average flow rate differs greatly from the average K_c value calculated from oscillating velocity profiles.

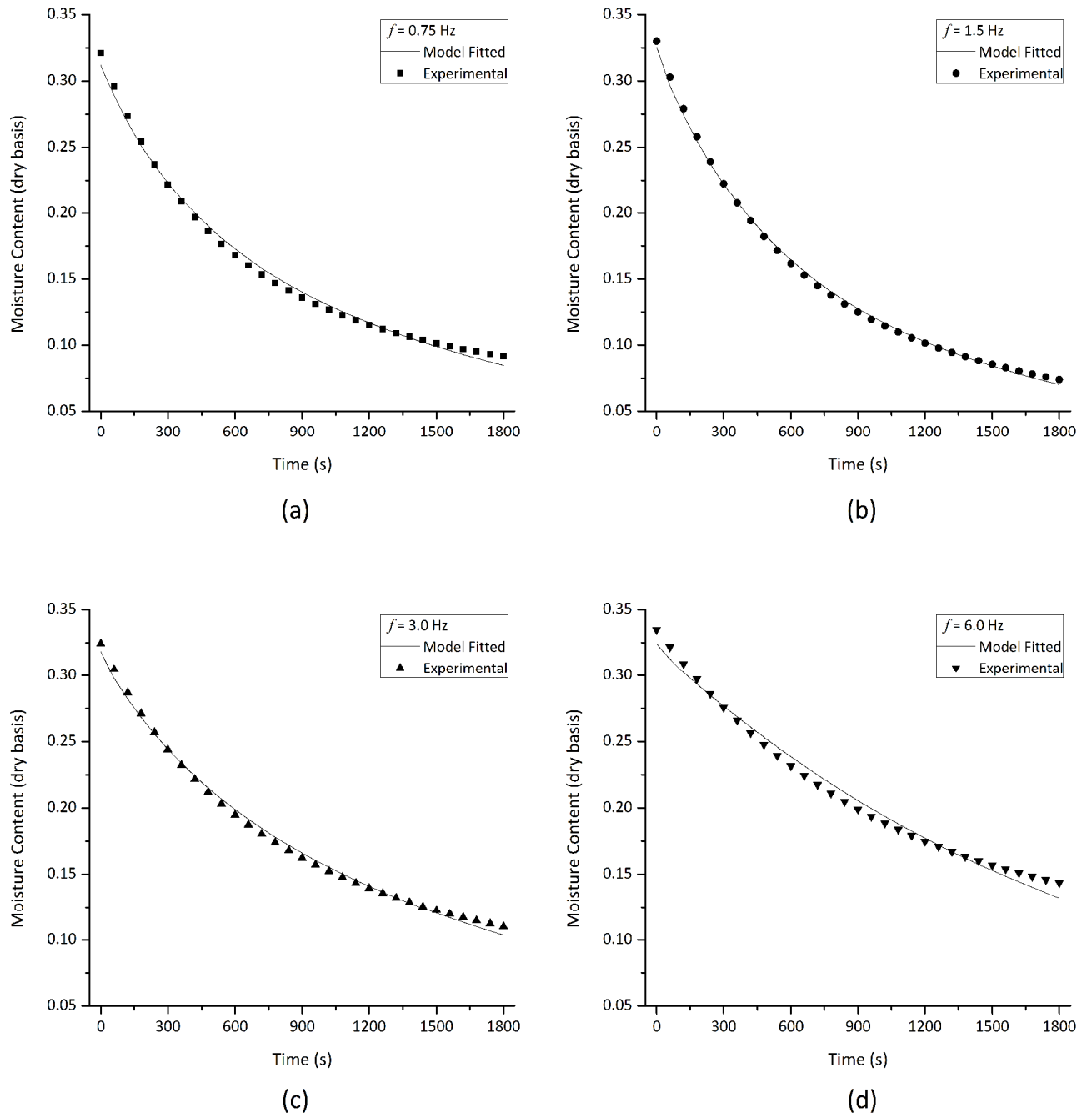


Figure 4.3 Experimental and model-fitted drying curves at different pulsation frequencies. (a) $\bar{U}/U_{mf}=1.1$, $f=0.75$ Hz; (b) $\bar{U}/U_{mf}=1.1$, $f=1.5$ Hz; (c) $\bar{U}/U_{mf}=1.1$, $f=3.0$ Hz; (d) $\bar{U}/U_{mf}=1.1$, $f=6.0$ Hz.

From above graph, it is fairly straightforward that a frequency such as 1.5 Hz offers gas pulsations sufficiently intense to penetrate the entire bed and to overcome cohesive forces while maintaining relatively frequent gas delivery and renewal. Moreover, pulsation frequency in this range is also closer to the natural frequency of the system, around which particle motion and mass transfer are enhanced because of the resonance effect (Hao & Bi, 2005). The prolonged "OFF" period affected drying at 0.75 Hz, while undesired behaviour such as channeling and partial defluidization undermined drying at 3.0 and 6.0 Hz. As shown in Table 4.2, compared to 6.0 Hz, an additional 20.5% of water was removed at the end of 30 min drying for 1.5 Hz.

Table 4.2 Summary of key parameters at various pulsation frequencies

Pulsation Frequency (Hz)	Effective Diffusivity (m²/s)	Coefficient of Determination (R²)	Amount of Water Removed
0.75	3.30×10 ⁻⁹	0.996	71.5%
1.5	4.43×10 ⁻⁹	0.999	77.6%
3.0	3.10×10 ⁻⁹	0.998	66.1%
6.0	2.24×10 ⁻⁹	0.996	57.1%

Unlike drying tests carried out under the same pulsation frequency, effective diffusivities calculated from different flow rates were far more spread out in this case. They also shared the same trend with the drying performance. It is clear that the greater variations of effective diffusivity stemmed from the simplifications made in the two-phase model where an average gas velocity was used instead of an oscillatory velocity profile, with bubble phase and dense phase behaviour only depending on the average flow rate (\bar{U}). The model therefore could not differentiate between various pulsation frequencies operated under the same average gas flow rate. Therefore, the magnitude of D_{eff} can be seen as a benchmark for hydrodynamic performance at different pulsation frequencies.

4.1.8 Effect of biomass species

Drying curves of pine, Douglas fir and switchgrass are depicted in Figure 4.4 (a). Experimental values were fitted to the two-phase drying model, as shown in Figure 4.4(b), Figure 4.4 (c) and Figure 4.4 (d), with the fitted model parameters summarized in Table 4.3. As can be seen from Figure 4.4(a), pine exhibited faster drying where the moisture content was reduced close to equilibrium moisture content at $t=1800$ s, while it took Douglas fir and switchgrass slightly longer. The two-phase model was able to predict the drying performance with sufficient accuracy, R^2 values above 0.99 for all three cases. The model-fitted effective diffusivities of Douglas fir and pine were $3.76 \times 10^{-9} \text{ m}^2/\text{s}$ and $4.93 \times 10^{-9} \text{ m}^2/\text{s}$, respectively. The similarity in D_{eff} did not come across as a surprise since pine and Douglas fir sawdust used in this experiment came from the same sawmill, with similar physical properties including bulk density, particle shape, particle size distribution and mean particle size. The slightly better drying performance and greater D_{eff} of pine may have stemmed from the difference in pore structure. Research has shown that besides molecular diffusion, drying in porous media is often accompanied by Knudsen diffusion of water vapour, which could take place in the capillary pores of the ligno-cellulosic biomass particles (Welty et al., 2009). It is probable that pine particles had slightly larger pores that promoted Knudsen diffusion and the internal moisture transport, although further verification is needed.

Table 4.3 Parameters for the drying curves obtained for various biomass materials

Biomass Species	Effective Diffusivity (m^2/s)	Coefficient of Determination (R^2)	Amount of Water Removed
Fir	3.76×10^{-9}	0.999	71.0%
Pine	4.93×10^{-9}	0.999	77.5%
Switchgrass	1.54×10^{-9}	0.999	70.8%

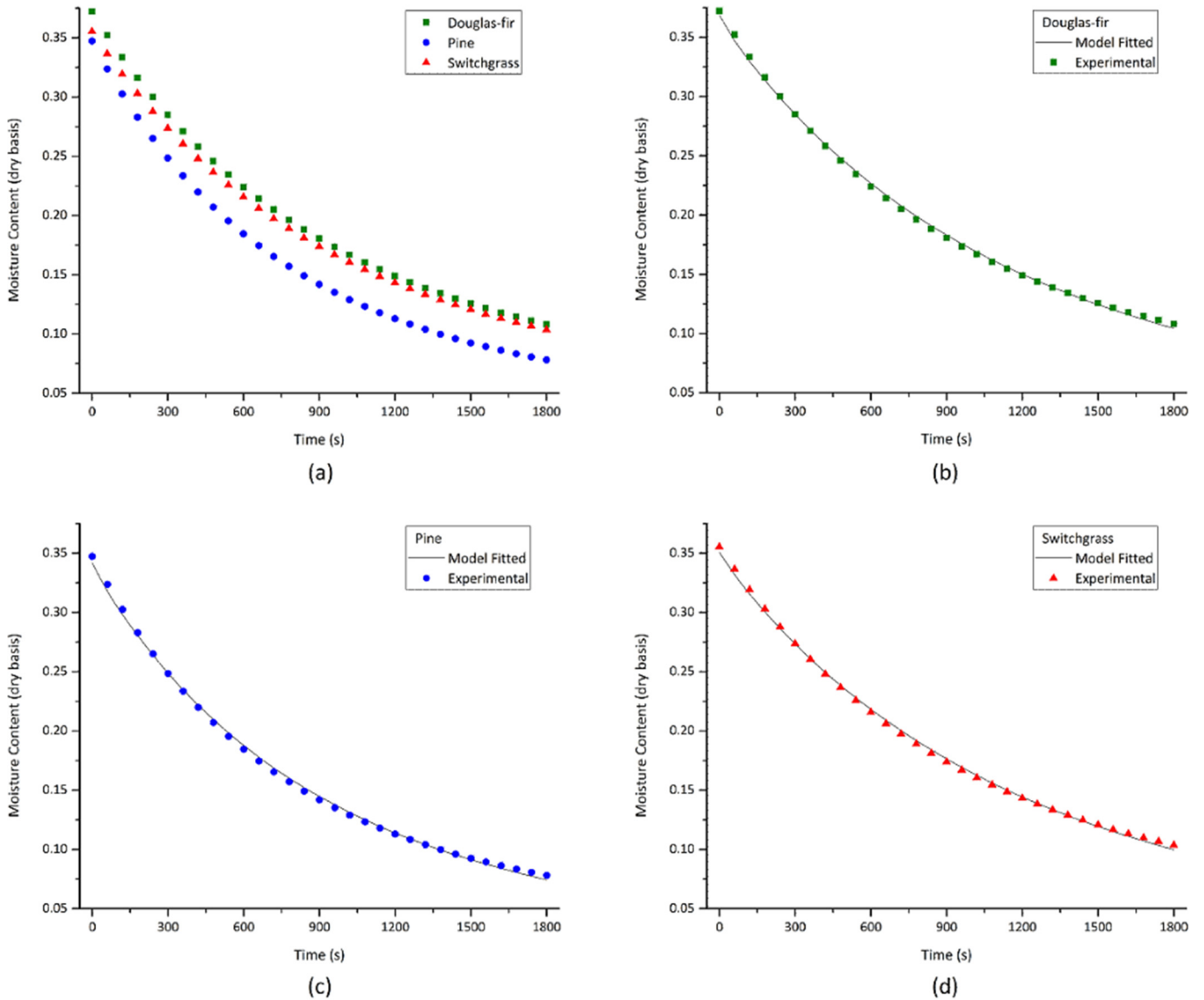


Figure 4.4 Comparison of experimentally obtained drying curves and the corresponding model-fitted ones, $\bar{U}/U_{mf}=1.2$, $f=1.0$ Hz. (a) Experimental drying curves of all three biomass species; (b) Douglas fir; (c) Pine; (d) Switchgrass.

Compared to pine and fir, the mean particle diameter of switchgrass was almost halved, which in theory should reduce the diffusion resistance because of the relatively shorter travel from the centre to the surface (Cho et al., 2005). Moreover, Yang et al. (2015) measured the pore size distribution of mixed-hardwood and switchgrass and revealed that size reduction could increase the volume of

pores to a certain degree. Switchgrass had larger pores compared to mixed-hardwood, which could accelerate Knudsen diffusion. However, no significant improvement regarding drying performance was observed for switchgrass, as it was almost the same as Douglas fir. There is a strong possibility that mass transfer was hindered by the cohesive nature of switchgrass particles originated from the highly irregular shapes. A large portion of needle-like particles was clearly visible, which were prone to induce channeling and partial defluidization, especially in the beginning of the batch drying process. Consequently, drying suffered from the poor gas–solid contact. Despite its higher rate of Knudsen diffusion, the effective diffusivity of switchgrass was relatively low.

4.1.9 Effect of drying temperature

Results of drying experiments carried out at different temperatures for Douglas fir are illustrated in Figure 4.5. It seems that drying temperature has considerable impact on drying. By raising drying temperature from 20 to 50 °C, the total amount of water removed after 30 min of drying increased from 44.5% to 92.1%. The amount of time required to bring moisture content down to 16% (dry basis) for 20, 30, 40 and 50 °C were 1585, 713, 594 and 472 s, respectively. Seen from Table 4.4, effective diffusivities also increased significantly with increasing temperature, ranging from $2.24 \times 10^{-9} \text{ m}^2/\text{s}$ at 20 °C to $6.05 \times 10^{-9} \text{ m}^2/\text{s}$ at 50 °C, which are of the same order of magnitude as values reported in the literature for similar agricultural products (Baroni & Hubinger, 1998; Reyes et al., 2008b; Tasirin et al., 2014).

For diffusion in solids, a number of theories have been proposed, including vacancy mechanism, ring mechanism and interstitialcy mechanism. When water molecules move through solids they have to surmount energy barriers, which is often represented by activation energy. The relationship between activation energy and diffusivity can be described by the Arrhenius equation,

$$D_{eff} = D_0 \exp\left(-\frac{E_a}{RT}\right) \quad (4.18)$$

where D_0 is the maximum diffusion coefficient, E_a is the activation energy.

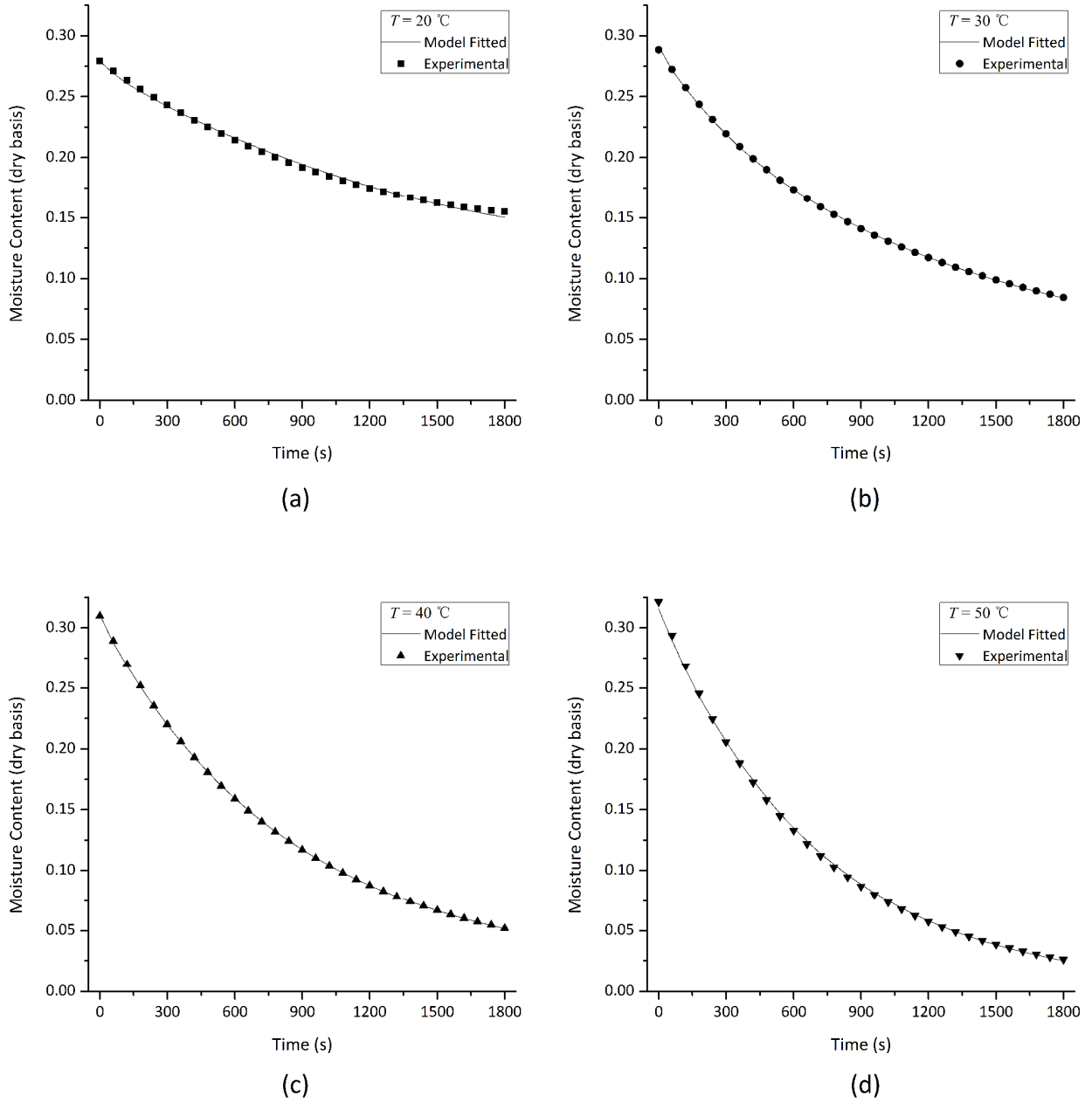


Figure 4.5 Experimental and model-fitted drying curves at various drying temperatures. (a) $T=20^\circ\text{C}$, $f=1.0\text{ Hz}$, $\bar{U}/U_{mf}=1.1$; (b) $T=30^\circ\text{C}$, $f=1.0\text{ Hz}$, $\bar{U}/U_{mf}=1.1$; (c) $T=40^\circ\text{C}$, $f=1.0\text{ Hz}$, $\bar{U}/U_{mf}=1.1$; (d) $T=50^\circ\text{C}$, $f=1.0\text{ Hz}$, $\bar{U}/U_{mf}=1.1$; R^2 values included in Table 4.4.

More water molecules will possess sufficient energy to overcome the energy barrier at higher temperatures, leading to faster diffusion and greater diffusion coefficient. Temperature also has a positive effect on Knudson diffusion as well as the evaporation of water from the particle surface, with both being beneficial for drying.

Effective diffusivity is plotted against drying temperature, as shown in Figure 4.6. In addition, an Arrhenius-type correlation was also obtained through non-linear curve fitting, which is plotted in logarithmic scale and illustrated in Figure 4.6,

$$D_{eff} = 4.3312 \times 10^{-4} \exp\left(-\frac{30101}{RT}\right) \quad (4.19)$$

D_0 and E_a values derived from experimental results are in good agreement with reported values in the literature (Chen et al., 2013; Ramesh, 2003; Thorpe et al., 1991).

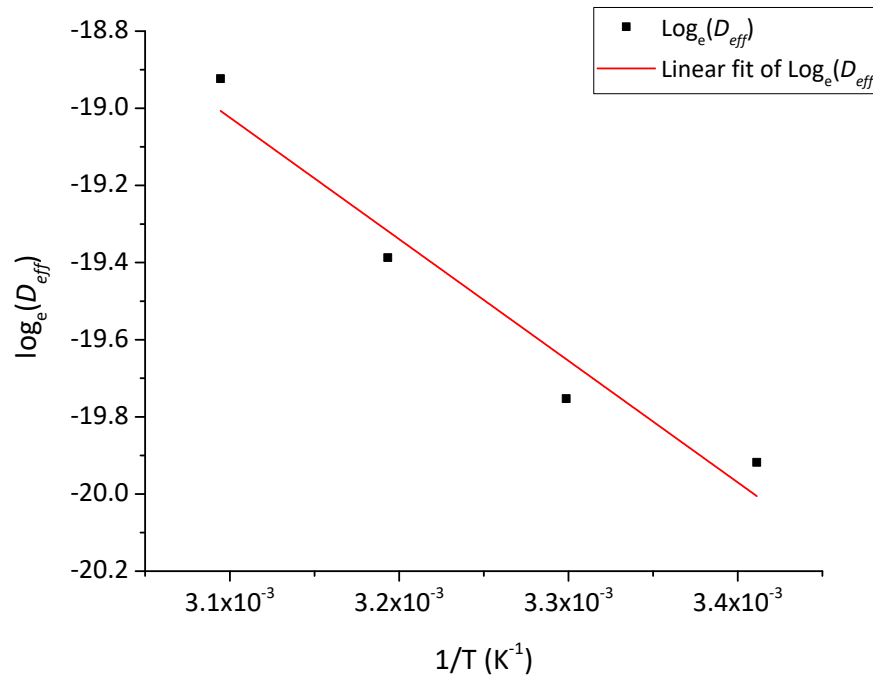


Figure 4.6 Effective diffusivity for the drying of Douglas fir sawdust in the pulsed fluidized bed dryer as a function of drying temperature

Table 4.4 Parameters for the drying curves obtained at various drying temperatures

Temperature (°C)	Effective Diffusivity (m ² /s)	Coefficient of Determination (R ²)	Amount of Water Removed
20	2.24×10 ⁻⁹	0.99916	44.5%
30	2.64×10 ⁻⁹	0.99987	70.7%
40	3.80×10 ⁻⁹	0.99995	83.2%
50	6.05×10 ⁻⁹	0.99952	92.1%

4.2 A model for tapered fluidized bed

4.2.1 Model basics

Because of the similarities between the rectangular and tapered fluidized beds, many aspects of the drying model developed for the rectangular bed also apply to the tapered geometry, where Eqns. (4.1) to (4.17) still stand. The key difference is that in the tapered fluidized bed, the cross-section area of the bed changes with bed height (z), which is demonstrated in Figure 4.7. Consequently, both bubble size and bubble rise velocity become a function of z . Similar to the rectangular bed, semi-empirical correlation of Mori and Wen (1975) was also used to calculate the bubble size at a given height z . To take the effect of height into consideration, the superficial gas velocity in the tapered section has to be written as a function of bed height,

$$U_z = \frac{1.97}{4.627z + 1} \cdot U \quad (4.20)$$

here U is the superficial gas velocity based on the cross-section area non-tapered section of the bed (A), and U_z is the superficial gas velocity at a given bed height z . It is noteworthy that height within the bed during the experiments never exceeded the tapered section, as a result above equation is able to cover the entire domain. Bubble size and bubble rise velocity are calculated accordingly,

$$d_{bm} = 1.64 \left[A(U_z - U_{mf}) \right]^{0.4} \quad (4.21)$$

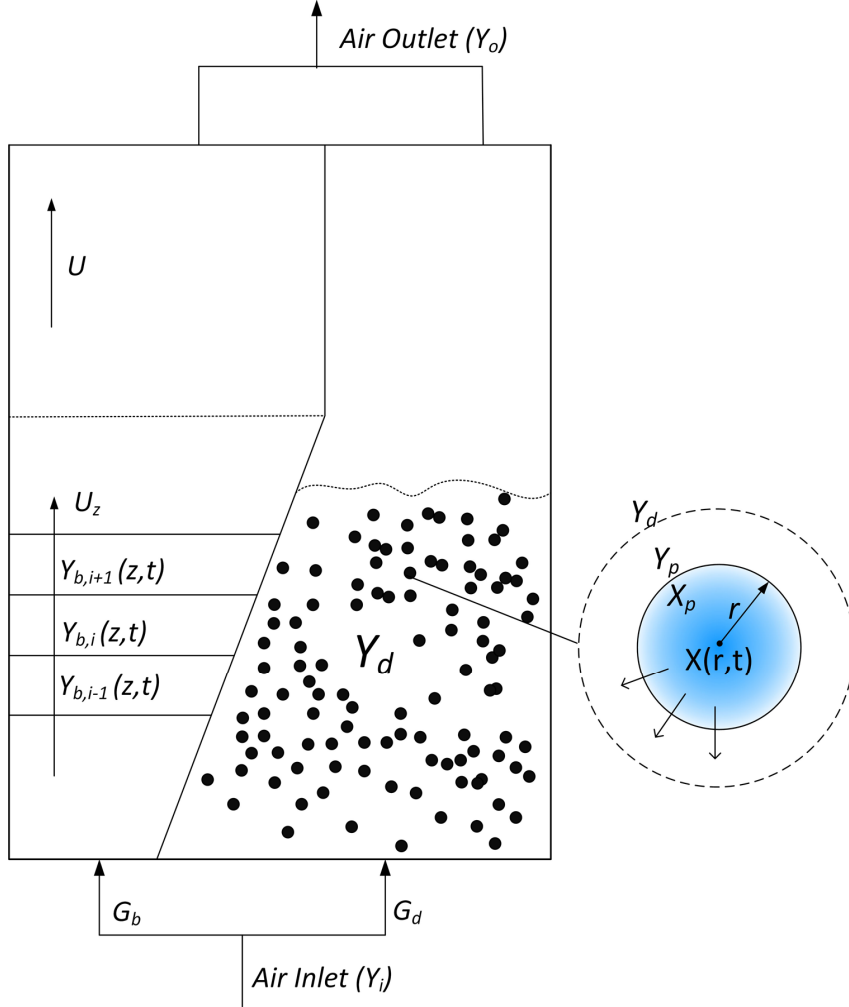


Figure 4.7 Schematics of the two-phase drying model in pulsed fluidized bed with tapered bottom section

$$d_b = d_{bm} - (d_{bm} - d_{b0}) \exp(-0.3z / D_t) \quad (4.22)$$

$$d_{b0} = \frac{1.38}{g^{0.2}} \left[\frac{A(U_z - U_{mf})}{N_{or}} \right]^{0.4} \quad (4.23)$$

The bubble rise velocity is calculated from Grace (1982),

$$U_b = 0.71 \sqrt{gd_b} + (U_z - U_{mf}) \quad (4.24)$$

By simply replacing Eqns. (4.11)–(4.14) with Eqns. (4.21)–(4.24), the two-phase drying model proposed for rectangular fluidized bed (Eqns. (4.1) to (4.17)) is applied to the tapered bed. The effects of pulsation frequency and flow rate were studied.

4.2.2 Effect of flow rate

Experimental data from drying tests at different gas velocities ($1.1U_{mf}$ – $1.4U_{mf}$) were fitted to the drying model. The effective diffusivity and the coefficient of determination between fitted and experimental data are listed in Table 4.5. Under the same pulsation frequency (1.5 Hz) and drying temperature (25 °C), predicted D_{eff} values were in close proximity to each other, averaged out at 7.405×10^{-9} m²/s, indicating the two-phase model was able to properly reflect the influence of operating conditions such as flow rate on drying. Similar values of D_{eff} at different flow rates are also consistent with the fact that diffusion is temperature dependent and should remain constant under the same drying temperature.

Table 4.5 Model-fitted effective diffusivity of Douglas fir at different gas flow rates in pulsed fluidized bed with tapered bottom section, $f=1.5$ Hz

Average Superficial Gas Velocity (\bar{U}/U_{mf})	Effective Diffusivity (m ² /s)	Coefficient of Determination (R ²)	Moisture Removed
1.1	7.320×10^{-9}	0.9888	78.3%
1.2	7.591×10^{-9}	0.9970	81.7%
1.4	7.305×10^{-9}	0.9854	90.6%

Figure 4.8 contains drying kinetics of Douglas fir sawdust at $1.1U_{mf}$ and $1.4U_{mf}$. The model-fitted drying rate curve was in good agreement with experimental data, with the fastest drying achieved

at $1.4U_{mf}$ where over 90% of moisture was removed after 30 min drying, as indicated in Table 4.5. This is likely associated with faster convective mass transfer from particle surface to the interstitial gas, as well as interfacial mass transfer between interstitial gas and bubbles at higher gas velocities.

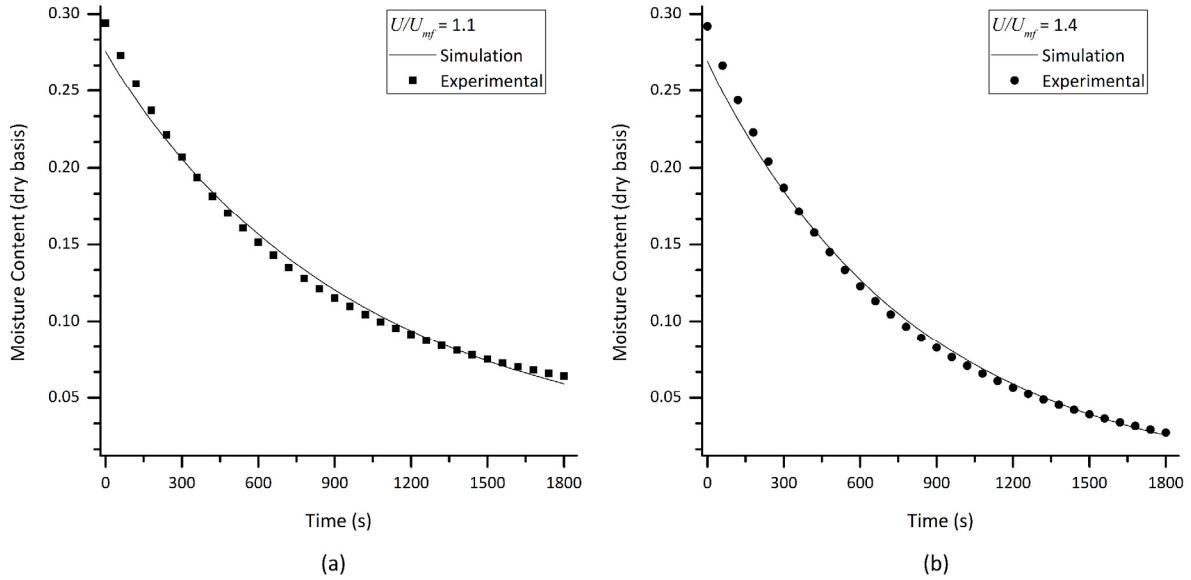


Figure 4.8 Experimental and modelled drying curves for Douglas fir sawdust in pulsed fluidized bed with a tapered bottom section at various gas flow rates. (a) $\bar{U}/U_{mf}=1.1$, $f=1.5$ Hz; (b) $\bar{U}/U_{mf}=1.4$, $f=1.5$ Hz.

4.2.3 Effect of pulsation frequency

Data on Douglas fir drying at different pulsation frequencies were also fitted to the two-phase drying model to obtain the effective diffusivity. Both the experimental and fitted drying curves are portrayed in Figure 4.9, with fitted effective diffusivity and coefficient of determination listed in Table 4.6. The calculated and literature reported D_{eff} values are of the same order of magnitude. However, unlike experiments carried out for the same pulsation frequency, but different gas flow rates, D_{eff} varied with pulsation frequency, with the maximum being $7.467 \times 10^{-9} \text{ m}^2/\text{s}$ at $f=1.5$ Hz. The effective diffusivity quickly declined as the pulsation frequency further increased beyond 1.5 Hz. The change of effective diffusivity with pulsation frequency can be attributed to the fact that

the influence of pulsation on fluidized bed hydrodynamics (e.g. bubble size and rise velocity, bed expansion) was not properly addressed in the two-phase drying model adopted in this study. Specifically, the influence of bubble size, bubble rise velocity at different pulsation frequencies with the same average flow rate on mass transfer was not taken into consideration. In the drying model, the bubble size was calculated according to the average superficial gas velocity. However, studies have shown that gas pulsation in fluidized beds has a strong influence on bubble behaviour (Hadi et al., 2011; van den Bleek & Schouten, 1993; Wang & Rhodes, 2005a).

Köksal and Vural (1998) measured the bubble size in a pulsed fluidized bed with turnip seeds at various gas flow rates and found that between $0 - 5f_N$ bubble size decreased with increasing pulsation frequency, in which f_N represents the natural frequency of the system calculated according to Hao and Bi (2005). Smaller bubble diameters at higher pulsation frequencies lead to higher interphase mass transfer (K_c) rate and longer bubble residence time, which in turn favour mass transfer and drying. Too high a pulsation frequency will unfortunately cause channeling that reduces the gas–solid contact efficiency and mass transfer. As a result, fastest drying was observed when the fluidized bed was operated around the natural frequency of the system, which not only offered ample momentum to break up the cohesive forces and avoid channeling, but also enhanced the gas–solid contact and mass transfer because of resonance effect. Effective diffusivity values obtained from the model reflected such influences on mass transfer.

Table 4.6 Model-fitted effective diffusivity at different pulsation frequencies in the pulsed fluidized bed with a tapered bottom section

Pulsation Frequency (Hz)	Effective Diffusivity (m²/s)	Coefficient of Determination (R²)	Moisture Removed
0.75	6.735×10 ⁻⁹	0.9978	77.8%
1.5	7.467×10 ⁻⁹	0.9926	82.9%
3.0	7.232×10 ⁻⁹	0.9943	71.5%
6.0	4.993×10 ⁻⁹	0.9953	63.5%

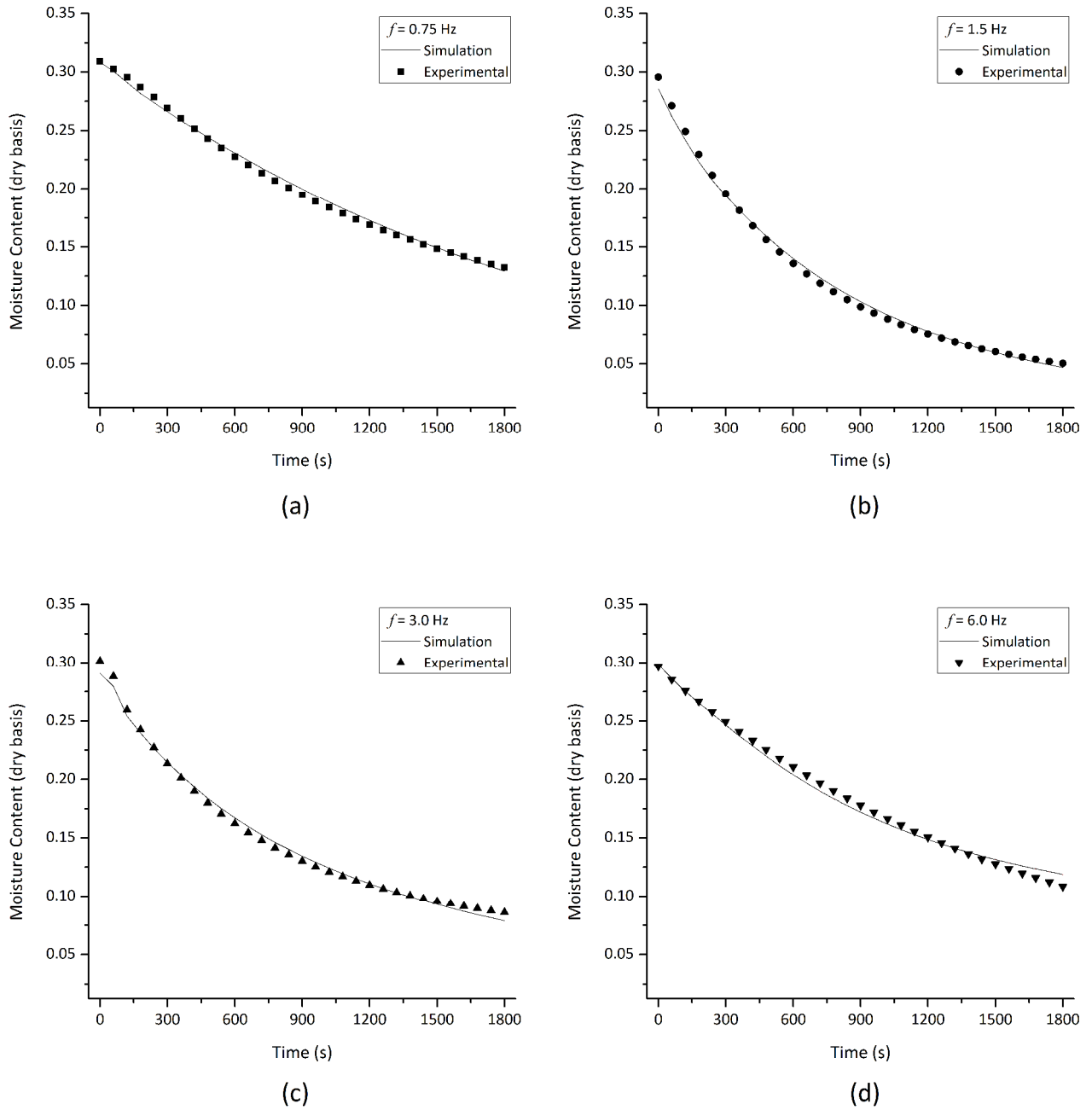


Figure 4.9 Experimental and predicted drying curves in pulsed fluidized bed with a tapered bottom section at different pulsation frequencies. (a) $\bar{U}/U_{mf}=1.1$, $f=0.75$ Hz; (b) $\bar{U}/U_{mf}=1.1$, $f=1.5$ Hz; (c) $\bar{U}/U_{mf}=1.1$, $f=3.0$ Hz; (d) $\bar{U}/U_{mf}=1.1$, $f=6.0$ Hz.

4.2.4 Comparison of two geometries

The amount of water removed from the Douglas fir sample after 30 min of drying, as well as the model-fitted effective diffusivity are plotted in Figure 4.10, for both the rectangular and tapered fluidized bed. As can be clearly seen in Figure 4.10(a), for both reactor geometries water removal efficiency increased with increasing gas flow rate. However, on average the tapered bed appears to be able to remove 5% more water when compared to the rectangular design. This is likely because of the reduced opening area of the distributor plate leading to a stronger gas pulsation that could better eliminate channeling, in addition to the improved solid circulation pattern where entrained particles were able to slowly recirculate to the bottom of the bed along the tapered column wall eliminating the dead zones. The improvement in mass transfer for the tapered design is also confirmed by the higher effective diffusivity values.

Figure 4.10(b) shows the amount of water removed at different pulsation frequencies. The resonance effect around 1.5 Hz improved the mass transfer rate, which could explain the higher water removal efficiency and effective diffusivity. As pulsation frequency moved away from 1.5 Hz, the effective diffusivity and water removal efficiency declined. As discussed in the previous section, it is highly probable that the change in effective diffusivity was caused by assuming pulsed fluidized bed operated at an average superficial gas velocity, rather than an oscillatory velocity profile. By doing so the effect of gas pulsation on bubble size, bubble rise velocity and bed expansion could no longer be reflected. Consequently, such effects were lumped into the effective diffusivity values. A higher D_{eff} indicates better gas–solid contact and mass transfer, which in essence is an indicator of hydrodynamics performance. The effective diffusivity and water removal efficiency in the tapered bed were 51% and 8% higher than rectangular bed, under identical operating conditions. This result confirms that tapered bed is preferred for biomass fluidization.

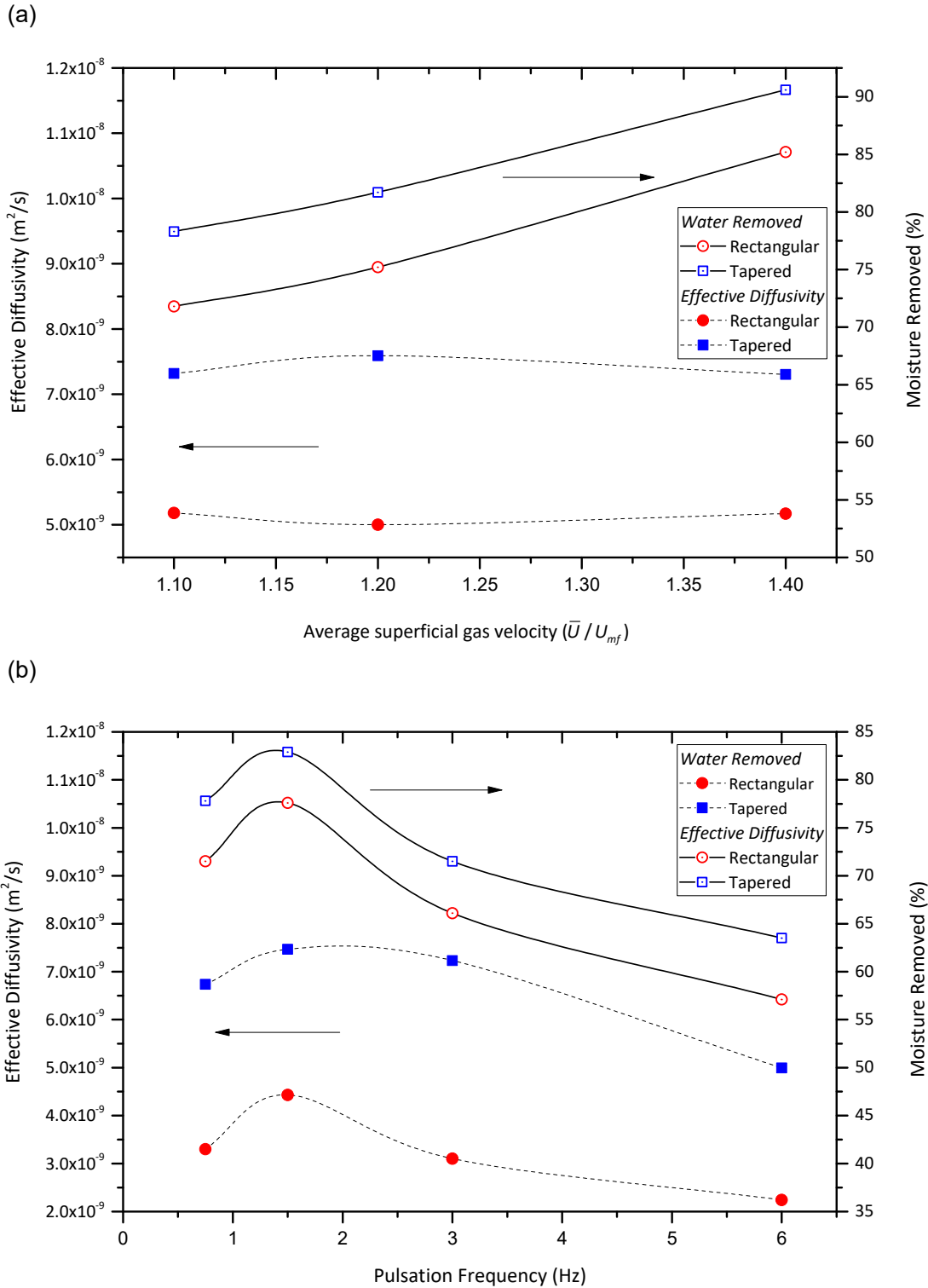


Figure 4.10 Effective diffusivity and amount of water removed in two reactor geometries as a function of (a) average superficial gas velocity and (b) pulsation frequency, plot consisted of experimental data points with splice interpolation lines

4.2.5 Conclusion

A fluidized bed two-phase drying model was proposed, in which key operating parameters of fluidized beds were taken into consideration. Unlike many models that merely focused on the internal mass transport of a biomass particle, the convective mass transfer on particle surfaces and the interphase mass transfer between interstitial gas and bubbles have also been included in this model. Changes were also made so that the model could be applied to the tapered bed as well. Effective diffusivity values were obtained from fitting experimental data, which showed a good agreement with the reported values, and may be used as an indicator for reactor performance. Both flow rate and frequency had a positive effect on drying, while pulsation was found to be most efficient when the frequency was set close to the natural frequency of the system. Fluidized bed with pulsed gas flow has proven to be effective for biomass processing without the need of inert bed materials. The advantage of tapered fluidized bed is manifested through greater effective diffusivities and higher water removal ratios. Future studies should focus on enhancing the gas–solid contact, reducing channeling and dead zones in the fluidized bed, so that the mass transfer efficiency could be further improved.

It is noteworthy that the two-phase drying model proposed in this chapter is intended for falling-rate drying. Predicting drying performance of biomass samples containing too high a moisture content may introduce more errors, and caution needs to be used. In addition, bed-to-surface heat transfer coefficient of fluidized bed reactors with biomass as the bed material should be obtained for the design of heat exchangers for indirect heat supply to the dryer. Such experiments and results are shown in the following chapter.

CHAPTER 5

HEAT TRANSFER IN PULSED FLUIDIZED BED

5.1 Heat transfer in rectangular fluidized bed

5.1.1 Effect of gas flow rate

A previous study of Zhang (2005) showed that splitting the gas supply into a pulsating stream and a steady fluidization stream instead of keeping only the pulsating stream dampened the 'shock' or additional acceleration introduced by pulsed gas flow and undermined the positive effect of pulsation on overcoming channeling, slugging and defluidization in fluidized beds. Additionally, the interaction between the pulsating stream and fluidization stream is further discussed in Appendix A2. Therefore, only the pulsating stream was used in the study of heat transfer. As in previous chapters, experimentally obtained minimum fluidization velocity (U_{mf}) of Douglas fir sawdust at 7% moisture content (dry basis) was used in the following figures to express the average superficial gas velocity \bar{U} in relation to U_{mf} .

Heat transfer coefficient measured in this chapter refers to the bed-to-surface heat transfer coefficient, between the dense phase and the immersed surface (heating probe). The effects of gas flow rate on heat transfer coefficient at different pulsation frequencies are clearly illustrated in Figure 5.1. In addition to $f=0.5, 1, 2$ and 5 Hz, special attention was paid to $f=1.25$ Hz as it was close to the natural frequency $f_N=1.28$ Hz of the system calculated according to Eqn. (3.2).

It is evident that higher gas flow rate leads to faster heat transfer, as the heat transfer coefficient at all frequencies investigated showed the same upward trend. Both $f=1$ and 1.25 Hz exhibited the highest heat transfer coefficient amongst all, roughly $104 \text{ W}/(\text{m}^2\cdot\text{K})$. However, the maximum was reached at a lower gas flow rate ($1.0U_{mf}$) at $f=1.25$ Hz than at 1 Hz ($1.25U_{mf}$), indicating less air was required to reach good gas–solid contact around natural frequency. This is likely attributable to the resonance effect as discussed in previous chapters.

Heat transfer coefficients at $f=2$ Hz had the same trend but the values were lower than that of 1 Hz and 1.25 Hz, presumably due to weaker gas pulsations and lower amplitude of pressure fluctuations from shortened opening time of the solenoid valve in a pulsation cycle that may also have reduced quality of gas–solid contact. A maximum of $98.6 \text{ W}/(\text{m}^2\cdot\text{K})$ was observed at $1.5U_{mf}$. At $f=5$ Hz, gas pulsations were too weak to lift the entire bed between $0.8\text{--}1.2U_{mf}$. Channeling greatly hindered gas–solid contact and heat transfer. For $\bar{U}=1.25\text{--}1.5U_{mf}$, improved fluidization and heat transfer were observed. As shown in Figure 5.1, the maximum heat transfer coefficient was $96.9 \text{ W}/(\text{m}^2\cdot\text{K})$.

At $f=0.5$ Hz, intermittent fluidization was achieved even at a flow rate as low as $0.7U_{mf}$, as a result of strong pulsations. Heat transfer coefficient increased from $89.1 \text{ W}/(\text{m}^2\cdot\text{K})$ at $0.7U_{mf}$ to $92.6 \text{ W}/(\text{m}^2\cdot\text{K})$ at $1.5U_{mf}$. The lower values and flattened profile of heat transfer coefficient at 0.5 Hz may be related to the longer “OFF” periods where the bed remained still. Despite higher flow rate and greater amplitude of pressure fluctuations achieved in the “ON” period with increasing \bar{U} , the overall heat transfer performance was offset by the “OFF” period.

Interestingly, at higher pulsation frequencies ($f \geq 1$ Hz) the heat transfer coefficient reached a maximum and plateaued. This may be because of the compensation between gas convective and particle convective heat transfer components that co-existed for the particles used in this study, as pointed out by Molerus and Wirth (1997a). Consequently, it is fair to infer that as gas flow rate increases, particle convective component decreases as the bed voidage is getting higher, heat

transfer slowly switches to gas convection, which is supported by the asymptotical increase of heat transfer coefficient.

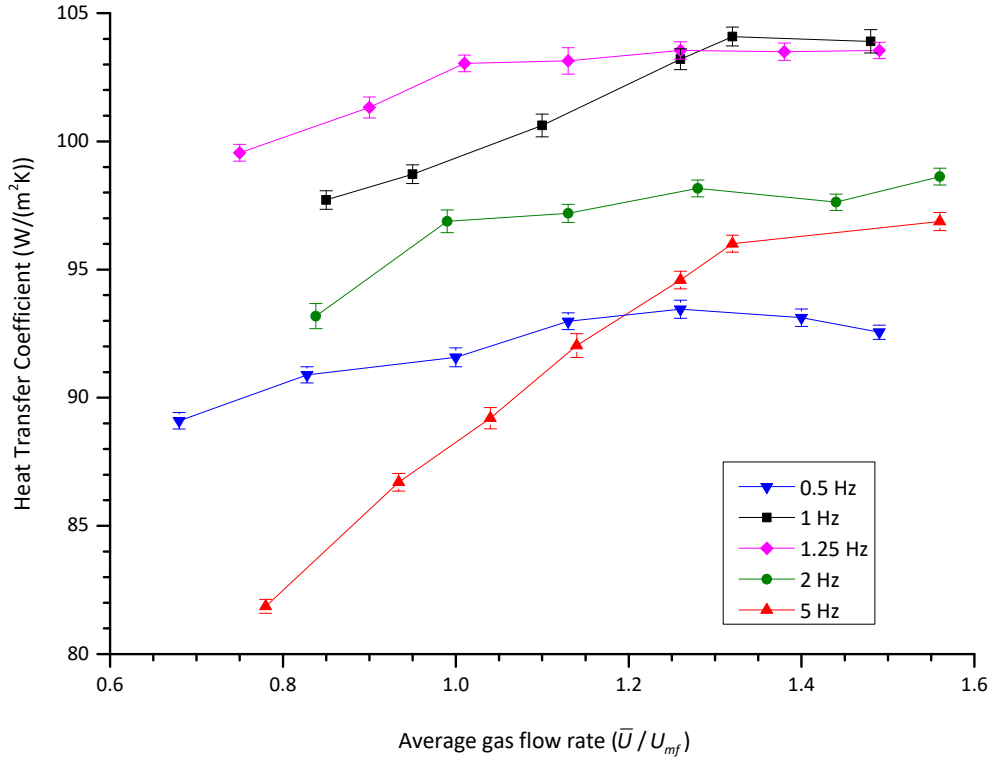


Figure 5.1 Effect of average flow rate on the bed-to-surface heat transfer coefficient at different gas pulsation frequencies in the pulsed fluidized bed of Douglas fir sawdust.

5.1.2 Effect of pulsation frequency

Figure 5.2 demonstrates the effect of pulsation frequency on bed-to-surface heat transfer in the pulsed fluidized bed. The highest heat transfer coefficients among all three flow rates were achieved between 1–1.5 Hz. This is consistent with the findings in Section 5.1.1. Higher gas flow rate promoted solid renewal on probe surfaces and gas convective heat transfer. As a result, $\bar{U}=1.5U_{mf}$ showed overall higher heat transfer coefficients than $1.1U_{mf}$ and $1.3U_{mf}$.

At $f=0.5$ Hz the bed was only fluidized intermittently. Both the "ON" and "OFF" periods were 1 s. Significant pressure build-up occurred during the "OFF" period, followed by the highest amplitude of peak pressure drops as well as standard deviation of pressure fluctuations during the "ON" period, leading to high gas flow rate and large yet infrequent bubble generations. A horizontal layer of slugs formed above the distributor was clearly visible soon as "ON" period was initiated. As stated by Ozkaynak and Chen (1980), smaller bubbles in shallow beds could easily miss the heating tubes, resulting in low heat transfer coefficients. During the ascent, smaller bubbles coalesce and form large bubbles and slugs, carrying many particles upward to the freeboard, which could explain the severe entrainment at 0.5 Hz. The time-averaged heat transfer coefficient remained low because of the less frequent bubble generation in the "ON" period and the prolonged "OFF" period. For $\bar{U}=1.1U_{mf}$, $1.3U_{mf}$ and $1.5U_{mf}$ at 0.5 Hz, the respective heat transfer coefficients were 86.8, 90.6 and 93.9 W/(m²·K).

As pulsation frequency increased from 0.5 to 1 Hz, both the time fraction and absolute length of "OFF" periods are shortened, and the fluidized bed gradually shifted from a seemingly intermittent fluidization regime to a more continuous one. In pulsed fluidized beds bubble behaviour are often influenced by gas pulsation, higher pulsation frequency normally leads to smaller yet more frequent bubbles, which in turn promote solid circulation and particle renewal on the heat transfer surface. For $1.3U_{mf}$ an increase of h as much as 10.1% could be seen in Figure 5.2. In addition, the resonance effect around the natural frequency of the system most certainly contributed to the improvement in gas–solid contact and the highest heat transfer coefficients at all three flow rates, with a maximum of 103.5 W/(m²·K) at $1.5U_{mf}$.

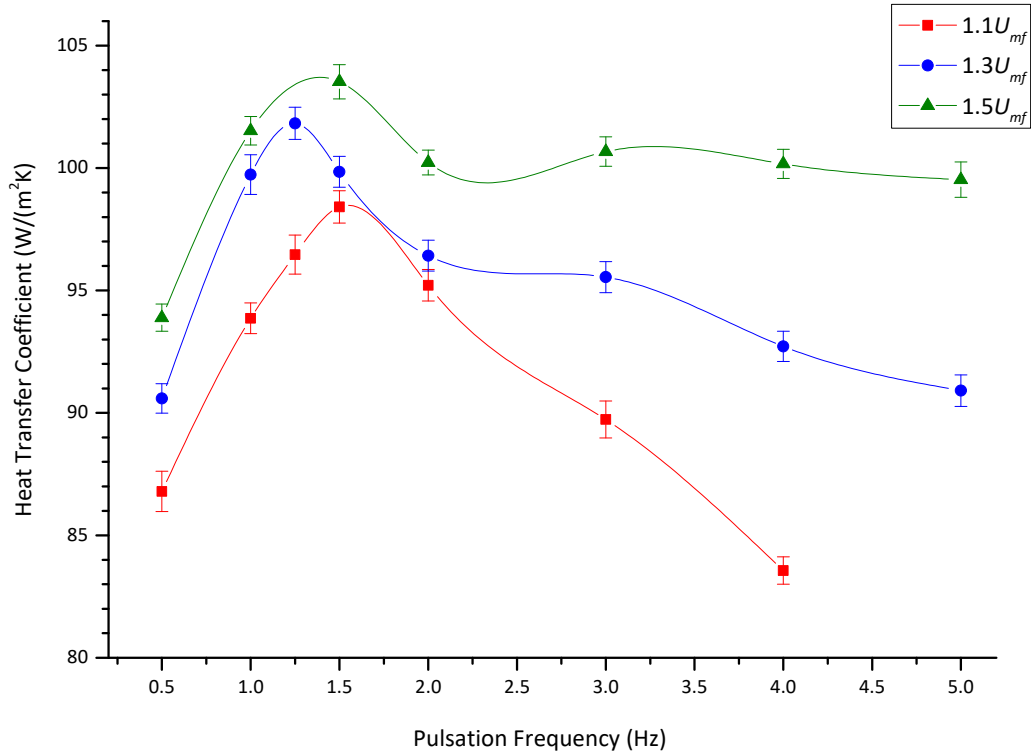


Figure 5.2 Effect of pulsation frequency on heat transfer coefficient at different gas flow rates in the pulsed fluidized bed of Douglas fir sawdust (experimental data points and spline interpolation lines).

Further increase in pulsation frequency beyond f_N led to faster bubble generation, which likely benefitted the particle convective heat transfer as packets could come in contact with the heating surface and get renewed more frequently, leading to a shorter residence time. Meanwhile, gas convection took a toll because of the reduced bubble rise velocity in spite of an increase in gas holdup. The interaction between gas convective and particle convective heat transfer and their similarity in magnitude may have contributed to the rather flat profile of heat transfer coefficient at $1.5U_{mf}$ as the dominating heat transfer mechanism switched from one to the other that had similar magnitude. $h=100.1\pm 0.4$ W/(m²·K) between 2 and 5 Hz. At $1.1U_{mf}$ and $1.3U_{mf}$, operating above f_N could no longer generate enough force to lift the entire bed. Consequently, channeling and other undesired flow behaviour frequently occurred, which may have reduced the gas–solid contact efficiency and undermined the bed-to-surface heat transfer. For $1.3U_{mf}$ heat transfer coefficients

declined slightly from 96.4 W/(m²·K) at 2 Hz to 90.9 W/(m²·K) at 5 Hz. A similar trend also existed at $1.1U_{mf}$. It should be noted that data point for $1.1U_{mf}$ at 5 Hz was excluded due to the fact that complete defluidization occurred during the experiment and it could no longer be considered a fluidized bed.

5.1.3 Heat transfer properties of pine and switchgrass

Besides Douglas fir, heat transfer coefficients of pine and switchgrass powders were also investigated. Average superficial gas velocities equivalent to $1.1U_{mf}$, $1.3U_{mf}$ and $1.5U_{mf}$ of Douglas fir sawdust (with 7% moisture content) were used to fluidize pine sawdust and switchgrass powders so that results could be better compared. The respective gas velocities were 0.26, 0.31 and 0.36 m/s.

Produced from the same sawmill, pine sawdust possessed similar size and shape to Douglas fir sawdust. Similar trend of heat transfer coefficients is illustrated in Figure 5.3(a). Heat transfer coefficients increased with gas flow rate. The highest heat transfer coefficient was 103.9 W/(m²·K) at $\bar{U}=0.36$ m/s, paired with a pulsation frequency of 1.5 Hz. Just like Douglas fir, at low pulsation frequencies such as 0.5 and 1 Hz, time-averaged heat transfer coefficients were low because of the long and dormant "OFF" periods. Further increasing flow rate to 0.36 m/s, similar h values were found across $f=2-4$ Hz as the increase in particle convection offset the decline in gas convection, until channeling occurred at 5 Hz that led to a decline in gas–solid contact efficiency and heat transfer. Both $\bar{U}=0.26$ and 0.31 m/s produced maximum of h at $f=1.5$ Hz as well, albeit the values were lower. Above 3 Hz for $\bar{U}=0.26$ and 0.31 m/s, the bed behaved like a fixed-bed reactor during the experiment because of severe channeling followed by defluidization. Therefore, data above this point were excluded.

Compared to pine and Douglas fir, switchgrass particles used in this study had a smaller Sauter mean diameter of 0.76 mm and seemingly more fines, this is consistent with the particle size distribution curves in Figure 2.5. The smaller size and higher percentage of fines are possible contributing factors to the higher particle convective heat transfer because of the shorter residence time of smaller particles on the heat transfer surface. Consequently, in addition to a normal peak of h observed around f_N in Figure 5.3(b), another more prominent peak was also present at 3 Hz for $\bar{U}=0.31$ and 0.36 m/s, indicating the increase in particle convection outweighed the decrease in gas convection. For the lower flow rate of 0.26 m/s, only one peak existed around f_N , which matched visual observations made during the experiments where channeling occurred that affected gas–solid contact and heat transfer.

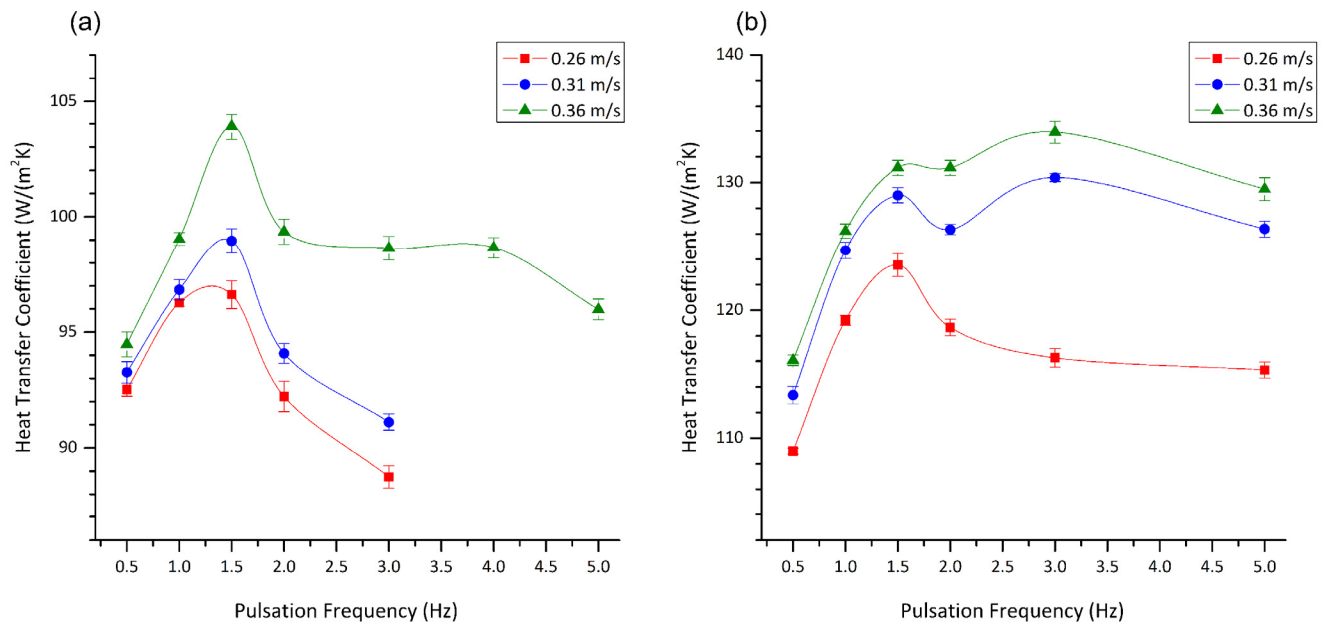


Figure 5.3 Effect of pulsation frequency on heat transfer coefficient at different gas flow rates in the pulsed fluidized bed (experimental data points and spline interpolation lines). (a) pine; (b) switchgrass.

5.1.4 Effect of particle size

Molerus and Wirth (1997b) analyzed experimental results from Wunder (1980) where heat transfer coefficients of glass beads of four different sizes (55, 400, 770 and 2230 μm) had been measured at different superficial gas velocities and concluded that for glass beads of 55 and 2230 μm the predominant heat transfer mechanisms were particle convection and gas convection, respectively, whereas for 400 and 770 μm particles heat transfer shifted from particle convection towards gas convection as flow rate increased. Moreover, it has been widely acknowledged that within bubbling regime an asymptotic relationship between excess superficial gas velocity and heat transfer coefficient only occurs when a single heat transfer mechanism is dominating, otherwise the heat transfer coefficient will most likely go through a maximum and eventually decline. In order to verify the effect of particle size on heat transfer, Douglas fir sawdust received from the sawmill was separated into different particle size fractions. After being dried sawdust was sieved through a series of screens (7, 4, 3.15 and 1 mm) where particles larger than 7 mm were discarded and the following particle fractions were obtained: 0–1 mm, 1–3.15 mm, 3.15–4 mm and 4–7 mm.

For particles of 4–7 mm fluidization could not be achieved, the bed was completely defluidized from the beginning. The bed became a fixed-bed reactor except a slight piston-like movement as the bed as a whole was lifted up by a few millimeters due to gas pulsations. Heat transfer resembled fixed-bed reactor as well, which are shown in Figure 5.4. The bed-to-surface heat transfer coefficient increased slightly with increasing superficial gas velocity, from 39.9 $\text{W}/(\text{m}^2\cdot\text{K})$ at 0.25 m/s to 54.3 $\text{W}/(\text{m}^2\cdot\text{K})$ at 0.38 m/s. For 3.15–4 mm particles, at low gas flow rates such as 0.25 and 0.28 m/s, the centre of the bed was emptied. Only a small percentage of particles around the centre were carried up and fallen down because of the gas pulsation, with the rest of the bed remained stationary. At a higher gas flow rate of 0.38 m/s, the bed was able to be partially fluidized, accompanied by severe channeling, leading to a minor increase in heat transfer. A maximum of 60.0 $\text{W}/(\text{m}^2\cdot\text{K})$ was reached at 0.38 m/s. Similarly, at $\bar{U}=0.25$ m/s the centre of the bed was emptied with bed particles of 1–3.15

mm. At 0.28 m /s, partial fluidization was resumed. Complete fluidization was restored when superficial gas velocity increased to 0.38 m/s. Consequently, heat transfer coefficient increased by 41%, from 56.3 W/(m²·K) at 0.25 m/s to 79.6 W/(m²·K) at 0.38 m/s. The highest heat transfer coefficient was discovered with 0–1 mm particles. Due to the smaller size, smooth fluidization was observed in this particle group, and no channeling was found even at 5 Hz. The presence of fine particles also resulted in additional entrainment when compared to the other particle size groups. Nevertheless, heat transfer coefficient almost doubled compared to 1–3.15 mm particle group, with a maximum of 117.1 W/(m²·K) at 0.28 m/s.

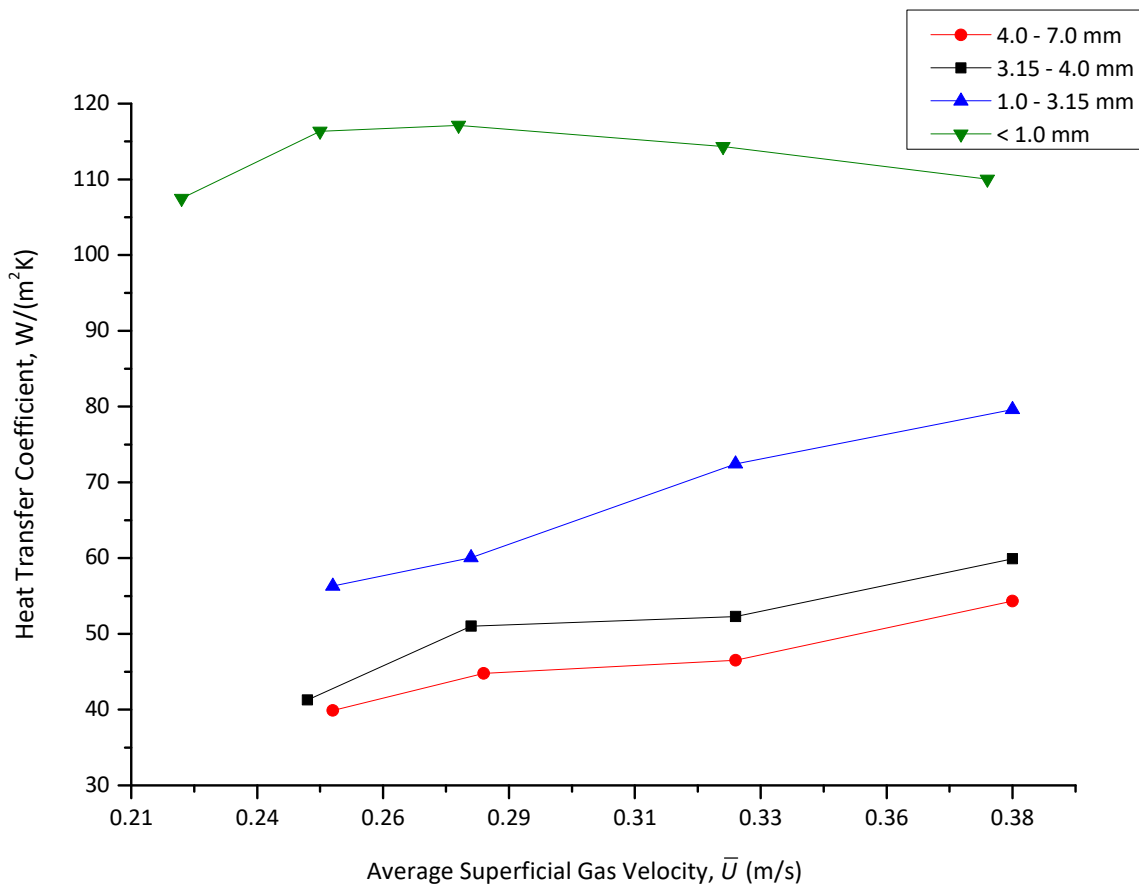


Figure 5.4 Effect of particle size on heat transfer at different gas flow rates in the pulsed fluidized bed with Douglas fir sawdust at a pulsation frequency of 1.25 Hz

5.1.5 Effect of fine particles

The presence of fine particles in the 0–1 mm particle group may have contributed to the smooth fluidization, mass transfer as well as heat transfer in this study. Agarwal et al. (1962) studied the effect of fines on the hydrodynamics of fluidized beds and compared the minimum fluidization velocity for closely sized fractions of iron ore to that with a wide size range, and discovered that the greater the fines content, the lower the minimum fluidization velocities. Sun (1991) showed that when the superficial gas velocity exceeded 0.1 m/s, the bed with wider particle size distribution usually gave the highest particle concentration inside the voids, the smallest bubble size and the greatest dense phase expansion at the same operating conditions, leading to a higher reaction rate and improved interfacial heat and mass transfer. In order to further investigate the possible effect of fine particles (or fines) on heat transfer, fine Douglas fir sawdust (0–1 mm) was added to the coarse fraction (3.15–4 mm) at certain ratios. Four mixtures were prepared with the weight percentage of fine particles ranging from 33% to 83%. Details of the mixtures are listed in Table 5.1.

Table 5.1 Details for the mixture of coarse and fine particle fractions of Douglas fir sawdust

Group Number	Weight of Particle Fractions (g)		Percentage of Fine Particles (w.t. %)
	0–1.0 mm	3.15–4.0 mm	
1	66	134	33
2	100	100	50
3	134	66	67
4	166	34	83

For Group 1 containing 33% of fines, severe channeling occurred at the lowest superficial gas velocity of 0.28 m/s, and the centre of the fluidized bed was quickly emptied, followed by complete defluidization. The heat transfer probe was exposed to the rising airflow with only a small percentage of particles being carried up and down by the pulsed gas flow. As a result, the measured heat transfer coefficient was 67.5 W/(m²·K). Such a low value was not a good representation of the

bed-to-surface heat transfer of the fluidized bed, but it did highlight the importance of suitable operating conditions. At higher gas velocities, the fluidized bed still suffered from occasional defluidization, but was able to recover owing to the pulsed gas flow. Heat transfer coefficient at 0.38 m/s was measured to be 77.0 W/(m²·K). Gas–solid contact was slightly improved in Group 2 because of the presence of more fines. However, at 0.26 and 0.28 m/s, the centre region of the bed surrounding the heat transfer probe was still emptied, with only a small portion of particles being fluidized. Neither apparent bed expansion nor gas–solid contact was observed. The measured h values only reflected the forced convection of fluidizing air around the probe. Similar to Group 1, at higher superficial gas velocities, good fluidization was established. As can be seen in Figure 5.5, heat transfer coefficient was 85.1 W/(m²·K) at $\bar{U}=0.38$ m/s.

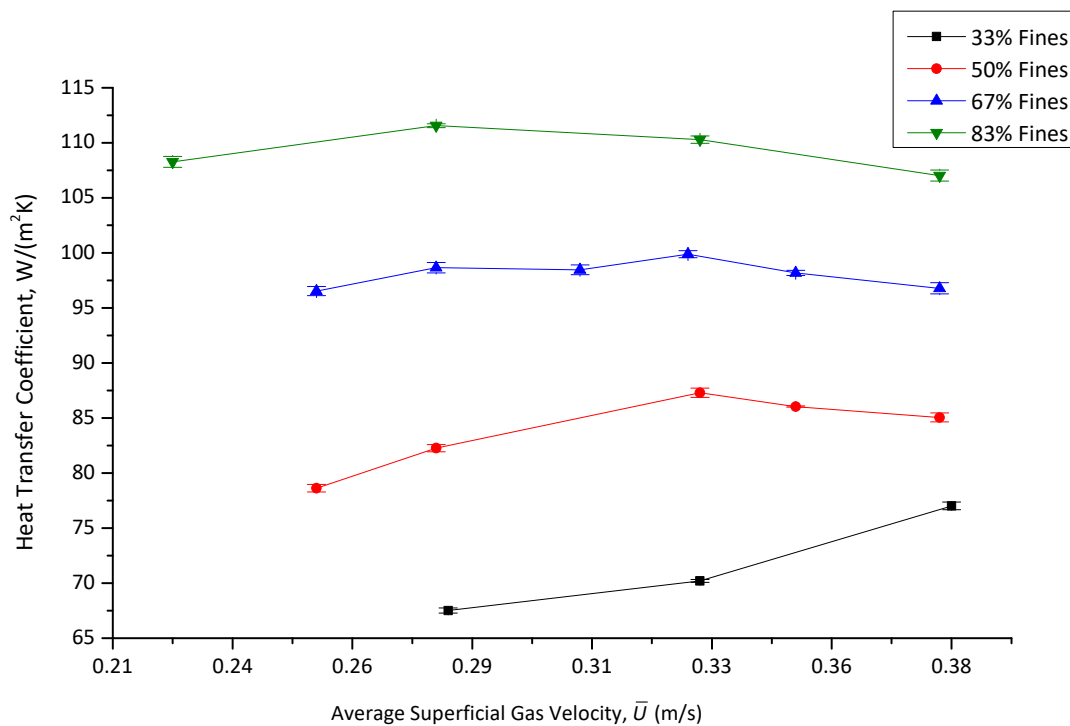


Figure 5.5 Effect of fine particles on heat transfer at different superficial gas velocities in the pulsed fluidized bed with Douglas fir sawdust at a pulsation frequency of 1.25 Hz

Gas–solid contact improved with Group 3 that had more fines. No channeling was observed with this group. Even at a low gas velocity of 0.26 m/s, the heat transfer coefficient reached 96.5 W/(m²·K). It appears that further increasing the gas flow rate may only achieve marginal improvement on the bed-to-surface heat transfer, as h only increased slightly to 99.9 W/(m²·K) at 0.31 m/s and fell back to 96.8 W/(m²·K) at 0.38 m/s.

The highest heat transfer coefficients were found in Group 4 containing 83% of fines. It is possible that by adding fine particles into coarse ones both stability and flowability of the latter were improved, in addition to improved gas–solid contact and heat transfer. One possible explanation is the lubrication effect. By examining earlier experimental work, Zenz and Othmer (1960) analyzed the effects of particle size distribution on the pseudo viscosity of fluidized beds and concluded that the fines between the coarse particles could act as a lubricant to reduce the friction between the coarse particles, thereby reducing the bed viscosity and helping to maintain good flowability. Numerical studies by Norouzi et al. (2012) also showed that by adding fines coarse particles were more readily to interact with each other, which resulted in enhanced mobility of larger particles.

5.1.6 Effect of vibration

Mechanical vibration has been widely utilized in fluidization of coarse particles (Jin et al., 2007; Kong et al., 2010), drying (Daleffe et al., 2005; Hasatani et al., 1991) and spray coating (Habibi et al., 2016; Hayes, 2006) likely because of its ability to overcome cohesive forces such as the van der Waals force. Chapter 3 has demonstrated that adding mechanical vibration to a pulsed fluidized bed is only beneficial when standalone gas pulsation is insufficient in breaking up the cohesive forces between particles, especially for biomass with high moisture content. In this section, the effect of vibration at two different superficial gas velocities across five pulsation frequencies is discussed, which is also portrayed in Figure 5.6. By turning on vibration heat transfer coefficient increased by 4.7% at $\bar{U}=1.05U_{mf}$. As the pulsation frequency increased, gas pulsation could no longer lift the entire bed,

reducing gas–solid contact efficiency. Soon as vibration was turned on good gas–solid contact was restored and h increased by 6.5% at 5 Hz.

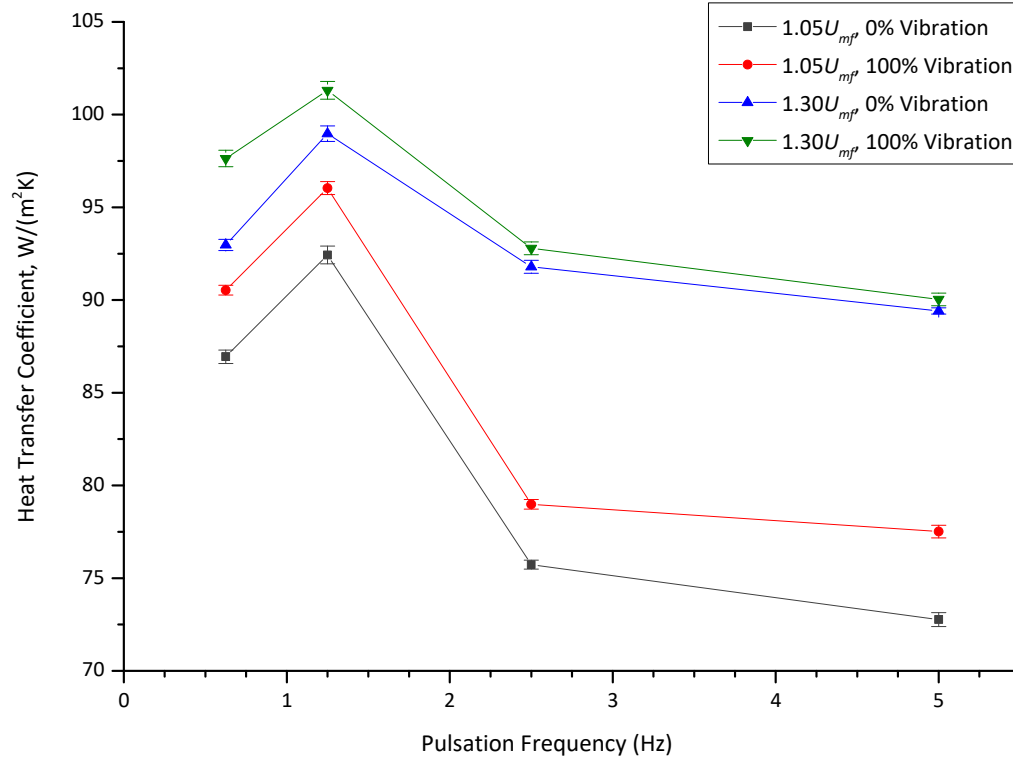


Figure 5.6 Effect of mechanical vibration and flow rate on heat transfer at different pulsation frequencies in the pulsed fluidized bed with Douglas fir sawdust

At a higher flow rate of $\bar{U}=1.3U_{mf}$, pulsation was more than enough to maintain good gas–solid contact. Therefore, the average improvement of h contributed by vibration was 2.3%, which was less than that at $1.05U_{mf}$ as shown in Figure 5.6. The biggest improvement occurred at the lowest pulsation frequency of 0.625 Hz where vibration mobilized the otherwise stationary particles during the “OFF” period, slightly enhancing heat transfer.

To estimate the possible contributions of vibration in gas–solid contact efficiency and heat transfer of biomass, Fast Fourier Transformation (FFT) analysis was performed on the differential bed pressure signals. In gas–solid fluidized beds, the power spectrum of pressure fluctuations reflects

bubble frequency, including bubble formation, splitting and coalescence. In pulsed fluidized beds, on the other hand, it is fairly common that there exists a dominant frequency identical to the pulsation frequency. As shown in Figure 5.7, peaks were more distinct for pulsed fluidized bed, and several orders of magnitude higher than that of a conventional fluidized bed. The dominant frequency was 1.25 Hz, with overtones at 2.5 Hz, 3.75 Hz and so on that could be attributed to the under-dampened pressure oscillations, and the fact that the pressure fluctuations in pulsed fluidized bed were not perfect sinusoids.

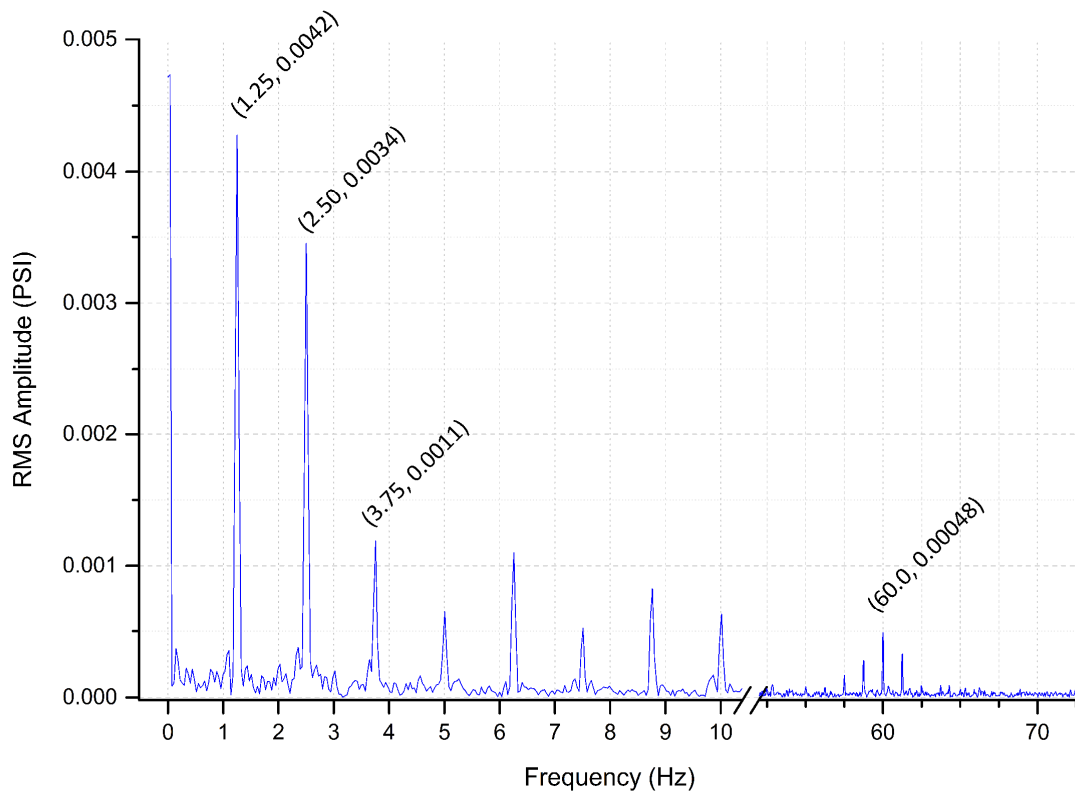


Figure 5.7 Spectrum analysis of the bed pressure drops during the heat transfer measurement of Douglas fir sawdust. $f=1.25$ Hz, $\bar{U}=1.05U_{mf}$ with 100% vibration

Besides the peaks associated with the dominant frequency of 1.25 Hz and its overtones, a few lower peaks were seen around 60 Hz, which corresponded to the frequency of the vibratory base. The root mean square (RMS) amplitude of vibration peak (60 Hz) was only one tenth of the pulsation peak (1.25 Hz). By increasing the amplitude or frequency of the vibratory base, the limited contribution of vibration could be further enhanced.

5.1.7 Heat transfer at various lateral positions

Results presented in this chapter so far were measured while the heater probe was mounted in the centre of the bed. In order to gauge the heat transfer performance at other parts of the bed, the probe was moved horizontally to two other lateral positions, as shown in Figure 5.8.

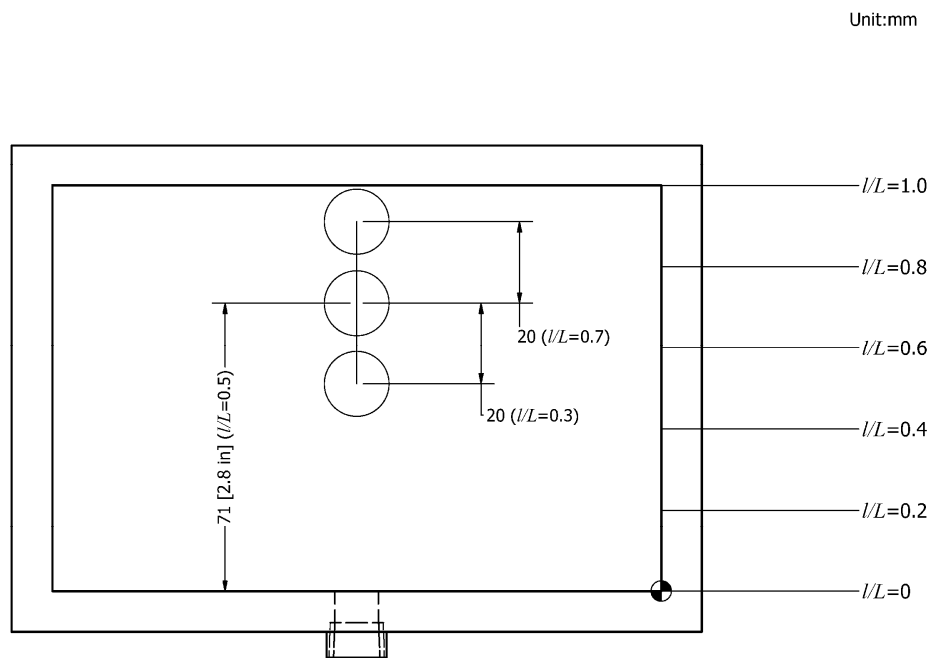


Figure 5.8 Lateral positions of the heater probe in the pulsed fluidized bed of biomass (top view, unit in mm)

The centre location was marked as $l/L=0.5$, the other two positions were 20 mm (0.8 in) apart. The probe could simply be moved from one position to another by sliding the horizontal section of the rigid acrylic connection. Heat transfer coefficients at three lateral positions as a function of pulsation frequency are displayed in Figure 5.9.

Figure 5.9(a) shows the heat transfer coefficients at a relatively low gas flow rate of $\bar{U}/U_{mf}=1.2$. The ridge in Figure 5.9(a) represents the highest heat transfer rate was found at 1.25 Hz. For $l/L=0.3, 0.5, 0.7$, the respective h values were 102.6, 99.3 and 98.5 W/(m²·K). As pulsation frequency moved away from 1.25 Hz the heat transfer coefficient declined. For $\bar{U}/U_{mf}=1.2$ the lowest heat transfer coefficients were found at 5 and 0.5 Hz, with an average of 87 W/(m²·K). It is noteworthy that for 0.5 Hz, the heat transfer coefficients at three different lateral positions were fairly close to each other (86.1±0.17 W/(m²·K)). This is likely because of the high-intensity gas pulsation, which ensured good gas–solid contact in “ON” periods. During “OFF” periods the bed was stationary, which lowered the average heat transfer coefficient. For 5.0 Hz, pulsed gas flow was much weaker. Consequently, heat transfer was slower than 1.25 and 2.5 Hz. The difference between the centre and two other lateral positions grew larger (96.2±1.1 W/(m²·K)), which may be attributable to the reduced pressure drop and uniformity.

As flow rate increased, both the heat transfer coefficients and the uniformity of h at various lateral positions were improved. As can be seen in Figure 5.9(b), respective h values were 96.8, 97.2 and 94.8 W/(m²·K). This serves as a reminder that operating conditions should be carefully monitored to ensure pulsations sufficiently strong so good gas-solid contact is achieved to avoid lateral segregation and other undesirable flow behaviour that may hinder heat and mass transfer.

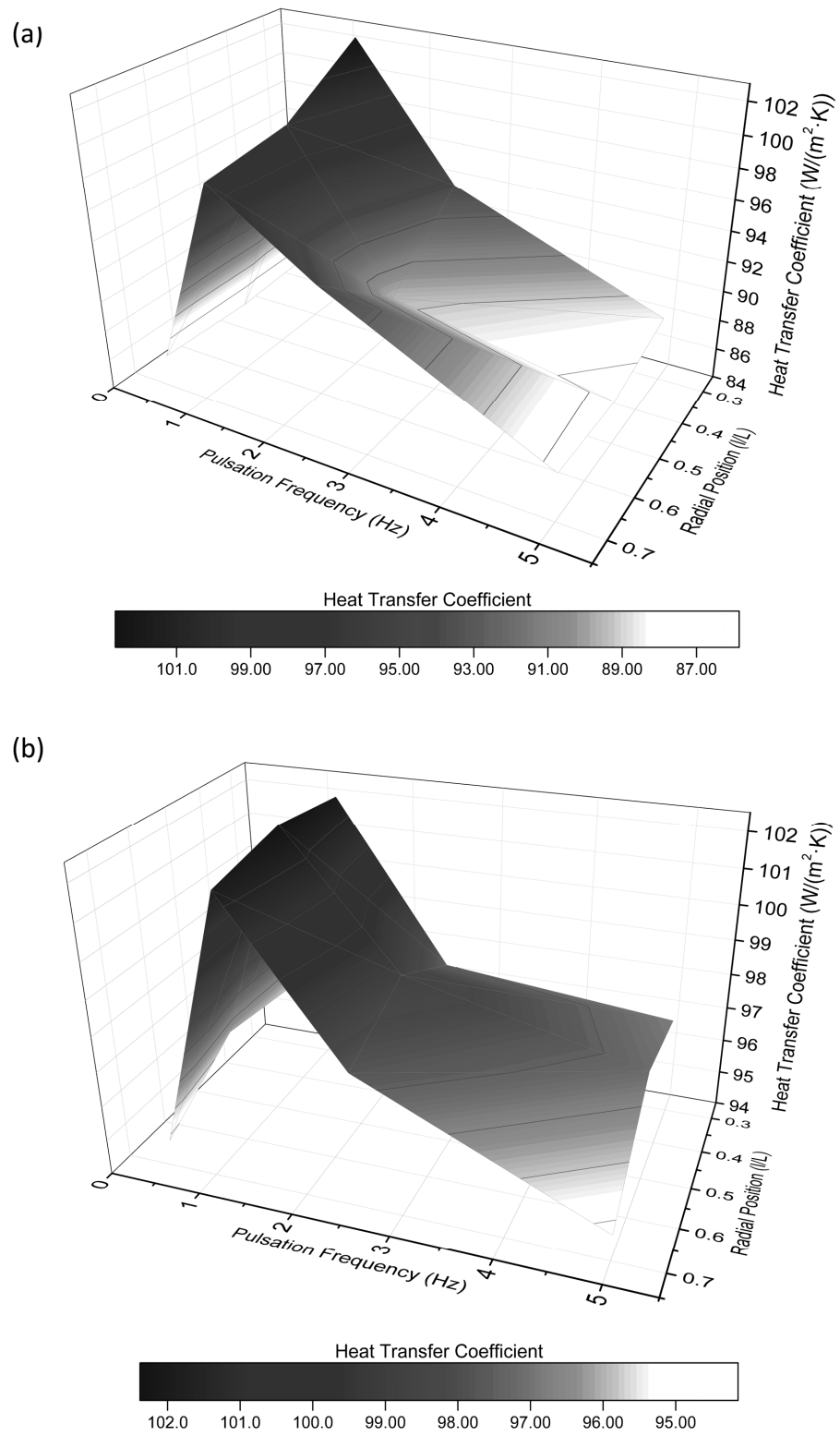


Figure 5.9 Heat transfer coefficients at different lateral positions as a function of pulsation frequency. (a) $\bar{U}/U_{mf}=1.2$; (b) $\bar{U}/U_{mf}=1.4$.

5.2 Heat transfer in tapered fluidized bed

5.2.1 Effect of flow rate

Just like in the original pulsed fluidized bed, gas–solid interaction in the tapered fluidized bed depends heavily on average superficial gas velocity as well as pulsation frequency, as both parameters influence the intensity of gas pulsations and bed pressure drops. Figure 5.10 illustrates a few bed patterns, in the tapered fluidized bed as flow rate gradually increased, from fixed-bed reactor to normal fluidization. The presence of such flow patterns is dictated by the intensity of the gas pulsation. The same flow patterns could be observed at different combinations of flow rate and gas pulsation.

At low gas flow rates the pulsed fluidized bed is essentially a fixed-bed reactor, as the buoyancy and drag force combined still cannot overcome the particle weight. Consequently, particles remain stationary in the bed, with fluid passing by, as shown in Figure 5.10(a). It is noteworthy that in a pulsed fluidized bed the superficial gas flow rate is constantly oscillating around the average in a sinusoidal fashion. When gradually increasing the airflow, the average around which the gas flow rate oscillates increases as well. Soon it will come to a point where within a pulsation cycle the ever-changing gas flow rate is high enough to be able to momentarily overcome the entire weight of the bed and push the bed up as a whole. Since the gas flow rate soon decreases, the pulsation will not be strong enough to penetrate the dense phase and form bubbles. As a result the bed will quickly fall back to the bottom, causing a piston-like behaviour as illustrated in Figure 5.10(b), similar to the case reported by Massimilla et al. (1966).

Further increasing the gas flow rate, pulsations become stronger, which is consistent with the greater pressure fluctuations observed during the experiments. However, at this point gas pulsations are not yet sufficiently intense to penetrate the bed entirely. The gas breaks out in the centre, forming a fountain instead, where the centre of the bed becomes the main passage for the

gas phase. As shown in Figure 5.10(c), particles near the centre are more likely to be carried up and subsequently fall back down to the region closer to the wall. Particles near the wall will slowly recirculate to the bottom of the bed. In some cases, strong jets are formed in the centre of the bed, further increasing the lateral segregation.

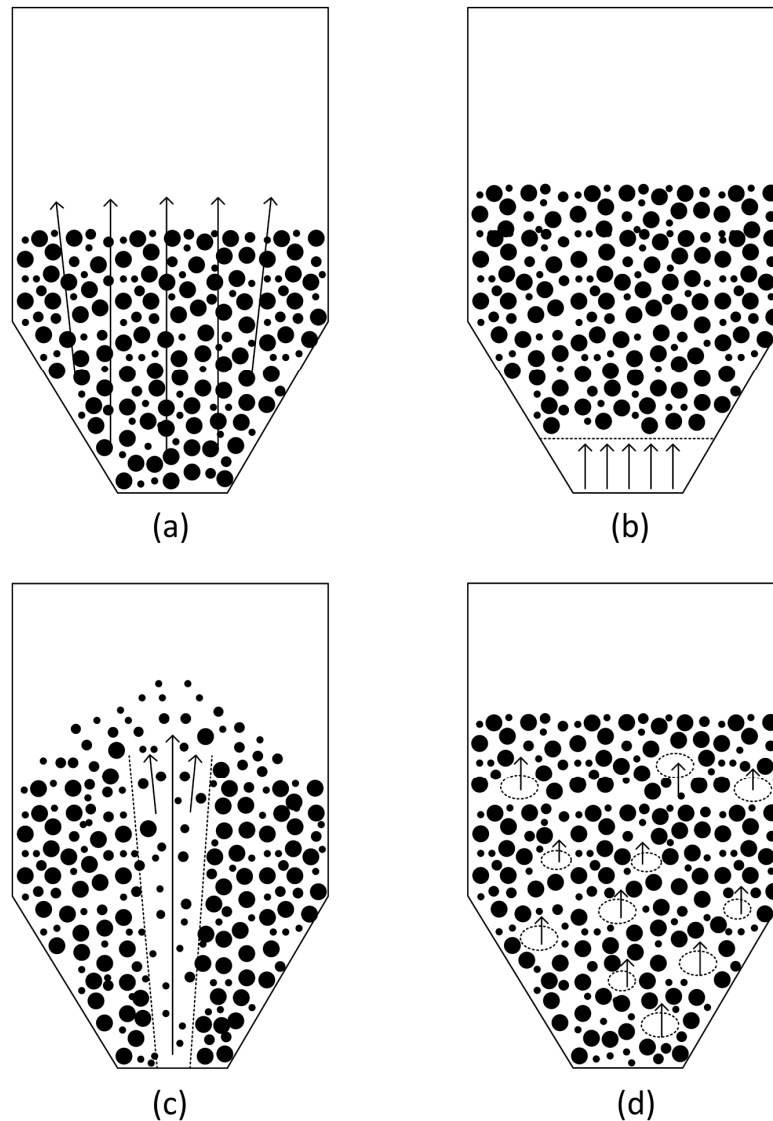


Figure 5.10 Flow behaviour at different superficial gas velocities in the pulsed fluidized bed with tapered bottom section. (a) Fixed bed behaviour; (b) Piston-like behaviour; (c) Segregated flow behaviour with a centre fountain; (d) Regular, fully fluidized flow pattern.

Eventually with the right combination of gas flow rate and pulsation frequency, ideal gas–solid contact and flow behaviour establish where regular bubbles are formed in the pulsed fluidized bed during “ON” periods (Figure 5.10(d)). The bubble size and bubble rise velocity may very well depend on the superficial gas velocity at the moment bubbles were formed.

In terms of heat transfer, the effect of flow rate in the tapered fluidized bed is demonstrated in Figure 5.11. Heat transfer coefficients in the tapered fluidized bed were 40% greater than in the original non-tapered bed.

At $1.0U_{mf}$, fluidization without channelling or partial defluidization was only observed at lower pulsation frequencies such as 0.5 and 1.0 Hz. Due to the longer “OFF” period and limited supply of airflow, both particle convection and gas convection were low. The overall heat transfer coefficient remained low for 0.5 Hz and 1.0 Hz, which were 102.5 and 110.3 W/(m²·K), respectively. For 2.5 Hz, the bed occasionally channelled, but was able to recover on its own. As to 5.0 Hz, only the central region of the bed was fluidized by the pulsating gas, which corresponds to the flow behaviour shown in Figure 5.10(c). Particles in the centre were carried up, fell back to the outer region of the column, and gradually moved downwards along the diverging channel to the bottom section of the bed. Such a flow behaviour bears distant resemblance to a spouted bed, with the heat transfer coefficient being 99.1 W/(m²·K) at 5.0 Hz.

As the average superficial gas velocity increased from $1.0U_{mf}$ to $1.1U_{mf}$ noticeable improvement in heat transfer could be seen, especially for 1.0, 2.5 and 5.0 Hz gas pulsations. Greater amplitude of bed expansion was observed during the experiment, which promoted particle movement and gas–solid contact. The excess gas flow in the pulsed fluidized bed also reduced residence time of particles on the heating surface, which was beneficial to particle convection. From $1.0U_{mf}$ to $1.1U_{mf}$, h soared by 28% at 5 Hz to 127.1 W/(m²·K). For 2.5 and 1.0 Hz, the respective heat transfer coefficients were 123.0 and 120.3 W/(m²·K).

For $\bar{U}=1.3U_{mf}$ strong jets were formed at the centre of the bed at 5.0 Hz. Particles were carried far upwards into the freeboard region, causing severe entrainment. Fallen particles gradually moved downwards along the tapered wall of the column until arriving at the bottom and being lifted up again. The measured heat transfer coefficient of 128.3 W/(m²·K) only reflected the heat transfer performance in the centre, while bed-to-surface heat transfer in the outer region is expected to be lower because of reduced particle movement and air flow. Reducing pulsation frequency to 2.5 Hz slugging regime replaced the jets in the centre of the bed. Numerous voids that were formed above the distributor at the beginning of "ON" periods quickly grew into bigger slugs while ascending. Meanwhile, particles travelled downward along the column wall. Lateral segregation finally abated once pulsation frequency was lowered to 1.0 Hz, and uniform gas–solid contact was restored. For 1.0 and 0.5 Hz the respective heat transfer coefficients were 125.6 and 112.0 W/(m²·K).

At $1.5U_{mf}$ slight decrease of h was clearly visible for all four pulsation frequencies investigated. For lower pulsation frequencies such as 0.5, 1.0 and 2.5 Hz, such decrease was likely attributable to the large amount of gas that rushed into the fluidized bed column at the beginning of "ON" periods where bed voidage dramatically decreased. Similar behaviour was observed in conventional fluidized beds when superficial gas velocity approached critical superficial gas velocity U_c that marked the transition from bubbling to turbulent fluidization regime (Molerus & Wirth, 1997b; Stefanova, 2009). For $f=5.0$ Hz lateral segregation finally subsided because of the stronger gas pulsations that led to more uniform gas–solid contact and heat transfer. As a result, the slightly lower h at $1.5U_{mf}$ represented a more uniform heat transfer in the pulsed fluidized bed, as opposed to the highly segregated bed-to-surface heat transfer at lower flow rates.

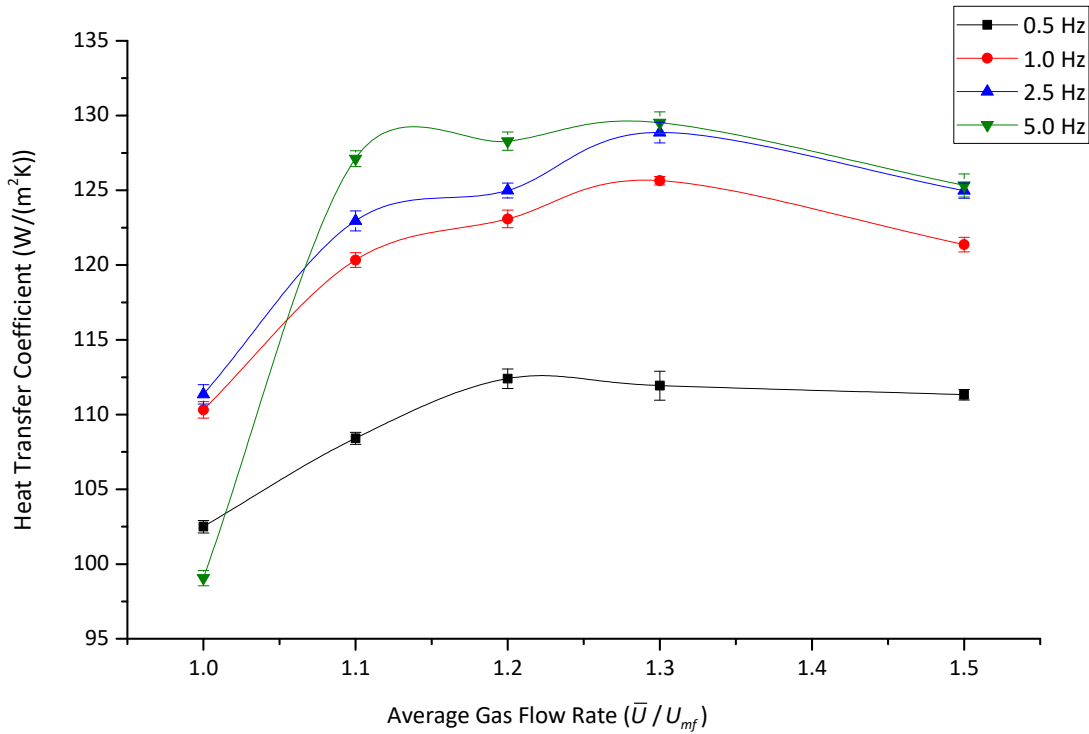


Figure 5.11 Effect of average gas flow rate on heat transfer in pulsed fluidized bed of Douglas fir sawdust with a tapered bottom section (experimental data points with spline interpolations) Effect of pulsation frequency

A closer look at the effect of pulsation frequency on heat transfer in Figure 5.12 reveals that as pulsation increased from 0.5 to 1.0 Hz, bed-to-surface heat transfer improved significantly. Peaks could be seen for all three flow rates between 1.0 and 1.5 Hz. Compared to 0.5 Hz, “OFF” periods were shorter at 1.0 Hz. Time fraction during which particles were fluidized instead of being stationary increased. The resonance effect around the natural frequency of 1.28 Hz was one other possible contributing factor to such an increase. The peak at $1.3U_{mf}$ was also 11% higher than that of $1.1U_{mf}$, probably caused by the higher gas flow rate and enhanced gas convection. However, the peak at $1.5U_{mf}$ (120.3 W/(m²·K)) was also slightly lower than $1.3U_{mf}$ (122.1 W/(m²·K)). It is highly likely that the much higher gas flow rate at $1.5U_{mf}$ is a contributing factor, as the solid concentration was greatly reduced for a moment as “ON” period initiated, with the particle convection reduced by the much larger voidage.

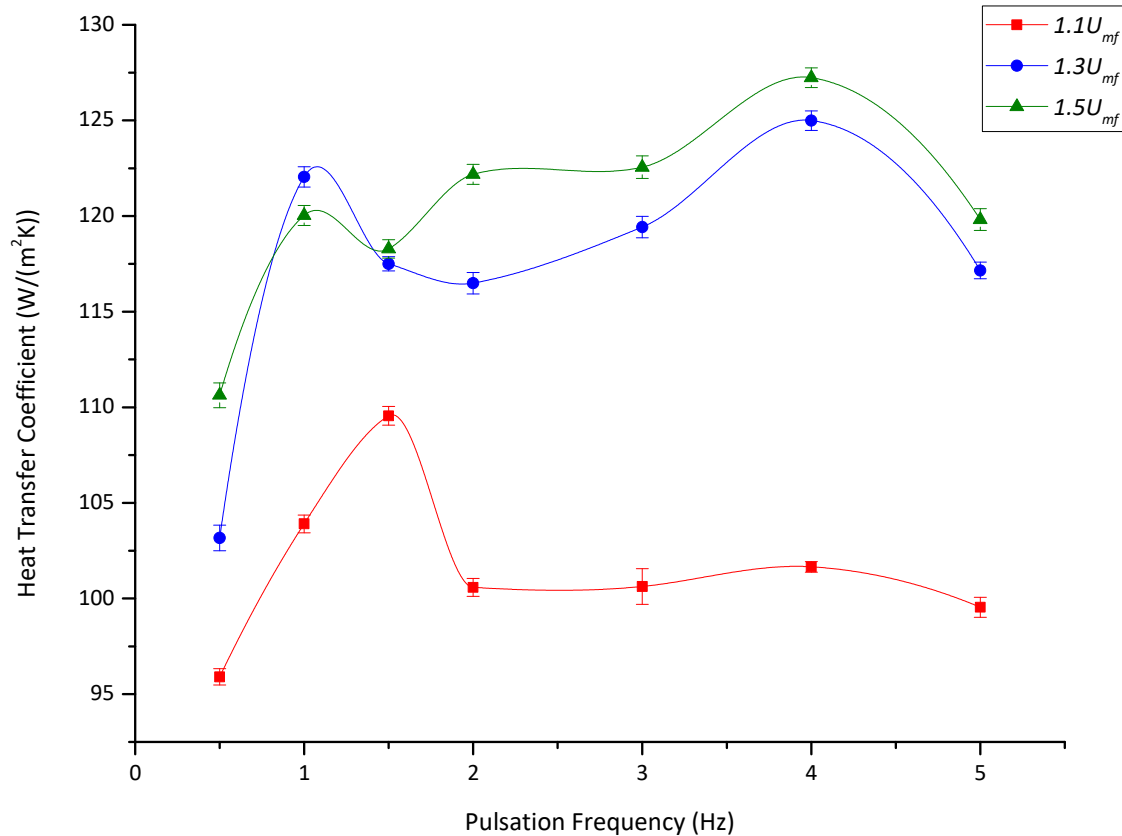


Figure 5.12 Effect of pulsation frequency on heat transfer in pulsed fluidized bed of Douglas fir sawdust with a tapered bottom section (experimental data points with spline interpolations)

For $1.3U_{mf}$ and $1.5U_{mf}$ as pulsation frequency moved beyond 1.5 Hz, lateral segregation started to manifest itself, jets were formed at the central region of bed surrounding the heater probe. As a result, in spite of the overall mediocre gas–solid contact and heat transfer performance as a result of the weaker pulsations, bed-to-surface heat transfer coefficients in the centre of the bed measured by the probe continued to increase with increasing pulsation frequency. Such phenomenon was not seen at $1.1U_{mf}$. Results also suggest that flow rate of $1.3U_{mf}$ combined with a pulsation frequency of 1.0 to 1.5 Hz should be a sufficient and effective condition for biomass fluidization.

5.2.2 Heat transfer at various lateral positions

Visual observations made during the experiment suggested that at higher pulsation frequencies such as 2 Hz and above, the bed at times experienced lateral segregation as jets or fountain could be seen at the centre of the bed, likely leading to a higher heat transfer coefficient than the exterior region of the bed. To further verify the difference of heat transfer rates at various lateral positions, the probe was moved horizontally by ± 0.02 m, therefore allowing heat transfer coefficients at lateral positions of $l/L=0.3$, 0.5 and 0.7 to be measured. Three lateral positions are demonstrated in Figure 5.8, with results shown in Figure 5.13. The same set of data are also interpreted in a different manner as displayed in Figure 5.14 where the average heat transfer coefficients at three lateral positions are plotted, with error bars showing the range of the heat transfer coefficients. Unless otherwise specified, error bars in all figures indicate standard error.

Relatively uniform heat transfer coefficients were observed at 1 Hz as the gas pulsations were sufficiently powerful to lift the entire bed and promoting gas–solid contact. The h values at centre ($l/L=0.5$), left ($l/L=0.3$) and right positions ($l/L=0.7$) were 116.5, 116.1 and 113.4 W/(m²·K), respectively. Pulsation became weaker at 2.5 and 5 Hz, causing the uprising air to form a fountain in the centre of the bed, with particles falling back to the bottom through the outer region of the bed along the wall. At 2.5 Hz, the difference of heat transfer coefficient at three lateral positions started to widen. At 5 Hz, a marked difference could be seen between the heat transfer coefficients of $l/L=0.3$ and 0.5 , which were 117.1 and 126.1 W/(m²·K), respectively.

As flow rate increased, pulsation became stronger, and the fountain in the centre of the bed was replaced by normal fluidization with significantly improved uniformity in gas–solid contact and heat transfer. As demonstrated in Figure 5.13(b), the differences of h at three lateral positions were greatly reduced at $\bar{U}/U_{mf}=1.2$. Faster solid renewal at 2.5 and 5 Hz also yielded higher heat transfer rates than at 1 Hz.

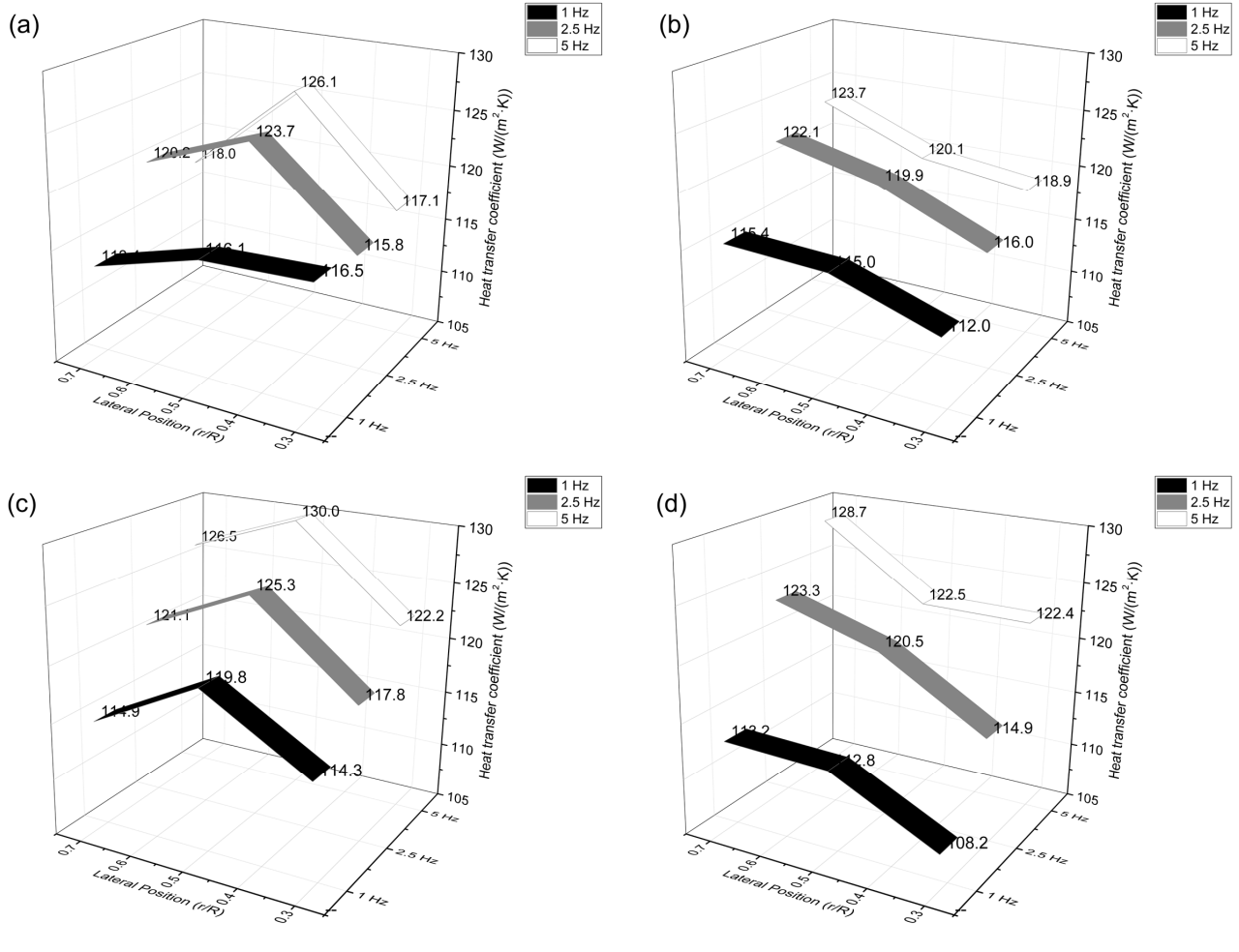


Figure 5.13 Heat transfer coefficients at three different lateral positions in the pulsed fluidized bed of Douglas fir sawdust under different average superficial gas velocities. (a) $\bar{U}/U_{mf}=1.1$; (b) $\bar{U}/U_{mf}=1.2$; (c) $\bar{U}/U_{mf}=1.3$; (d) $\bar{U}/U_{mf}=1.5$.

Visually, similar flow behaviour was observed as superficial gas velocity increased from $1.2U_{mf}$ to $1.3U_{mf}$, with higher amplitude of bed expansion and pressure fluctuations. However, both bubble size and bubble rise velocity were greater at $1.3U_{mf}$, which enhanced gas convection. Heat transfer coefficients at $1.3U_{mf}$ on average were 8.3% higher than that at $1.2U_{mf}$. The tapered design also allowed slightly more bubbles to pass through the centre region of the bed than the outer area,

which is consistent with the heat transfer profile illustrated in Figure 5.13(c). The centre region again showed higher heat transfer rate, but the difference was less pronounced compared to $1.1U_{mf}$.

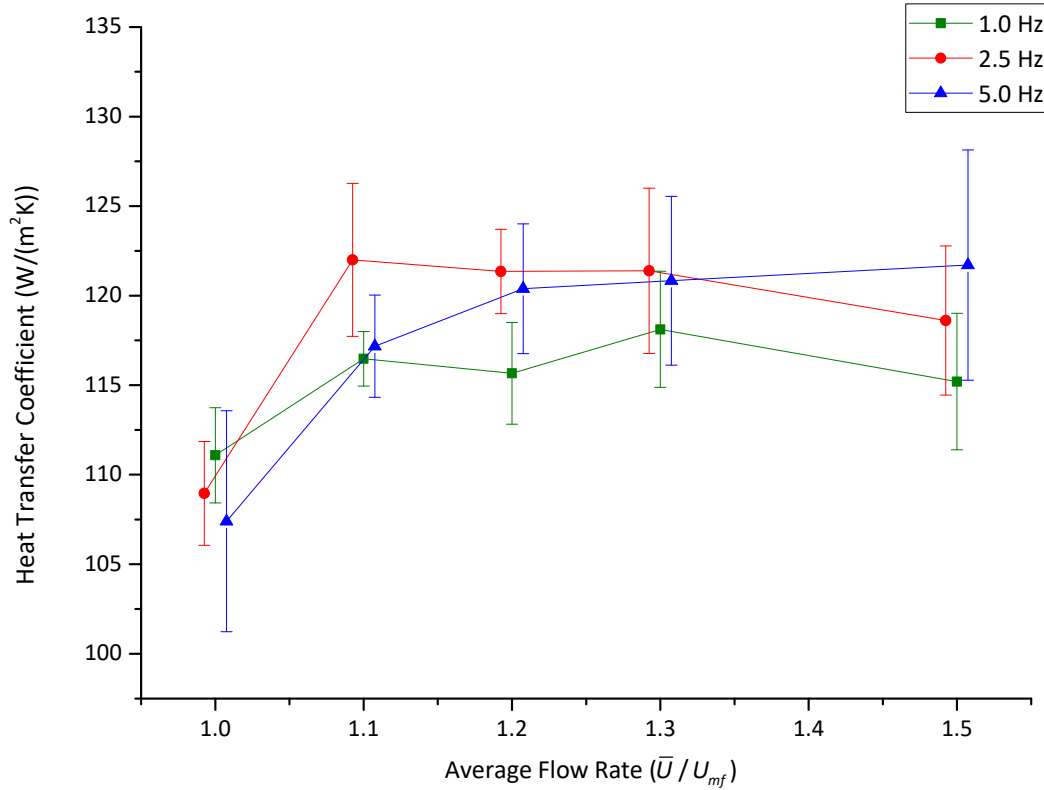


Figure 5.14 Average heat transfer coefficients at three different lateral positions in the pulsed fluidized bed of Douglas fir sawdust under different average superficial gas velocities, with error bars indicating the standard deviation of measured h values

$\bar{U}=1.5U_{mf}$ was the highest gas velocity investigated, yet the average heat transfer coefficient values were similar, or even marginally less than that at $\bar{U} = 1.3U_{mf}$. At $f=1$ Hz the subpar heat transfer performance may be attributable to the fact that the maximum superficial gas velocity in a pulsation cycle was close to the critical superficial gas velocity (U_c) where for a brief moment in a pulsation cycle the bubbling bed was in transition to turbulent fluidization regime, where particle volume fraction would be greatly reduced. At 2.5 and 5 Hz heat transfer coefficients were much greater. However, the increased gas hold-up may have promoted bubble coalescence. It is possible that larger bubbles (or slugs) at the centre of the bed hindered particle convection, while pushing

particles randomly towards the exterior of the fluidized bed. As a result, for 2.5 and 5.0 Hz, the right side ($l/L=0.7$) had higher h values than the centre ($l/L=0.5$) and the left side ($l/L=0.3$).

Further analyzing the averaged heat transfer coefficients plotted in Figure 5.14, it can be concluded that unlike the results shown in Figure 5.11 where the frequency of 5 Hz seems to have the best heat transfer performance, overall the highest and laterally-averaged heat transfer performance occurred at 2.5 Hz. Lower pulsation frequencies such as 1 Hz has its merit in this case, as they are able to offer the best stability and uniformity in gas–solid contact and heat transfer, despite its slightly lower heat transfer rate.

5.2.3 Effect of pulsation duty cycle

A 50% pulsation duty cycle was used for all previous heat transfer experiments in this chapter. To test the effect of duty cycle on heat transfer, a wide range of duty cycles from 10% to 90% were investigated at two different gas flow rates, $1.1U_{mf}$ and $1.3U_{mf}$. Duty cycle is defined in Eqn. (3.1). Results are demonstrated in Figure 5.15.

Figure 5.15(a) shows the measured heat transfer coefficients at a relatively low gas flow rate of $1.1U_{mf}$. The pulsed fluidized bed went through three distinct phases as duty cycle increased from 10% to 90%. Piston-like behaviour was discovered when the duty cycle was small, such as 10%–30%. For $\eta_D=10\%$ the opening time of the solenoid valve was only 1/5 of a normal 50% duty cycle. In the case of 0.5 Hz, when reducing duty cycle from 50% to 10%, the opening time was shortened from 1 s to 0.2 s, which increased the pressure build-up during the “OFF” period, but in the meanwhile limited the amount of air allowed into the column. The sudden but strong gas pulsation resulted in piston-like behaviour as the gas was shut off before any further gas–solid interaction could take place. The heat transfer coefficients were low, 79.3, 98.6 and 95.4 W/(m²·K), respectively.

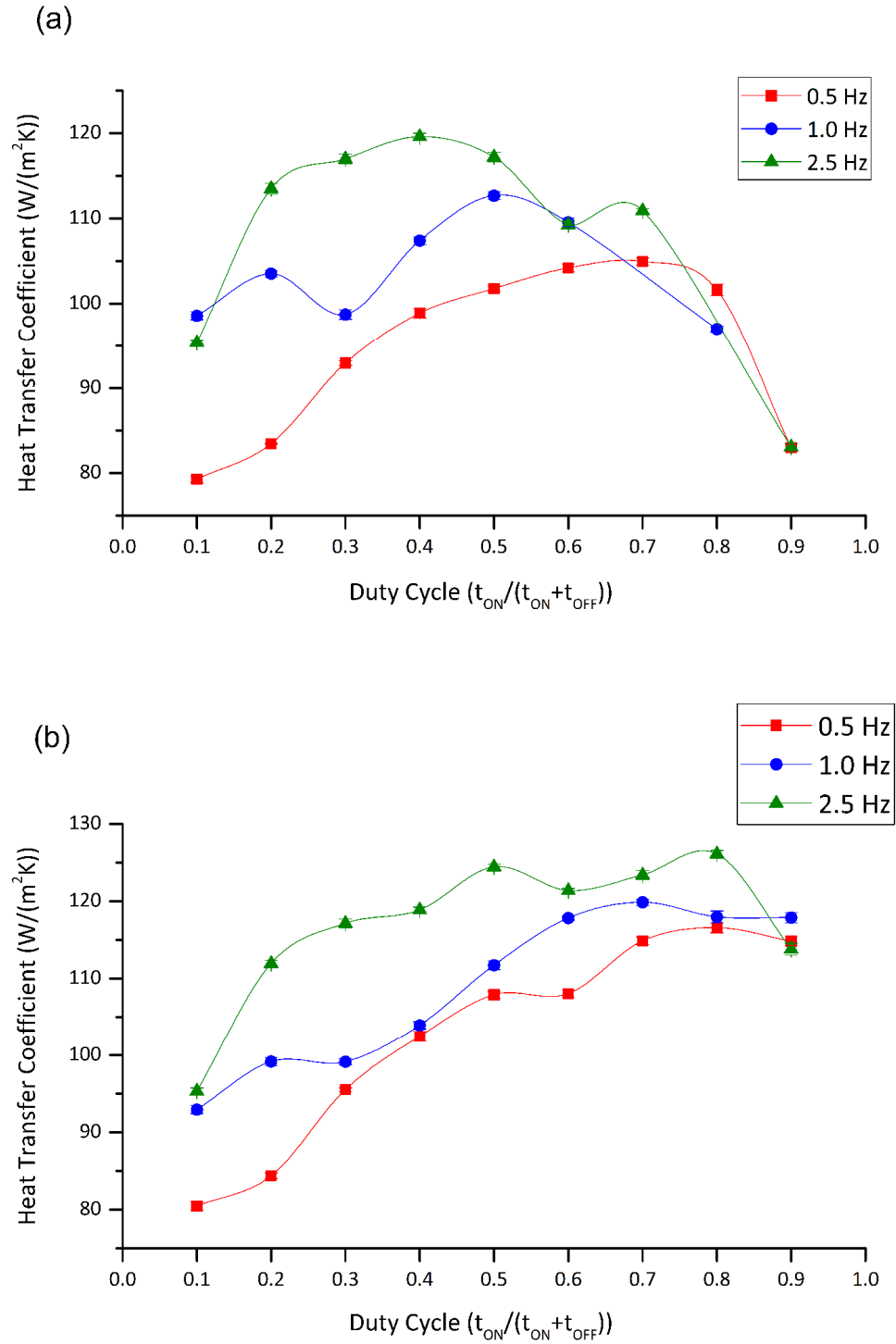


Figure 5.15 Heat transfer coefficient at different gas pulsation duty cycles with Douglas fir sawdust (experimental data points with spline interpolations). (a) $\bar{U}/U_{mf}=1.1$; (b) $\bar{U}/U_{mf}=1.3$.

Gas pulsations with 40%–60% duty cycles were sufficiently intense that cohesive forces were tackled. The longer opening time of solenoid valve also enabled more bubbles to be formed above the distributor, enhancing the gas–solid contact and heat transfer. The highest heat transfer coefficient was $104.9 \text{ W}/(\text{m}^2\cdot\text{K})$ with a 60% duty cycle.

For $\eta_D \geq 70\%$ the effect of pulsation started to wear off, as the “OFF” period in a pulsation cycle became overwhelmingly short so that barely any pressure was built up. The pressure fluctuation was reduced. Severe channeling limited the heat transfer rates. For $\eta_D=90\%$ h reduced to $83.0 \text{ W}/(\text{m}^2\cdot\text{K})$.

Similarly, at a higher flow rate of $1.3U_{mf}$ piston-like behaviour was still present at 10% and 20% duty cycle where no visible bubbles could be seen. Instead, the bed was lifted up as a whole while the solenoid valve was open and quickly fell down as the valve was shut off. Proper fluidization was restored once duty cycle was increased to 30%. Highest heat transfer coefficient was $124.5 \text{ W}/(\text{m}^2\cdot\text{K})$ with 50% duty cycle at 2.5 Hz. For $\eta_D \geq 0.7$ the bed relapsed to lateral segregation where the bed was emptied in the centre. Despite the high heat transfer coefficients measured at the centre of the bed, heat transfer rates were expected to be quite low at the exterior region and as a whole.

In conclusion, when operating the pulsed fluidized bed, duty cycle should not exceed 50%, as above 50% the intensity and effectiveness of pulsation on breaking up cohesiveness of particles start to wear off. For particles with extra high moisture content, the duty cycle can be further lowered. As the stronger pulsation may be beneficial in breaking down the inter-particle forces and preventing the bed from channeling. Once moisture content reduces, duty cycle could be gradually increased to improve the gas throughput and heat/mass transfer rates.

5.2.4 Effect of particle size and fines

Similar to the rectangular fluidized bed, the effect of particle size on heat transfer was also studied in the tapered bed. Particle fractions used for the regular bed heat transfer were implemented, except for the 4–7 mm fraction where complete defluidization occurred. As a result, heat transfer properties of the following Douglas fir sawdust fractions were measured: 0–1, 1–3.15 and 3.15–4.0 mm. Results are displayed in Figure 5.16.

Fixed-bed behaviour illustrated in Figure 5.10(a) was discovered for the 3.15–4.0 mm particle fraction, as the bed was completely defluidized because of the larger particle size and the lack of fine particles lubricating and reducing bed viscosity. Consequently, heat transfer coefficients were relatively low for this particle fraction, no significant increase in h can be seen in Figure 5.16, even at higher flow rates. The bed-to-surface heat transfer coefficient increased slightly from 53.4 W/(m²·K) at $1.0U_{mf}$ to 64.6 W/(m²·K) at $1.4U_{mf}$.

For the 1–3.15 mm particle fraction, as gas flow rate increased from 1.0 to $1.5U_{mf}$ the bed exhibited a series of different flow behaviours, from fixed-bed at $1.0U_{mf}$, piston-like at $1.1U_{mf}$, partially fluidized at $1.2U_{mf}$, channeling at $1.3U_{mf}$ to proper fluidization at $1.4U_{mf}$ and above. The overall heat transfer coefficient was higher than that of the 3.15–4.0 mm fraction. The highest heat transfer rates were found with the 0–1 mm particle fraction. The smaller average particle diameter likely reduced the thermal residence time of particles, contributing to faster particle convective heat transfer. The presence of fine particles may also have enhanced the gas–solid flow and heat transfer. As a result, heat transfer coefficients were over 120 W/(m²·K) at all flow rates, with a maximum of 129.3 W/(m²·K) found at $1.1U_{mf}$.

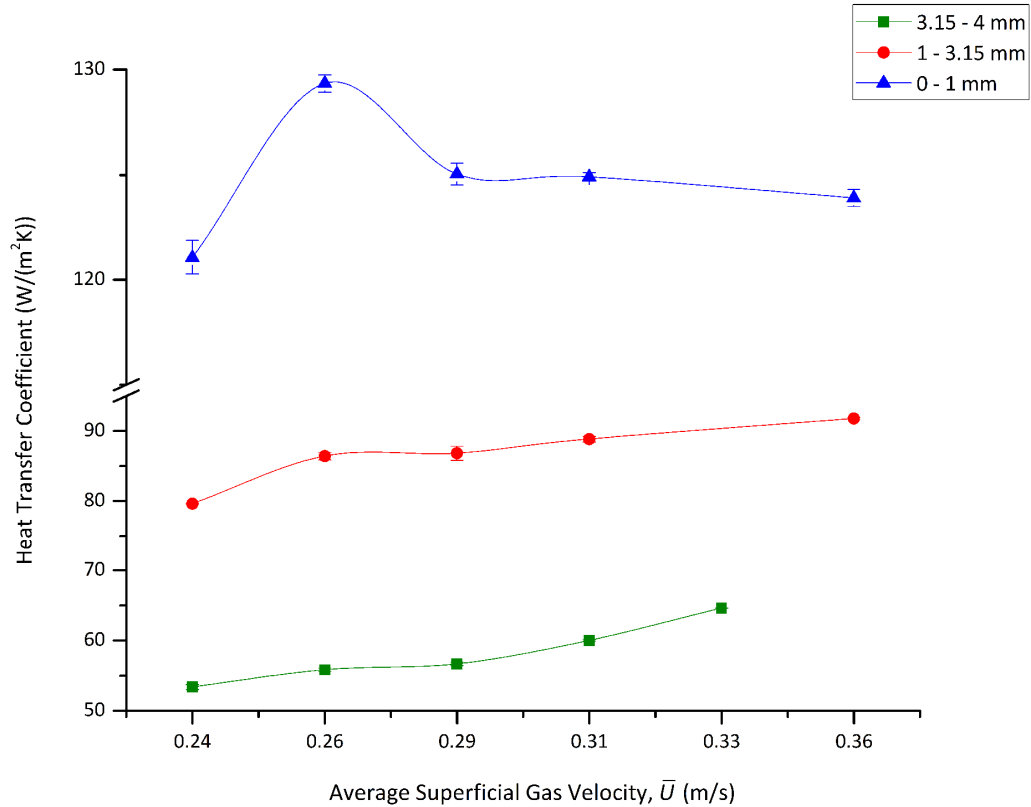


Figure 5.16 The effect of particle size on heat transfer in the tapered pulsed fluidized bed with Douglas fir sawdust (experimental data points with spline interpolations)

The influence of fines was verified by testing the heat transfer coefficients of particle mixtures with different weight percentage of fine particles. Douglas fir sawdust of 0–1 mm was added to the 1–3.15 mm particle fraction at the following weight percentages: 0%, 33%, 50% and 75%. Results of the heat transfer coefficients are plotted in Figure 5.17. Similar to the rectangular fluidized bed, non-ideal flow behaviour was observed in the 0%, 33% and even 50% groups, including partial defluidization, channeling and bridging. It is possible that by adding more fines into a coarse particle mixture the coarse particles more readily to adhere to each other, which increases the mobility of the bed. Small particles also have smaller thermal capacity, which leads to higher particle convective heat transfer. As a result, exceptional gas–solid contact and heat transfer rate were observed for the 75% fines group where the maximum heat transfer coefficient was 126.8 W/(m²·K).

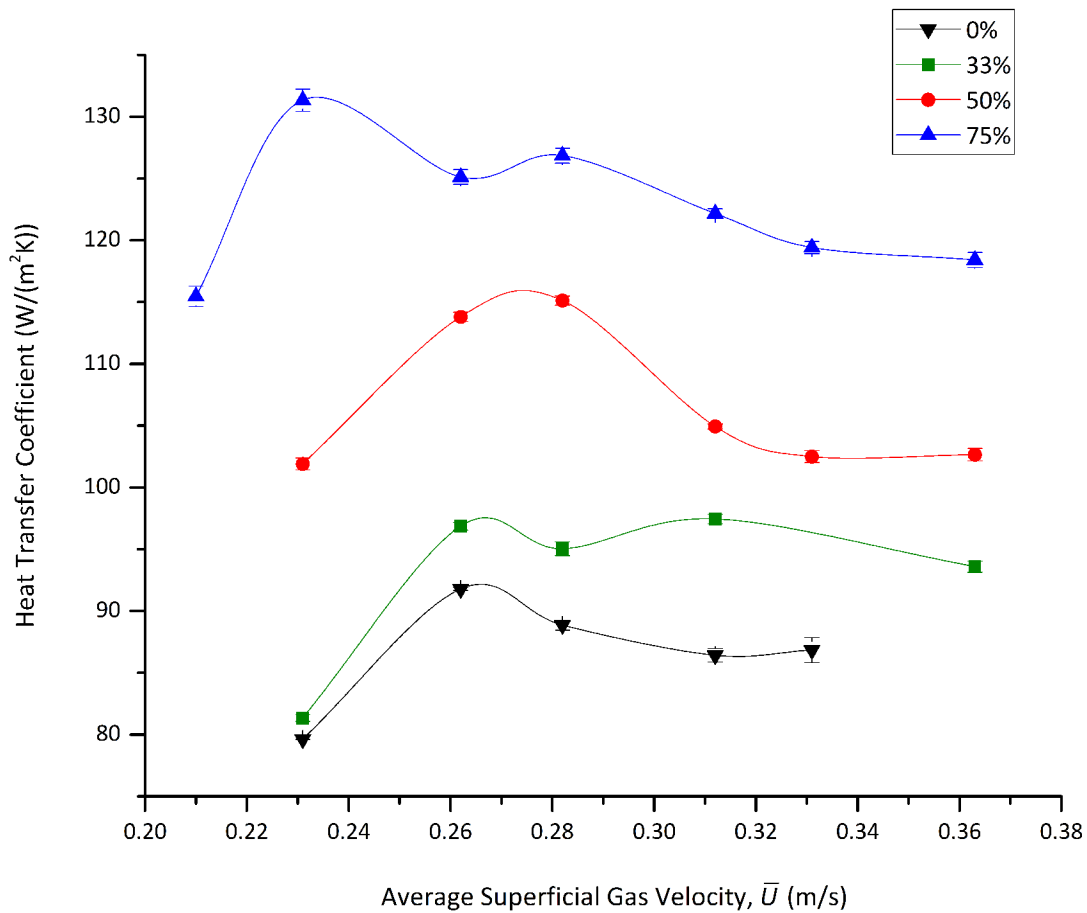


Figure 5.17 Effect of fine particles on the bed-to-surface heat transfer of Douglas fir sawdust in the pulsed fluidized bed of tapered bottom section (experimental data points with spline interpolations)

5.2.5 Pine and switchgrass

The bed-to-surface heat transfer coefficients of both pine and switchgrass particles were tested in the pulsed fluidized bed with tapered bottom section. Unique heat transfer trends were discovered, as can be seen from Figure 5.18.

For pine sawdust, there were two distinct peaks of heat transfer coefficient as a function of pulsation frequency, as shown in Figure 5.18(a). The first peak was observed at $f=1.0$ Hz where $h=108.3, 110.9$ and 113.3 W/(m²·K) for $\bar{U}=0.26, 0.31$ and 0.36 m/s, respectively. As soon as pulsation frequency

reached 2 Hz, another peak was observed, where $h=110.0 \text{ W}/(\text{m}^2\cdot\text{K})$ for $\bar{U}=0.26 \text{ m/s}$. Above 4 Hz pulsation frequency, the measured heat transfer coefficient increased again. Interestingly, no second peaks were observed during the heat transfer tests of pine sawdust in the tapered fluidized bed, nor during the heat transfer measurements of switchgrass and pine in rectangular fluidized bed. Although the fluctuations of heat transfer coefficient were not very significant, from roughly 96 to $120.0 \text{ W}/(\text{m}^2\cdot\text{K})$, it is still a unique phenomenon, as the average superficial gas velocity remained the same for all the pulsation frequencies investigated. It is likely that this phenomenon is associated with the flow behaviour in the tapered fluidized bed. As pulsation frequency slowly increases, the oscillating gas flow rate in the "ON" period reduces, which is caused by the reduced pressure build-up in the shorter "OFF" periods. It is highly likely that the heat transfer coefficient is affected by the decline in the gas flow rate. Moreover, besides the actual duration of "OFF" periods getting shorter, the time percentage of "OFF" period in a pulsation cycle also decreases with increasing pulsation frequency. The intermittent fluidization where only a fraction of time that the bed is fluidized gradually transitions to a more continuous fluidization as pulsation frequency increases, which is beneficial to heat transfer. Consequently, the reduction in gas flow rate and intermittence more or less offset each other, and without other contributing factors, the heat transfer coefficient across all pulsation frequencies should remain the same. However, as demonstrated in Figure 5.10(c), the core–annulus flow behaviour is unique to the tapered fluidized bed, and it may have played a role in this case.

There is a strong possibility that the first peak around 1 Hz for pine was associated with the resonance effect around the natural frequency of the system where gas–solid contact was enhanced. As pulsation frequency moved away from this range and further increased to 1.5 Hz, the effect of particle resonance wore off and the heat transfer coefficient declined. At 2 Hz pulsation frequency, the core–annulus flow behaviour was observed, where an increasing amount of gas went through the dense phase in the centre of the bed adjacent to the heat transfer probe, causing a local increase in heat transfer coefficient, while in fact the heat transfer coefficient of the fluidized

bed decreased due to the lateral segregation. Further increasing frequency to 3 Hz, the intensity of the pulsation became too weak to support even the core–annulus flow. Instead, the piston-like flow took place in the tapered bed, as illustrated in Figure 5.10(c). The dense phase particles moved up and down as a whole as the gas phase could no longer overcome the cohesive forces and penetrate the bed. Particles were brushing against the heat transfer probe at a relatively high frequency, attributing to the slight decrease in heat transfer coefficient at 3 Hz. At 5 Hz and above, the bed became partially defluidized as the pulsation became weaker. During experiment, it was also observed that a significant amount of air went through the gap between the probe and the dense phase particles, entraining particles in this area, which may have resulted in an increase in local heat transfer coefficient. However, the overall heat transfer as well as gas–solid contact was very poor.

Such a phenomenon occurred at all flow rates because of the geometry in the tapered fluidized bed, but was not encountered in the rectangular bed. This is likely associated with the geometry of the tapered bed and the unique properties of the sawdust particles under pulsed gas flow. Further investigation is need to better understand the phenomenon in the future.

Compared to pine, switchgrass particles had a smaller average diameter and larger weight percentage of fines, which is consistent with the fact that switchgrass particles had better heat transfer performance than pine and Douglas fir. The maximum heat transfer coefficient measured for pine was $120.4 \text{ W}/(\text{m}^2\cdot\text{K})$ with $f=5 \text{ Hz}$ and $\bar{U}=0.36 \text{ m/s}$. For switchgrass, the maximum was $158.5 \text{ W}/(\text{m}^2\cdot\text{K})$ with $f=5 \text{ Hz}$, $\bar{U}=0.36 \text{ m/s}$. From Figure 5.18(b) it is also clear that at 1 Hz heat transfer coefficient reached a peak, which could be attributed to the increase in particle resonance. Lateral segregation at 4 and 5 Hz may have resulted in the higher local heat transfer coefficients.

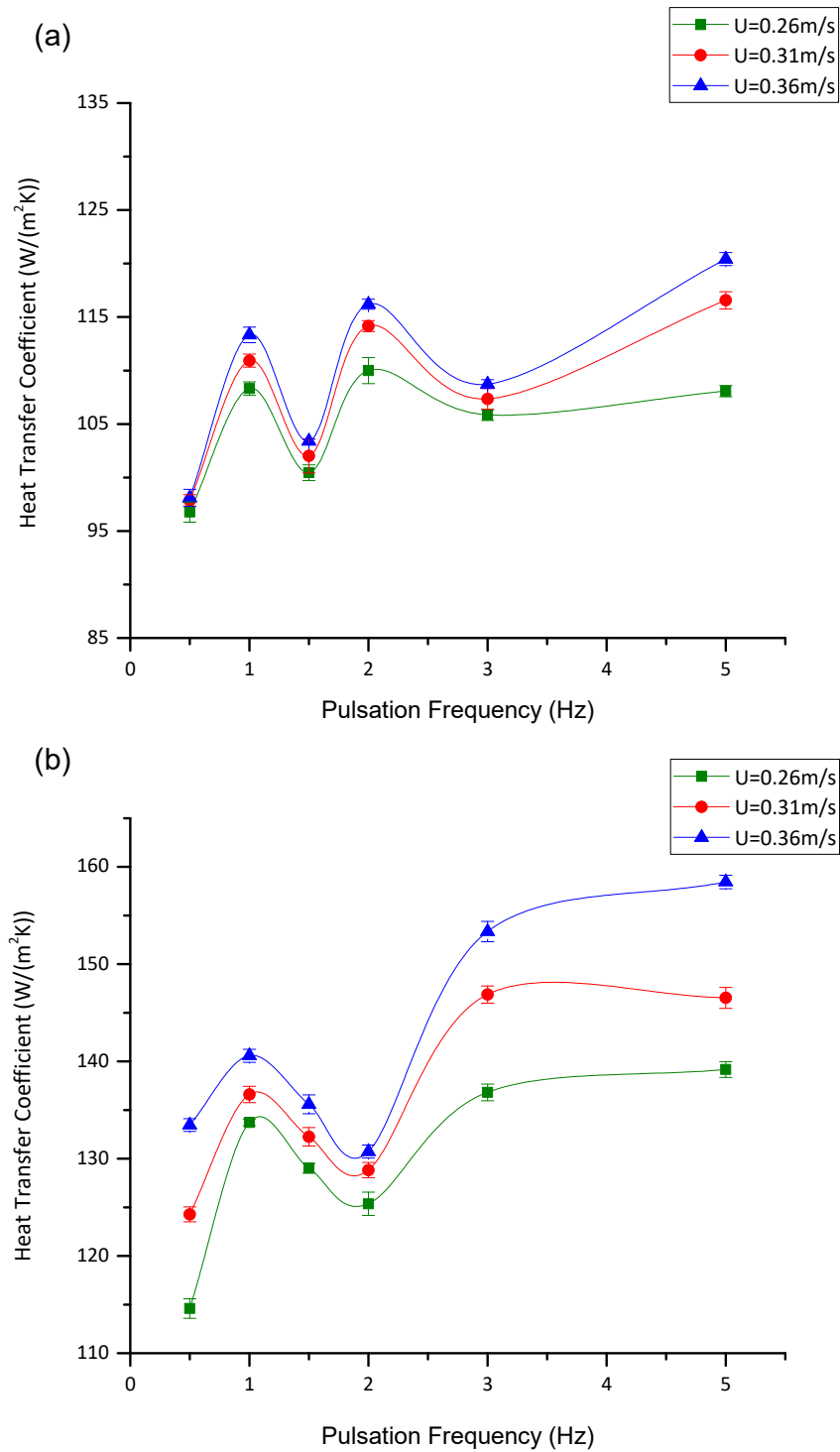


Figure 5.18 Heat transfer coefficients of various biomass species in pulsed fluidized bed with tapered bottom section at various pulsation frequencies (experimental data points with spline interpolation lines). (a) Pine; (b) Switchgrass.

5.3 Comparison of two geometries

The differences in flow behaviour and heat transfer rates between the two reactor geometries have been demonstrated in previous sections. To better visualize the difference, heat transfer coefficients in two reactor geometries are plotted against superficial gas velocity in Figure 5.19 where the tapered bed exhibited higher heat transfer rates compared to the rectangular bed. It is very likely that the improvement stems from the improved gas–solid contact efficiency in the tapered bed. Channeling is greatly suppressed in the tapered design because of the diverging column wall. When the operating conditions are not ideal and the pulsations are weak, instead of forming gas channels like in the rectangular bed (illustrated in Figure 5.20(c)), a fountain is instead formed in the centre of the bed, pushing particles upwards and eventually gliding down the column wall, making their way to the distributor (Figure 5.10(c)).

Results generated from the heat transfer measurements seem to corroborate the batch drying test results where the tapered bed outperformed the rectangular geometry. Both the heat transfer coefficient and water removal efficiency were higher in the tapered bed, indicating its improvement in heat and mass transfer. It should be noted, however, that the heat transfer coefficients displayed in Figure 5.19 are measured from the centre of the bed, which may not reflect the heat transfer rates at other regions of the bed, especially the wall area.

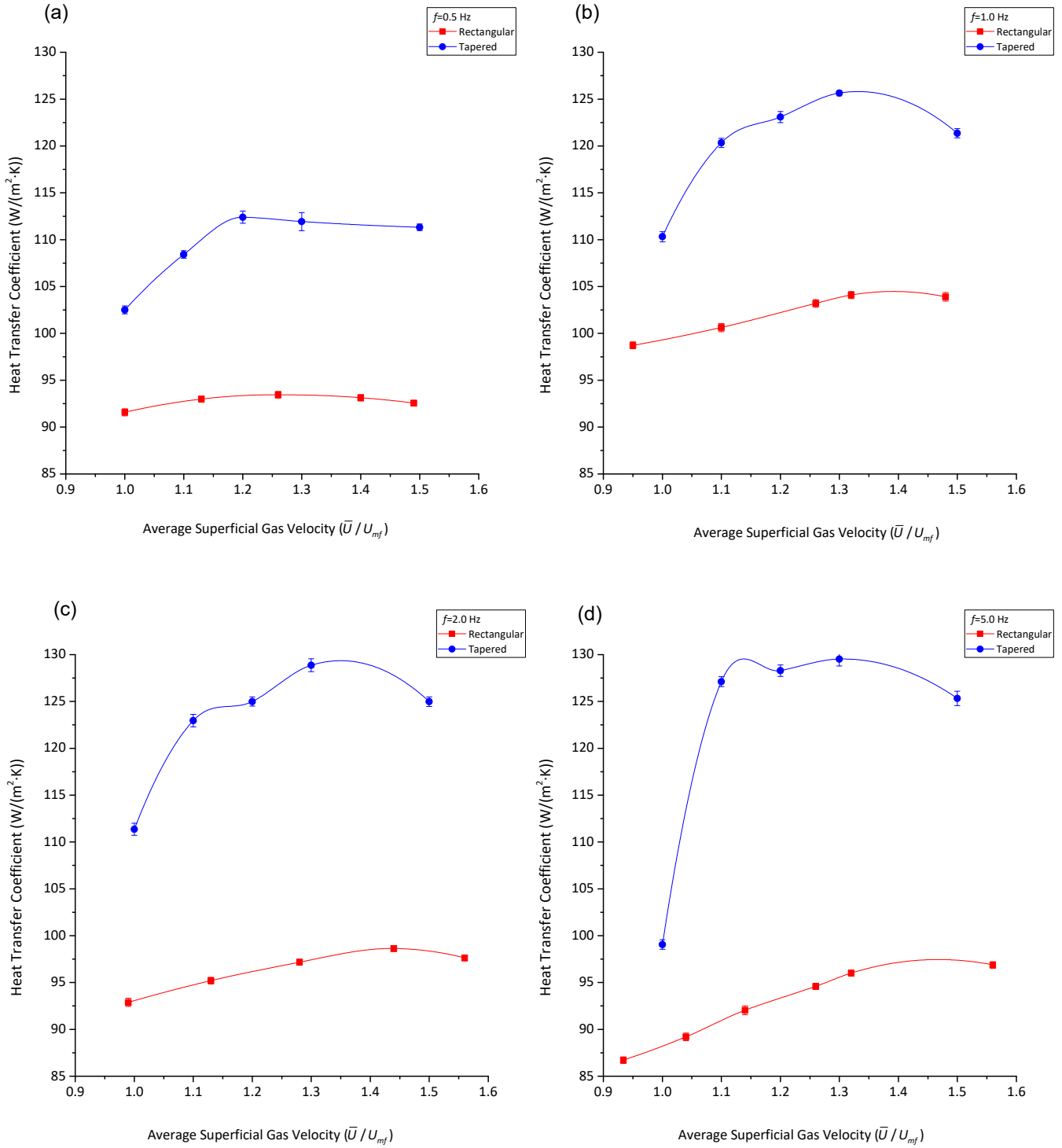


Figure 5.19 Bed-to-surface heat transfer coefficients vs. superficial gas velocity of Douglas fir sawdust at four different pulsation frequencies in two reactor geometries (experimental data points with spline interpolation lines). (a) $f=0.5$ Hz; (b) $f=1.0$ Hz; (c) $f=2.0$ Hz; (d) $f=5.0$ Hz.

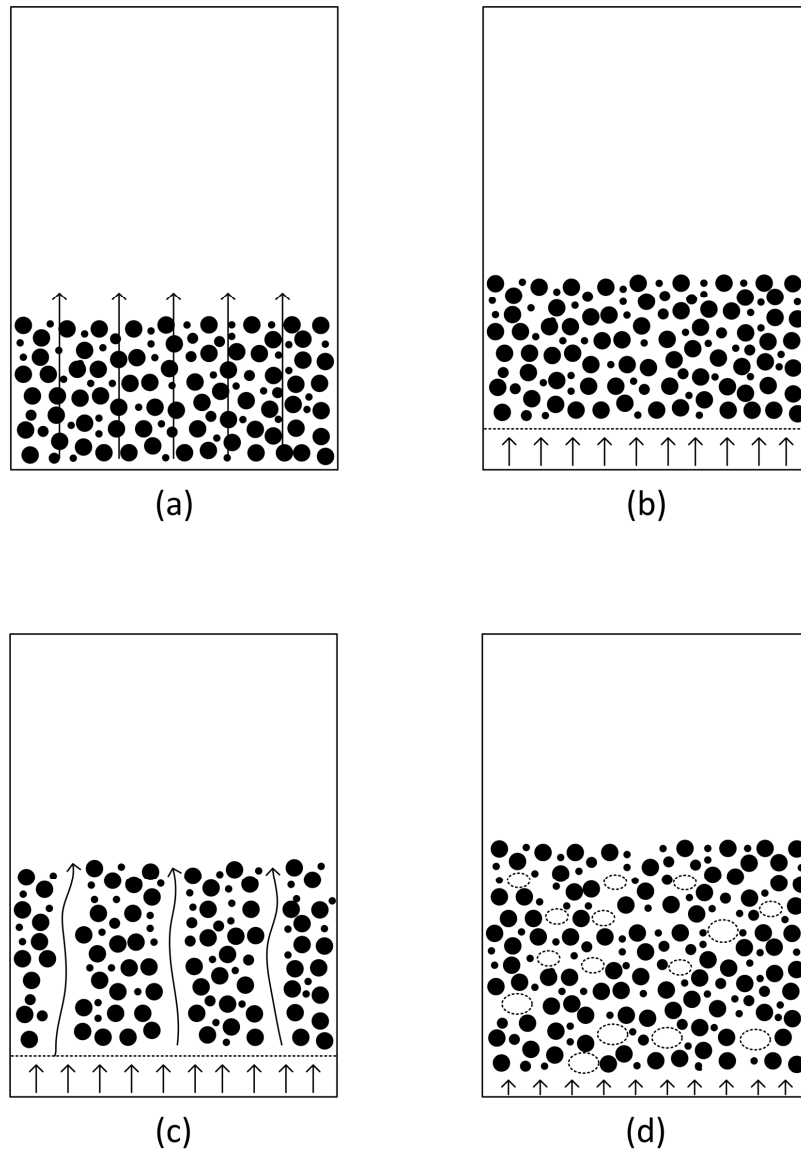


Figure 5.20 Flow behaviour at different superficial gas velocities in the rectangular pulsed fluidized bed. (a) Fixed bed behaviour; (b) Piston-like behaviour; (c) Segregated flow behaviour with severe channeling; (d) Regular, fully fluidized flow pattern.

5.4 Heat transfer modelling in pulsed fluidized bed

5.4.1 Overview and particle convective heat transfer

Different approaches could be taken when it comes to modelling and predicting the heat transfer coefficient in fluidized beds. Many attempts have been made to link heat transfer coefficient with gas flow rate and other properties of the fluid and particles. In most cases, empirical correlations are established between Nusselt number (Nu), the fluid Prandtl number (Pr) and Reynolds number (Re).

Another approach is mechanistic modelling. The packet theory proposed by Mickley and Fairbanks (1955) is one of the most appropriate models for fluidized bed heat transfer. In this model an analogy is made with the surface renewal theory for mass transfer (Danckwerts, 1951) where heat transfer surface is contacted alternately by gas bubbles and the dense phase (or packets). Heat transfer is achieved by transient conduction between packet and heating surface through the gas film, over the brief periods of time when the packets reside on the surface. The instantaneous heat transfer coefficient between an isothermal heating surface and the packet is shown in Eqn. (1.14). The time-averaged heat transfer coefficient may be calculated if the residence time distribution of the packets is available. In the slugging regime where the upward velocity of the dense phase has been shown to be $(U - U_{mf})$ (Kay & Nedderman, 1974). Therefore, for a short vertical surface of Length L_s (m), residence time is,

$$\tau = L_s / (U - U_{mf}) \quad (5.1)$$

whereas in bubbling fluidized beds the upward motion of packets is mostly attributable to the motion of gas bubbles, specifically the wake and drift of the bubbles. Assume the upward velocity of the bubble wake is close to the bubble rise velocity U_B (m/s), then the residence time of the packets could be expressed as,

$$\tau = L_s / U_B \quad (5.2)$$

When the heat transfer surface is longer than the distance travelled by the packet before it is interrupted by a rising bubble, the characteristic length L_C (m) of the contact time should replace the surface length L_S . It has been shown that L_C can be taken as about half the bubble diameter d_B (m). In a fluidized bed with a multi-orifice distributor, bubble size at a given bed height z (m) can be calculated based on the semi-empirical correlation proposed by Mori and Wen (1975),

$$d_B = d_{Bm} - (d_{Bm} - d_{B0}) \exp(-0.3z / D_t) \quad (5.3)$$

$$d_{Bm} = 1.64 \left[A(U - U_{mf}) \right]^{0.4} \quad (5.4)$$

$$d_{B0} = \frac{1.38}{g^{0.2}} \left[\frac{A(U - U_{mf})}{N_{or}} \right]^{0.4} \quad (5.5)$$

D_t (m) is the diameter of the fluidized bed column, A is the cross-section area of the bed, and N_{or} is the number of orifices on the distributor plate. Bubble rise velocity can be estimated by equation developed by Grace (1982),

$$U_B = 0.71 \sqrt{gd_B} + (U - U_{mf}) \quad (5.6)$$

The average heat transfer coefficient between the dense phase and the heat transfer surface can then be obtained through integration, assume $L_C < L_S$,

$$h_p = \int_0^\tau \frac{h_i}{\tau} dt = 2 \sqrt{\frac{k_{eff} \rho_{mf} c_{p,mf} U_B}{L_C}} \quad (5.7)$$

where $c_{p,mf}$ and ρ_{mf} can be estimated respectively by c_{pp} (heat capacity of the solids) and $\rho_p(1 - \varepsilon_{mf})$. Since heat transfer surface is alternately contacted by dense phase and bubbles, the fraction of bed that is occupied by bubbles must be taken into consideration for the calculation of particle convective heat transfer,

$$h_{pc} = h_p(1 - \varepsilon_B) \quad (5.8)$$

The effective conductivity k_{eff} (W/(m·K)) is generally acknowledged to be the sum of two components, k_{es} and k_{ef} (Davidson et al., 1985),

$$k_{eff} = k_{es} + k_{ef} \quad (5.9)$$

in which k_{ef} represents conductivity due to fluid flow, and k_{es} is the thermal conductivity of fixed beds filled with stagnant fluid. k_{es} has been thoroughly studied; correlations can be found in Yagi and Kunii (1960), as well as Kunii and Smith (1960). A correlation proposed by Deissler and Boegli (1958) also applies,

$$\frac{k_{es}}{k_g} = \left(\frac{k_p}{k_g} \right)^{0.28 - 0.757 \log_{10} \varepsilon - 0.057 \log_{10} (k_p/k_g)} \quad (5.10)$$

k_{es} values calculated from above equation are in good agreement with that predicted by Kunii and Smith (1960) and experimental data by Dietz (1979). k_{ef} on the other hand is given by Ranz (1952),

$$k_{ef} = 0.1 \rho_g c_{pg} d_p U_{mf} \quad (5.11)$$

5.4.2 Gas convective heat transfer

For a system with large particles, the contribution of gas phase to overall heat transfer should not be neglected. This is mostly due to the fact that in systems with larger particles, heat penetrates fewer layer of particles at the heat transfer surface, and it has been shown that the void fraction near the wall is larger than that at the core of a fixed-bed reactor (Kimura et al., 1955), which indicates that the influence of gas properties is no longer negligible. In fact gas convection becomes dominant when particle diameter is larger than 3 mm (Baskakov et al., 1973).

For a vertical cylinder immersed in a fluidized bed, Gabor (1970) showed the integral mean gas convective heat transfer coefficient over the entire length could be expressed as,

$$h_s = \sqrt{\frac{4k_{eff} \rho_g c_{pg} U}{\pi L_s}} + \frac{k_{eff}}{D_s} \quad (5.12)$$

where D_s (m) is the diameter of the cylinder. It has been verified experimentally that bed-to-surface heat transfer is heavily influenced by gas thermal conductivity, as well as the volumetric heat capacity of solids ($\rho_p c_{pp}$). Better agreement was obtained if a thin gas layer of thickness $d_p/6$ was assumed at the wall in series with the dense phase (Catipovic, 1979; Gabor, 1970),

$$h_w = 6k_g / d_p \quad (5.13)$$

Many researchers considered the simple approach of factoring the wall resistance along with the bed resistance (Calderbank & Pogorski, 1957; Denloye, 1976), such that the overall gas convection component h_{gc} (W/(m²·K)) is in the form of,

$$h_{gc} = \frac{1}{1/h_s + 1/h_w} \quad (5.14)$$

Therefore, the overall heat transfer coefficient h is simply the sum of particle convective and gas convective component,

$$h = h_{gc} + h_{pc} \quad (5.15)$$

5.4.3 Application to pulsed fluidized beds

The oscillating nature of the pulsed fluidized bed has made heat transfer modeling rather challenging. Kobayashi et al. (1970b) experimentally investigated the effects of pulsation on heat transfer in a gas-fluidized bed. Pulsation resulted in an attenuation of the bubbling phenomenon,

shorter particle residence times, and a lower bubble volume fraction compared with a conventional fluidized bed with continuous gas flow. Increases in heat transfer were attributed to active particle gas–solid contact below minimum fluidization (Kobayashi et al., 1970a).

Pulsed fluidized beds exhibit different behaviour at different pulsation frequencies. At lower pulsation frequencies, distinct “ON” and “OFF” periods where vigorous gas–solid contact occurs in the “ON” period, followed by the motionless “OFF” period. As pulsation frequency increases above natural frequency of the system, “OFF” periods become less discernable. However, velocity and pressure still vary greatly in each cycle. Therefore, it seems reasonable to take different approaches to model heat transfer in pulsed fluidized beds operating above or below natural frequency, which are elaborated in Section 5.4.4 and 0, respectively. It should be noted that the proposed heat transfer model is intended for the rectangular fluidized bed only, as in the tapered fluidized bed certain unique flow behaviour was observed, such as core–annulus flow, which may alter the hydrodynamics and heat transfer. Moreover, the following model is intended for uniform fluidization in the bubbling regime operated under periodic gas pulsations. Channeling, jetting and other non-ideal flow behaviour is not considered.

5.4.4 Model for low pulsation frequency (Model 1)

For fluidized beds operated below the natural frequency where intermittent fluidization occurs, the “ON” period could simply be treated as a continuous fluidized bed while the “OFF” period to be treated as a fixed-bed reactor with motionless fluids. The overall heat transfer coefficient should be a combination of the two. In this case, the average superficial gas velocity in the “ON” period can be calculated by,

$$\bar{U}_{ON} = \frac{\bar{U}}{\beta} \quad (5.16)$$

here \bar{U} (m/s) is the average superficial gas velocity based on the entire cycle of gas pulsation, whereas \bar{U}_{ON} (m/s) represents the average superficial gas velocity in the “ON” period, with β being the time fraction of the “ON” period. It is noteworthy that β increases with pulsation frequency. The value of β can be gathered from the high-speed camera footage, as well as the bed pressure drop signals. By substituting U with \bar{U}_{ON} in Eqns. (5.3)–(5.6) bubble size and bubble rise velocity in the intermittently fluidized pulsed bed are obtained. Although the above equations are intended for Group B particles with regular shape and that most particles used in this study are on the B/D boundary with low sphericity, reasonable results have been gathered from equations above.

The overall heat transfer coefficient of the “ON” period h_{ON} that consists of a particle convective and gas convective component can be evaluated from Eqns. (5.7)–(5.15) by simply replacing U with \bar{U}_{ON} . Heat transfer coefficient of the “OFF” period h_{OFF} (W/(m²·K)) is equivalent to that of a fixed-bed reactor with stagnant fluid,

$$h_{OFF} = k_{es} / L_C \quad (5.17)$$

Finally, the overall heat transfer coefficient calculated according to Model 1 adds up to be,

$$h_1 = \beta \cdot h_{ON} + (1 - \beta) \cdot h_{OFF} \quad (5.18)$$

5.4.5 Model for high pulsation frequency (Model 2)

Above the natural frequency, only one set of voids (slugs or bubbles) are formed above the distributor in each pulsation cycle, as the gas is cut off before a new set could be formed. The bubble frequency becomes increasingly close to pulsation frequency as pulsation frequency increases. Bubble size decreases with bubble frequency. In light of the oscillating velocity profile, initial gas velocity at the beginning of each “ON” period when bubbles are formed (U_{inv} m/s) is considered to be the velocity from which bubble size and bubble rise velocity are calculated.

In order to obtain U_{in} , high-speed camera footage was deconstructed into full-resolution uncompressed images frame by frame, resulted images were imported into ImageJ (ver. 1.46r) so that velocimetry could be performed. The boundary of biomass particles and the voids (bubbles or slugs) was tracked to determine the inlet velocity of the air. In the beginning of each cycle, large amount of gas enters the fluidized bed where a horizontal layer of slugs is formed. By tracing the movement of the boundary, U_{in} could be calculated by,

$$U_{in} = \frac{\sum_{j=1}^N \lambda_j}{N t_0} \quad (5.19)$$

where λ_j (m) is the distance of the boundary travelled within t_0 (s), which is the time interval between each frame of footage. Since the footage was filmed at 240 frame per second, $t_0 \approx 4.17 \times 10^{-3}$ s. Substitute U_B with U_{in} in Eqn. (5.7) and U with U_{in} in Eqn. (5.12) and the overall heat transfer coefficient h_2 (W/(m²·K)) could be calculated.

5.4.6 Results from the heat transfer modelling

Heat transfer coefficient in the rectangular fluidized bed at $\bar{U} = 1.1U_{mf}$ from both models were calculated, plotted against the experimental data in Figure 5.21. Both models seem to be capable of predicting heat transfer coefficients in their designated frequency ranges. The overestimation of heat transfer coefficients in Model 1 for $f > f_N$ is likely caused by the fact that above f_N "OFF" period started to disappear, the bed could no longer be divided into two distinct heat transfer processes. As a result, h_1 values increased asymptotically with pulsation frequency.

In the second model designated for $f > f_N$ good agreement with the experimental data was achieved. The slight overestimation at higher pulsation frequencies is presumably caused by some mild channeling occurring at such frequencies, where gas pulsations were simply not strong enough to penetrate the entire bed. Apply such a model for $f < f_N$ would likely produce higher h_2

values because the bed could no longer be fluidized continuously, and the increasing “OFF” period should now be taken into consideration.

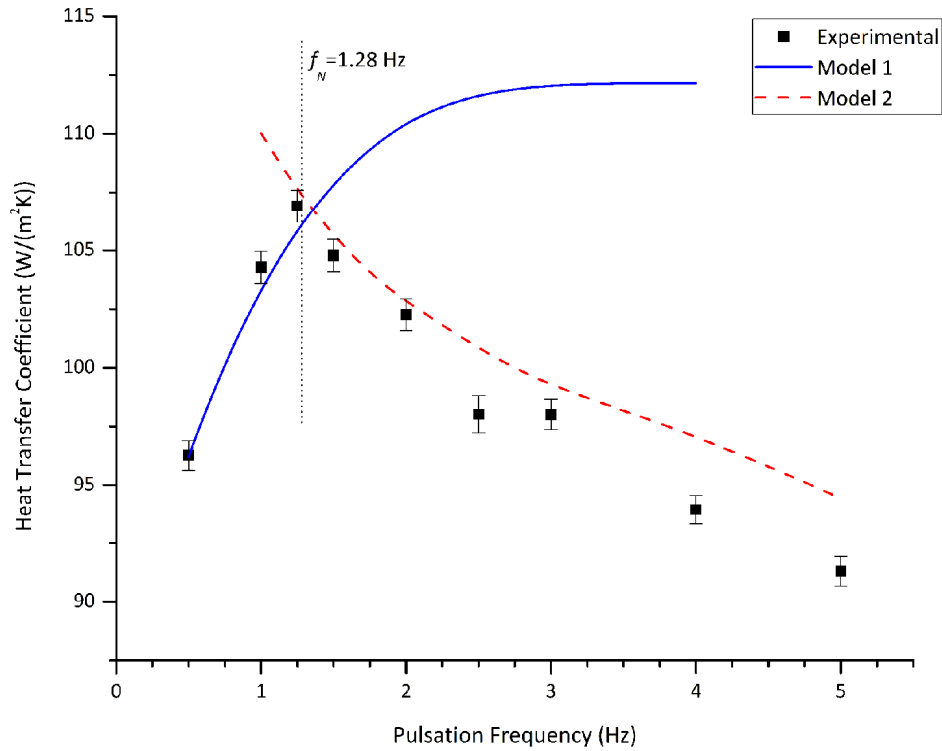


Figure 5.21 Experimental and fitted heat transfer coefficients from two models in pulsed fluidized bed, with Douglas fir sawdust at $\bar{U} = 1.1U_{mf}$

Natural frequency of the pulsed fluidized bed system was calculated based on Eqn. (3.2). Around f_N heat transfer coefficient predictions from Model 1 and Model 2 were very close, so that the heat transfer coefficient could be calculated from either model for $f = f_N$. Consequently, combining Model 1 and Model 2 the overall heat transfer model for pulsed fluidized bed has the final form of,

$$h = \begin{cases} h_1 & f < f_N \\ h_2 & f \geq f_N \end{cases} \quad (5.20)$$

The above model was also verified at a higher average superficial gas velocity of $1.4U_{mf}$, as seen in Figure 5.22. For both flow rates, the highest heat transfer rate occurred around the natural frequency of the system, which was calculated to be approximately 1.28 Hz, which is consistent with the experimental results listed in previous sections of this chapter. Again, the enhanced heat transfer may have stemmed from the resonance effect that occurs when external excitation (pulsed gas flow) frequency approaching the natural frequency of the system. In fluidized beds, it translates to better gas–solid contact and faster renewal of packets on heating surfaces, and consequently a higher heat transfer coefficient.

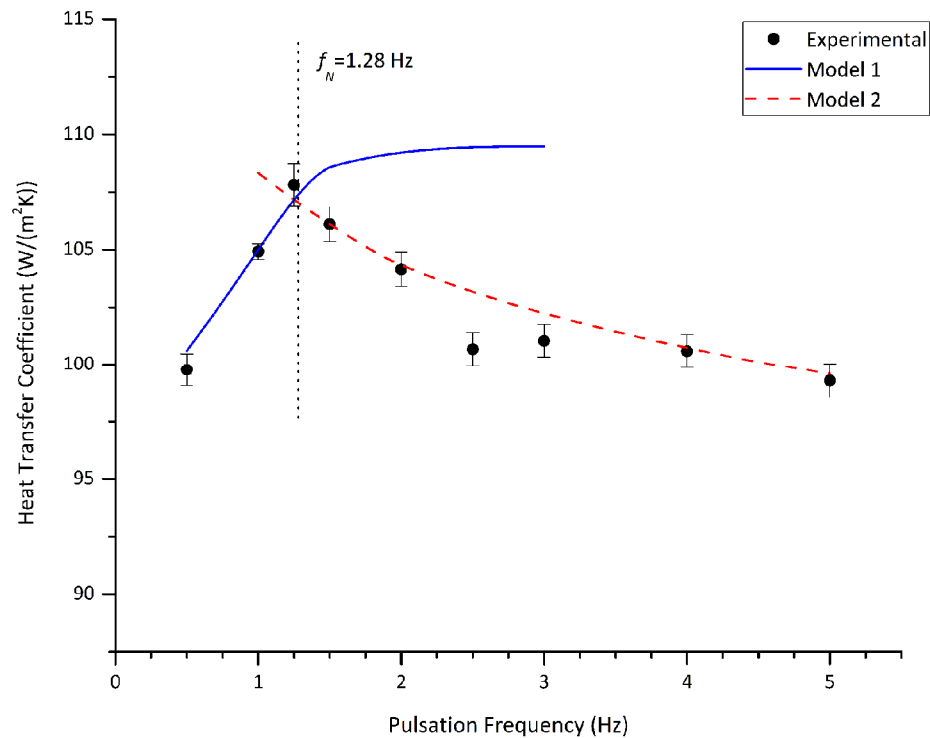


Figure 5.22 Experimental and fitted heat transfer coefficients from two models in pulsed fluidized bed, with Douglas fir sawdust at $\bar{U} = 1.4U_{mf}$

It is noteworthy that above heat transfer model was developed based on a specific pulsed fluidized bed system demonstrated in this work, which contained Douglas fir sawdust with an average

particle diameter of 1.45 mm. Parameters such as particle density, thermal conductivity as well as gas inlet velocity have to be determined before the model is applied to another system. In addition, due to the oscillatory nature of the system, heat transfer coefficients obtained from the experiments and from above model may deviate significantly from the values obtained through common heat transfer correlations such as Eqn. (1.12) in which pulsation was not considered.

5.4.7 Conclusion

Bed-to-surface heat transfer coefficient was investigated as an essential step towards utilizing pulsed fluidized bed as a potential reactor for biomass torrefaction and pyrolysis. The effect of gas flow rate and pulsation frequency was thoroughly researched. Heat transfer coefficient generally increases with flow rate. In the case of pulsation an optimum frequency exists, which is the natural frequency of the pulsed fluidized bed system. At such frequency, gas pulsations are strong enough to lift the entire bed without too much entrainment that could also enable the pulsed gas flow to overcome channeling. In the meanwhile, the pulsations are frequent enough so that the motionless "OFF" period is eliminated. Together with the resonance effect, highest bed-to-surface heat transfer coefficient was observed. The interaction between particle convective and gas convective heat transfer is also a bit more complex than for conventional fluidized beds because the ever-changing gas flow rate varies not only with the overall gas flow rate, but also with pulsation frequency. A low pulsation frequency will likely momentarily generate a very high superficial gas velocity at the beginning of "ON" periods, which leads to higher gas convection. On the other hand, at higher pulsation frequencies, the faster bubble generation and solid circulation enhance particle convection. The heat transfer as a result is comprised of two different mechanisms, divided around the natural frequency of the system. The combined model showed good agreement with experimental results.

In addition, the influence of particle size distribution as well as fine particles on heat transfer was analyzed. The lubricant effect of fines promotes movement of coarse particles and enhances heat transfer, which could explain the measured higher heat transfer coefficient of switchgrass. Pine on the other hand, exhibited similar heat transfer rates as Douglas fir. The addition of vibration was found to be optional, as it offered marginal improvement in terms of gas–solid contact and mass transfer. Dead zones were eliminated by the tapered bottom section. Improved heat transfer rates were also observed in the tapered bed. Flow behaviour unique to the tapered geometry was discovered where a fountain formed in the centre of the bed, with lower particle fraction and higher gas flow rates, leading to lateral segregation and enhanced gas convection. It is one of the main contributors for the higher-than-expected heat transfer coefficients measured in the tapered bed at high pulsation frequencies, despite the fact that the bed was visually confirmed to be behaving rather poorly in terms of gas–solid contact.

By moving the heat transfer probe away from the centre and measuring the heat transfer coefficients at different lateral positions it was confirmed that lateral segregation did exist in the tapered fluidized bed. The difference in heat transfer coefficients between the centre and the annulus region could be as much as $10 \text{ W}/(\text{m}^2\cdot\text{K})$. In order to maintain ideal gas–solid contact and decent heat transfer rates, pulsation needs to be sufficiently strong, which means the pulsation frequency should never be too far away from the natural frequency of the system. Experimental results regarding duty cycle indicate that in order to maximize heat transfer rates, duty cycle should not be too small such that the amount of air allowed into the unit is small, causing channeling and piston-like flow behaviour. In the meanwhile, duty cycle should not be too large such that the effect of pulsation is diminished. This is consistent with the experimental findings that a duty cycle of 40%–50% offered highest heat transfer coefficients.

The difference in particle size and thermal properties between various biomass particles reveals the challenge in fluidizing biomass particles from different sources. Properties such as minimum

fluidization velocity and angle of repose could vary significantly with moisture content, particle size, density and sphericity. Nevertheless, with a reasonable pulsation frequency and gas flow rate, flow behaviour of biomass particles could be restored to normal in pulsed fluidized beds, especially in the tapered bed where marked improvement in mass transfer and heat transfer was observed compared to the non-tapered bed.

CHAPTER 6

CONCLUSIONS AND RECOMMENDATIONS

6.1 Conclusions

This work addresses a number of issues that are key to the utilization of biomass as a potential energy source via thermal conversion such as torrefaction and pyrolysis. Pulsed gas flow has been identified as a highly effective technique in fluidizing biomass particles with high moisture content, low bulk density and irregular shapes in the absence of any inert bed particles, therefore eliminating any chance of contamination of biochar product. Thorough studies in Chapter 3 have identified the optimum operating conditions at which pulsed gas flow is most effective in terms of gas–solid contact and mass transfer by employing batch drying as an indirect indicator for gas–solid contact and mass transfer performance. Two-phase drying models for both the rectangular and tapered fluidized bed geometry proposed in Chapter 4 further corroborate the experimental findings, and can be easily adopted in process simulations for designing thermal conversion processes.

The bed-to-surface heat transfer coefficients of different biomass species under a number of operating conditions are presented in Chapter 5, which are key to the design and operation of heat exchangers in fluidized bed dryers, torrefiers and pyrolysis reactors. Such data are rarely reported in the literature. In addition, the heat transfer mechanism in pulsed fluidized bed is discussed in Chapter 5, where slight modifications are made to the packet model for heat transfer in fluidized beds to allow for the influence of gas pulsations to be included. The model shows good agreement with experimental data.

Key findings of this work are listed below.

- Biomass particles can be successfully fluidized with the assistance of gas pulsation, without the need of any other bed particles. The hydrodynamics of the pulsed fluidized bed is heavily influenced by the pulsation frequency. At low pulsation frequencies, fluidized bed is intermittently fluidized with half of the time being stationary and the other half rigorously fluidized, exhibiting great amplitude of pressure fluctuations and bed expansion. Increasing the pulsation frequency reduces intermittence, leading to faster bubble generation, gas–solid contact and consequently higher mass transfer rate. However, too high a frequency will ultimately weaken the gas pulsation, which could lead to undesired flow behaviour such as channeling, partial and complete defluidization.
- The oscillating nature of the pulsed gas flow enables the fluidized bed to be intermittently fluidized even when the average gas flow rate is below what is required for minimum fluidization. Faster drying and mass transfer are accompanied by higher gas flow rates. The optimum operating condition seems to be $\bar{U} = 1.1 - 1.3U_{mf}$, coupled with a pulsation frequency of 0.75 – 1.5 Hz. Such an operating condition guarantees that the pulsation is sufficiently intense so that the undesired flow behaviour such as channeling can be eliminated. In addition, the proximity to the natural frequency also ensures enhanced gas–solid contact efficiency.
- By adding a tapered bottom section to the original rectangular fluidized bed, different flow behaviour was observed, with dead zones at the bottom of the bed eliminated. In general, as the intensity of gas pulsation increases, instead of becoming partially or completely defluidized, as in the rectangular bed, a fountain forms in the centre of the tapered fluidized bed where particles are carried upwards and returned slowly downwards through the exterior area closer to the wall. Under the same operating conditions, tapered fluidized bed possesses higher heat and mass transfer rates.
- The two-phase drying model links mass transfer within an individual particle to the macroscopic mass balance of the fluidized bed, therefore allowing better prediction of

drying performance in the fluidized bed with known operating conditions such as flow rate, temperature and particle properties. Effective diffusivity calculated by fitting experimental data to the model, is in good agreement with values reported in the literature. Effective diffusivity can be used as an indicator of mass transfer performance in pulsed fluidized bed. Similar to the experiments, the positive effects of gas flow rate and drying temperature on mass transfer have been shown by the model.

- Heat transfer in pulsed fluidized bed is heavily influenced by gas pulsation, especially the pulsation frequency. Below natural frequency of the system, intermittence caused by the “OFF” period is relatively long, which essentially renders the fluidized bed as a fixed-bed reactor with no fluids passing through. Consequently, despite the satisfying gas–solid contact efficiency, the overall heat transfer coefficient remains low. The higher gas flow rate also determines that over this frequency range and for these particles the dominant heat transfer mechanism is gas convection. Above the natural frequency, higher pulsation frequency reduces bubble size and increases gas throughput, so that packets are more frequently renewed on the probe surface, which increases the particle convective heat transfer. As soon as the pulsation becomes too weak, undesired flow behaviour will significantly reduce the heat transfer rates. Therefore, a pulsation frequency around the natural frequency is likely the optimum for heat transfer. This is also consistent with the conclusion from the batch drying studies.
- The heat transfer model is able to take advantage of the previously identified heat transfer regimes in pulsed fluidized bed, and split the heat transfer into two mechanisms, one below and one above natural frequency, which shows good agreement with experimental work.
- Vibration is proven an extremely useful add-on for a fluidized bed of biomass, as the additional energy from vibration is able to overcome the cohesive forces between biomass particles, and restore good gas–solid contact in the fluidized bed, especially with large particles and particles with high moisture content. Therefore, the implementation of

vibration is favourable, but not essential, as pulsation alone is able to tackle the cohesive nature of biomass if properly configured.

- Heat transfer rates of three different biomass species under a variety of operating conditions have been investigated. The heat transfer coefficients are in good agreement with those reported in the literature. In addition, heat transfer coefficients in pulsed fluidized bed are significantly greater than that of fixed-bed reactors, indicating higher gas–solid contact efficiency, as well as heat transfer rates.

6.2 Recommendations for future research

- This work was performed in a rectangular fluidized bed made of acrylic that limited the drying temperature to 50 °C. The square cross-section may also have influenced the hydrodynamics and mass transfer in the fluidized bed column. Future test in a cylindrical fluidized column with a larger diameter that is made of more temperature-resistant material such as steel could further clarify the influence of temperature on mass transfer, as well as the flow behaviour of biomass particles in a more traditional reactor geometry.
- The two-phase drying model focused mainly on the effect of flow rate, temperature and biomass species. However, the intricate relationship between pulsation frequency and mass transfer was not properly addressed. Instead of using an average gas flow rate, the oscillating gas flow rate within a pulsation cycle should be used to evaluate bubble size and bubble rise velocity at different pulsation frequencies. A parameter that is related to pulsation frequency could also be added to the drying model such that the influence of pulsation frequency could be better addressed. A mathematical model that better incorporates the effect of gas pulsation is strongly favoured.
- The heat transfer measurements performed in this work were time-averaged values, as the response time of the thermocouples in the heater probe was not short enough to capture

the dynamics of the pulsed fluidized bed. A sensitive heat transfer measurement device such as platinum film could be used to measure the instantaneous heat transfer coefficient, which may shed light on the complex relationship between hydrodynamics and heat transfer.

- At lower pulsation frequencies increased entrainment was observed when compared to operations at higher pulsation frequencies. Since pulsation frequency affects not only entrainment but also attrition, further tests should be performed to investigate the possible effects of pulsation on entrainment.
- The pulsed fluidized bed as a suitable reactor for biomass drying and thermal conversion has been proven by previous studies, as well as this work. In order to make the transition from a promising concept to a feasible commercial solution, hot tests such as biomass torrefaction and pyrolysis utilizing pulsed fluidized beds should be carried out. Furthermore, economic analysis through process simulation should also be performed.

REFERENCES

- Agarwal, J., Davis, W., King, D. 1962. Fluidized bed coal dryer. *Chemical Engineering Progress*, **58**, 85-90.
- Akhavan, A., van Ommen, J.R., Nijenhuis, J., Wang, X.S., Coppens, M.-O., Rhodes, M.J. 2008. Improved Drying in a Pulsation-Assisted Fluidized Bed. *Industrial and Engineering Chemistry Research*, **48**(1), 302-309.
- Al-Qodah, Z., Al-Busoul, M. 2001. The effect of magnetic field on local heat transfer coefficient in fluidized beds with immersed heating surface. *Journal of Heat Transfer-Transactions of the Asme*, **123**(1), 157-161.
- ASABE. 2010. S358.2 Moisture measurement - forages. in: *ASABE Standards 2010*, Vol. ASABE S358.2, American Society of Agricultural and Biological Engineers. St. Joseph, MI.
- Atienza-Martínez, M., Fonts, I., Ábrego, J., Ceamanos, J., Gea, G. 2013. Sewage sludge torrefaction in a fluidized bed reactor. *Chemical Engineering Journal*, **222**(0), 534-545.
- Bacelos, M.S., Camargo, C.F.S., Silveira, A.M., Freire, J.T. 2011. Local heat-transfer coefficient of immersed cylindrical surface in fluidized and vibrated fluidized beds. *Chemical Engineering and Processing: Process Intensification*, **50**(11-12), 1152-1159.
- Baroni, A.F., Hubinger, M.D. 1998. DRYING OF ONION: EFFECTS OF PRETREATMENT ON MOISTURE TRANSPORT. *Drying Technology*, **16**(9-10), 2083-2094.
- Baskakov, A.P., Berg, B.V., Vitt, O.K., Filippovsky, N.F., Kirakosyan, V.A., Goldobin, J.M., MaskaeV, V.K. 1973. Heat transfer to objects immersed in fluidized beds. *Powder Technology*, **8**(5-6), 273-282.
- Beck Steven, R., Wang Maw, J., Hightower James, A. 1981. Gasification of Oak Sawdust, Mesquite, Corn Stover, and Cotton Gin Trash in a Countercurrent Fluidized Bed Pilot Reactor. in: *Biomass as a Nonfossil Fuel Source*, Vol. 144, AMERICAN CHEMICAL SOCIETY, pp. 335-349; 17.
- Beeckmans, J.M., Macwilliam, K. 1986. Stabilization of a fluidized bed by horizontal vibrations. *Powder Technology*, **45**(2), 177-181.
- Bhattacharya, S.C., Harrison, D. 1976. Heat Transfer In a Pulsed Fluidised Bed. *Transactions of the Institution of Chemical Engineers*, **54**(4), 281-286.
- Bi, H.T. 2007. A critical review of the complex pressure fluctuation phenomenon in gas-solids fluidized beds. *Chemical Engineering Science*, **62**(13), 3473-3493.
- Bi, X.T., Liu, X. 2010. High density and high solids flux CFB risers for steam gasification of solids fuels. *Fuel Processing Technology*, **91**(8), 915-920.
- Borodulya, V.A., Teplitsky, Y.S., Markevich, I.I., Hassan, A.F., Yeryomenko, T.P. 1991. Heat transfer between a surface and a fluidized bed: consideration of pressure and temperature effects. *International Journal of Heat and Mass Transfer*, **34**(1), 47-53.
- Botterill, J.S.M. 1975. *Fluid-bed heat transfer. Gas-fluidized bed behaviour and its influence on bed thermal properties*. Academic Press, New York; None.
- Bratu, E., Jinescu, G.I. 1971. Effect of vertical vibrations on the pressure drop in a fluidised layer. *Brazilian Journal of Chemical Engineering*, **16**, 691-695.
- Busciglio, A., Vella, G., Micale, G., Brandani, S. 2015. Modeling of Magnetic-Field-Assisted Fluidization: Model Development and CFD Simulation of Magnetically Stabilized Fluidized Beds. *Kona Powder and Particle Journal*(32), 217-226.
- Calderbank, P.H., Pogorski, L. 1957. Heat transfer in packed beds. *Trans. Inst. Chem. Eng*, **35**, 195-207.
- Catipovic, N.M. 1979. Heat transfer to horizontal tubes in fluidized beds: experiment and theory. in: *Chemical Engineering*, Vol. Ph. D., Oregon State University. Corvallis, OR, pp. 194.

- Celma, A.R., Cuadros, F., López-Rodríguez, F. 2012. Convective drying characteristics of sludge from treatment plants in tomato processing industries. *Food and Bioproducts Processing*, **90**(2), 224-234.
- Chen, D., Zheng, Y., Zhu, X. 2012. Determination of effective moisture diffusivity and drying kinetics for poplar sawdust by thermogravimetric analysis under isothermal condition. *Bioresource Technology*, **107**, 451-455.
- Chen, D.Y., Liu, X., Zhu, X.F. 2013. A one-step non-isothermal method for the determination of effective moisture diffusivity in powdered biomass. *Biomass & Bioenergy*, **50**, 81-86.
- Chen, J.C. 2003a. Heat Transfer. in: *Handbook of fluidization and fluid-particle systems*, (Ed.) W.-c. Yang, Vol. 91, CRC Press, pp. 265-266.
- Chen, J.C. 2003b. Surface Contact—Its Significance for Multiphase Heat Transfer: Diverse Examples. *Journal of Heat Transfer*, **125**(4), 549-566.
- Chen, J.C., Grace, J.R., Golriz, M.R. 2005. Heat transfer in fluidized beds: design methods. *Scale-Up in Particle Processing*, **150**(2), 123-132.
- Chen, Y.-L., Lin, P.-S., Peng, Y.-L. 1991. Particle Agglomeration Characteristics in Vibro-Fluidized Bed Dryers. *JOURNAL OF CHEMICAL ENGINEERING OF JAPAN*, **24**(5), 669-673.
- Cheng, H., Zhang, Y., Meng, A., Li, Q. 2007. Municipal Solid Waste Fueled Power Generation in China: A Case Study of Waste-to-Energy in Changchun City. *Environmental Science & Technology*, **41**(21), 7509-7515.
- Cho, J., Annable, M.D., Rao, P.S.C. 2005. Measured Mass Transfer Coefficients in Porous Media Using Specific Interfacial Area. *Environmental Science & Technology*, **39**(20), 7883-7888.
- Coppens, M.-O., van Ommen, J.R. 2003. Structuring chaotic fluidized beds. *Chemical Engineering Journal*, **96**(1-3), 117-124.
- Corella, J., Aznar, M.P., Delgado, J., Aldea, E. 1991. Steam gasification of cellulosic wastes in a fluidized bed with downstream vessels. *Industrial and Engineering Chemistry Research*, **30**(10), 2252-2262.
- Crank, J. 1979. *The mathematics of diffusion*. Oxford University Press, Oxford, England.
- Dahikar, S.K., Sonolikar, R.L. 2006. Influence of magnetic field on the fluidization characteristics of circulating fluidized bed. *Chemical Engineering Journal*, **117**(3), 223-229.
- Daleffe, R.V., Ferreira, M.C., Freire, J.T. 2005. Drying of Pastes in Vibro-Fluidized Beds: Effects of the Amplitude and Frequency of Vibration. *Drying Technology*, **23**(9-11), 1765-1781.
- Danckwerts, P.V. 1951. Significance of Liquid-Film Coefficients in Gas Absorption. *Industrial & Engineering Chemistry*, **43**(6), 1460-1467.
- Davidson, J.F., Clift, R., Harrison, D. 1985. *Fluidization*. Academic Press.
- de Souza, L.F.G., Nitz, M., Lima, P.A., Taranto, O.P. 2010. Drying of Sodium Acetate in a Pulsed Fluid Bed Dryer. *Chemical Engineering and Technology*, **33**(12), 2015-2020.
- Deissler, R., Boegli, J. 1958. An investigation of effective thermal conductivities of powders in various gases. *ASME Transactions*, **8**, 1417-1425.
- Denloye, A.O. 1976. Heat transfer in packed and gas fluidized beds, Vol. Ph., University of Birmingham (United Kingdom). Ann Arbor.
- Devahastin, S., Mujumdar, A.S. 2001. Some hydrodynamic and mixing characteristics of a pulsed spouted bed dryer. *Powder Technology*, **117**(3), 189-197.
- Dhungana, A., Basu, P., Dutta, A. 2012. Effects of Reactor Design on the Torrefaction of Biomass. *Journal of Energy Resources Technology*, **134**(4), 041801-041801.
- Dietz, P.W. 1979. Effective thermal conductivity of packed beds. *Industrial & Engineering Chemistry Fundamentals*, **18**(3), 283-286.
- Doymaz, I., Gorel, O., Akgun, N.A. 2004. Drying Characteristics of the Solid By-product of Olive Oil Extraction. *Biosystems Engineering*, **88**(2), 213-219.
- Eccles, E.R. 1990. Flow and heat transfer phenomena in aerated vibrated beds. *Drying Technology*, **8**(4), 895-898.

- Eccles, E.R.A., Mujumdar, A.S. 1992. CYLINDER-TO-BED HEAT TRANSFER IN AERATED VIBRATED BEDS OF SMALL PARTICLES. *Drying Technology*, **10**(1), 139-164.
- Elsdon, R., Shearer, C.J. 1977. Heat transfer in a gas fluidized bed assisted by an alternating electric field. *Chemical Engineering Science*, **32**(10), 1147-1153.
- Environment and Climate Change Canada. 2012. Canadian Environmental Sustainability Indicators: Greenhouse Gas Emissions. Accessed on August 3, 2016. http://www.ec.gc.ca/Publications/253AE6E6-5E73-4AFC-81B7-9CF440D5D2C5/793-Canada's-Emissions-Trends-2012_e_01.pdf.
- Erdész, K., Mujumdar, A.S. 1986. Hydrodynamic aspects of conventional and vibrofluidized beds — a comparative evaluation. *Powder Technology*, **46**(2-3), 167-172.
- Espin, M.J., Valverde, J.M., Quintanilla, M.A.S., Castellanos, A. 2011. Stabilization of gas-fluidized beds of magnetic powders by a cross-flow magnetic field. *Journal of Fluid Mechanics*, **680**, 80-113.
- Everitt, B.S. 2006. *The Cambridge dictionary of statistics*. Cambridge University Press.
- Forest Products Laboratory. 2010. *Wood handbook – Wood as an engineering material*. Department of Agriculture, Forest Service, Forest Products Laboratory, Madison, Wisconsin.
- Fotovat, F., Chaouki, J., Bergthorson, J. 2014. Distribution of Large Biomass Particles in a Sand-Biomass Fluidized Bed: Experiments and Modeling. *AIChE Journal*, **60**(3), 869-880.
- Froessling, N. 1938. Über die verdunstung fallender tropfen. *Gerlands Beiträge zur Geophysik*, **52**, 170-215.
- Gabor, J.D. 1970. Heat transfer to particle beds with gas flows less than or equal to that required for incipient fluidization. *Chemical Engineering Science*, **25**(6), 979-984.
- Geldart, D. 1986. *Gas fluidization technology*. John Wiley, Chichester.
- Geldart, D., Abdullah, E.C., Verlinden, A. 2009. Characterisation of dry powders. *Powder Technology*, **190**(1-2), 70-74.
- Gernon, T.M., Gilbertson, M.A., Sparks, R.S.J., Field, M. 2007. Tapered fluidized beds and the role of fluidization in mineral emplacement.
- Gishler, P.E., Mathur, K.B. 1957. Method of contacting solid particles with fluids, Ca Nat Research Council. USA, pp. 7.
- Godoi, F.C., Pereira, N.R., Rocha, S.C.S. 2011. Analysis of the drying process of a biopolymer (polyhydroxybutyrate) in rotating-pulsed fluidized bed. *Chemical Engineering and Processing*, **50**(7), 623-629.
- Goransson, K., Soderlind, U., Engstrand, P., Zhang, W. 2015. An experimental study on catalytic bed materials in a biomass dual fluidised bed gasifier. *Renewable Energy*, **81**, 251-261.
- Grace, J.R. 1982. Fluidized bed hydrodynamics. in: *Handbook of multiphase systems*, (Ed.) G. Hetsroni, Hemisphere Pub. Corp.
- Gupta, R., Mujumdar, A.S. 1980. Aerodynamics of a vibrated fluid bed. *The Canadian Journal of Chemical Engineering*, **58**(3), 332-338.
- Habibi, M., Eslamian, M., Soltani-Kordshuli, F., Zabihi, F. 2016. Controlled wetting/dewetting through substrate vibration-assisted spray coating (SVASC). *J. Coat. Technol. Res.*, **13**(2), 211-225.
- Hadi, B., van Ommen, J.R., Coppens, M.-O. 2011. Enhanced Particle Mixing in Pulsed Fluidized Beds and the Effect of Internals. *Industrial and Engineering Chemistry Research*, **51**(4), 1713-1720.
- Han, J., Kim, H., Cho, S., Shimizu, T. 2008. Fluidized bed combustion of some woody biomass fuels. *Energy Sources Part a-Recovery Utilization and Environmental Effects*, **30**(19), 1820-1829.
- Han, W., Mai, B., Gu, T. 1991. RESIDENCE TIME DISTRIBUTION AND DRYING CHARACTERISTICS OF A CONTINUOUS VIBRO-FLUIDIZED BED. *Drying Technology*, **9**(1), 159-181.
- Hao, B., Bi, H.T. 2005. Forced bed mass oscillations in gas-solid fluidized beds. *Powder Technology*, **149**(2-3), 51-60.
- Hasatani, M., Itaya, Y., Miura, K. 1991. Drying of granular materials in an inclined vibrated fluidized bed by combined radiative and convective heating. *Drying Technology*, **9**(2), 349-366.

- Hayes, M. 2006. Method of coating a medical appliance utilizing vibration, a system for vibrating a medical appliance, and a medical appliance produced by the method, Boston Scientific Scimed, Inc., USA . pp. 10pp.
- Hristov, J. 2002. Magnetic field assisted fluidization - A unified approach: A series of review papers. *Reviews in Chemical Engineering*, **18**(4-5), I-III.
- Jin, H., Zhang, J., Zhang, B. 2007. The effect of vibration on bed voidage behaviors in fluidized beds with large particles. *Brazilian Journal of Chemical Engineering*, **24**(3), 389-397.
- Jing, S., Hu, Q., Wang, J., Jin, Y. 2000. Fluidization of coarse particles in gas-solid conical beds. *Chemical Engineering and Processing: Process Intensification*, **39**(4), 379-387.
- Karmakar, M.K., Haldar, S., Chatterjee, P.K. 2013. Studies on fluidization behaviour of sand and biomass mixtures. *Int. J. Emerg. Technol. Adv. Eng.*, **3**.
- Karunanithy, C., Muthukumarappan, K., Donepudi, A. 2013. Moisture sorption characteristics of switchgrass and prairie cord grass. *Fuel*, **103**(0), 171-178.
- Kay, J.M., Nedderman, R.M. 1974. *An Introduction to Fluid Mechanics and Heat Transfer with Applications in Chemical and Mechanical Process Engineering*. Cambridge University Press.
- Keshwani, D.R., Cheng, J.J. 2010. Microwave-based alkali pretreatment of switchgrass and coastal bermudagrass for bioethanol production. *Biotechnology Progress*, **26**(3), 644-652.
- Khanna, P., Pugsley, T., Tanfara, H., Dumont, H. 2008. Radioactive particle tracking in a lab-scale conical fluidized bed dryer containing pharmaceutical granule. *The Canadian Journal of Chemical Engineering*, **86**(3), 563-570.
- Kimura, M., Nono, K., Kaneda, T. 1955. Distribution of void in a packed tube. *Journal of Chemical Engineering of Japan*, **14**, 397-400.
- Kleijn van Willigen, F., van Ommen, J.R., van Turnhout, J., van den Bleek, C.M. 2005. Bubble size reduction in electric-field-enhanced fluidized beds. *Journal of Electrostatics*, **63**(6-10), 943-948.
- Kobayashi, M., Ramaswami, D., Brazelton, W. 1970a. Heat transfer from an internal surface to a pulsed bed. *Chem. Eng. Prog. Symp. Ser.* pp. 58-67.
- Kobayashi, M., Ramaswami, D., Brazelton, W. 1970b. Pulsed-Bed Approach to Fluidization. *Chemical Engineering Progress Symposium Series*. Argonne National Laboratory. pp. 47-57.
- Köksal, M., Vural, H. 1998. Bubble size control in a two-dimensional fluidized bed using a moving double plate distributor. *Powder Technology*, **95**(3), 205-213.
- Kong, X., Kang, X., Li, B., Song, Z. 2010. Analysis of dynamic behavior of a large-sized vibration fluidized bed. *2nd International Conference on Advances in Product Development and Reliability, PDR'2010, July 28, 2010 - July 30, 2010*, Shenyang, China. Trans Tech Publications. pp. 912-915.
- Kouprianov, V.I., Permchart, W. 2003. Emissions from a conical FBC fired with a biomass fuel. *Applied Energy*, **74**(3-4), 383-392.
- Kudra, T., Gawrzynski, Z., Glaser, R., Stanislawski, J., Poirier, M. 2002. DRYING OF PULP AND PAPER SLUDGE IN A PULSED FLUID BED DRYER. *Drying Technology*, **20**(4-5), 917-933.
- Kunii, D., Smith, J. 1960. Heat transfer characteristics of porous rocks. *AIChE Journal*, **6**(1), 71-78.
- Kuprianov, V.I., Janvijitsakul, K., Permchart, W. 2006. Co-firing of sugar cane bagasse with rice husk in a conical fluidized-bed combustor. *Fuel*, **85**(4), 434-442.
- Legros, R., Alan Millington, C., Clift, R. 1994. Drying of tobacco particles in a mobilised bed. *Drying Technology*, **12**(3), 517-543.
- Levenspiel, O. 1998. *Chemical Reactions Engineering. 3rd Edition ed.* Wiley.
- Levey Jr, R.P. 1965. Gas-solids contacting method, (Ed.) U.S.P. Office, Vol. 3164440. USA, pp. 4.
- Lewis, W.K. 1921. The Rate of Drying of Solid Materials. *Journal of Industrial & Engineering Chemistry*, **13**(5), 427-432.
- Li, H., Liu, X., Legros, R., Bi, X.T., Lim, C.J., Sokhansanj, S. 2012. Torrefaction of sawdust in a fluidized bed reactor. *Bioresource technology*, **103**(1), 453-458.

REFERENCES

- Liu, X., Tian, W. 2008. Modeling for pyrolysis of biomass particle in fluidized bed of heat carrier. *Taiyangneng Xuebao/Acta Energiæ Solaris Sinica*, **29**(7), 905-909.
- Liu, Y. 2016. Pulsation-assisted fluidized bed for the fluidization of high moisture and irregular particles and its application for brown coal fluidization. *Fluidization XV*, Montebello, Quebec, Canada. Engineering Conferences International.
- Lyczkowski, R.W. 1982. Drying '82, A. S. Mujumdar, Editor, Hemisphere Publishing Corp., Washington, 1982, 254 pages, \$70. *AIChE Journal*, **28**(6), 1041-1041.
- Ma, X.X., Kato, K. 1998. Effect of interparticle adhesion forces on elutriation of fine powders from a fluidized bed of a binary particle mixture. *Powder Technology*, **95**(2), 93-101.
- Mabee, W., Saddler, J. 2010. Bioethanol from lignocellulosics: Status and perspectives in Canada. *Bioresource technology*, **101**(13), 4806-4813.
- Mabee, W.E., McFarlane, P.N., Saddler, J.N. 2011. Biomass availability for lignocellulosic ethanol production. *Biomass and Bioenergy*, **35**(11), 4519-4529.
- Malhotra, K., Mujumdar, A.S. 1987. Immersed surface heat transfer in a vibrated fluidized bed. *Industrial & Engineering Chemistry Research*, **26**(10), 1983-1992.
- Markowski, A., Kaminski, W. 1983. Hydrodynamic characteristics of jet-spouted beds. *The Canadian Journal of Chemical Engineering*, **61**(3), 377-381.
- Martín, L.d., Coppens, M.-O., Wu, K., Lepek, D. 2016. Pattern formation in fluidized and vibrated beds: Experimental and computational insights. *Fluidization XV*, Montebello Quebec, Canada. ECI Symposium Series.
- Martinez-Vera, C., Vizearra-Mendoza, M., Galin-Domingo, O., Ruiz-Martinez, R. 1995. Experimental Validation of a Mathematical Model for the Batch Drying of Corn Grains. *Drying Technology*, **13**(1-2), 333-350.
- Massimilla, L., Volpicelli, G., Raso, G. 1966. A study on pulsating gas fluidization of beds of particles. in: *Chemical Engineering Progress Symposium Series*, Vol. 62 American Institute of Chemical Engineers, pp. 63.
- Mastellone, M.L., Arena, U. 2002. Fluidized-bed pyrolysis of polyolefins wastes: Predictive defluidization model. *AIChE Journal*, **48**(7), 1439-1447.
- Meili, L., Daleffe, R.V., Ferreira, M.C., Freire, J.T. 2010. Analysis of the Influence of Dimensionless Vibration Number on the Drying of Pastes in Vibrofluidized Beds. *Drying Technology*, **28**(3), 402-411.
- Meili, L., Daleffe, R.V., Freire, J.T. 2012. Fluid Dynamics of Fluidized and Vibrofluidized Beds Operating with Geldart C Particles. *Chemical Engineering & Technology*, **35**(9), 1649-1656.
- Mickley, H.S., Fairbanks, D.F. 1955. Mechanism of heat transfer to fluidized beds. *AIChE Journal*, **1**(3), 374-384.
- Molerus, O. 1967. *Proceedings of the International Symposium on Fluidization, June 6-9, 1967, Eindhoven*. Netherlands University Press.
- Molerus, O., Burschka, A., Dietz, S. 1995. Particle migration at solid surfaces and heat transfer in bubbling fluidized beds—II. Prediction of heat transfer in bubbling fluidized beds. *Chemical Engineering Science*, **50**(5), 879-885.
- Molerus, O., Wirth, K.-E. 1997a. *Heat Transfer in Fluidized Beds. First Edition ed.* Chapman & Hall, Dordrecht.
- Molerus, O., Wirth, K.-E. 1997b. Heat transfer mechanisms in bubbling fluidized beds. in: *Heat Transfer in Fluidized Beds*, Springer Netherlands. Dordrecht, pp. 35-47.
- Mori, S., Wen, C. 1975. Estimation of bubble diameter in gaseous fluidized beds. *AIChE Journal*, **21**(1), 109-115.
- Mushtaev, V.I., Timomin, A.S., LAbedev, V.Y. 1991. *Construction and Design of Equipment with a Suspended Bed*. Khimiya, Moscow.
- Natural Resources Canada. 2013. Wood pellet production trends in Canada. Accessed on Feb 5, 2015. <https://cfs.nrcan.gc.ca/selective-cuttings/57>.

- Newman, A.B. 1931. *The drying of porous solids: Diffusion calculations*. Office of the Executive Secretary.
- Niamnuy, C., Devahastin, S. 2005. Drying kinetics and quality of coconut dried in a fluidized bed dryer. *Journal of Food Engineering*, **66**(2), 267-271.
- Nilson, L., Wimmerstedt, R. 1987. DRYING IN LONGITUDINAL-FLOW VIBRATING FLUID-BEDS. *Drying Technology*, **5**(3), 337-361.
- Nitz, M., Taranto, O.P. 2007. Drying of beans in a pulsed fluid bed dryer: Drying kinetics, fluid-dynamic study and comparisons with conventional fluidization. *Journal of Food Engineering*, **80**(1), 249-256.
- Norouzi, H.R., Mostoufi, N., Sotudeh-Gharebagh, R. 2012. Effect of fines on segregation of binary mixtures in gas-solid fluidized beds. *Powder Technology*, **225**, 7-20.
- Okekunle, P.O., Pattanotai, T., Watanabe, H., Okazaki, K. 2011. Numerical and Experimental Investigation of Intra-Particle Heat Transfer and Tar Decomposition during Pyrolysis of Wood Biomass. *Journal of Thermal Science and Technology*, **6**(3), 360-375.
- Olazar, M., San Jose, M.J., Aguayo, A.T., Arandes, J.M., Bilbao, J. 1992. Stable operation conditions for gas-solid contact regimes in conical spouted beds. *Industrial & engineering chemistry research*, **31**(7), 1784-1792.
- Ozkaynak, T.F., Chen, J.C. 1980. Emulsion phase residence time and its use in heat transfer models in fluidized beds. *AIChE Journal*, **26**(4), 544-550.
- Papadakis, K., Gu, S., Bridgwater, A.V. 2010. Computational modelling of the impact of particle size to the heat transfer coefficient between biomass particles and a fluidised bed. *Fuel Processing Technology*, **91**(1), 68-79.
- Pence, D.V., Beasley, D.E. 1998. Chaos suppression in gas-solid fluidization. *Chaos*, **8**(2), 514-519.
- Ponomarenko, V.G., Kurlyand, Y.A., Belomyttsev, S.N., Onufriev, D.N., Kovalev, N.P. 1989. Hydrodynamics of a pulsating fluidized bed. *Chemical and Petroleum Engineering*, **24**(11-12), 591-594.
- Powell, M.J. 2009. The BOBYQA algorithm for bound constrained optimization without derivatives. University of Cambridge.
- Prachayawarakorn, S., Tia, W., Poopaiboon, K., Soponronnarit, S. 2005. Comparison of performances of pulsed and conventional fluidised-bed dryers. *Journal of Stored Products Research*, **41**(5), 479-497.
- Prins, M.J., Ptasinski, K.J., Janssen, F.J.J.G. 2006. More efficient biomass gasification via torrefaction. *Energy*, **31**(15), 3458-3470.
- Province of British Columbia. 2011. British Columbia's wood pellet industry. Accessed on Dec 6, 2015. <https://www.pellet.org/images/WoodPelletFactsheet.pdf>.
- Pugsley, T., Chaplin, G., Khanna, P. 2007. Application of advanced measurement techniques to conical lab-scale fluidized bed dryers containing pharmaceutical granule. *Food and Bioproducts Processing*, **85**(3), 273-283.
- Ramesh, M.N. 2003. Moisture transfer properties of cooked rice during drying. *LWT - Food Science and Technology*, **36**(2), 245-255.
- Ranz, W. 1952. Friction and transfer coefficients for single particles and packed beds. *Chemical Engineering Progress*, **48**(5), 247-253.
- Resch, H., Kang, H., Hoag, M.L. 1989. DRYING DOUGLAS-FIR LUMBER - A COMPUTER-SIMULATION. *Wood and Fiber Science*, **21**(3), 207-218.
- Reyes, A., Campos, C., Vega, R. 2006. Drying of Turnip Seeds with Microwaves in Fixed and Pulsed Fluidized Beds. *Drying Technology*, **24**(11), 1469-1480.
- Reyes, A., Herrera, N., Vega, R. 2008a. Drying Suspensions in a Pulsed Fluidized Bed of Inert Particles. *Drying Technology*, **26**(1), 122-131.
- Reyes, A., Mahn, A., Guzmán, C., Antoniz, D. 2012. Analysis of the Drying of Broccoli Florets in a Fluidized Pulsed Bed. *Drying Technology*, **30**(11-12), 1368-1376.

- Reyes, A., Moyano, P., Paz, J. 2007. Drying of Potato Slices in a Pulsed Fluidized Bed. *Drying Technology*, **25**(4), 581-590.
- Reyes, A., Vega, R., García, G. 2008b. Drying Sawdust in a Pulsed Fluidized Bed. *Drying Technology*, **26**(4), 476-486.
- Riley, N.A. 1941. Projection sphericity. *Journal of Sedimentary Research*, **11**(2), 94-95.
- Roy, R., Davidson, J.F., TuPONOGOV, V.G. 1990. The velocity of sound in fluidised beds. *Chemical Engineering Science*, **45**(11), 3233-3245.
- Saad, Y., Schultz, M.H. 1986. GMRES: A Generalized Minimal Residual Algorithm for Solving Nonsymmetric Linear Systems. *SIAM Journal on Scientific and Statistical Computing*, **7**(3), 856-869.
- Sablani, S., Rahman, S., Al-Habsi, N. 2000. Moisture diffusivity in foods-an overview. in: *Drying technology in agriculture and food sciences*, (Ed.) A.S. Mujumdar, Publishers Inc. Enfield, USA, pp. 35-50.
- Sacilik, K., Elicin, A.K. 2006. The thin layer drying characteristics of organic apple slices. *Journal of Food Engineering*, **73**(3), 281-289.
- Sau, D.C., Mohanty, S., Biswal, K.C. 2007. Minimum fluidization velocities and maximum bed pressure drops for gas–solid tapered fluidized beds. *Chemical Engineering Journal*, **132**(1–3), 151-157.
- Savage, S.B. 1988. Streaming motions in a bed of vibrationally fluidized dry granular material. *Journal of Fluid Mechanics*, **194**, 457-478.
- Schaafsma, S., Marx, T., Hoffmann, A. 2006. Investigation of the particle flowpattern and segregation in tapered fluidized bed granulators. *Chemical Engineering Science*, **61**(14), 4467-4475.
- Secretariat, R. 2015. *Renewables 2015 Global Status Report*. REN21, Paris.
- Sedjo, R.A. 2013. Comparative life cycle assessments: carbon neutrality and wood biomass energy. *Resources for the Future DP*.
- Seville, J.P.K., Clift, R. 1984. The effect of thin liquid layers on fluidisation characteristics. *Powder Technology*, **37**(1), 117-129.
- Sherwood, T.K. 1929. The Drying of Solids—I. *Industrial & Engineering Chemistry*, **21**(1), 12-16.
- Shryaeva, N.P., Sapozhnikov, B.G., Belousov, V.S., Tasnikov, G.P. 1990. Effective thermal diffusivity of a vibrationally fluidized bed. *Journal of engineering physics*, **58**(4), 458-465.
- Siebert, A.W., Highgate, D., Newborough, M. 1999. Heat transfer characteristics of mechanically-stimulated particle beds. *Applied Thermal Engineering*, **19**(1), 37-49.
- Sit, S., Grace, J. 1981. Effect of bubble interaction on interphase mass transfer in gas fluidized beds. *Chemical Engineering Science*, **36**(2), 327-335.
- Stefanova, A. 2009. Heat transfer near the transition to turbulent fluidization. in: *Chemical and Biological Engineering*, Vol. Doctor of Philosophy - PhD, University of British Columbia. Vancouver, Canada.
- Sun, G. 1991. Influence of particle size distribution and the performance of fluidized bed reactors, Vol. NN69797, The University of British Columbia (Canada). Ann Arbor, pp. 230.
- Sun, J., Wang, J., Yang, Y., Zhu, Z. 2015. Effects of external electric field on bubble and charged particle hydrodynamics in a gas–solid fluidized bed. *Advanced Powder Technology*, **26**(2), 563-575.
- Sun, P., Hui, S.e., Gao, Z., Zhou, Q., Tan, H., Zhao, Q., Xu, T. 2013. Experimental investigation on the combustion and heat transfer characteristics of wide size biomass co-firing in 0.2 MW circulating fluidized bed. *Applied Thermal Engineering*, **52**(2), 284-292.
- Tannous, K., Lam, P.S., Sokhansanj, S., Grace, J.R. 2013. Physical Properties for Flow Characterization of Ground Biomass from Douglas Fir Wood. *Particulate Science and Technology*, **31**(3), 291-300.
- Tasirin, S.M., Puspasari, I., Lun, A.W., Chai, P.V., Lee, W.T. 2014. Drying of kaffir lime leaves in a fluidized bed dryer with inert particles: Kinetics and quality determination. *Industrial Crops and Products*, **61**(0), 193-201.

- Thomas, B., Mason, M.O., Squires, A.M. 2000. Some behaviors of shallow vibrated beds across a wide range in particle size and their implications for powder classification. *Powder Technology*, **111**(1-2), 34-49.
- Thorpe, G.R., Alberto Ochoa Tapia, J., Whitaker, S. 1991. The diffusion of moisture in food grains—II. Estimation of the effective diffusivity. *Journal of Stored Products Research*, **27**(1), 11-30.
- Toyohara, H., Kawamura, Y. 1992. Fluidization of a tapered fluidized-bed of a binary particle-mixture. *Int. Chem. Eng.*, **32**(1), 164-171.
- Turnbull, J.H. 1993. Use of biomass in electric power generation: the california experience. *Biomass and Bioenergy*, **4**(2), 75-84.
- van den Bleek, C.M., Coppens, M.-O., C. Schouten, J. 2002. Application of chaos analysis to multiphase reactors. *Chemical Engineering Science*, **57**(22-23), 4763-4778.
- van den Bleek, C.M., Schouten, J.C. 1993. Deterministic chaos: a new tool in fluidized bed design and operation. *Chemical Engineering Journal*, **53**(1), 75-87.
- van der Wielen, L.A.M., Fa, A.W.K.G.S.K., Potters, J.J.M., Luyben, K.C.A.M. 1997. Transient behavior of pulsed particulate fluidized beds. *AIChE Journal*, **43**(3), 625-630.
- Venkatesh, R.D., Chaouki, J., Klvana, D. 1996. Fluidization of cryogels in a conical column. *Powder technology*, **89**(3), 179-186.
- Walzel, P. 2013. Effects and New Applications of Pulsed Flow. *Chemical Engineering & Technology*, **36**(1), 15-21.
- Wang, C., Peng, J., Li, H., Bi, X.T., Legros, R., Lim, C.J., Sokhansanj, S. 2013. Oxidative torrefaction of biomass residues and densification of torrefied sawdust to pellets. *Bioresource Technology*, **127**(0), 318-325.
- Wang, X.S., Rhodes, M.J. 2005a. Pulsed fluidization—a DEM study of a fascinating phenomenon. *Powder Technology*, **159**(3), 142-149.
- Wang, X.S., Rhodes, M.J. 2005b. Using pulsed flow to overcome defluidization. *Chemical Engineering Science*, **60**(18), 5177-5181.
- Welty, J.R., Wicks, C.E., Rorrer, G., Wilson, R.E. 2009. *Fundamentals of momentum, heat, and mass transfer*. John Wiley & Sons.
- Wiens, J., Pugsley, T. 2006. Tomographic imaging of a conical fluidized bed of dry pharmaceutical granule. *Powder Technology*, **169**(1), 49-59.
- Wong, H.W., Baird, M.H.I. 1971. Fluidisation in a pulsed gas flow. *Chemical Engineering Journal*, **2**(2), 104-113.
- Wormsbecker, M., Pugsley, T., Tanfara, H. 2009. Interpretation of the hydrodynamic behaviour in a conical fluidized bed dryer. *Chemical Engineering Science*, **64**(8), 1739-1746.
- Wunder, R. 1980. Wärmeübergang an vertikalen Wärmeaustauscherflächen in Gas-swirbelschichten, Vol. Dr.-Ing., Technische Universität München.
- Yagi, S., Kunii, D. 1960. Studies on heat transfer near wall surface in packed beds. *AIChE Journal*, **6**(1), 97-104.
- Yang, D., Parlange, J.-Y., Walker, L.P. 2015. Revisiting size-exclusion chromatography for measuring structural changes in raw and pretreated mixed hardwoods and switchgrass. *Biotechnology and Bioengineering*, **112**(3), 549-559.
- Yoshida, T., Kousaka, Y. 1969. Flow of Granular Solids through a Vibrating Orifice. *International Chemical Engineering*, **9**(1), 177-180.
- Zahed, A., Zhu, J., Grace, J.R. 1995. Modelling and simulation of batch and continuous fluidized bed dryers. *Drying Technology*, **13**(1-2), 1-28.
- Zaitsev, E.D., Redekop, V.I., Shvetsov, V.V. 1976. Hydrodynamics and external heat exchange of a vibrated fluidized layer of pharmaceutical preparations. *Pharmaceutical Chemistry Journal*, **10**(3), 354-358.
- Zanchi, G., Pena, N., Bird, N. 2012. Is woody bioenergy carbon neutral? A comparative assessment of emissions from consumption of woody bioenergy and fossil fuel. *GCB Bioenergy*, **4**(6), 761-772.

REFERENCES

- Zenz, F.A., Othmer, D.F. 1960. *Fluidization and fluid-particle systems*. Reinhold.
- Zhang, D. 2005. Hydrodynamics and heat transfer in a pulsed bubbling fluidized bed, Vol. MR01992, Dalhousie University (Canada). Ann Arbor, pp. 214-214 p.
- Zhang, L., Hou, J., Bi, X.T., Grace, J.R., Janke, T., Arato, C. 2012. Fluidization characteristics and charging behavior of fly ash in a vibro-fluidized bed. *Powder Technology*, **215–216**(0), 235-241.
- Zhao, G.-B., Yang, Y.-R. 2003. Multiscale resolution of fluidized-bed pressure fluctuations. *AIChE Journal*, **49**(4), 869-882.
- Zhong, W.Q., Jin, B.S., Zhang, Y., Wang, X.F., Xiao, R. 2008. Fluidization of Biomass Particles in a Gas-Solid Fluidized Bed. *Energy & Fuels*, **22**(6), 4170-4176.
- Zhu, X., Ye, S., Pan, X. 2008. The local heat transfer mathematical model between vibrated fluidized beds and horizontal tubes. *Experimental Thermal and Fluid Science*, **32**(6), 1279-1286.

APPENDICES

Appendix A. Supplementary experimental results

A1. Minimum fluidization velocity

In a conventional fluidized bed, minimum fluidization velocity is normally measured experimentally by gradually increasing (or decreasing) the superficial gas velocity while measuring the pressure drop across the entire bed. At minimum fluidization velocity, the drag force and buoyancy force counteract the weight of the bed, and bed particles become completely fluidized at this point. By plotting bed pressure drop against superficial gas velocity, minimum fluidization velocity could be obtained.

In the pulsed fluidized bed, however, bed pressure drop is periodically oscillating because of the pulsed gas flow. Therefore, it is impossible to obtain U_{mf} directly from plotting pressure drop vs. U . It was discovered visually during the experiments and confirmed by high-speed imaging that the incipience of fluidization was strongly associated with the peak pressure drop in every pulsation cycle, which corresponded to the maximum pressure drop within a pulsation cycle. By plotting the average peak pressure drop vs. average superficial gas velocity, minimum fluidization velocity in pulsed fluidized bed was obtained. An example is shown in Figure A.1, where the superficial gas velocity of Douglas fir sawdust that was used in the majority of experiments was measured. For the same biomass particles, a few pulsation frequencies were used. Minimum fluidization velocity obtained at different pulsation frequencies were different, but in close proximity to each other. The Douglas fir sawdust for instance, had close values of minimum fluidization velocity at 5 and 1.25 Hz, which were 0.240 and 0.238 m/s, respectively. Finally, an average value of 0.238 m/s was taken among values measured at five pulsation frequencies as the minimum fluidization velocity.

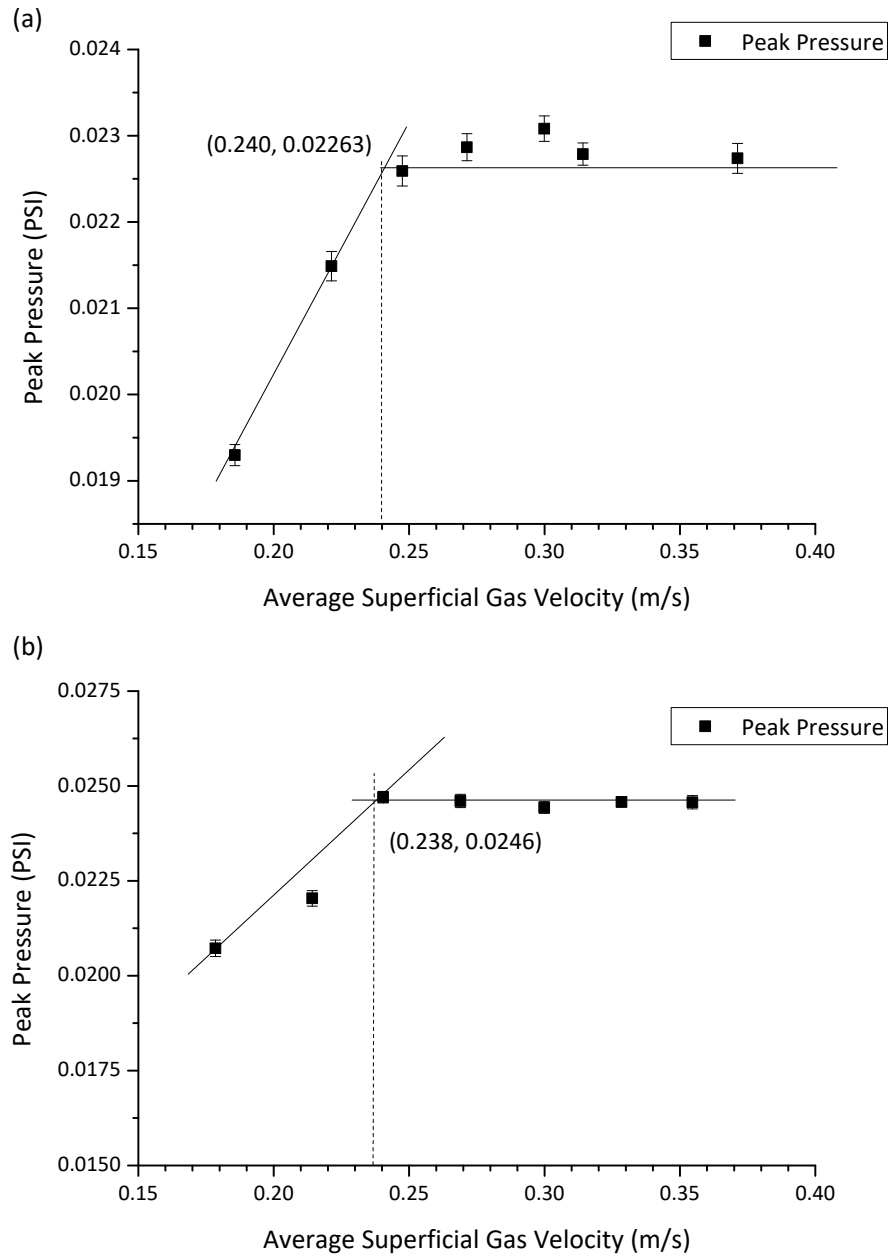


Figure A.1 Peak pressure in pulsed fluidized bed of biomass as a function of gas velocity. (a) $f=5.0$ Hz; (b) $f=1.25$ Hz.

A2. Pulsating stream and fluidization stream

It is evident that a higher flow rate leads to better gas–solid contact, which in turn enhances both heat transfer and mass transfer. The increase in flow rate could come from either the pulsed gas flow stream, or the stable fluidization stream. However, when the overall flow rate is kept the same, the ratio between the pulsating stream and fluidization stream becomes important, as it determines the flow behaviour and the intensity of gas pulsation.

Figure A.2 displays the final moisture content of Douglas fir sawdust after 30 min of batch drying, with different pulsating stream/fluidization stream ratios. The overall flow rate was kept at 6 SCFM, while the ratio between pulsating stream and fluidization stream was adjusted from 35% to 100%. By increasing the percentage of pulsating stream, stronger pulsation was generated as a result. It is consistent with the fact that by allocating more gas flow into the pulsating stream, peak pressure drop, standard deviation of pressure fluctuations, bubble size and bubble rise velocity all tend to increase, therefore enhancing the gas–solid contact, heat and mass transfer process.

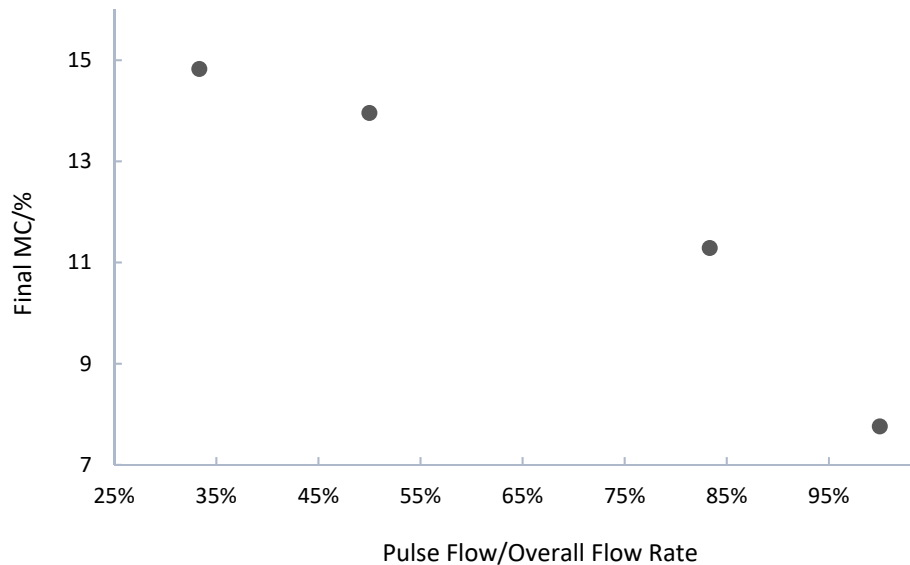


Figure A.2 Final moisture content after 30 min of batch drying in pulsed fluidized bed for Douglas fir at different pulsed flow ratios

Similarly, by increasing the ratio of pulsation stream from 35% to 60% during the heat transfer study of Douglas fir sawdust, channeling disappeared because of stronger gas pulsations. The bed-to-surface heat transfer coefficient increased from 70.1 W/(m²·K) to 88.9 W/(m²·K) for 1.25 Hz, as can be seen from Figure A.3.

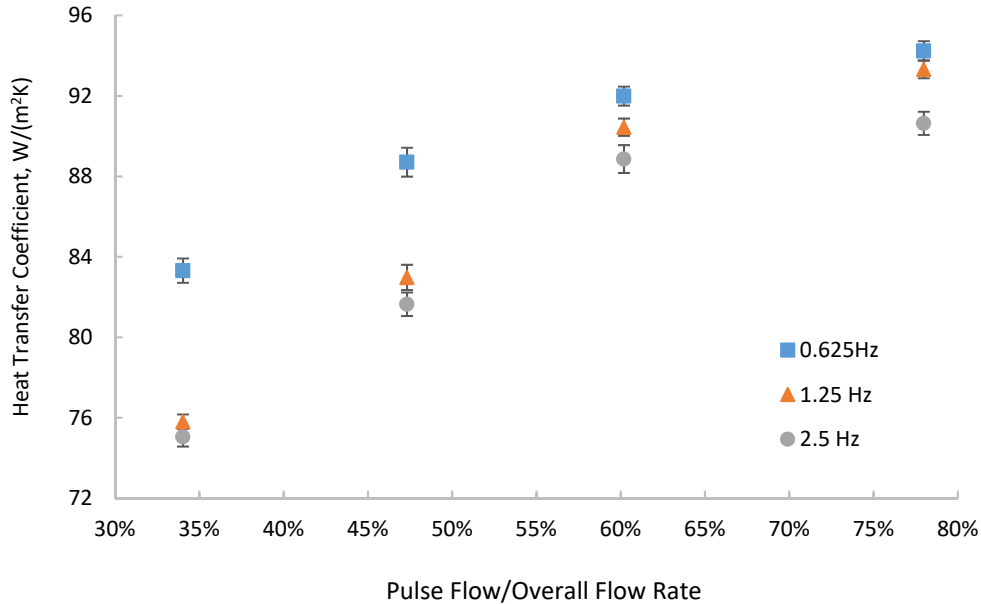


Figure A.3 Heat transfer coefficient in pulsed fluidized bed for Douglas fir, at different pulsed flow ratios

Based on the experimental result, in order to maximize the positive effect of pulsed gas flow, more gas flow should be allocated to the gas line on which gas pulsations are generated. The addition of fluidization stream is beneficial to heat and mass transfer in pulsed fluidized bed, since it is able to mobilize particles even during “OFF” periods when normally the bed remains stationary. For processes such as drying and torrefaction where increasing fluidization medium usage may be costly, eliminating the fluidization stream, or simply reducing its ratio with pulsating stream, could bring in economic benefits to the entire operation. This is also the reason that only pulsating stream was used in this work.

A3. Angle of repose of biomass powders

Angle of repose (AOR) is an important parameter for particles and powders as it reflects the internal friction and interparticle forces. In order to better quantify the cohesiveness of biomass particles, and to better design the tapered bottom section for the pulsed fluidized bed, AOR measurement was performed to ensure that the diverging column wall of the insert would be able to allow wet particles to fall down, as opposed to being stuck on the side of the wall. The AOR measurements were performed on the Powder Research Ltd AOR tester (Mark 4) developed by Professor D. Geldart. AOR for three biomass species, Douglas fir, pine and switchgrass, with different moisture content tested.

Ideally, for conventional particles, the angle of repose could be calculated from the indicating marks on the tester, as shown in Figure A.4(a). However, because of the low particle density and irregular shapes, biomass particles scattered all over the tester, which made it very difficult to distinguish the margin and determining the angle of repose from the scales. Instead, a photo was taken at front centre of the particles, and the angle of repose could be directly measured from the photo, as shown in Figure A.4(b). Autodesk AutoCAD (Version 2015, student license) was used to measure the AOR from the photos.

Results of the AOR measurement are presented in Figure A.5. In general, the AOR value increases with moisture content, which is consistent with the fact that van der Waals force increase with moisture content. The highest AOR observed was less than 70°, so it was reasonable to choose the angle of the tapered bed section to be 80°.

AOR will likely change with temperature. AOR values in this work were obtained in room temperature. Caution must be exercised when applying these experimental results to elevated temperatures.

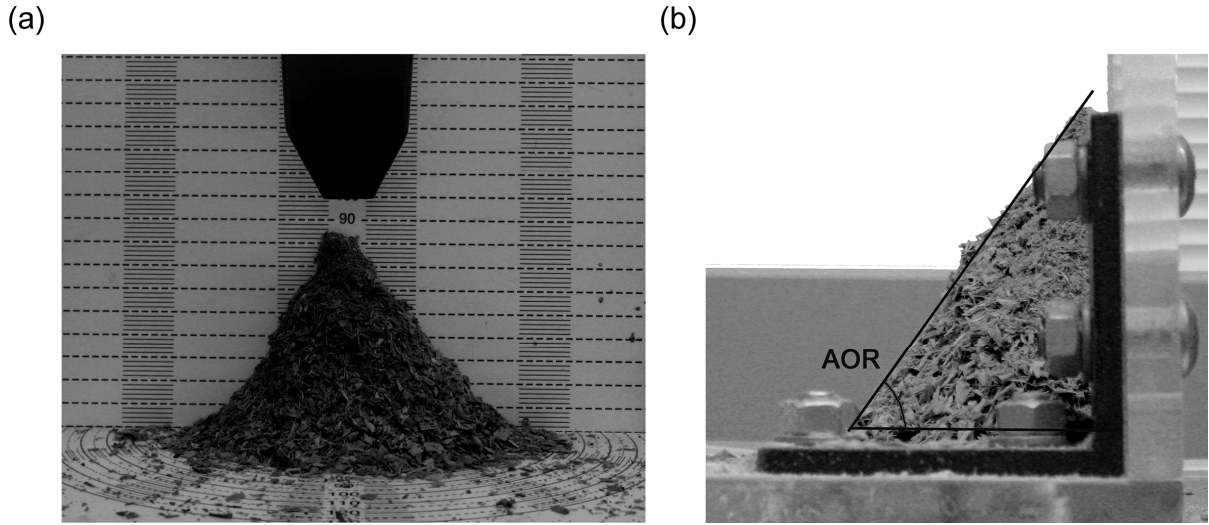


Figure A.4 Angle of repose method of measurement for Douglas fir sawdust. (a) Indicating marks for traditional particles; (b) new approach for biomass particles.

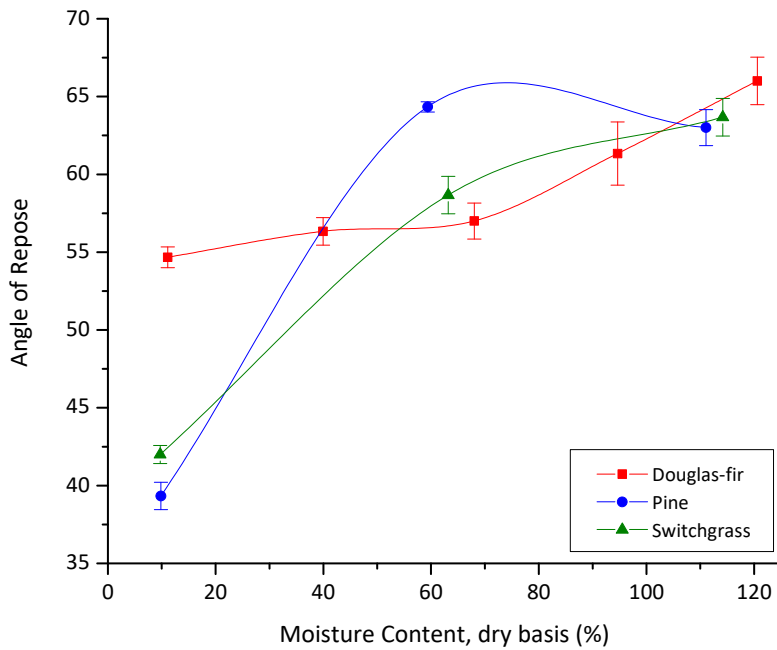


Figure A.5 Angle of repose for all three biomass species at different moisture contents (experimental data points with spline interpolations)

A4. The calculation of drying rate and amount of water evaporated

In this work the instantaneous drying rate was obtained based on the readings of the relative humidity probes, as specified in Eqn. (2.5). Before using this method to monitor and calculate the drying rate, the accuracy and reliability of the method was first verified by a set of experiments and calculations. Batch drying tests of Douglas fir sawdust in the pulsed fluidized bed under different pulsation duty cycles were performed. The final moisture content of biomass was first determined by oven drying at 103 °C for 24 h, and then calculated from the drying rate and initial moisture content. Specifically, the total amount of water evaporated at a given time t in the batch drying process could be obtained by integrating drying rate over time,

$$m_t = \int_0^t W \cdot dt = M \int_0^t (Y_o - Y_i) \cdot dt \quad (\text{A-1})$$

Less than 2.5% in error was observed between the experimentally obtained moisture content at the end of 30 minutes drying and the values calculated from measured relative humidity of the exhaust gases, as can be seen in Table A.1, which indicates that this approach has enough accuracy for biomass drying.

Table A.1 Measured final moisture content and calculated from measured exhaust gas humidity after 30 min of batch drying

Pulsation duty cycle	Total water in sample	Final moisture content (measured)	Water remaining after drying	Water removed (measured)	Water removed (calculated, m_t)	Calculated final moisture content	Error
%	g	%	g	g	g	%	%
100.0%	53.4	7.8	14.4	39.0	43.3	5.3	2.4
83.3%	53.4	11.3	20.3	33.1	36.4	9.3	2.0
66.7%	53.4	14.8	25.8	27.6	30.4	13.0	1.8
50.0%	53.4	14.0	24.5	28.9	29.3	13.7	0.2

With the instantaneous drying rate and moisture content at any given time available, the relationship between drying rate and moisture content could be obtained. Drying rates of three biomass species are plotted against bed moisture content in Figure A.6.

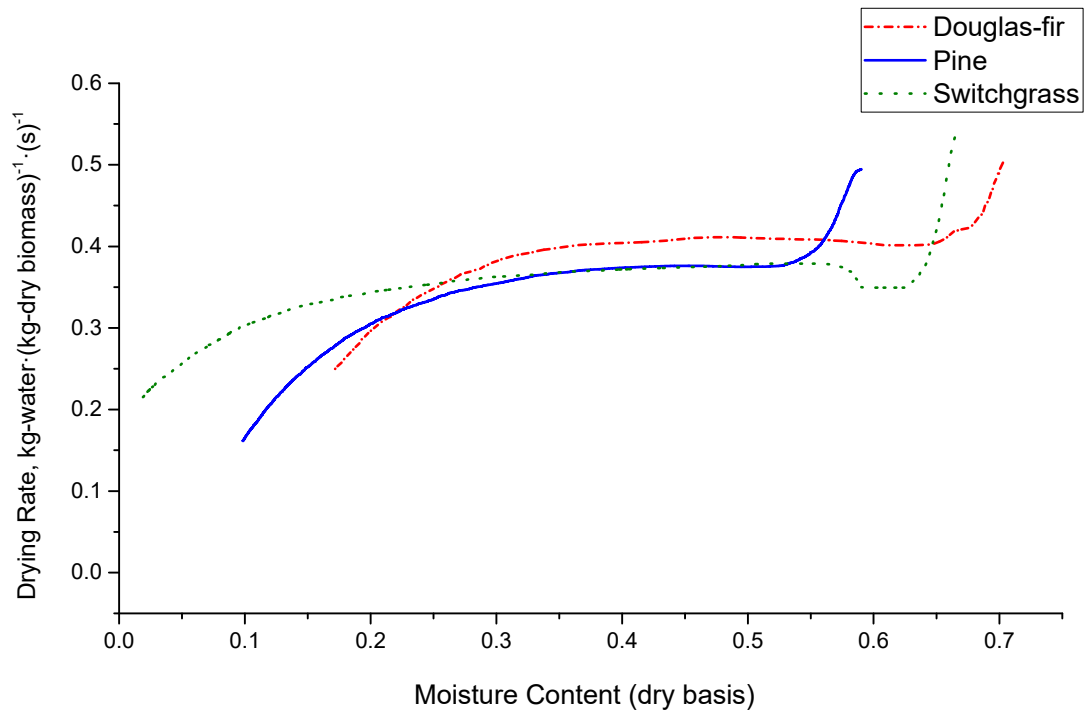


Figure A.6 Drying rate curve of three biomass species in rectangular pulsed fluidized bed, $U/U_{mf}=1.1$.

A5. Sample data set from two-phase drying model

The two-phase drying model proposed in Chapter 4 was implemented in COMSOL Multiphysics version 4.4. A complete set of key parameters that are essential to the model is listed in Table A.2.

Table A.2 Model parameters used for drying modelling, for the case of Douglas fir sawdust in rectangular fluidized bed, drying temperature 20°C, flow rate $U/U_{mf}=1.1$.

Name	Expression	Description
M0	0.31187	Initial moisture content
D_eff	1e-9 [m ² /s]	Effective diffusivity
dp	1.45 [mm]	Particle average diameter
rho_p	475 [kg/m ³]	Particle Density
e_mf	0.57	Voidage at U_{mf}
rho_g	1.204 [kg/ m ³]	Density of Air
T	20 [°C]	Air Temperature
P	101325 [Pa]	Atmosphere Pressure
A	0.015 [m ²]	Cross section area of bed
U_mf	0.238 [m/s]	Minimum fluidization velocity
N_or	190	Number of orifices for the distributor plate
H	0.141 [m]	Static bed height
D_t	0.12 [m]	Column hydraulic diameter
D	0.282e-4 [m ² /s]	Molecular diffusivity of water in air
Gd	1.473	Gas flow rate in dense phase per unit volume of bed
Yi	0	Absolute humidity in inlet air
n	1.1	U/U_{mf}
e_p	0.33	Particle volume fraction
e_b	0.234	Bubble volume fraction
Re_mf	22	Reynolds number
Sc	0.66	Schmidt number of water in air
y_ratio	0.004	Mole ratio of non-diffusion component
Dv	2.4e-6 [m ² /s]	Water vapour-air mass diffusivity

Additional data that are not included in the main body of the thesis are shown below, including the moisture content in biomass particles and gas bubbles.

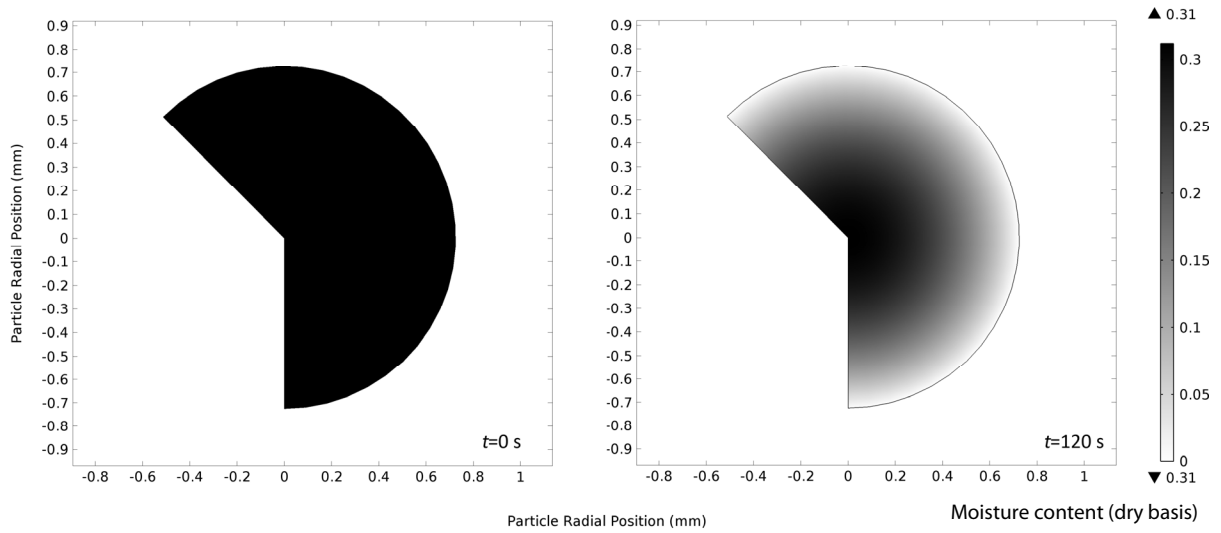


Figure A.7 Moisture content distribution within a single biomass particle during the batch drying test at different drying times, Douglas fir sawdust in rectangular fluidized bed, $T=20^{\circ}\text{C}$, flow rate $U/U_{mf}=1.1$.

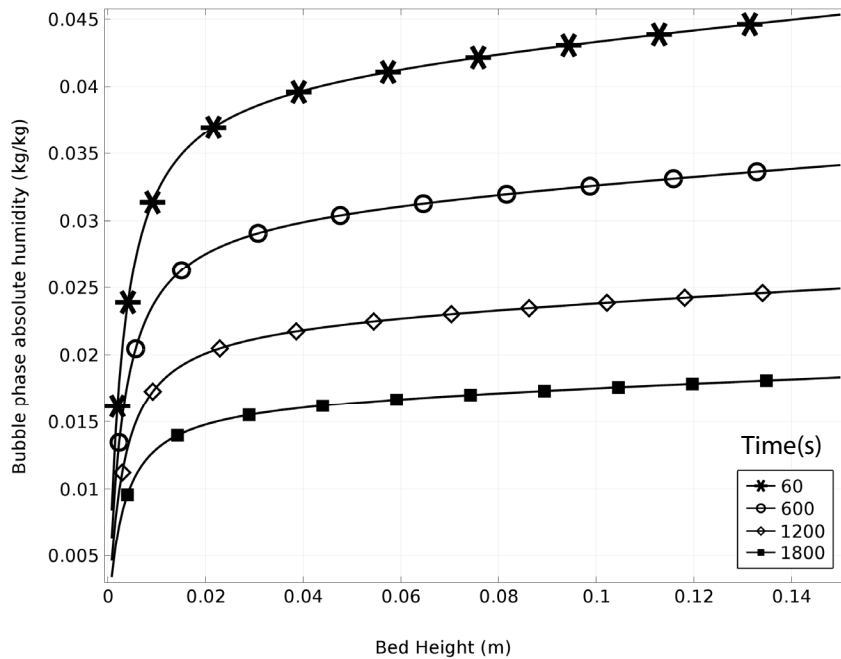


Figure A.8 Absolute humidity inside gas bubbles at different bed heights and different drying times, Douglas fir sawdust in rectangular fluidized bed, $T=20^{\circ}\text{C}$, flow rate $U/U_{mf}=1.1$.

A6. Equilibrium moisture content of biomass particles

Equilibrium moisture content (EMC) is defined as the moisture content at which the biomass is neither gaining nor losing moisture (Forest Products Laboratory, 2010). When biomass is shielded from contacting liquid water and sunlight, the moisture content is a function of both relative humidity (RH) and temperature of the surrounding air.

Equilibrium moisture content is an important parameter for biomass particles. Since drying air used in this study had less than 2% relative humidity, the equilibrium moisture contents of Douglas fir, pine and switchgrass particles in dry air ($RH < 2\%$) were tested according to ASABE S358.2 standard (ASABE, 2010). The wet biomass samples (moisture content above equilibrium moisture content) were placed in the oven at 20, 30, 40 and 50 °C until equilibrium was reached. The moisture content of the samples was then determined by oven drying at 103 °C for 24 h. Results are shown below.

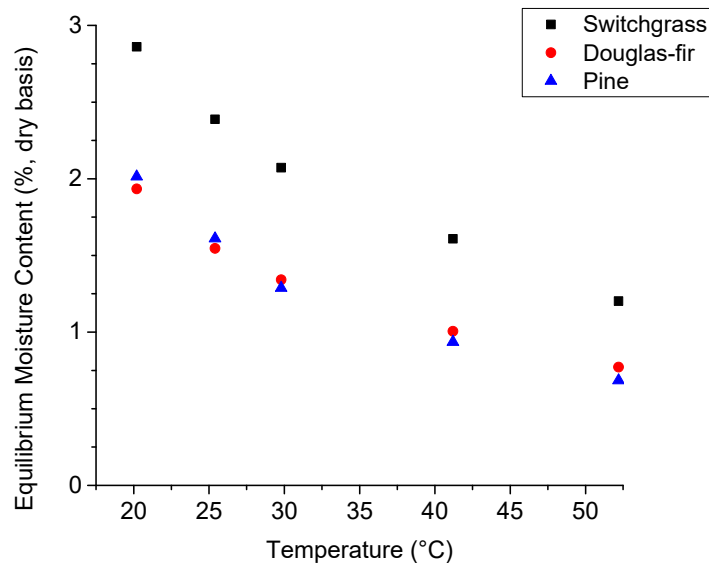


Figure A.9 Equilibrium moisture content of three biomass species at different temperatures (environment relative humidity 0.1%)

Appendix B. Heat loss estimation

In order to use the fabricated heater probe to measure heat transfer coefficient, potential heat loss from the heater probe should be made available. A simple CFD simulation was performed on the heater probe in COMSOL Multiphysics (Version 4.4). Two main modules were used, namely the heat transfer module and the fluid flow module. As can be seen from Figure B.1(a), the heater probe was simplified to a number of domains, including insulations from the top, bottom and the core, as well as thermally conductive layers such as the thermal adhesive and the copper surface. Centre of the heater was not included into this simulation as there was only a small amount of air trapped in this space. The entire numerical domain is illustrated in Figure B.1(b).

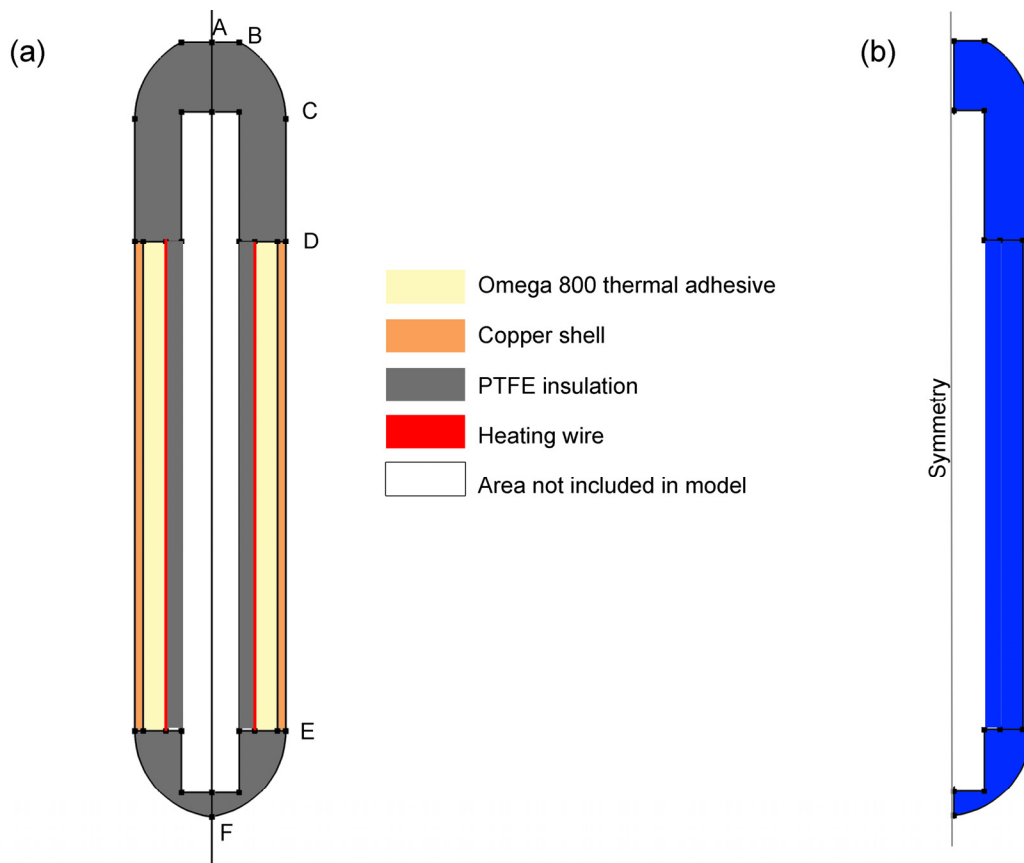


Figure B.1 Simulation domain for the heat loss estimation. (a) Simplified assembly of the heater probe for heat loss estimation; (b) Simulation domain for the heat loss estimation.

Parameters of the simulation were obtained from an experiment. In this experiment, the heater probe was mounted vertically on a ridged connection in an enclosed room and connected to the DC power supply to generate heat, so that natural convection of air could take place on the vertical surface of the probe without interference. Temperatures of multiple locations that were of interest to this study were measured and recorded, including top cap, a few points on the copper surface and the end cap.

For the numerical simulation, the same amount of heat that had been provided by the DC power supply to the heater in the experiment was set to the heating wires in the model. The temperatures measured during the experiments were set as boundary conditions. An iterative solver was chosen in COMSOL, the simulation was considered complete when the modeled temperatures matched the experimentally measured values. Both the temperature profile and velocity profile are shown in Figure B.2. More importantly, heat loss Q , or amount of heat, which was not emitted on the copper surface, but instead travelled through the insulation could be directly obtained from COMSOL.

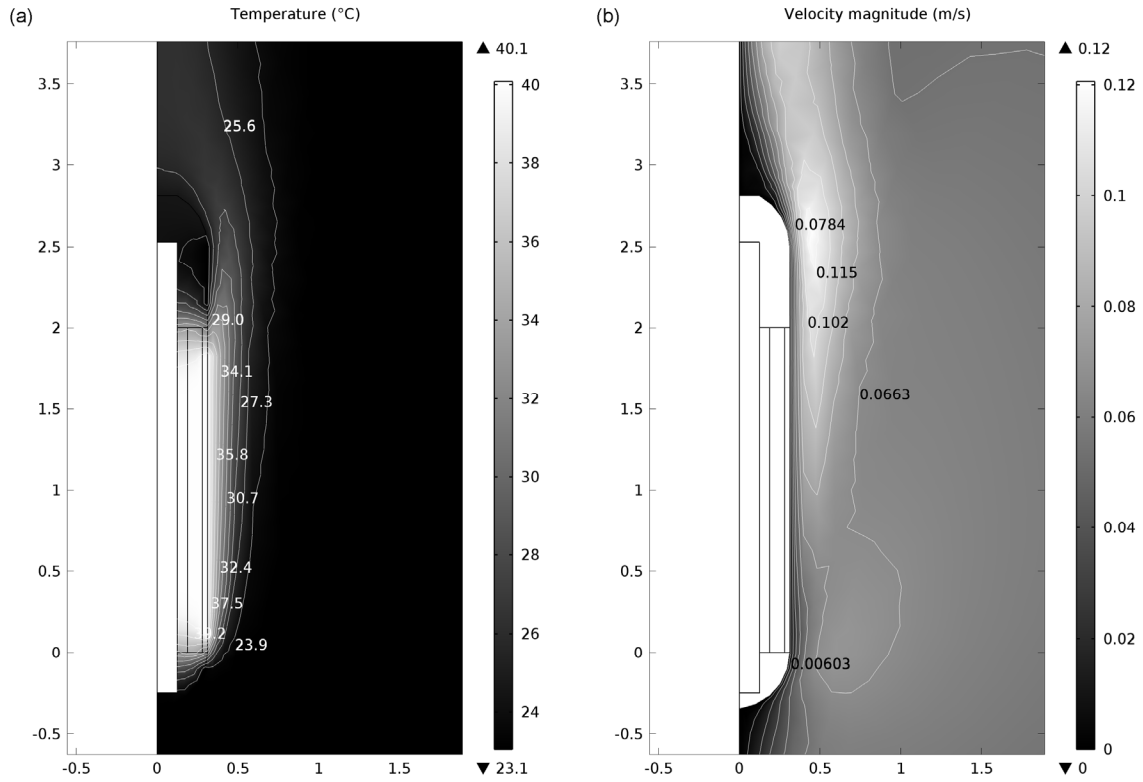


Figure B.2 Graphs from the simulation for heat loss estimation. (a) Temperature profile around and within the heater probe during natural convection; (b) Velocity profile of surrounding air during natural convection simulation.

As can be seen from Figure B.3, the majority of heat provided by the heating wires was dissipated by the copper surface via convection with surrounding air. A small percentage of heat was also conducted to the PTFE caps on both sides and dissipated to the surrounding air, which was the actual heat loss. As summarized in Table B.3, the total amount of heat lost from both the top cap and end cap was 0.046 W, while the total amount of heat provided by the power supply was 5.66 W. Consequently, the heat loss was 0.81%. Therefore, it is reasonable to have considered the heat loss negligible during the bed-to-surface heat transfer measurements.

Arrow: Temperature gradient

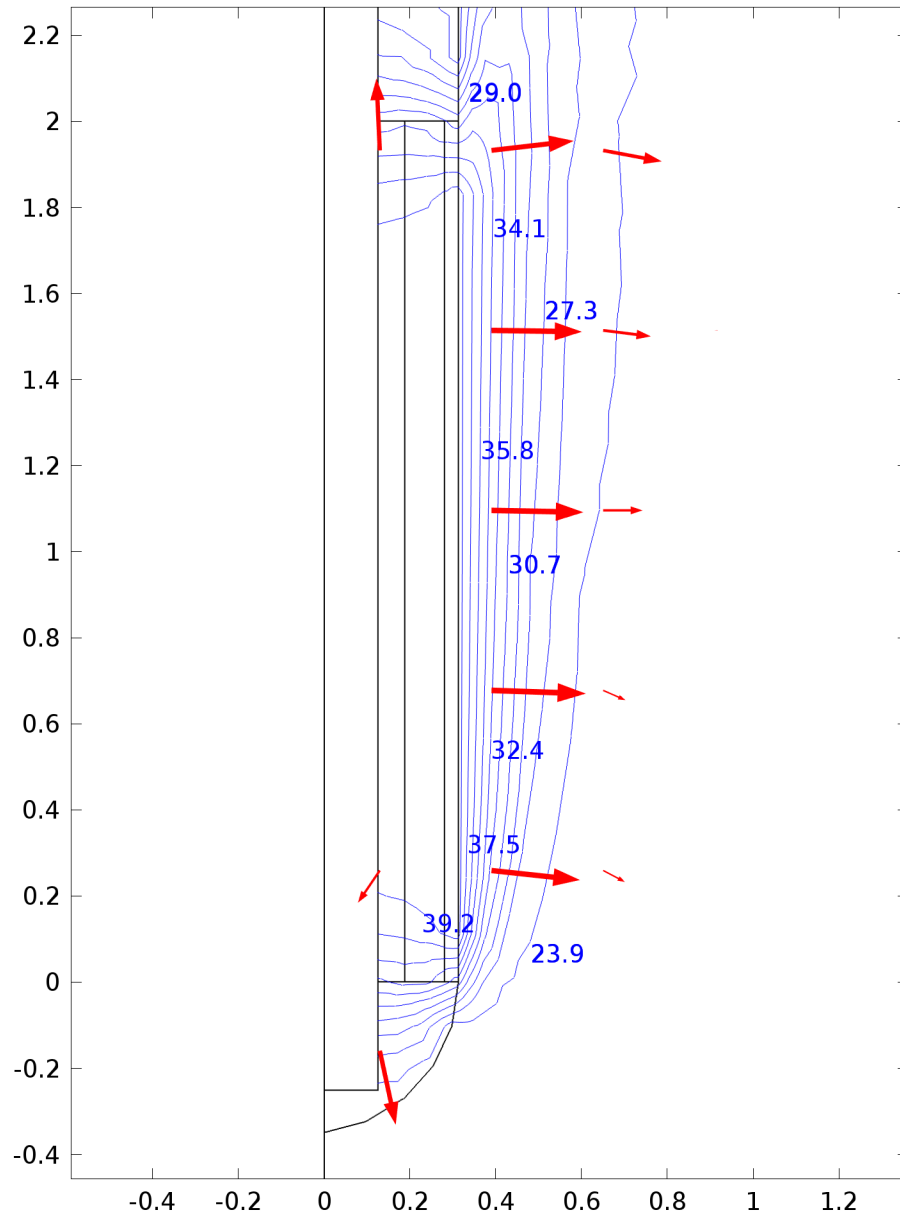


Figure B.3 Temperature gradient inside and outside the heater probe during natural convection

Table B.3 Heat loss estimation summary

	Heat Flux	Heat	Q_i	Q	Total Heat Loss
Unit	W/m ²	W	W	W	/
Top Cap	0.143	0.0245	0.046	5.66	0.81%
End Cap	0.417	0.0211			
Copper Surface	2215	5.61			

In Table B.3 the heat flux referred to the heat flux on certain parts of the probe. With known surface areas, the amount of heat emitted from the surfaces could be calculated. The heat loss was then calculated by the difference between provided heat from the power supply, and the amount emitted from the copper surface only.

Appendix C. Data acquisition system

This work includes high-speed data logging, online analysis and system automation. In order to achieve such goals, NI LabVIEW was used to perform data acquisition from multiple sources, calibrate data online, perform real-time signal processing and exert control on the solenoid valve. On the hardware side, multiple analog to digital converters (DAC) were used to import data into the computer, with details listed in Table 2.2. A universal program was written in LabVIEW so that pressure, temperature as well as relative humidity data could be displayed and recorded. In addition, real time processing of data was also included so that the standard flow rate could be converted in real time to actual flow rate based on temperature and pressure readings. Additionally, the standard deviation of pressure fluctuations, average cycle frequency (Akhavan et al., 2008) and instant drying rate were also calculated.

Appendix C1 shows the block diagram of the LabVIEW program that handled the pressure and temperature readings. The pressure readings came from the PCI DAS-08 DAC board, the voltage signals were then converted into pressure readings (PSI) with the calibration data. The data were fed to other blocks to generate standard deviation and average cycle frequencies. Temperature readings came pre-calibrated from the NI 9214 board. All data were saved to files and displayed on the computer monitor.

Appendix C2 includes the block diagram for converting relative humidity readings to instantaneous drying rates. Processes included the conversion from relative humidity to absolute humidity, as well as the flow rate conversion.

Appendix C3 contains the actual front panel/user interface of the program, which consisted multiple graphs and charts for various parameters, as well as inputs for rotameter readings.

C1. Pressure and temperature signal acquisition, display and processing

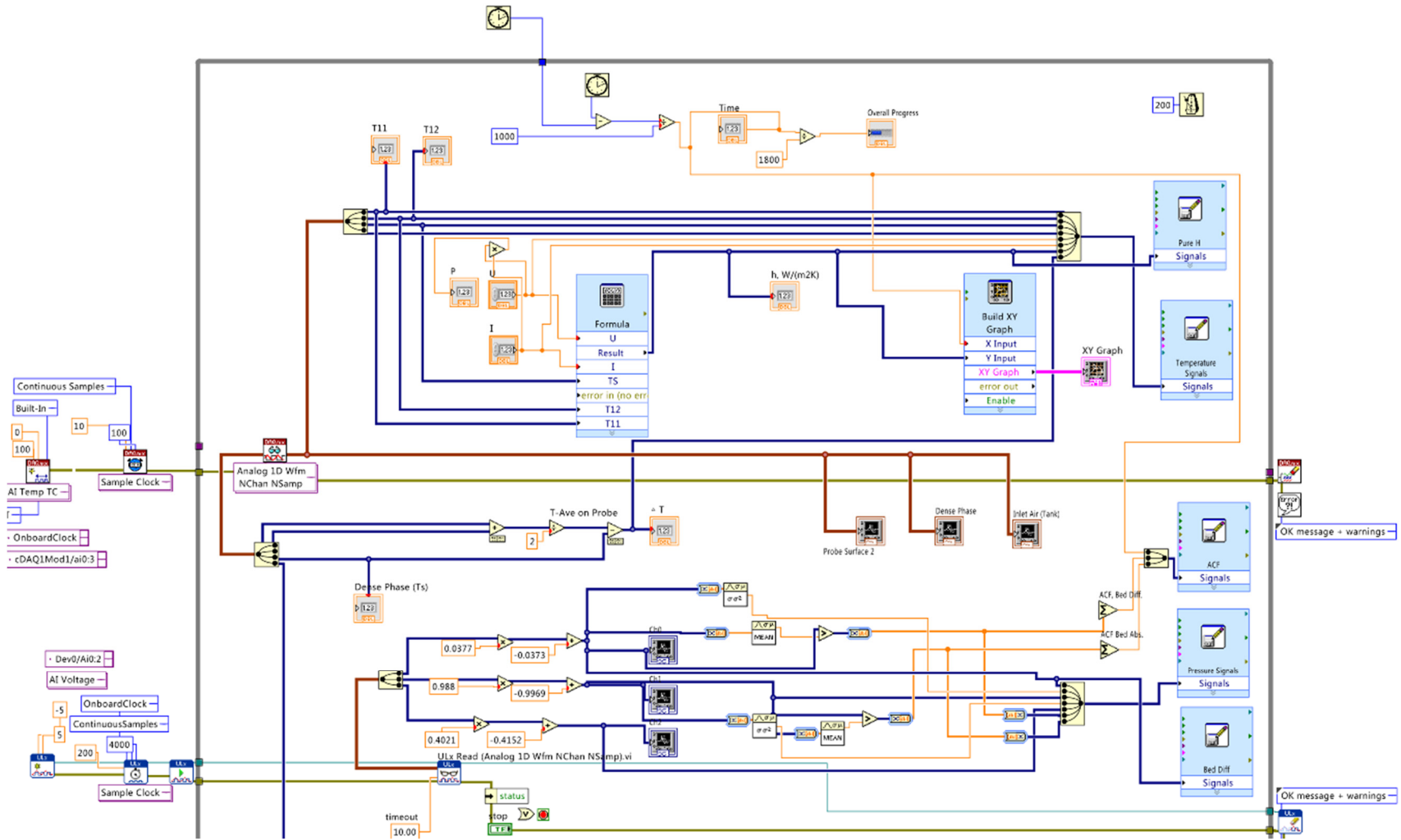


Figure C.1 Block diagram of the pressure and temperature measurement virtual instrument in LabVIEW

C2. Relative humidity and real time drying rate

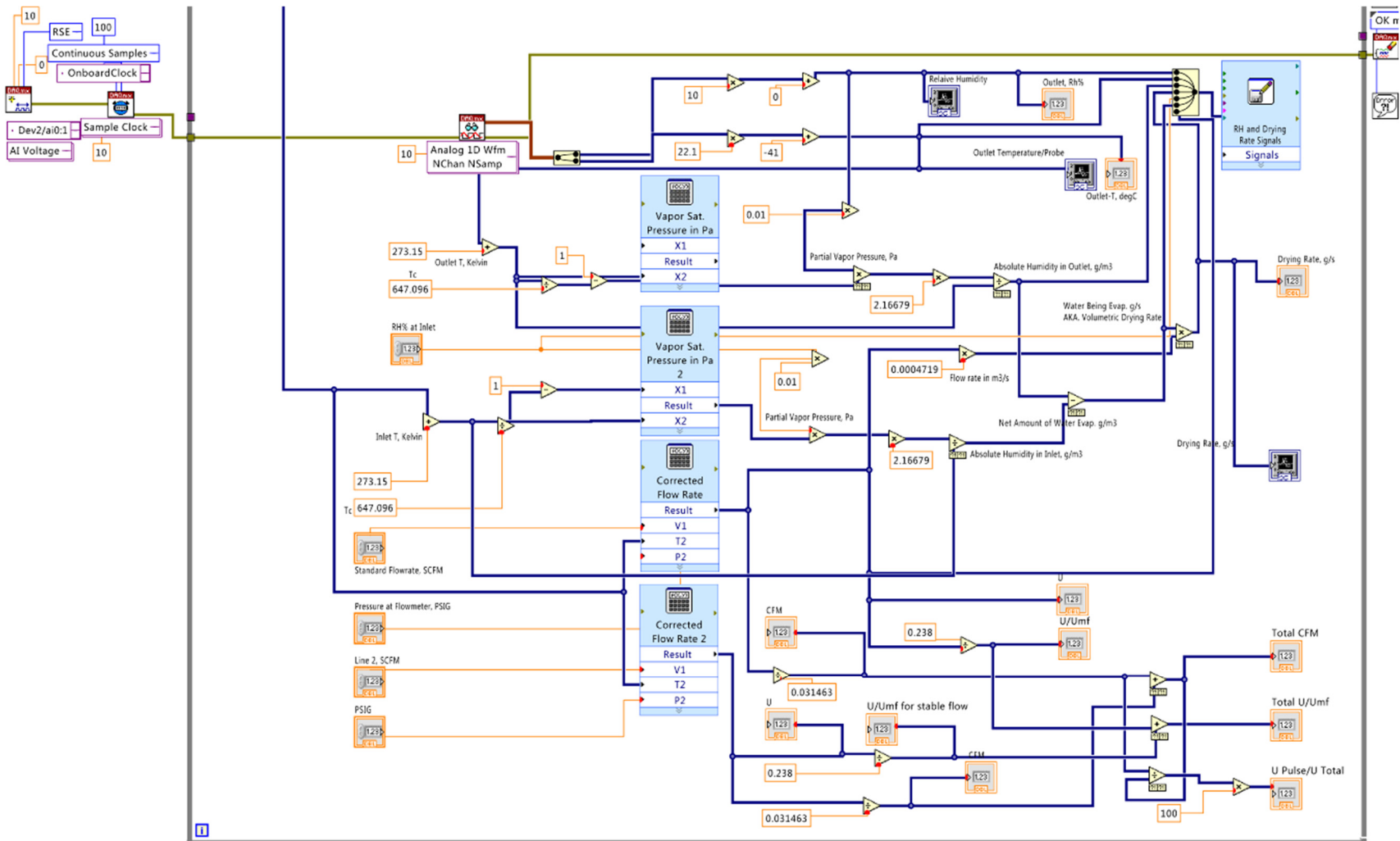


Figure C.2 Block diagram of RH and drying rate processing virtual instrument in LabVIEW

C3. Overall block diagram

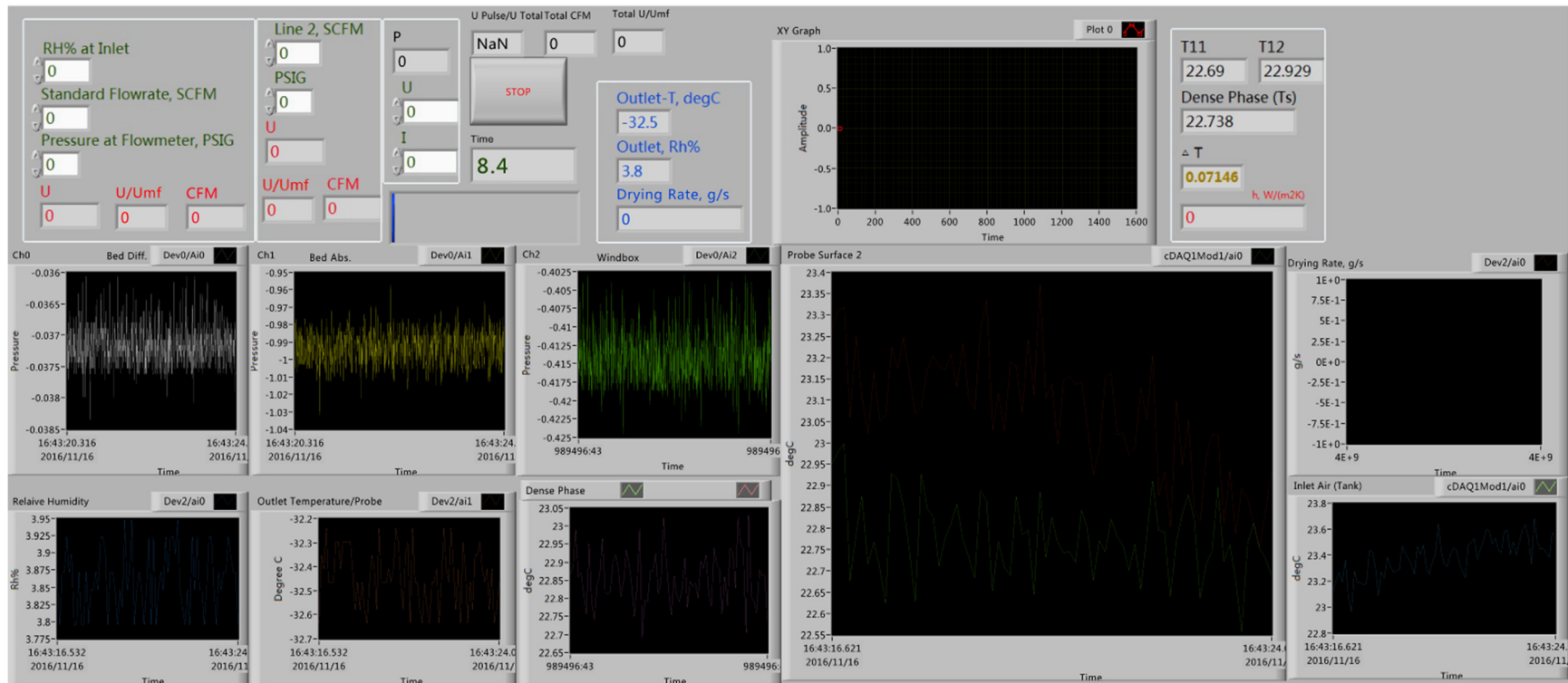


Figure C.3 Front panel of the system built in LabVIEW

Appendix D. High-speed camera images

With the correct flow rate and pulsation frequency combination, biomass could be successfully fluidized in the pulsed fluidized bed. Good gas–solid contact behaviour is discussed and illustrated in Sections 3.1 and 3.3. However, when the moisture content was extremely high, or with larger irregular particles, certain undesirable flow behaviours such as channeling, core–annulus flow and piston-like flow emerged. Snap shots of such flow behaviours captured by the high-speed camera are shown below.

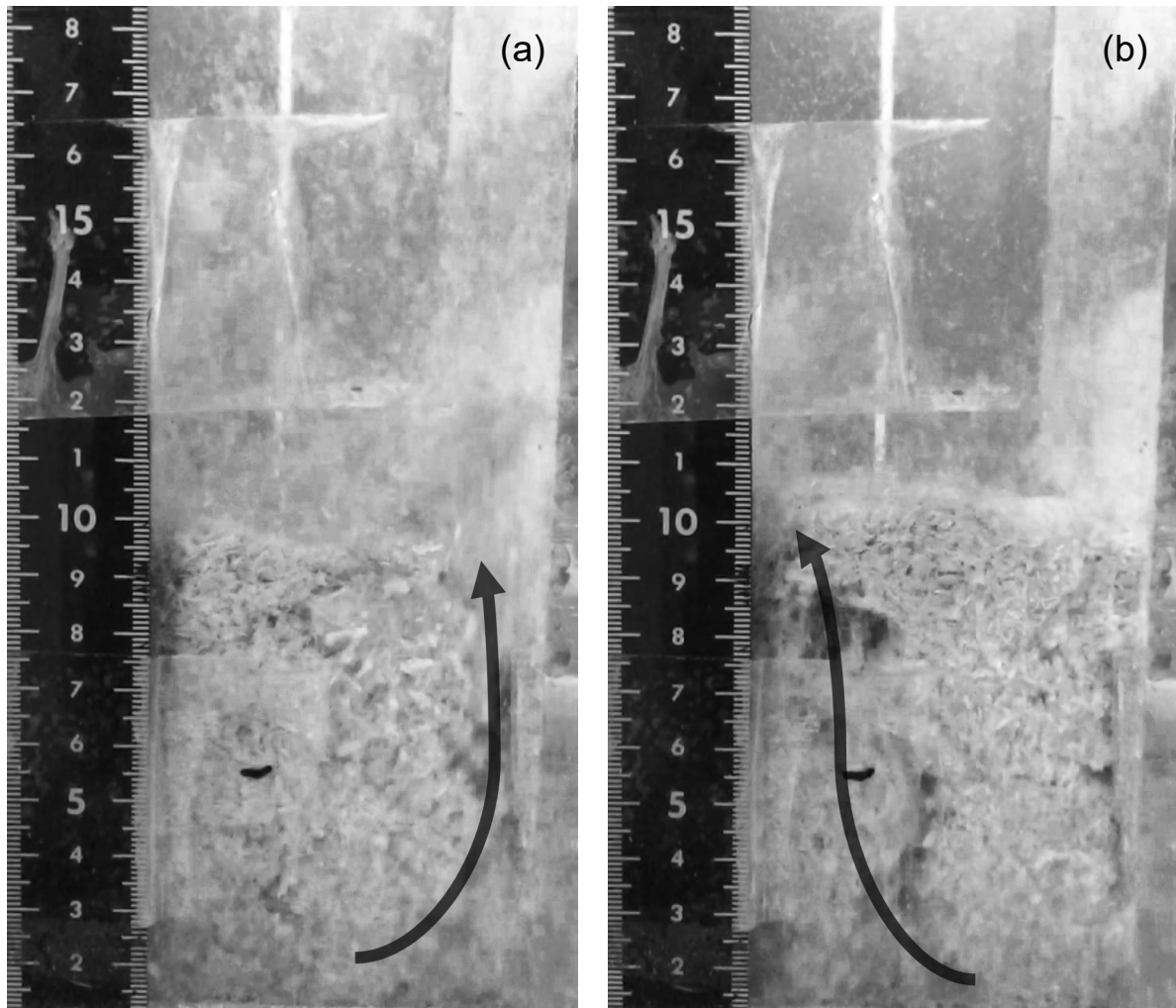


Figure D.1 Images of gas bypassing in pulsed fluidized bed

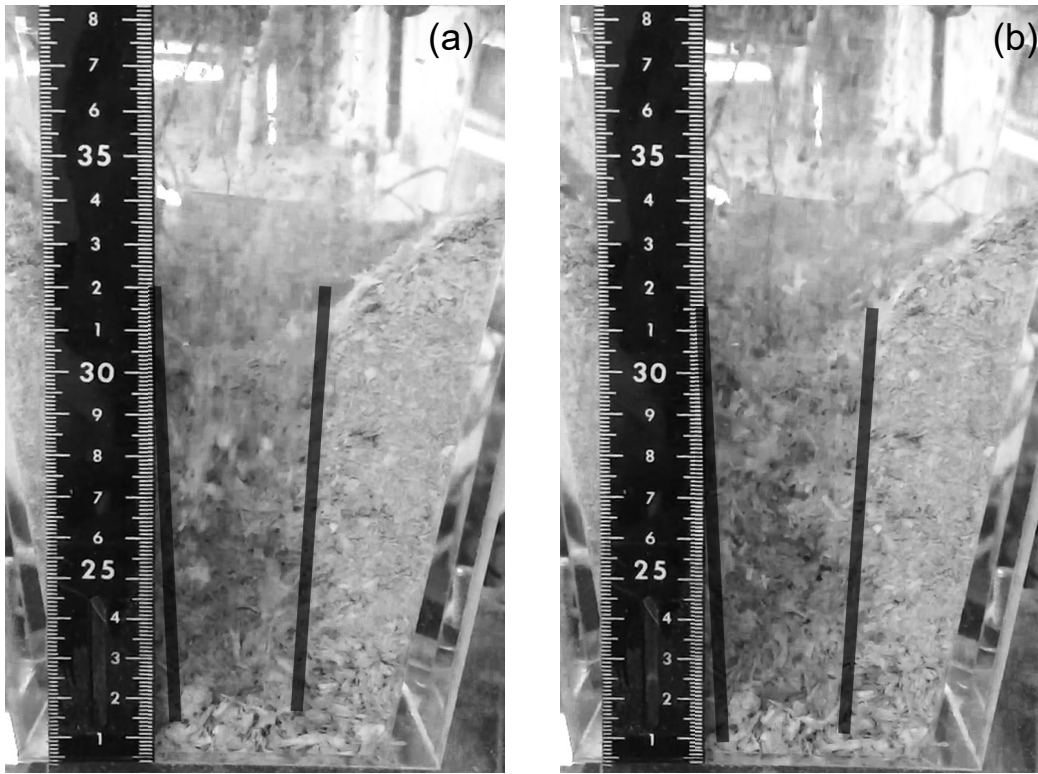


Figure D.2 Images of channeling in pulsed fluidized bed

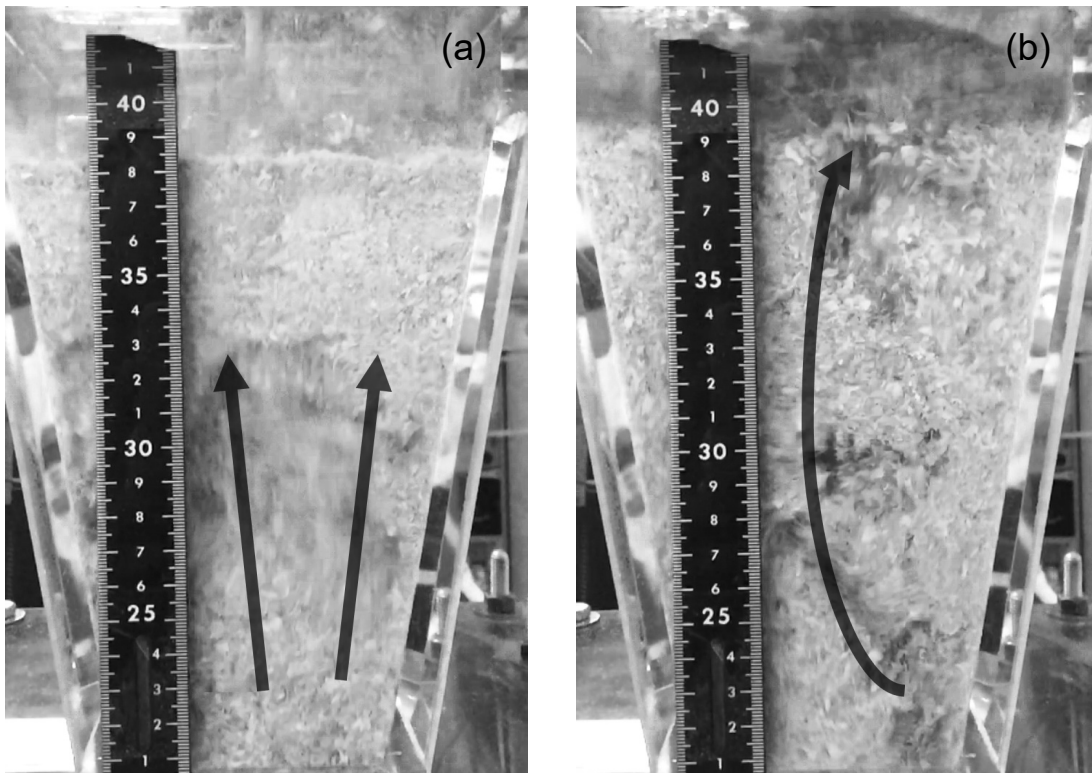


Figure D.3 Images of core-annulus flow in pulsed fluidized bed

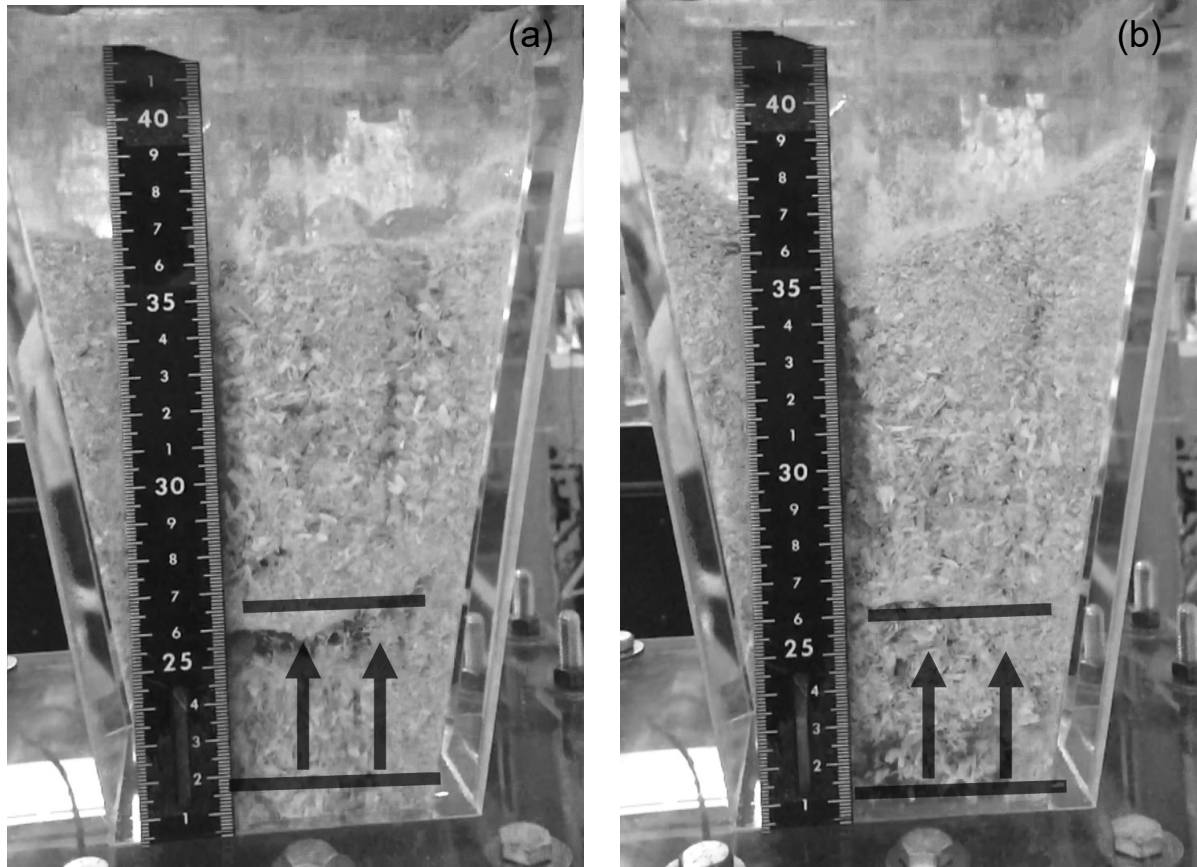
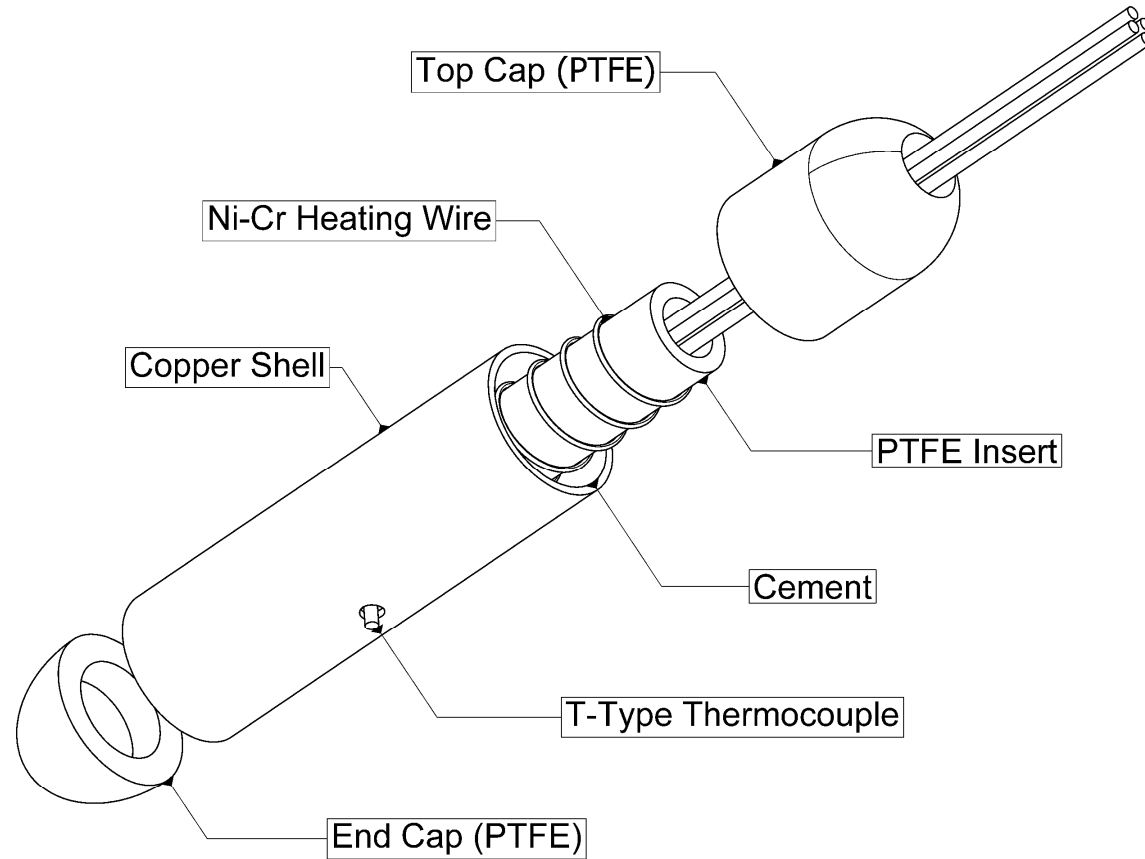


Figure D.4 Images of piston-like behaviour in pulsed fluidized bed

Appendix E. Heat transfer probe assembly

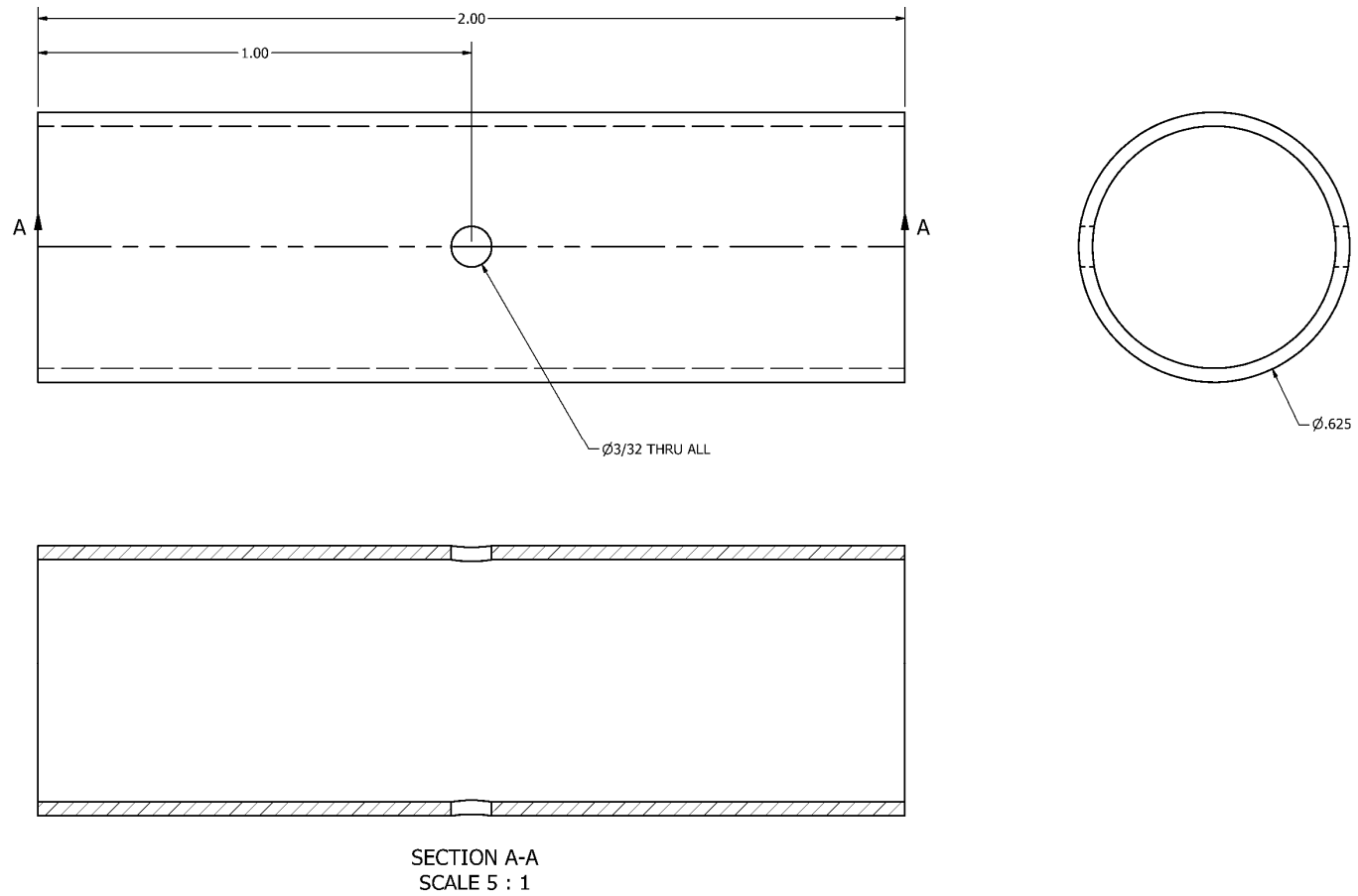
(1/7)



Unit Assembly

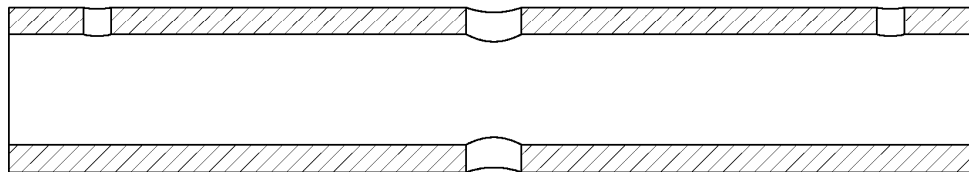
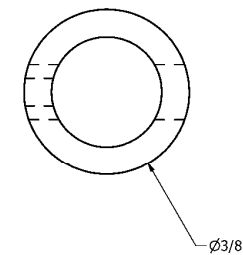
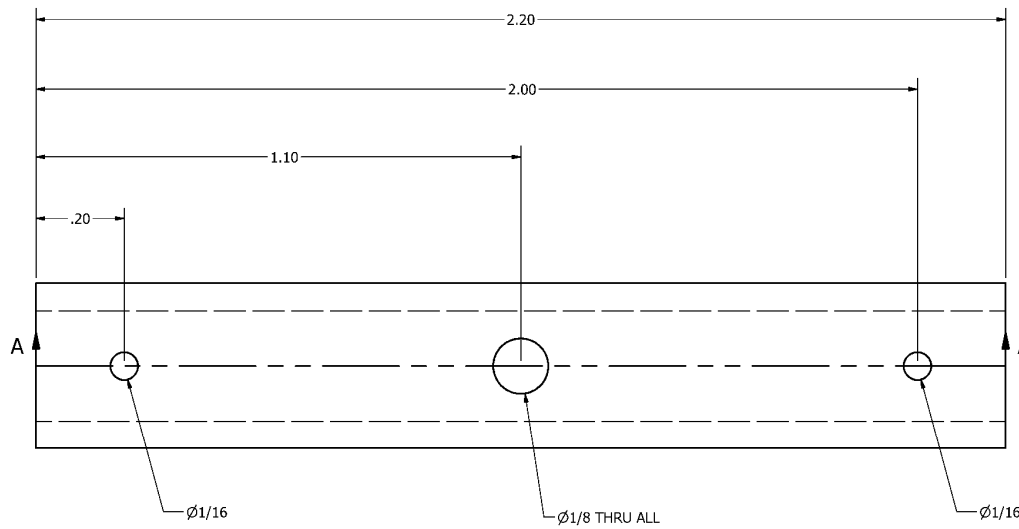
APPENDICES

(2/7)



Copper shell dimensions

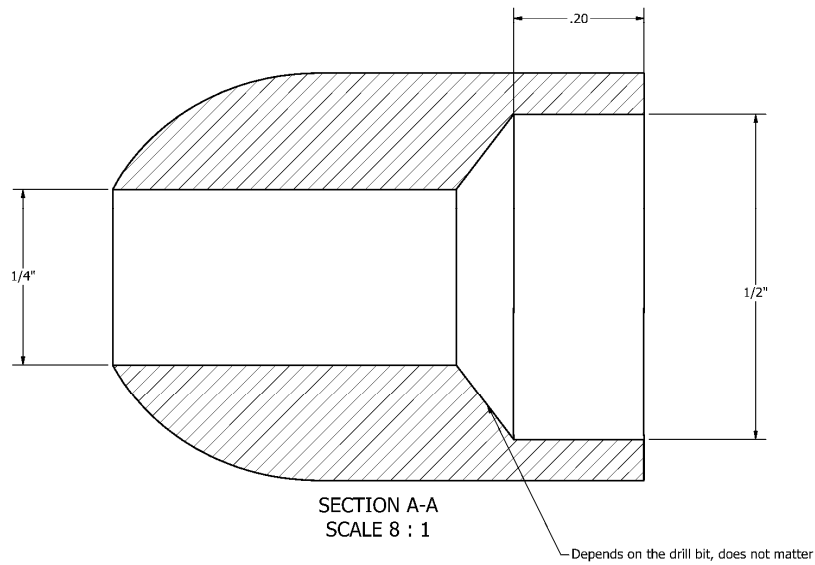
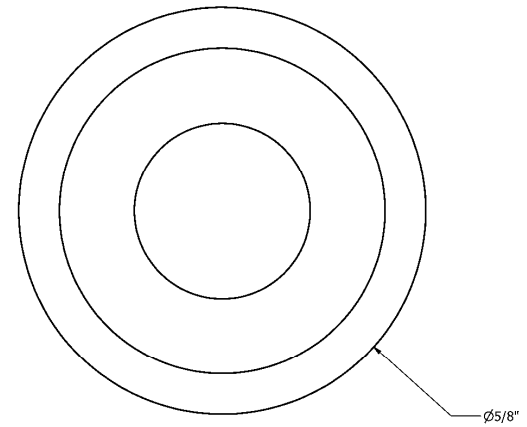
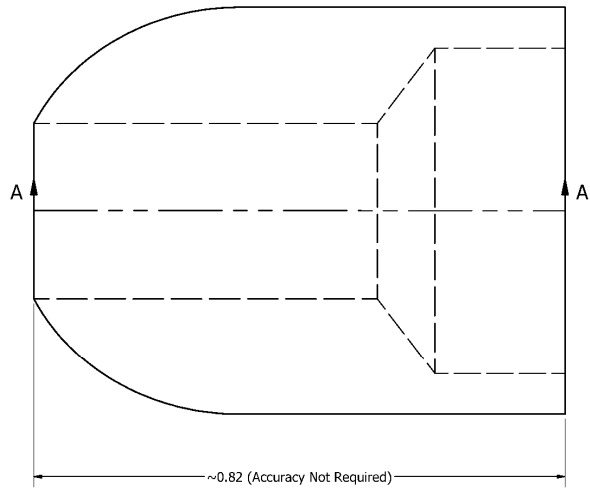
(3/7)



SECTION A-A
SCALE 5: 1

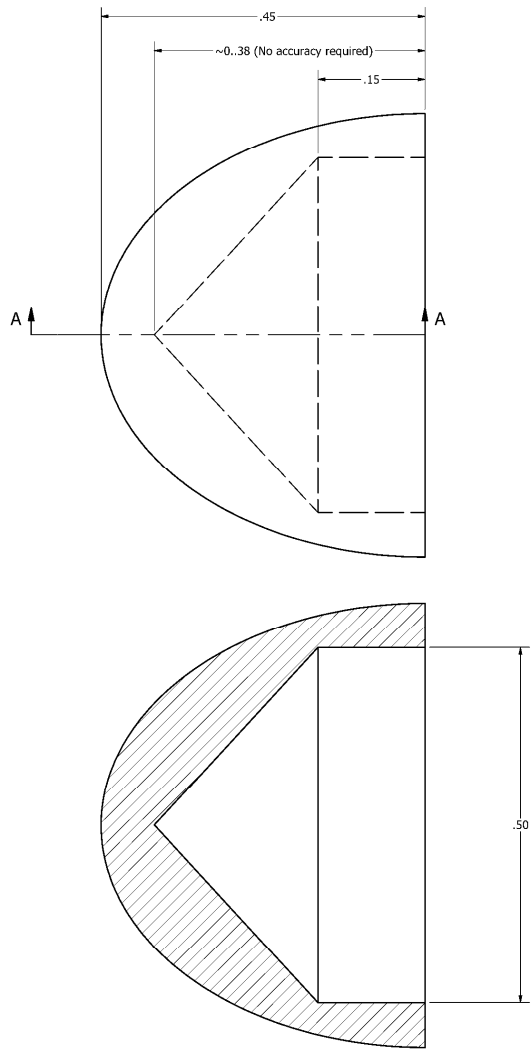
PTFE tube dimensions

(4/7)

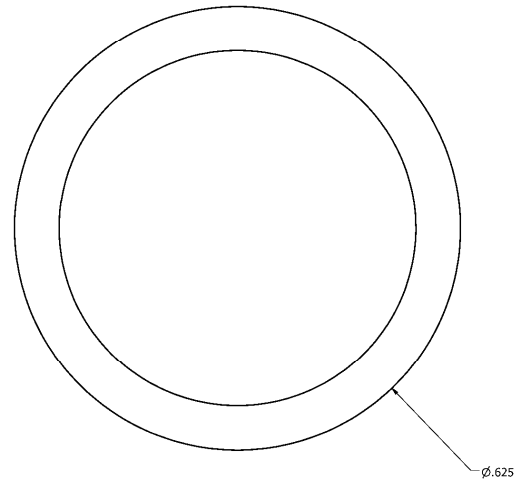


Top cap dimensions (PTFE)

(5/7)

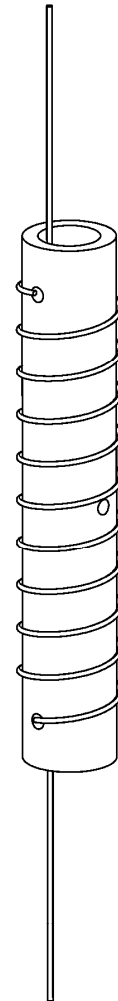
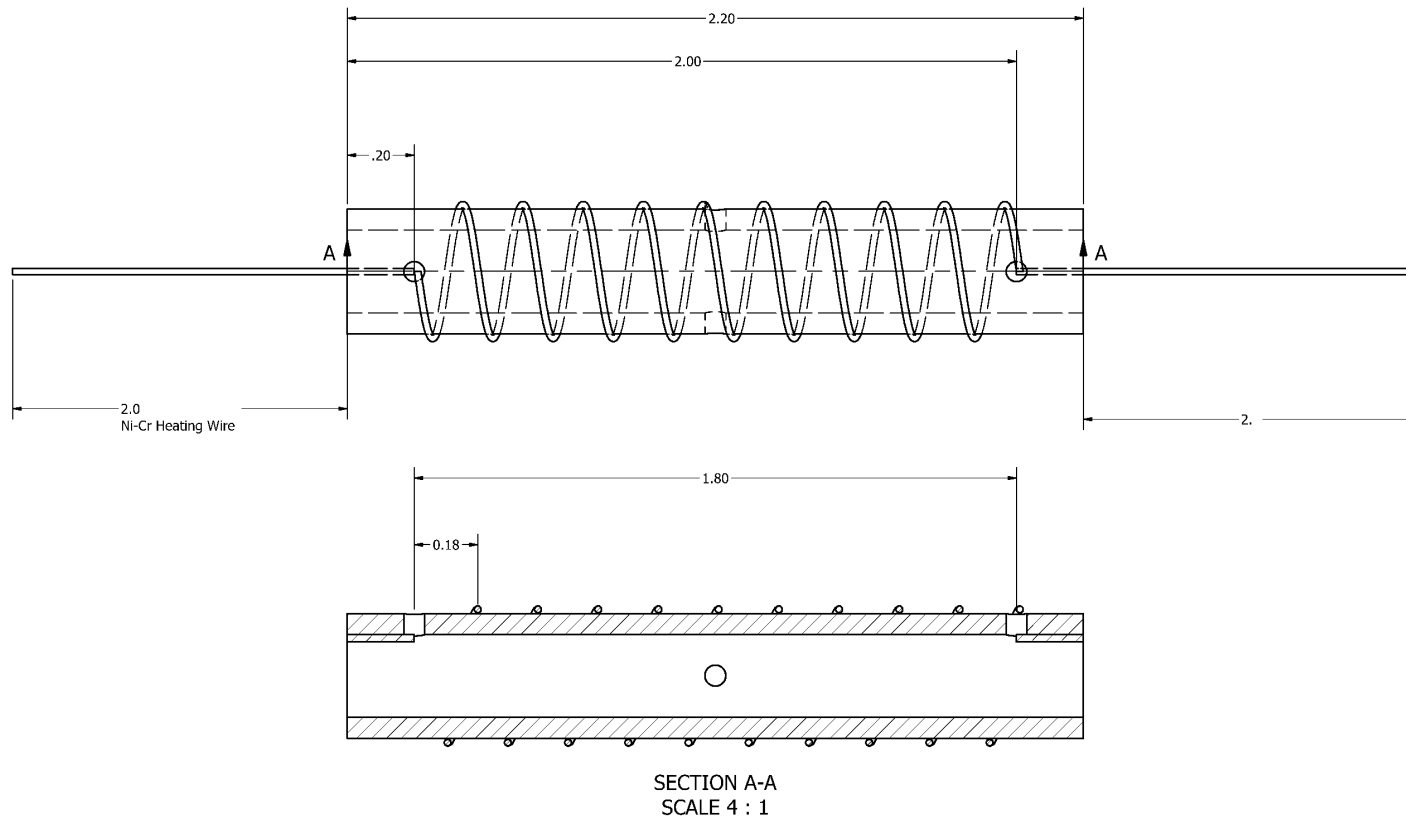


SECTION A-A
SCALE 10 : 1



End cap dimensions (PTFE)

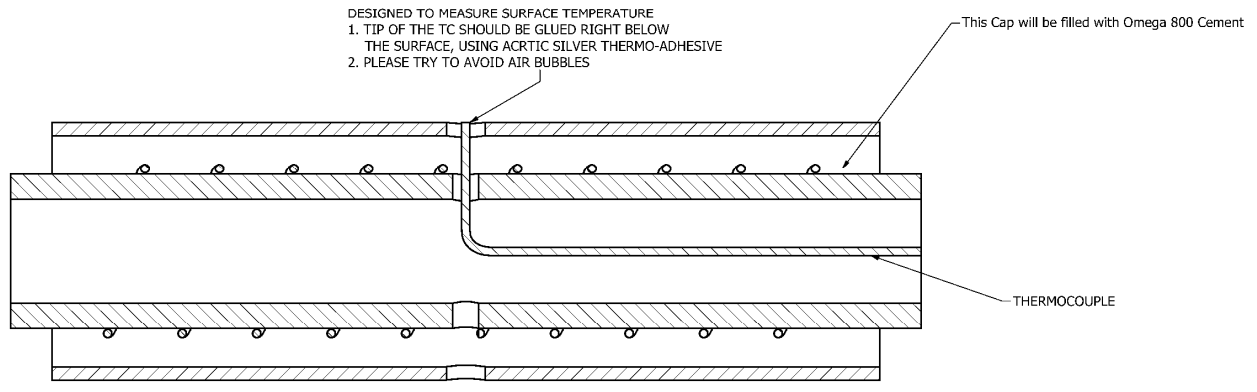
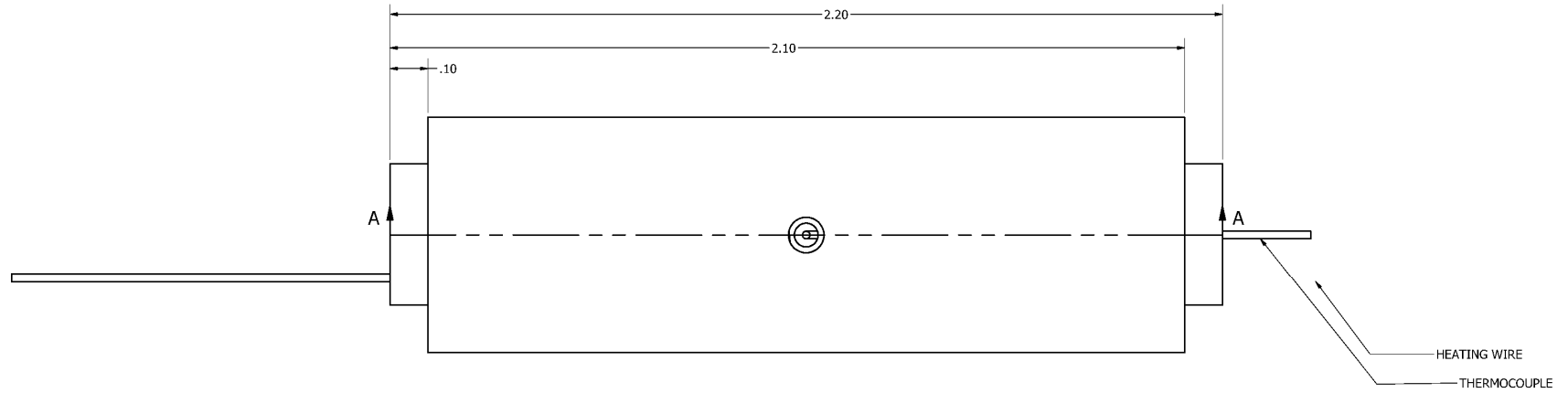
(6/7)



Heating wire assembly

APPENDICES

(7/7)



SECTION A-A
SCALE 5 : 1

Thermocouple position